Nanofiber-based spectroscopy of organic molecules

DISSERTATION

zur Erlangung des Grades
Doktor der Naturwissenschaften
am Fachbereich Physik, Mathematik und Informatik
der Johannes Gutenberg-Universität Mainz

vorgelegt von
Ariane Stiebeiner
aus Dortmund

Mainz 2013

Gutachter:
Zweit-Gutachter:

Tag der Prüfung: 9. Mai 2014

D77

Declaration of Authorship

I hereby declare that I wrote the dissertation submitted without any unauthorized external assistance and used only sources acknowledged in the work. All textual passages which are appropriated verbatim or para-phrased from published and unpublished texts as well as all information obtained from oral sources are duly indicated and listed in accordance with bibliographical rules. In carrying out this research, I complied with the rules of standard scientific practice as formulated in the statutes of Johannes Gutenberg-University Mainz to ensure standard scientific practice.

_____

Ariane Stiebeiner

Abstract

This thesis reports on the experimental realization of nanofiber-based spectroscopy of organic molecules. The light guided by subwavelength diameter optical nanofibers exhibits a pronounced evanescent field surrounding the fiber which yields high excitation and emission collection efficiencies for molecules on or near the fiber surface.

The optical nanofibers used for the experiments presented in this thesis are realized as the sub-wavelength diameter waist of a tapered optical fiber (TOF). The efficient transfer of the light from the nanofiber waist to the unprocessed part of the TOF depends critically on the geometric shape of the TOF transitions which represent a nonuniformity of the TOF. This nonuniformity can cause losses due to coupling of the fundamental guided mode to other modes which are not guided by the taper over its whole length. In order to quantify the loss from the fundamental mode due to tapering, I have solved the coupled local mode equations in the approximation of weak guidance for the three layer system consisting of fiber core and cladding as well as the surrounding vacuum or air, assuming the taper shape of the TOFs used for the experiments presented in this thesis. Moreover, I have empirically studied the influence of the TOF geometry on its transmission spectra and, based on the results, I have designed a nanofiber-waist TOF with broadband transmission for experiments with organic molecules.

As an experimental demonstration of the high sensitivity of nanofiber-based surface spectroscopy, I have performed various absorption and fluorescence spectroscopy measurements on the model system 3,4,9,10-perylene-tetracarboxylic dianhydride (PTCDA). The measured homogeneous and inhomogeneous broadening of the spectra due to the interaction of the dielectric surface of the nanofiber with the surface-adsorbed molecules agrees well with the values theoretically expected and typical for molecules on surfaces. Furthermore, the self-absorption effects due to reasorption of the emitted fluorescence light by circumjacent surface-adsorbed molecules distributed along the fiber waist have been analyzed and quantified. With time-resolved measurements, the reorganization of PTCDA molecules to crystalline films and excimers can be observed and shown to be strongly catalyzed by the presence of water on the nanofiber surface. Moreover, the formation of charge-transfer complexes due to the interaction with localized surface defects has been studied. The collection efficiency of the molecular emission by the guided fiber mode has been determined by interlaced measurements of absorption and fluorescence spectra to be about 10 % in one direction of the fiber.

The high emission collection efficiency makes optical nanofibers a well-suited tool for experiments with dye molecules embedded in small organic crystals. As a first experimental realization of this approach, terrylene-doped para-terphenyl crystals attached to the nanofiber-waist of a TOF have been studied at cryogenic temperatures via fluorescence and fluorescence excitation spectroscopy. The statistical fine structure of the fluorescence excitation spectrum for a specific sample has been observed and used to give an estimate of down to 9 molecules with center frequencies within one homogeneous width of the laser wavelength on average for large detunings from resonance. The homogeneous linewidth of the transition could be estimated to be about 190 MHz at 4.5 K.

Zusammenfassung

Die vorliegende Arbeit berichtet über Experimente zur nanofaserbasierten Spektroskopie organischer Moleküle. Optische Nanofasern mit Durchmessern unterhalb der Wellenlänge des geführten Lichts zeichnen sich durch ein starkes evaneszentes Feld der Fasermode aus. Dieses Feld umgibt die Nanofaser und ermöglicht hohe Anregungs- und Fluoreszenzsammeleffizienzen für Moleküle auf der Faseroberfläche oder in unmittelbarer Nähe der Oberfläche.

Als optische Nanofaser wird hier die Taille einer verjüngten optischen Faser (*engl. tapered optical fiber*, TOF) verwendet. Der Transfer des Lichts von der Nanofasertaille zum unbehandelten Teil der TOF hängt stark von der geometrischen Form der Verjüngungsübergänge ab. Diese Übergänge stellen eine Ungleichmäßigkeit in der Fasergeometrie dar und können zu Verlusten führen, die auf der Kopplung der geführten Grundmode an Fasermoden, die nicht über die gesamte Länge des Übergangs geführt werden, beruhen. Um diese Verluste quantitativ zu bestimmen, habe ich für die geometrischen Übergangsformen der verjüngten Fasern, die in dieser Arbeit verwendet werden, die gekoppelten Gleichungen für lokale Moden gelöst. Dafür habe ich ein Dreischichtsystem bestehend aus Faserkern und -mantel sowie der umgebenden Luft oder Vakuum in der Näherung schwacher Führung angenommen. Ferner habe ich den Einfluss der TOF-Geometrie auf die Transmissionsspektren der verjüngten Faser empirisch untersucht. Basierend auf den Ergebnissen habe ich eine verjüngte Faser mit Nanofaser-Taille und Breitbandtransmission für Experimente mit organischen Molekülen entwickelt.

Als experimentelle Demonstration der hohen Empfindlichkeit Nanofaser-basierter Oberflächenspektroskopie habe ich verschiedene Absorptions- und Fluoreszenzspektroskopiemessungen an dem Modellsystem 3,4,9,10-Perylentetracarbonsäuredianhydrid (PTCDA) durchgeführt. Die gemessene homogene und inhomogene Verbreiterung der Spektra aufgrund der Wechselwirkung der dielektrischen Nanofaseroberfläche mit den Oberflächen-adsorbierten Molekülen stimmt gut mit den theoretisch erwarteten bzw. typischen Werten überein. Außerdem habe ich die Selbstabsorption aufgrund von Reabsorption des emittierten Fluoreszenzlichts durch die umgebenden Oberflächen-adsorbierten Moleküle, die entlang der Fasertaille verteilt sind, analysiert und quantifiziert. Zeitaufgelöste Messungen wurden dafür verwendet, die Reorganisation von PTCDA-Molekülen zu kristallinen Filmen und Excimeren auf der Faseroberfläche zu beobachten und die stark katalysierende Wirkung von Wasser auf der Faseroberfläche für diese Prozesse zu zeigen. Ferner habe ich die Bildung von Ladungstransferkomplexen durch die Wechselwirkung der Moleküle mit lokalisierten Oberflächendefekten untersucht. Die Sammeleffizienz für molekulare Emission konnte durch abwechselnde Messung von Absorption und Fluoreszenz zu ungefähr 10 % bestimmt werden.

Durch die hohe Fluoreszenzsammeleffizienz sind optische Nanofasern sehr gut für Experimente mit Farbstoffmolekülen, die in organische Kristalle eingebettet sind, geeignet. Als erste experimentelle Realisierung dieses Ansatzes wurden Terrylen-dotierte para-Terphenyl-Kristalle auf die Nanofasertaille einer TOF aufgebracht und bei kryogenen Temperaturen mittels Fluoreszenz- und Fluoreszenzanregungsspektroskopie untersucht. Anhand der statistischen Feinstruktur des Fluoreszenzanregungsspektrums einer Probe wurde abgeschätzt, dass die Anzahl von Molekülen mit einer Übergangsfrequenz innerhalb einer homogenen Linienbreite der Anregungswellenlänge durch weite Verstimmung von der Resonanz auf ca. 9 reduziert werden kann. Die homogene Linienbreite des Übergangs konnte zu ungefähr 190 MHz bei 4.5 K abgeschätzt werden.

Publications

Parts of this thesis have been published in the following peer-reviewed journal articles:

- A. Stiebeiner, O. Rehband, R. Garcia-Fernandez, and A. Rauschenbeutel, *Ultra-sensitive fluorescence spectroscopy of isolated surface-adsorbed molecules using an optical nanofiber*, Opt. Express **17**, 21704–21711 (2009).
- A. Stiebeiner, R. Garcia-Fernandez, and A. Rauschenbeutel, *Design and optimization of broadband tapered optical fibers with a nanofiber waist*, Opt. Express **18**, 22677–22685 (2010).
- R. Garcia-Fernandez, W. Alt, F. Bruse, C. Dan, K. Karpetyan, O. Rehband, A. Stiebeiner, U. Wiedemann, D. Meschede, and A. Rauschenbeutel, *Optical nanofibers and spectroscopy*, Appl. Phys. B **105**, 3–15 (2011).

Contents

Introduction

The interaction between light and matter has been one of the main research topics in physics over the last century. Persistent efforts to improve the interaction efficiency have led to a deep understanding of the nature of light and matter down to the fundamental level of single quantum systems.

Moreover, an efficient and highly controlled light-matter interaction paves the way for fascinating applications in quantum information processing, like the utilization of single quantum systems as light sources or for the storage of information in their internal degrees of freedom. Here, single organic molecules trapped in a transparent organic crystal are of particular interest. As solid state emitters, they are robust and easy to localize, while their very small size permits a much higher emitter density than possible for larger systems like quantum dots or diamond nanocrystals containing color centers [1]. In addition, the resonance frequency of single organic molecules can be controlled via the Stark effect by applying a local electric field, as has been experimentally demonstrated recently [2].

Most approaches tackling the enhancement and control of the interaction between light and matter rely on modifying or storing the light field. Here, the most widely pursued approch is the use of resonant structures, like Fabry-Pérot, whispering-gallery-mode (WGM), or photonic crystal resonators [3]. These structures provide a three-dimensional confinement of the light field and, thereby, an increased coupling probability. The importance of this approach is reflected in the award of half of the 2012 Nobel prize in physics to Serge Haroche [4]. However, also two-dimensional confinement of the light field, like, for instance, in a strongly focussed laser beam [5, 6], can be employed for the enhancement of the interaction.

In this context, optical nanofibers offer highly attractive properties for interfacing light and matter. Due to their sub-wavelength diameter, they exhibit a strong radial confinement of the guided mode and a pronounced evanescent field surrounding the nanofiber [7]. If the optical nanofiber is realized as the waist of a tapered optical fiber (TOF), the coupling of light into and out of the nanofiber waist is readily achieved via the TOF taper transitions. This approach offers the additional advantage of a low-loss transmission of the light before and after the interaction. These properties open the route for a wide range of applications [8], including, but not limited to optical sensing [9–11], nonlinear optics [12–18], nanofiber-based dye lasers [19, 20], and cold atom physics [21–25].

Another promising application of TOFs with a nanofiber waist is evanescent wave spectroscopy [26]. In previous experiments, it has been demonstrated that the sensitivity of nanofiber-based surface absorption spectroscopy (SAS) exceeds the sensitivity of free-beam SAS by several orders of magnitude [27]. For surface-adsorbed organic molecules, the optical properties depend strongly on their interactions with the surface and the circumjacent molecules. This is particularly interesting for the study of thin films of organic semiconductors where a high degree of interaction is advantageous for the required high mobility of charge carriers [28].

In the context of quantum information processing, molecules that are efficiently coupled to the guided nanofiber mode can be used as sources of optical nonlinearity. It has been shown for dibenzanthanthrene embedded in n-hexadecane that a single molecule can attenuate a

strongly focussed laser beam by more than 10 % [29] or affect a phase shift greater than 3 ° on the laser beam [30].

For the realization of nanofiber-based single photon sources, both, the excitation of a single molecule in the evanescent field of the nanofiber as well as the fluorescence collection from this molecule via the nanofiber-based interface and the TOF transitions, have to be highly efficient. Theoretically, about 20 % of the fluorescence from a single dipole emitter on the nanofiber surface is expected to be coupled back into the guided mode of the nanofiber [31]. For single quantum dots, coupling efficiencies between 7 % and 22 % have been measured [32, 33]. More recently, the couling efficiency of a single nitrogen vacancy center hosted in a diamond nanocrystal to the nanofiber waist of a TOF of 6.8 % has been achieved [34].

Various non-deterministic approaches to the deposition of solid state emitters onto the nanofiber waist of a TOF have been developed [32, 33, 35]. However, the highly accurate sample preparation remains a challeging task. Only this year, the on-demand positioning of a single nanocrystal onto the nanofiber waist has been realized [34].

In this work, I demonstrate that tapered optical fibers are a well-suited tool for experiments with organic molecules. While the coupling of molecules on or near the nanofiber surface to the guided light field is significantly enhanced due to the properties of the nanofiber, the overall efficiency of the TOF as a fiber coupled interface is also influenced by the efficiency of coupling light into and out of the nanofiber waist. This efficiency depends critically on the shape of the TOF taper transitions. Therefore, in the first part of this thesis, I present detailed theoretical and experimental studies of the transmission properties of tapered optical fibers with a nanofiber waist.

In the second part of my work, I show various absorption and fluorescence spectroscopy measurements on the model system 3,4,9,10-perylene-tetracarboxylic dianhydride (PTCDA). The experimental results demonstrate the high collection efficiency of the guided nanofiber mode for the fluorescence emitted by surface-adsorbed molecules. In order to utilize the robustness of solid states systems, first experiments with dye-doped organic crystals attached to the nanofiber-surface are performed and discussed in the third part of this thesis. For this purpose, terrylene-doped para-terphenyl crystals are grown from solution and placed on the nanofiber surface from a drop of this solution. I present fluorescence and fluorescence exitation spectroscopy studies of these nanofiber-crystal-samples at low temperatures where the homogeneous linewidth of the terrylene molecules is significantly reduced. This opens the route towards nanofiber-based single molecule spectroscopy at cryogenic temperatures and the realization of building blocks for quantum information processing.

1. Light propagation in tapered optical fibers

Optical glass fibers have become the most important medium for data transmission in the modern communication society. The realization of low-loss fibers in 1970 [36] has opened the route to low-loss and low-disturbance optical communication over long distances [37]. Figure 1.1(a) shows the structure of a circular step-index single mode fiber. This type of fiber is widely used in telecommunications and for scientific purposes. Typically, the cladding has a radius b of 62.5µm and consists of pure silica (SiO_2). The core has a radius a of a few micrometers and is doped with germanium ions to increase the refractive index by about 1 %. The difference between the refractive indices of core, n_{core}, and cladding, n_{cladding}, determines the numerical aperture NA of the fiber which characterizes the coupling of light into the fiber [38]:

$$\mathrm{NA} = \sqrt{\mathrm{n}_{\mathrm{core}}^2 - \mathrm{n}_{\mathrm{cladding}}^2}. \tag{1.1}$$

The resulting refractive index profile of a fiber surrounded by vacuum is schematically depicted in Fig. 1.1(b). The increase of the refractive index at the interface between cladding and core causes the light inside the core to be totally internally reflected and, therefore, to be radially confined to the core. However, due to the boundary conditions for electromagnetic fields at the interface, the light will penetrate the cladding in form of an evanescent field. This evanescent field propagates inside the cladding along the fiber with its intensity decaying approximately exponentially with increasing distance from the interface. Since the radius of the cladding is large compared to the decay length of the evanescent field, the light does not reach the interface between cladding and vacuum. As a result, there is no interaction between the guided light and the surroundings of the fiber. The light is thus isolated from the environment by the cladding.

In contrast, optical nanofibers do not provide any isolation of the light from the environment. Here, the light is guided by total internal reflection at the interface between a

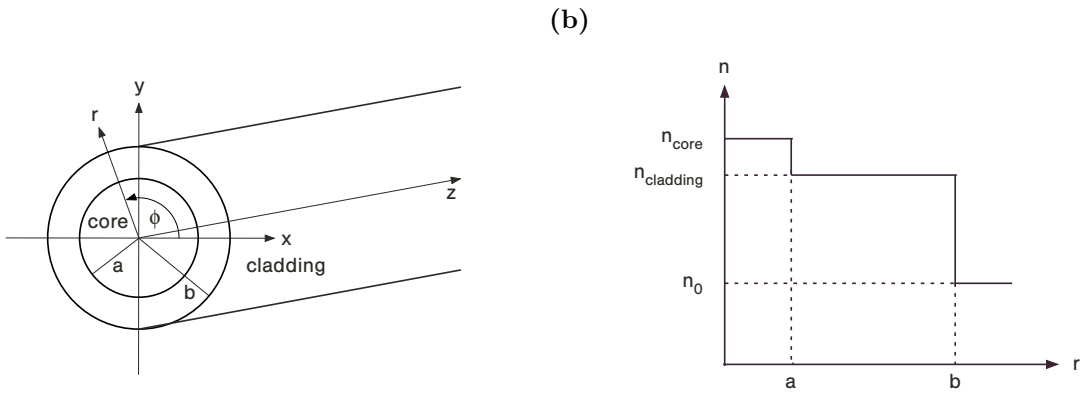

Figure 1.1.: a) Geometric structure of a circular step-index optical fiber. b) Refractive index profile of a step-index fiber as a function of the distance from the fiber axis. n_0 denotes the refractive index of the medium surrounding the fiber. The diagrams are not to scale.

sub-wavelength diameter cylindric silica rod and the surrounding medium. Such fibers therefore exhibit a strong radial confinement of the guided mode and a pronounced evanescent field surrounding the fiber [7]. This makes them well suited for the efficient and controlled interaction of the guided light with matter on or near the fiber surface.

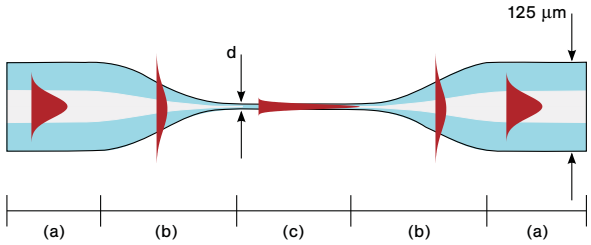

Figure 1.2.: Schematic of a tapered optical fiber (TOF) indicating the mode conversion from the unprocessed fiber (a) via the taper transition (b) to the nanofiber waist with a sub-wavelength diameter d and back. The intensitiy distribution of the guided mode is schematically represented by the filled curves

Optical nanofibers can be realized as the sub-wavelength diameter waist of a tapered optical fiber (TOF), fabricated by flame pulling of a commercial single mode optical fiber [15,39–44]. Such a TOF consists of three sections shown schematically in Fig. 1.2: the unprocessed fiber (a) at both ends of the TOF, the two taper transitions (b) in which the fiber is narrowed down to the desired sub-wavelength diameter d, and the nanofiber waist (c). In the first taper transition, the core-guided mode of the unprocessed fiber is transformed into the cladding-guided mode of the nanofiber due to the geometric change of the refractive index profile of the fiber. At the second taper transition, the mode transformation is reversed. The intensity distribution of the corresponding guided mode is schematically represented by filled curves in Fig. 1.2. In order to use this process to efficiently couple light into and out of the nanofiber, this mode conversion should be adiabatic, i.e., there should be no coupling of the fundamental mode to higher transverse or radiative modes. This is achieved by maintaining shallow taper angles of a few milliradians [45,46].

This chapter will discuss the light propagation properties of the three sections of a TOF surrounded by vacuum or air. For this purpose, it is assumed that each section of such a TOF can be represented by a refractive index profile that consists of three layers: the core with radius a and refractive index n_{core}, the cladding with radius b and refractive index n_{cladding}, and the surrounding vacuum with refractive index $n_0 = n_{\text{vac}} = 1$, as schematically shown in Fig. 1.1(b).

In the unprocessed optical fiber, the light is confined to the core with the evanescent field leaking out into the cladding, but not reaching the interface between cladding and vacuum. Thus, the influence of the surrounding vacuum is negligible and the system can be simplified to a two layer system consisting only of core and cladding.

In the nanofiber waist of a tapered optical fiber, the radius of the core becomes negligibly small, resulting in an effective two layer system consisting of cladding and surrounding vacuum.

In the transistion regions of a tapered optical fiber, however, the modes are transferred from the core to the cladding. Here, the full three layer system has to be taken into account, since the core is not yet small enough to be neglected, but the mode already penetrates the vacuum outside the fiber.

For all three sections of the TOF, Maxwell's equations for the electric and magnetic field vectors $\vec{E}$ and $\vec{H}$, respectively, in a charge- and current-free medium need to be solved. Due to the symmetry of the system, Maxwell's equations in cylindrical coordinates can be used [37]:

$$\vec{\nabla} \times \vec{H} = \varepsilon(r)\frac{\partial \vec{E}}{\partial t}, \tag{1.2}$$

$$\vec{\nabla} \times \vec{E} = -\mu_0\frac{\partial \vec{H}}{\partial t}, \tag{1.3}$$

$$\vec{\nabla} \cdot (\varepsilon(r)\vec{E}) = 0, \tag{1.4}$$

$$\vec{\nabla} \cdot \vec{H} = 0. \tag{1.5}$$

Here, all three layers are assumed to have a magnetic permeability equal to the vacuum permeability μ_0. The respective refractive index profile for each section of the TOF is taken into consideration by the radius dependent permittivity $\varepsilon(r) = n^2(r)\varepsilon_0$, where ε_0 is the vacuum permittivity. From Eqns. (1.2)–(1.5), the vector wave equation of the fields

$$\vec{\nabla}^2\vec{E} - \mu_0\varepsilon(r)\frac{\partial^2\vec{E}}{\partial t^2} = -\vec{\nabla}(\frac{\vec{E}}{\varepsilon(r)} \cdot \vec{\nabla}\varepsilon(r)) \tag{1.6}$$

can be deduced. The form of the vector wave equation for the magnetic field vector is identical to Eq. (1.6) and will not be explicitly given. In the following, the wave equation will be solved for the three different sections of the TOF.

1.1. Unmodified standard optical fibers

For the two layer system of a standard optical fiber consisting only of core and cladding, the vector wave equation given by Eq. (1.6) can be solved exactly. Here, the solution will only be discussed briefly, closely following the detailed treatment in [37] and [47].

1.1.1. Solution of the vector wave equation

Since the refractive index profile of a standard optical fiber does not change along the fiber, $\partial\varepsilon(r)/\partial z$ vanishes. Therefore, the vector wave equations can be solved for the components E_z and H_z by using the following ansatz:

$$\begin{bmatrix} E_z(\vec{r},t) \\ H_z(\vec{r},t) \end{bmatrix} = R(r)\exp[i(\omega t - \beta z \pm l\phi)], \tag{1.7}$$

where β is the axial propagation constant of the field, ω the angular frequency, and $l = 0, 1, 2, ...$ With the wavenumber of the light field $k(r) = n(r)k_0 = n(r)\omega\sqrt{\mu_0\varepsilon_0}$, Eq. (1.6) becomes the Bessel differential equation for the radial functions $R(r)$:

$$\Big[\partial_r^2 + \frac{1}{r}\partial_r + (k^2(r) - \beta^2 - \frac{l^2}{r^2})\Big]R(r) = 0. \tag{1.8}$$

Since the light does not leak out of the fiber, the axial propagation constant β of a guided mode has to lie within the range of values given by

$$n_{\text{clad}}k_0 \leq \beta \leq n_{\text{core}}k_0. \tag{1.9}$$

In the fiber core, where $h^2 := k^2 - \beta^2 \geq 0$, the solution for the z-components of the fields is given by

$$\begin{bmatrix} E_z(\vec{r},t) \\ H_z(\vec{r},t) \end{bmatrix} \propto J_l(hr)\exp[i(\omega t - \beta z \pm l\phi)]. \tag{1.10}$$

J_l denotes the Bessel function of the first kind of order l, which, in contrast to the Bessel function of the second kind, Y_l, does not diverge for small arguments.

In the cladding, where $q^2 := \beta^2 - k^2 \geq 0$, the wave equation is solved by

$$\begin{bmatrix} E_z(\vec{r},t) \\ H_z(\vec{r},t) \end{bmatrix} \propto K_l(qr)\exp[i(\omega t - \beta z \pm l\phi)]. \tag{1.11}$$

Since the modified Bessel function of the first kind, I_l, which also solves the wave equation in the cladding, diverges for $r \to \infty$, the fields are described by the modified Bessel function of the second kind of order l, K_l, for them to vanish for large arguments as expected for the evanescent field.

Using Eqns. (1.2) and (1.3), E_r, E_ϕ, H_r and H_ϕ can be calculated from the expressions for E_z and H_z. They can be found in [37] and will not explicitly be given here. The field components tangential to the interface between core and cladding have to be continous for $r = a$. This condition leads to a transcendental equation for the propagation constant β [37]:

$$\Big(\frac{J_l'(ha)}{haJ_l(ha)} + \frac{K_l'(qa)}{qaK_l(qa)}\Big)\Big(\frac{n_1^2 J_l'(ha)}{haJ_l(ha)} + \frac{n_2^2 K_l'(qa)}{qaK_l(qa)}\Big) = \Big(\frac{\beta l}{k_0}\Big)^2\Big[\Big(\frac{1}{ha}\Big)^2 + \Big(\frac{1}{qa}\Big)^2\Big]^2, \tag{1.12}$$

where $J_l'(ha)$ and $K_l'(qa)$ denote $dJ_l(hr)/d(hr)$ and $dK_l(qr)/d(qr)$, respectively. This equation can be solved numerically to obtain a discrete set of values for the propagation constant β for each value of l. Each of these solutions corresponds to a different propagation mode of the light in the fiber. These modes are called hybrid modes because they have both, E_z and H_z components. Since Eq. 1.12 is quadratic in $J_l'(ha)/haJ_l(ha)$, the solutions can be separated into two classes which are designated as the EH and HE modes based on the contribution of E_z and H_z to the mode: While the contribution of E_z is larger than the one of H_z for the EH modes, it is smaller than the one of H_z for the HE modes [48]. In ray optics, the hybrid modes EH and HE can be described as so-called skew rays spiraling on a helical path within the fiber core [47]. Since the polarization components mix after each reflection at the interface between core and cladding, it is impossible to maintain either $E_z = 0$ or $H_z = 0$ for these rays which is consistent with the definition of hybrid modes. The hybrid modes are labelled as $\mathrm{EH}_{\mathrm{lm}}$ and $\mathrm{HE}_{\mathrm{lm}}$, where m accounts for the different solutions of Eq. 1.12 for a fixed l and indicates the number of radial intensity maxima of the corresponding mode. The number l can be associated with the z-component of the orbital angular momentum of the propagating electromagnetic field [37,49,50]. It has been introduced in Eqn. (1.7), the ansatz function for the solution of the wave equation in cylindrical coordinates.

In the special case when $l = 0$, the derivative of the electromagnetic fields with respect to ϕ vanishes and all field components are radially symmetric. Here, the only non-vanishing field components for the modes are E_r, E_z, H_ϕ for $\mathrm{EH}_{0\mathrm{m}}$ and H_r, H_z, E_ϕ for $\mathrm{HE}_{0\mathrm{m}}$. Due to the vanishing z-component of the magnetic (electric) field, the $\mathrm{EH}_{0\mathrm{m}}$ ($\mathrm{HE}_{0\mathrm{m}}$) are referred to as transversal magnetic, $\mathrm{TM}_{0\mathrm{m}}$ (transversal electric, $\mathrm{TE}_{0\mathrm{m}}$) modes. In order to maintain this vanishing z-component of the electromagnetic field, the TM and TE modes have to exhibit

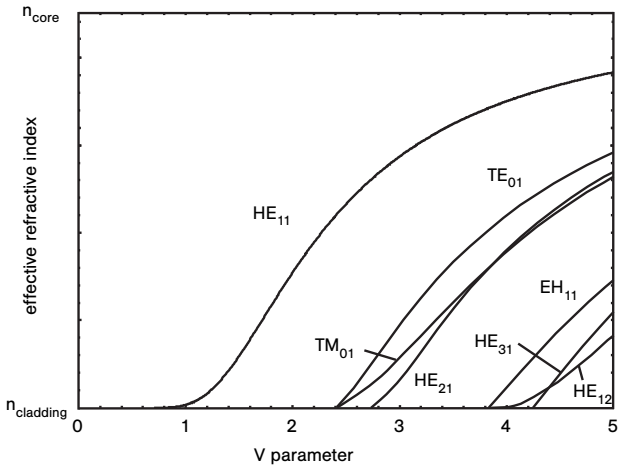

Figure 1.3.: Effective refractive index of the lowest step-index fiber modes as a function of the V parameter for a numerical aperture of 1.05, adapted from [50].

non-rotationg trajectories in the ray optics picture. These modes can therefore be identified by the so-called meridional rays that lie in a plane comprising the fiber axis [47].

The propagation properties of a mode depend on the normalized frequency V (V parameter) which is the fundamental parameter describing the system. It is given by

$$V = k_0 a \cdot \sqrt{n_{\text{core}}^2 - n_{\text{clad}}^2} = k_0 a \cdot \text{NA}. \tag{1.13}$$

Figure 1.3 shows the effective refractive index $n_{\text{eff}} = \beta/k_0$ of the lowest modes of a step-index optical fiber as a function of the V parameter. Note that the plot does not hold universally for all numerical apertures. The effective refractive index for the modes shown in Fig. 1.3 has been calculated for a relatively large numerical aperture of 1.05 in order to clearly demonstrate the separation of the different modes. The cut-off behaviour discussed in the following, however, holds universally for all numerical apertures.

All modes apart from the HE_{11} mode exhibit a cut-off value for a certain normalized frequency [37]. As the V parameter of the system decreases, the confinement of the modes decreases and the fraction of the light propagating in the cladding increases. Therefore, the effective refractive index n_{eff} approaches n_{cladding} near the cut-off. Far above the cut-off, however, the mode is tightly bound to the core and the effective refractive index n_{eff} approaches n_{core}. The cut-off values for the modes EH_{lm}, TM_{lm} and TE_{lm} are given by the mth root of $J_l(x)$, whereas the value for the HE_{lm} mode is given by the $(m-1)$th root of $J_l(x)$ for $l = 1$ and by the mth root of $xJ_l(x) - (l-1)(1 + n_{\text{core}}^2/n_{\text{cladding}}^2)J_{l-1}(x)$ for $l > 1$ [37]. Below $V = 2.405$, the cutoff of the TM_{01} and TE_{01} modes, only the fundamental HE_{11} mode is guided by the fiber. Such a single mode operation of a fiber is essential for many of applications in telecommunications and research where well defined phase fronts and group velocities are required.

1.1.2. Linearly polarized modes

Due to the low refractive index difference between core and cladding ($n_{\text{core}}/n_{\text{cladding}} \approx 1.0035$) in an unmodified standard optical fiber, the wave equation (Eq. (1.6)) can be approximately

solved by so-called linearly polarized (LP) modes [37]. For such a weakly guiding fiber [51], the term on the right of Eq. (1.6) can be assumed to vanish, resulting in a scalar wave equation for all components of the electric and magnetic field. Without loss of generality, a y-polarized solution for the electric field is considered. In analogy to Eq. (1.7), the y-component takes the form of

$$E_y(\vec{r},t) = R(r)\exp[i(\omega t - \beta z) \pm il\phi]. \tag{1.14}$$

Following the same argument as above, E_y can be expressed as

$$E_y(r,\phi,z,t) \propto J_l(hr)\exp[i(\omega t \pm l\phi - \beta z)] \tag{1.15}$$

in the fiber core and as

$$E_y(r,\phi,z,t) \propto K_l(qr)\exp[i(\omega t \pm l\phi - \beta z)] \tag{1.16}$$

in the cladding. Since the solution for the electric field has been chosen to be y-polarized, the x-component will be zero. Using the expressions above together with Eqns. (1.2) and (1.3) and assuming $E_z \ll E_y$, the components E_z, H_x , H_y and H_z can be expressed in terms of E_y. The continuity of E_z at the inteface between core and cladding determines the mode condition for linearly polarized modes [37]:

$$h\frac{J_{l+1}(ha)}{J_l(ha)} = q\frac{K_{l+1}(qa)}{K_l(qa)}. \tag{1.17}$$

This mode condition is much simpler than the exact expression given by Eq. (1.12). Moreover, it has only half as many solutions as the exact mode condition. The other half of the solutions is given by x-polarized modes which obey the same mode condition as the y-polarized modes. Therefore, these two transversely orthogonal modes are degenerate in the propagation constant β. They are designated by $\mathrm{LP_{lm}}$ and can be expressed as two independent linear superpositions of the hybrid modes $\mathrm{HE_{l+1,m}}$ and $\mathrm{EH_{l-1,m}}$ in the limit of $n_{\mathrm{core}} \to n_{\mathrm{cladding}}$. The cut-off values for the $\mathrm{LP_{lm}}$ modes are determined by the mth root of $J_{l-1}(x)$. The first 6 linearly polarized modes with the associated hybrid modes and the corresponding cut-off values for the V parameter are listed in Tab. 1.1.

$\mathrm{LP_{lm}}$	hybrid modes	cut-off
$\mathrm{LP_{01}}$	$\mathrm{HE_{11}}$	0
$\mathrm{LP_{11}}$	$\mathrm{HE_{21}}$, $\mathrm{TM_{01}}$, $\mathrm{TE_{01}}$	2.405
$\mathrm{LP_{21}}$	$\mathrm{HE_{31}}$, $\mathrm{EH_{11}}$	3.832
$\mathrm{LP_{02}}$	$\mathrm{HE_{12}}$	3.832
$\mathrm{LP_{31}}$	$\mathrm{HE_{41}}$, $\mathrm{EH_{21}}$	5.136
$\mathrm{LP_{12}}$	$\mathrm{HE_{22}}$, $\mathrm{TM_{02}}$, $\mathrm{TE_{02}}$	5.520

Table 1.1.: The first 6 LP modes with the associated hybrid modes and corresponding cut-off values for V.

1.2. Nanofiber waist

Like the unmodified part of a TOF described in Sec. 1.1, the nanofiber waist of a TOF can be treated as an effective two layer system. However, in the case of an optical nanofiber, the

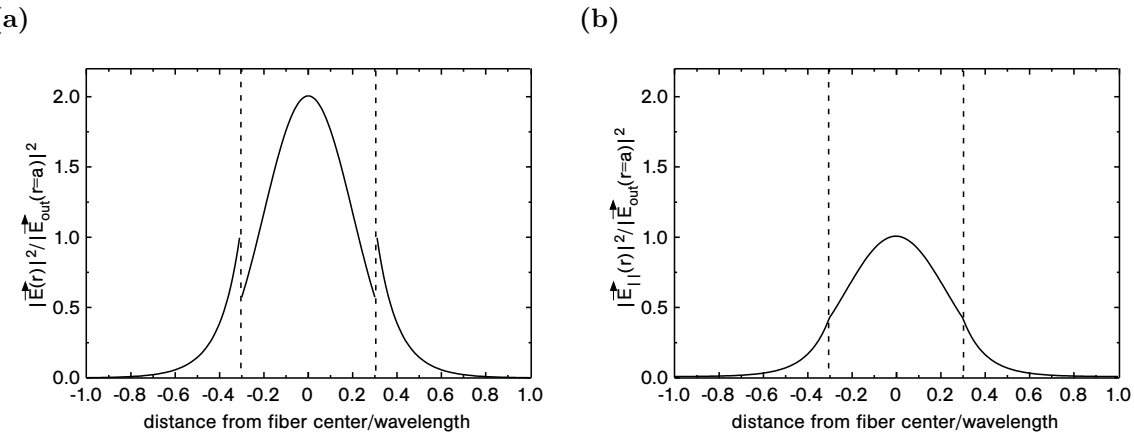

Figure 1.4.: Radial distribution of the electric field strength of the fundamental mode HE_{11} guided through a nanofiber as a function of the distance from the fiber center normalized to the total electric field strength $|\vec{E}_{\text{out}}(r = a)|^2$ at the nanofiber surface. Calculated for circularly or unpolarized light, $d/\lambda = 0.6$, and a refractive index of the nanonfiber of $n = 1.46$. (a) Total electric field $|\vec{E}(r)|^2 = |E_r(r)|^2 + |E_\phi(r)|^2 + |E_z(r)|^2$. (b) Tangential electric field components $|\vec{E}_{||}(r)|^2 = |E_\phi(r)|^2 + |E_z(r)|^2$.

two layers are usually made of pure silica, with a refractive index between 1.45 and 1.47 for the visible wavelength range, and the surrounding vacuum or air, with a refractive index of approximately 1. As a result, these so-called strongly guiding fibers with a refractive index difference of almost 50 % cannot be treated in the approximation of weakly guiding fibers discussed in Sec. 1.1.2. Here, the full vector equation for the electromagnetic fields (Eq. (1.6)) has to be solved and the modes of the nanofiber are given by the hybrid modes EH_{lm} and HE_{lm} as well as the transversal modes TM_{0m} and TE_{0m} discussed in Sec. 1.1.1. The expressions for the components of the electric and magnetic field are the same as for a standard optical fiber and are explicitly given in [37].

Due to the small radius and the large refractive index difference of optical nanofibers, however, the properties of the light fields differ substantially from the properties of the guided light fields of a standard optical fiber. A comprehensive study of the intensity distributions and polarization orientations of the electric field for the fundamental HE_{11} mode of an optical nanofiber has been presented by F. L. Kien and coworkers [52]. Here, I will briefly discuss the distribution of the electric field strength for the circularly and quasi-linearly polarized HE_{11} mode.

1.2.1. Rotating polarization

For rotating polarization, the distribution of the electric field strength is cylindrically symmetric, and, therefore, independent of the azimuthal angle ϕ [52]. Figure 1.4(a) shows the magnitude $|\vec{E}(r)|^2 = |E_r(r)|^2 + |E_\phi(r)|^2 + |E_z(r)|^2$ normalized to the electric field strength $|\vec{E}_{\text{out}}(r = a)|^2$ at the nanofiber surface for the circularly or unpolarized fundamental mode as a function of the distance from the fiber center. The electric field strength is maximal at the fiber center and decreases towards the surface. Due to the boundary conditions at the fiber surface, the radial component of the electric field exhibits a discontinuity. For the large refractive index contrast characteristic for an optical nanofiber, the effect is cor-

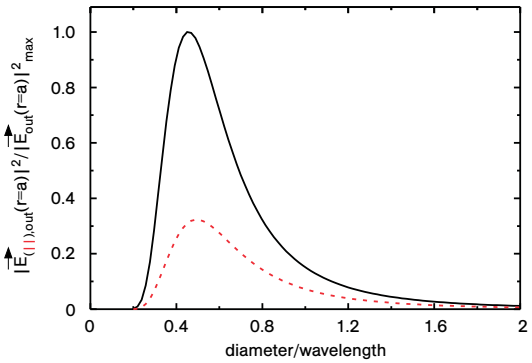

Figure 1.5.: Electric field strength at the fiber surface for the fundamental mode HE_{11} as a function of the nanofiber diameter in units of the wavelength. Calculated for the total electric field $|\vec{E}_{\text{out}}(r=a)|^2 = |E_{r,\text{out}}(r=a)|^2 + |E_{\phi,\text{out}}(r=a)|^2 + |E_{z,\text{out}}(r=a)|^2$ (solid line) and the tangential field components $|\vec{E}_{||,\text{out}}(r=a)|^2 = |E_{\phi,\text{out}}(r=a)|^2 + |E_{z,\text{out}}(r=a)|^2$ (dashed line) of circularly or unpolarized light and normalized to the maximum value $|\vec{E}_{\text{out}}(r=a)|^2_{\text{max}}$. Assuming a refractive index of 1.46 and ignoring material dispersion, both plots hold universally for any λ.

respondingly strong. Since the radial component is on the same order as the tangential (azimuthal and axial) components of the electric field, this discontinuity of the radial component results in a clearly visible discontinuity of the total electric field strength plotted in Fig. 1.4(a). The distribution of the tangential components of the electric field given by the quantity $|\vec{E}_{||}(r)|^2 = |E_\phi(r)|^2 + |E_z(r)|^2$ normalized to the strength of the total electric field $|\vec{E}_{\text{out}}(r=a)|^2$ at the nanofiber surface is displayed in Fig. 1.4(b). The electric field strength is about half as high as the total intensity of the electric field, and it is continous at the fiber surface.

For both, the total electric field as well as the tangential components, the electric field strength at the fiber surface is about half as high as in the fiber center. This pronounced electric field at the surface is due to the small transversal dimension of the fiber compared to the wavelength of the guided light which is typical for optical nanofibers. Figure 1.5 shows the electric field strength at the fiber surface as a function of the fiber diameter for the total electric field $|\vec{E}_{\text{out}}(r=a)|^2$ and the transversal components $|\vec{E}_{||,\text{out}}(r=a)|^2$. It exhibits a strong dependence on the fiber diameter and reaches a maximum for $d^{\text{tot}}_{\text{max}} = 0.450 \cdot \lambda$ and $d^{\text{trans}}_{\text{max}} = 0.488 \cdot \lambda$, considering the total electric field and the transversal components, respectively. For small diameters, it rapidly goes to zero because the radial confinement of the mode decreases and the mode diameter diverges.

1.2.2. Quasi-linear polarization

In contrast to the circularly polarized fundamental mode, the electric field strength of the quasi-linearly polarized fundamental mode exhibits a strong azimuthal dependence [52]. Figure 1.6 shows the strength of the electric field of the fundamental mode with quasi-linear polarization along the x-axis as a function of the distance from the fiber center in x- ((a)) and y-direction ((b)). The solid lines indicate the distribution of the magnitude $|\vec{E}(r)|^2$ while for the dashed lines show the magnitude $|\vec{E}_{||}(r)|^2$. All shown quantities are normalized to the electric field strength $|\vec{E}_{\text{out}}(r=a)|^2$ at the nanofiber surface in x-direction.

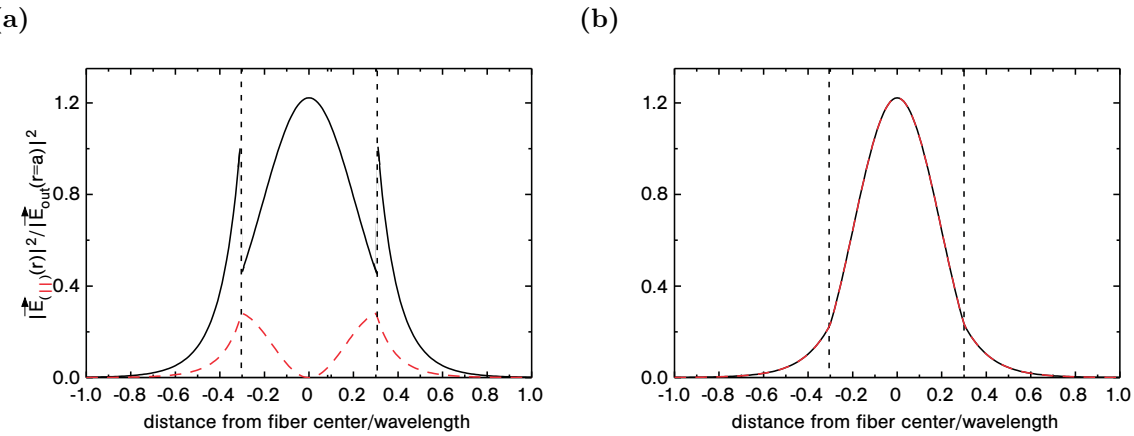

Figure 1.6.: Radial distribution of the electric field strength of the fundamental mode HE_{11} guided through a nanofiber as a function of the distance from the fiber center normalized to the total electric field strength $|\vec{E}_{\text{out}}(r=a)|^2$ at the nanofiber surface. Shown are the magnitudes $|\vec{E}(r)|^2 = |E_r(r)|^2 + |E_\phi(r)|^2 + |E_z(r)|^2$ (solid lines) and $|\vec{E}_{||}(r)|^2 = |E_\phi(r)|^2 + |E_z(r)|^2$ (dashed lines). The field is chosen to be quasi-linearly polarized along the x-axis ($\phi_0 = 0$), and the parameters correspond to the ones for Fig. 1.4. (a) Distribution along the x-axis ($\phi = 0$, $r = x$). (b) Distribution along the y-axis ($\phi = \pi/2$, $r = y$).

For the total electric field, the behaviour of the field strength outside the fiber differs significantly from the behaviour inside the fiber. Inside the fiber, the distribution depends only slightly on the azimuthal position and hardly deviates from the intensity distribution for a circularly polarized field. Outside the fiber, however, a strong azimuthal dependence is visible. Along the polarization axis, $|\vec{E}(r)|^2$ exhibits a strongly pronounced discontinuity at the fiber surface yielding a high value at the surface. This is due to the fact that E_x, which is the radial component here, dominates the electric field as can also be seen from the comparison with $|\vec{E}_{||}(r)|^2$ indicated by the dashed lines in Fig. 1.6(a). Along the x-direction, the tangential components only consist of the z-component of the electric field because the y-component is zero along the x- and y-direction for a field which is quasi-linearly polarized along the x-axis [52]. Perpendicular to the polarization axis, also the axial component of the electric field vanishes, and the strength of the total as well as of the tangential electric field is determined by E_x, the azimuthal component along this direction. As a result, the distribution of the quantities $|\vec{E}(r)|^2$ and $|\vec{E}_{||}(r)|^2$ along the y-direction displayed in Fig. 1.6(b) is continous at the fiber surface, and the values at the surface are much lower. The average of the electric field strength at the fiber surface over the total circumference of the fiber for quasi-linearly polarized light is the same as the electric field strength at the fiber surface of a circularly polarized light field with the same total power. It therefore also exhibits the radius dependency shown in Fig. 1.5.

1.2.3. Power flow in a nanofiber

The power flow in the modes of a nanofiber is determined by the z-component of the time-averaged Poynting vector [37]:

$$\langle S_z \rangle = \frac{1}{2}\text{Re}[E_x H_y^* - E_y H_x^*]. \tag{1.18}$$

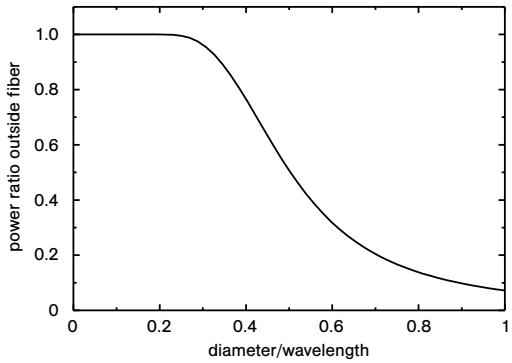

Figure 1.7.: Fraction of the power of the circularly polarized fundamental mode travelling outside the fiber as a function of the fiber diameter in units of the wavelength of the guided light.

The power propagating inside and outside the fiber is given by

$$\begin{aligned} P_{\text{in}} &= \int_0^{2\pi} d\phi \int_0^b \langle S_z \rangle_{in} r dr, \\ P_{\text{out}} &= \int_0^{2\pi} d\phi \int_b^\infty \langle S_z \rangle_{out} r dr. \end{aligned} \tag{1.19}$$

For the circularly or unpolarized fundamental HE_{11} mode, this can be expressed by [50]:

$$\begin{aligned} P_{\text{in}} &= |A|^2 \frac{\pi b^2 \beta}{4\omega\mu_0} \times \left[(1-\tilde{s}) \left[1 + (1-\tilde{s}) \frac{\beta^2}{h^2} \right] [J_0^2(hb) + J_1^2(hb)] + \right. \\ &\quad \left. + (1+\tilde{s}) \left[1 + (1+\tilde{s}) \frac{\beta^2}{h^2} \right] [J_2^2(hb) - J_1(hb) J_3(hb)] \right], \\ P_{\text{out}} &= |A|^2 \frac{\pi b^2 \beta}{4\omega\mu_0} \times \left[\frac{J_1^2(hb)}{K_1^2(qb)} (1-\tilde{s}) \left[1 - (1-\tilde{s}) \frac{\beta^2}{q^2} \right] [K_0^2(qb) - K_1^2(qb)] + \right. \\ &\quad \left. + (1+\tilde{s}) \left[1 - (1+\tilde{s}) \frac{\beta^2}{q^2} \right] [K_2^2(qb) - K_1(qb) K_3(qb)] \right], \end{aligned} \tag{1.20}$$

whith $\tilde{s} = [(qb)^{-2} + (hb)^{-2}] / [J_1'(hb)/hJ_1(hb) + K_1'(qb)/qbK_1(qb)]$, the cladding radius b of the nanofiber, and the normalization constant A.

The fraction of the power travelling outside the fiber given by $P_{\text{out}}/(P_{\text{out}} + P_{\text{in}})$ is plotted in Fig. 1.7 as a function of the fiber diameter. The figure shows the strong enhancement of the power fraction of the field outside the fiber which is characteristic for optical nanofibers. It reaches 50 % for a fiber diameter of about half the wavelength of the guided light. For a vanishing fiber diameter, the light field is transformed into a plane wave, and the power fraction travelling outside the fiber approaches 1. For fiber diameters bigger than the wavelength of the light, more than 90 % of the power are guided inside the fiber with the fraction of power travelling outside the fiber approaching zero for infinitely large fiber radii.

1.3. Taper transition

Tapered optical fibers are not translationally invariant and, therefore, they cannot support the modes described in Sec. 1.1. In general, there are no exact solutions of Maxwell's equations for a TOF. However, if the radius of the TOF varies slowly, the solution within a local region can be approximated by the modes of an unperturbed fiber with the same refractive index profile. These approximations are called local modes [47]. In the taper transitions of a TOF, the weakly core-guided LP_{01} mode of the unstretched fiber is transformed into the strongly cladding-guided HE_{11} mode of the nanofiber and back. Since during the conversion process, the modes extend over core, cladding, and the surrounding medium, the local modes of the taper transition should be determined by considering the full three layer system consisting of fiber core and cladding as well as the surrounding vacuum or air.

The exact solution of the vector wave equation (Eq. (1.6)) and the corresponding mode condition for the three layer system can, for example, be found in [53–56]. It follows the same steps as the solution for the two layer system discussed in Sec. 1.1. However, due to the complexity of the problem, solving the mode condition is a challenging task. Therefore, in this thesis, I will only discuss the solution in the approximation of weak guidance [57, 58]. The resulting linearly polarized modes are a good approximation for the core guided modes and the lower order cladding guided modes in the beginning of the taper transition where the modes do not significantly penetrate the vacuum outside the fiber, yet [46]. In the thinner parts of the transition, the mode will be almost completely guided by the cladding due to the negligible core size, allowing to determine the propagation constants in the approximation of a two layer system.

1.3.1. Local modes

The derivation of the mode conditions for the linearly polarized local modes in the weak guidance approximation given considering the full three layer system can be found in Appendix A and will not be explicitly given here. From Eqs. (A.21) and (A.22), the propagation constants β of the local modes at each position along the taper transition of a TOF can be obtained. For this purpose, the refractive indices of core, cladding, and the surrounding vacuum as well as the ratio of core and cladding diameter are assumed to be constant along the taper transition. Figure 1.8 shows the effective refractive index $n_{\text{eff}} = \beta/k_0$ of the first six modes of the three layer system as a function of the cladding diameter for a core/cladding diameter ratio of $a/b = 2.5\,\mu\text{m}/125\,\mu\text{m} = 0.02$, a refractive index profile of $n_{\text{core}} = 1.47132$, $n_{\text{clad}} = 1.46557$, and $n_{\text{vac}} = 1$, and a wavelength of 450 nm. These parameters will be used for all calculations presented in this chapter unless stated otherwise. The nomenclature for the shown modes has been adopted from the linearly polarized modes of the two layer system (cf. 1.1.2). The fundamental mode LP_{01} of the system is a core mode for cladding diameters bigger than $2b \approx 38\,\mu\text{m}$ where its effective refractive index reaches the refractive index of the cladding indicated by the dashed line in Fig. 1.8(a). For diameters smaller than $2b \approx 38\,\mu\text{m}$, the LP_{01} mode is guided as a cladding mode. Note that this does not mean that the core mode is cut off at this cladding diameter. In a three layer system, the weak confinement by the interface between core and cladding at small V parameters leads to an increased light propagation outside the fiber cladding. Therefore, the effective refractive index of the mode can drop below the refractive index of the cladding instead of approaching n_{clad} as it is the case in the infinitely extended cladding of a two layer system. Even though the mode is

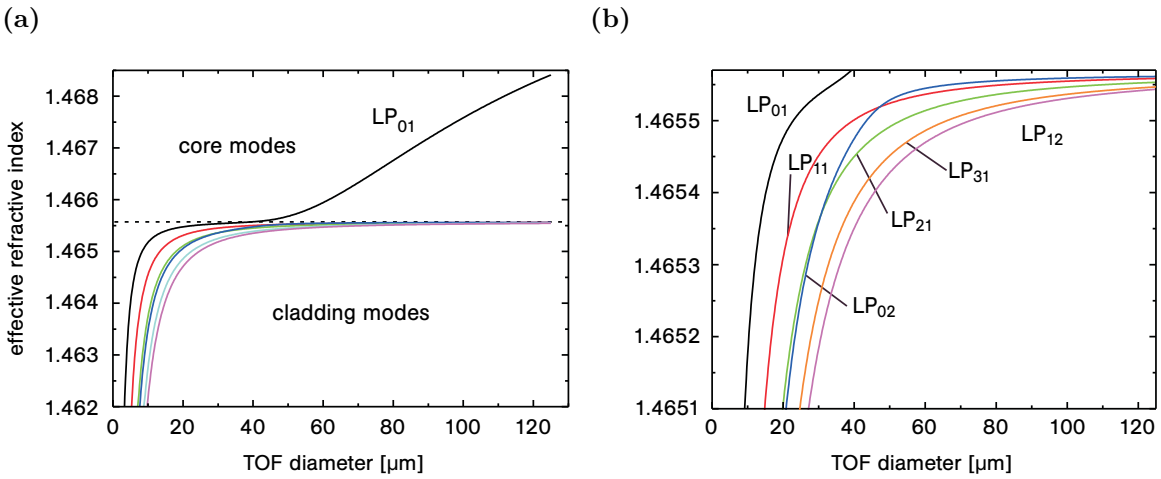

Figure 1.8.: (a) Effective refractive index of the lowest three layer system modes in the taper transition of a TOF (weak guidance approximation). The dashed line indicates the refractive index of the fiber cladding. (b) Magnification of the of the effective refractive index range below the division between core and cladding modes.

technically still guided by the core/cladding interface and thus not cut off as a core mode, it is now referred to as cladding mode according to the definition given in Sec. A.

Since the unprocessed fiber with the parameters assumed here exhibits a V parameter of $V = 2.2 < 2.405$ (cf. Eq. (1.13)), all higher order modes are cladding modes within the whole taper transition. Figure 1.8(b) displays a magnification of the effective refractive index range below the division between core and cladding modes. Near cut-off, the effective refractive index of all higher order modes approaches $n_{\mathrm{vac}} = 1$. In this regime, however, the modes are strongly guided and the approximation presented here cannot be applied.

In order to investigate the reliablility of the approximate solutions obtained from the scalar semi-analytical approach presented here, numerical simulations of the local eigenmodes of the three layer system have been performed together with C. Wuttke using the freely available MIT Photonic-Bands (MPB) package [59]. This package can be employed to compute definite-frequency eigenstates of Maxwell's equations in periodic dielectric structures for arbitrary wavevectors by means of fully-vectorial and three-dimensional methods. For a sufficiently high resolution, these simulations should therefore yield the propagation constants of the exact local hybrid modes solving the three layer system. Figure 1.9 shows the numerically simulated effective refractive indices for three local hybrid modes which correspond to the first three linearly polarized modes obtained for the weak guidance approximation as a function of the cladding diameter (dots). The effective refractive indices of the local modes in the weak guidance approximation are depicted by the solid lines. For cladding diameters between 10 and 60 µm, the effective refractive indices calculated for the LP_{01} mode (black line) show an excellent agreement with the values obtained from numerical simulation of the HE_{11} mode (black dots). The deviations of the numerical data from the results for the weakly guided core mode LP_{01} for diameters bigger than 60 µm is due to an insufficient resolution of the numerical simulations. The simulations have been performed with 78 grid-points in the fiber core yielding an insufficient resolution for the description of a mode which is mainly guided inside the core. An increase of the resolution from 78 to 176 grid-points (not shown in the

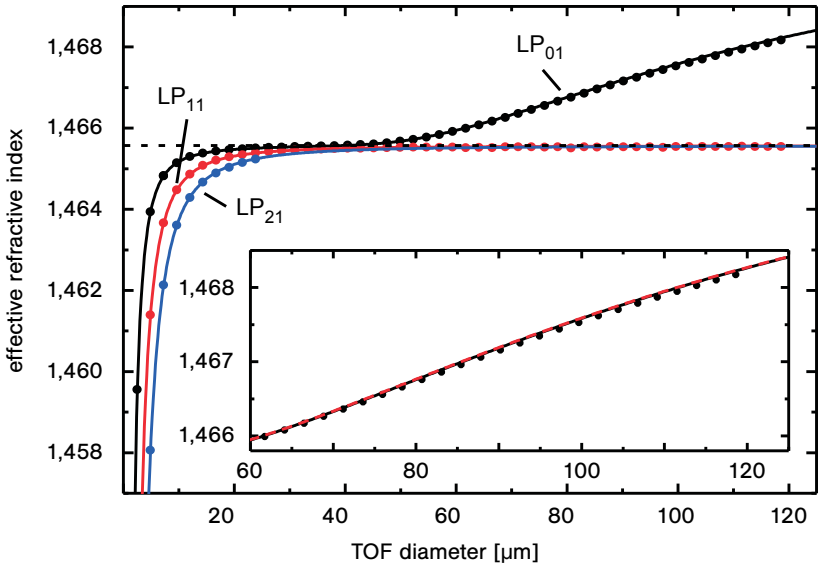

Figure 1.9.: Comparison of the fully-vectorial numerical (dots) and the scalar semi-analytical (lines) solution for the first three linearly polarized eigenmodes of the three layer system and the corresponding hybrid modes. The refractive index of the cladding is indicated by the black dashed line. The inset shows a magnification of the core guided part of the HE_{11}/LP_{01} mode together with the HE_{11} mode of the core/cladding two layer system (red dashed line).

figure) showed a significantly improved agreement with the weakly guided LP_{01} mode at large cladding diameters. However, in this regime, the propagation of the fundamental mode can also be described by the full vector solution for the two layer system consisting of fiber core and cladding. The effective refractive index of this two layer HE_{11} mode is depicted by the dashed line in the inset of Fig. 1.9 as a function of cladding diameter. It shows an excellent agreement with the three layer fundamental mode. If the core size decreases, the mode extends more into the cladding which is very well resolved by the grid of the numerical simulations, and the numerical simulations yield reliable results. Due to the limited computing power available for the numerical simulations, the resolution had to be limited to 10^{-9} yielding it impossible to distinguish between modes with very close effective refractive indices. Thus, the composition of the LP_{11} mode by the HE_{21}, TM_{01}, and TE_{01} hybrid modes (cf. Tab. (1.1)) cannot be resolved, and the red dots result from a superposition of these modes. The same holds for the LP_{21} mode which is composed by the HE_{31} and EH_{11} hybrid modes (blue dots). For TOF diameters larger than approximately 25 µm, the effective refractive indices of all cladding modes are so close that the numerical simulations cannot distinguish between the linearly polarized (LP) modes. However, even despite these insufficiencies of the numerical simulations, it is clearly apparent from the figure that the scalar semi-analytical solutions describe the three layer system very well.

Figure 1.10 shows a magnification of the properties of the effective refractive index of the fundamental mode for cladding diameters below 60 µm, where the resolution of the numerical simulation is high enough to yield reliable results. In the range of cladding diameters between 10 and 60 µm, the fully-vectorial HE_{11} modes of the core/cladding and cladding/vacuum two layer systems cannot characterize the system sufficiently since they do not consider either the surrounding vacuum or the fiber core, respectively (dashed lines in Fig. 1.10(a)). The

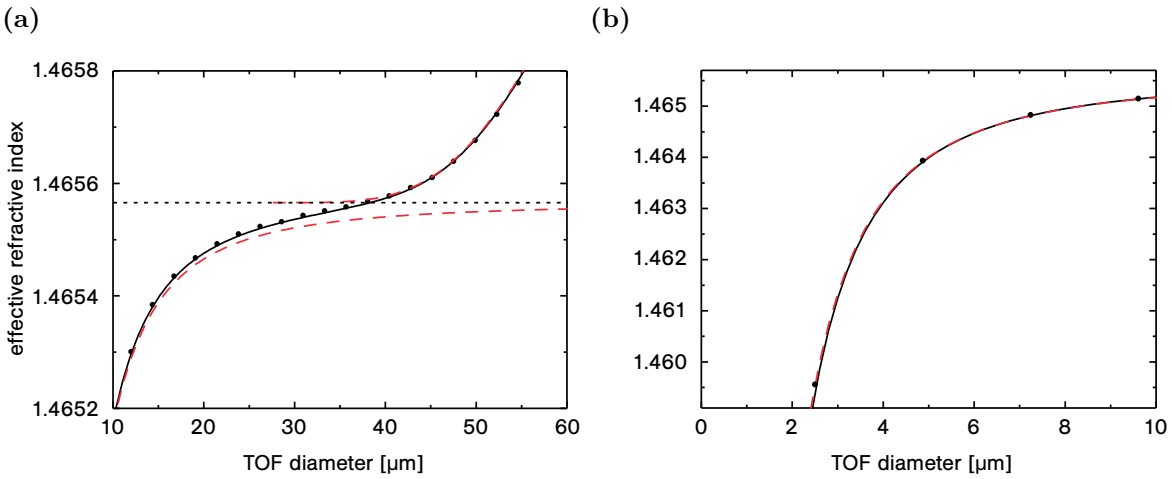

Figure 1.10.: Effective refractive index of the fundamental mode as a function of the cladding diameter: fully-vectorial numerical HE_{11} mode of the three layer system (dots), scalar semi-analytical LP_{01} mode of the three layer system (solid lines) and fully-vectorial semi-analytical HE_{11} modes of the core/cladding and cladding/vacuum two layer systems (red dashed lines). The refractive index of the cladding is indicated by the black dashed line in (a) and by the upper border of the graph in (b).

fundamental mode of the three layer system (solid line), however, describes the transition from a core to a cladding mode very well. As has been mentioned above, the comparison with the fully-vectorial numerical solution (dots) shows that for this diameter range, the scalar approximation for weak guidance can be assumed to be valid. For cladding diameters below 10 µm, the scalar solution starts to slightly deviate from the fully-vectorial numerical one. Figure 1.10(b) shows the effective refractive index for the numerical vectorial (dots) and semi-analytical scalar (solid line) solution of the three layer system as well as for the semi-analytical vectorial solution of the cladding/vacuum two layer system (dashed line). For cladding radii below 5 µm, the three layer system can be approximated by the cladding/vacuum two layer system.

1.3.2. Electric field distribution

Once the progation constants $\beta = n_{\text{eff}} k_0$ of the weakly guided modes of the three layer system are known, the electric field components for each mode can be determined from Eqns A.11 to A.18 derived in Appendix A. Figure 1.11 shows the electric field components E_y ((a),(c),(e)) and E_z ((b),(d),(f)) as a function of the distance from the fiber center for the fundamental mode and four higher order modes at three different positions along the taper transition. The core/cladding and cladding/vacuum interfaces are indicated by the dotted lines. In contrast to a strongly guided quasi-linearly polarized mode, the transverse electric field component E_y of the fundamental linearly polarized mode in the weak guidance approximation is rotationally symmetric (see Sec. 1.2.2 for comparison). The same holds for all higher order modes with zero orbital angular momentum. For higher orbital angular momentum, the transverse electric field depends, in general, on the azimuthal position. In Fig. 1.11, the transverse field component is plotted along the x-axis because, along this direction, it reaches a maximum for all modes. The axial electric field component E_z exhibits an azimuthal dependence for all orbital angular

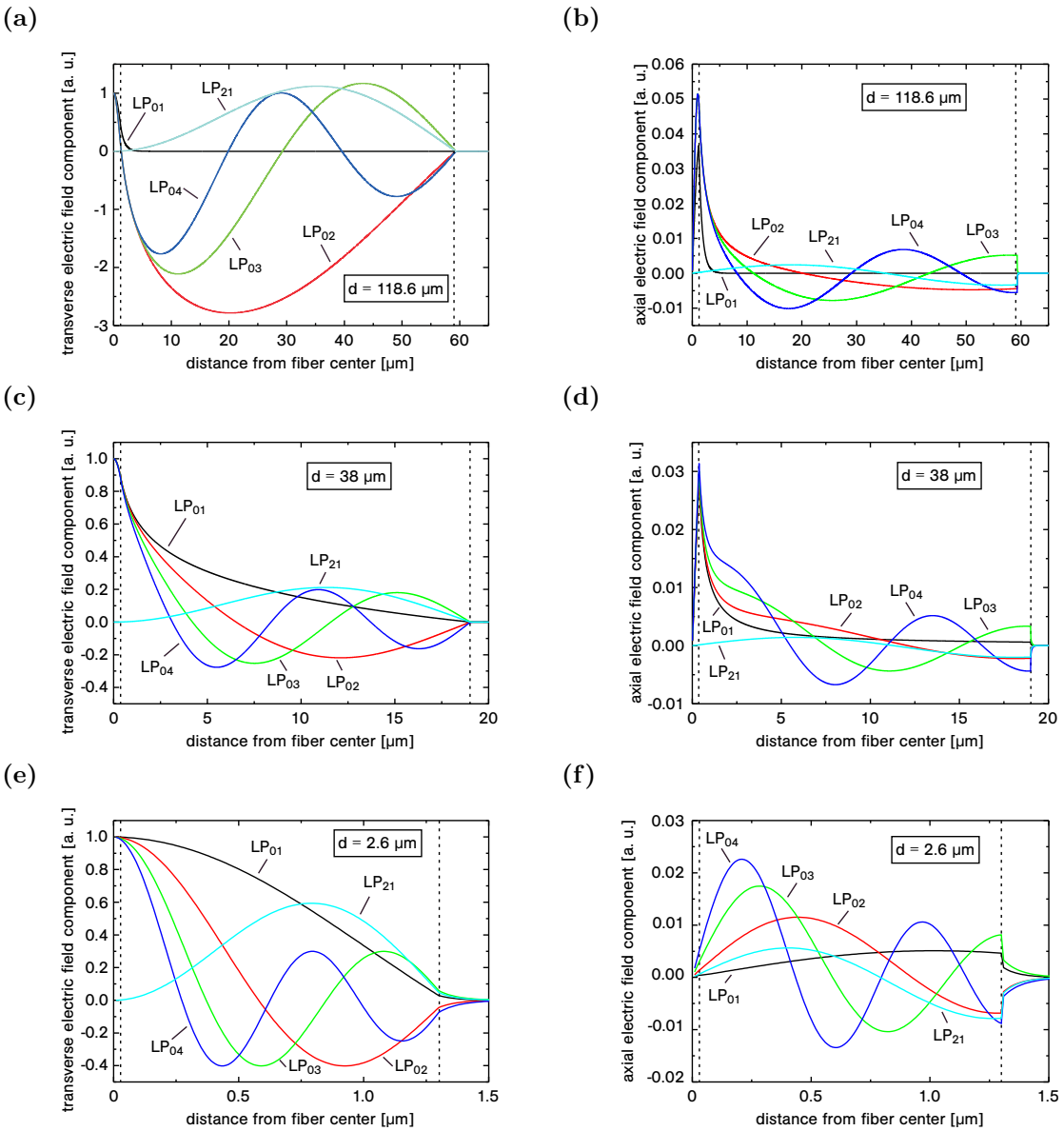

Figure 1.11.: Electric field distribution for the fundamental mode and four higher order modes obtained for the three layer system in the weak guidance approximation (linear polarization): Transverse electric field components E_y for TOF diameters of 118.6 µm (a), 38 µm (c), and 2.6 µm (e) as a function of the distance from the fiber center along the x-axis. Axial electric field components E_z for the same TOF diameters ((b), (d), and (f), respectively) as a function of the distance from the fiber center along the y-axis. The core/cladding and cladding/vacuum interfaces are indicated by vertical dotted lines.

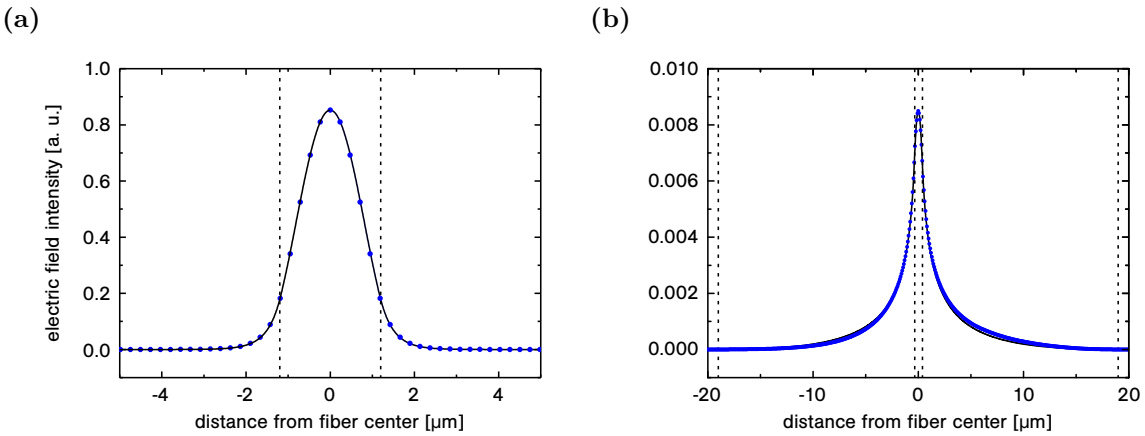

Figure 1.12.: Radial distribution of the electric field intensity as a function of the distance to the fiber center along the y-axis for a TOF diameter of 118.6 µm (a) and 38 µm (b). The results from the scalar semi-analytical approach (solid line) are compard to those of the fully-vectorial numerical simulations (dots). The dotted lines indicate the core/cladding and cladding/vacuum interfaces.

momenta and is zero along the direction of the x-axis. The electric field component E_z is therefore plotted along the y-axis in Fig. 1.11(b), (d), and (f), where it reaches a maximum.

At a TOF diameter of 118.6 µm ((a), (b)), the influence of the fiber core is strong for modes with zero orbital angular momentum (LP_{0m}). The fundamental mode is guided by the core/cladding interface and hardly extends into the cladding. The higher order modes with the same azimuthal symmetry are guided by the cladding/vacuum interface, but their electric field distribution is significantly modified by the presence of the core/cladding interface. As expected, the LP_{0m} exhibit m radial intensity maxima for both electric field components. Since the electric field components of the LP_{21} mode have a minimum at the fiber center, the influence of the fiber core is negligible already at large TOF diameters. Note that the electric field components are not normalized to the same total guided power in order to facilitate the comparison of the electric field distribution for the different modes. The relative strength of the two field components for each mode and TOF diameter is, however, to scale, and it can be seen from the figure that the transverse component of the electric field is about two orders of magnitude stronger than the axial field component, as expected for weakly guided modes.

At a TOF diameter of 38 µm ((c), (d)), the transition from a core guided to a cladding guided LP_{01} mode is clearly visible. The electric field extends far into the cladding, but its distribution is still modified by the presence of the fiber core. For the higher order LP_{0m} modes, the influence of the fiber core decreases as well, whereas the LP_{21} mode is still almost unaffected by the presence of the fiber core.

At a TOF diameter of 2.6 µm ((e), (f)), the influence of the fiber core is negligible for all modes. The electric field distribution is dominated by the confinement due to the interface between cladding and vacuum, and an evanescent field outside the TOF is clearly visible. Due to the relatively large ratio of the TOF diameter to the wavelength of the guided light of more than 5 and the assumption of weak guidance, the confinement of the mode is not strong enough to generate a pronounced evanescent field with surface intensities as high as in an optical nanofiber.

For the LP_{01} mode, the fields calculated with the scalar semi-analytical approach presented here can be compared to the results from the fully-vectorial numerical simulations. Figure 1.12 exemplarily shows the intensity distribution of the fundamental mode for a TOF diameter of 118.6 µm ((a)) and 38 µm ((b)) for both, the scalar approximation (solid lines) and the fully-vectorial solution (dots). The dotted lines indicate the interfaces between core and cladding as well as between cladding and surrounding vacuum. For a TOF diameter of 118.6 µm, the intensity distribution obtained in the scalar approximation shows an excellent agreement with the fully-vectorial numerical results. For a TOF diameter of 38 µm, however, the intensity in the cladding shows a slightly asymmetric decay behavior for the fully-vectorial approach which deviates from the behavior of the scalar semi-analytical solution. This is probably due to the insufficient resolution of the numerical simulation already discussed above, since the intensity distribution for the fundamental mode should be rotationally symmetric as the result of the scalar approximation suggests. Still, the comparison to the numerical simulations can give a good estimate for the high quality of the results obtained by solving the scalar wave equation for the three layer system.

1.3.3. Power flow in the taper transition

The power flow in the local modes of the taper transition is determined by the z-component of the time-averaged Poynting vector [37]:

$$\langle S_z \rangle = \frac{1}{2}\mathrm{Re}[E_x H_y^* - E_y H_x^*] = -\frac{1}{2}\mathrm{Re}[E_y H_x^*]. \tag{1.21}$$

Integration over the transverse plane and use of the field components given by Eqs. (A.11) to (A.18) leads to the expressions for the power propagating inside each of the three layers:

$$\begin{aligned}
P_{\mathrm{core}} &= \int_0^{2\pi} d\phi \frac{\beta}{\omega\mu_0} \int_0^a A^2 J_l^2(hr) r dr, \\
P_{\mathrm{clad}}^{\mathrm{core}} &= \int_0^{2\pi} d\phi \frac{\beta}{\omega\mu_0} \int_a^b (CI_l(sr) + DK_l(sr))^2 r dr, \\
P_{\mathrm{clad}}^{\mathrm{clad}} &= \int_0^{2\pi} d\phi \frac{\beta}{\omega\mu_0} \int_a^b (CJ_l(pr) + DY_l(pr))^2 r dr, \\
P_{\mathrm{vac}} &= \int_0^{2\pi} d\phi \frac{\beta}{\omega\mu_0} \int_b^\infty B^2 K_l^2(qr) r dr,
\end{aligned} \tag{1.22}$$

where $P_{\mathrm{clad}}^{\mathrm{core}}$ and $P_{\mathrm{clad}}^{\mathrm{clad}}$ is the power propagationg inside the cladding for a core and a cladding mode, respectively.

For cladding modes, the integration over products of Bessel functions can be carried out by means of the following relations [60]:

$$\begin{aligned}\int x\left[Z_p(\alpha x)\right]^2 dx &= \frac{x^2}{2}\left\{\left[Z_p(\alpha x)\right]^2 - Z_{p-1}(\alpha x)Z_{p+1}(\alpha x)\right\},\\ \int xZ_p(\alpha x)\zeta_p(\alpha x)dx &= \frac{x^4}{4}\Big\{2Z_p(\alpha x)\zeta_p(\alpha x) - Z_{p-1}(\alpha x)\zeta_{p+1}(\alpha x) - \\ &\quad Z_{p+1}(\alpha x)\zeta_{p-1}(\alpha x)\Big\},\end{aligned} \tag{1.23}$$

where the first relation holds for any Bessel function or modified Bessel function of order p, and the second relation is only valid for Bessel functions of order p, but not for modified Bessel functions.

In a TOF which is fabricated from a single mode fiber as considered here, there is only one core mode (LP_{01}) which has a zero z-component of the orbital angular momentum, i. e. $l = 0$. In this case, the integration over the product of modified Bessel functions can be carried out by means of the following relation [61]:

$$\int x^{p+l+1}Z_p(\alpha x)\zeta_l(\alpha x)dx = \frac{x^{p+l+2}}{2(p+l+1)}\left[Z_p(\alpha x)\zeta_l(\alpha x) + Z_{p+1}(\alpha x)\zeta_{l+1}(\alpha x)\right], \tag{1.24}$$

where Z_p and ζ_l denote any two different Bessel functions or modified Bessel functions of order p and l, respectively.

This yields a total transmitted power $P^{\mathrm{i}} = P_{\mathrm{core}} + P^{\mathrm{i}}_{\mathrm{clad}} + P_{\mathrm{vac}}$ which can be expressed as follows:

$$P^{\mathrm{i}} = |A^{\mathrm{i}}|^2\frac{\pi\beta}{2\omega\mu_0}D^{\mathrm{i}}, \tag{1.25}$$

with $\mathrm{i} = \{\mathrm{core}, \mathrm{clad}\}$, the normalization constants A^{i} for core and cladding modes, and

$$\begin{aligned}D^{\mathrm{core}} &= b^2\left(\frac{B}{A}\right)^2\left(1 - \frac{n^4_{\mathrm{clad}}q^2}{n^4_{\mathrm{vac}}s^2}\right)K_1^2(qb) + a^2\left(1 + \frac{n^4_{\mathrm{clad}}h^2}{n^4_{\mathrm{core}}s^2}\right)J_1^2(ha),\\ D^{\mathrm{clad}} &= b^2\left(\frac{B}{A}\right)^2\left(1 + \frac{n^4_{\mathrm{clad}}q^2}{n^4_{\mathrm{vac}}p^2}\right)K_{l+1}(qb)\cdot K_{l-1}(qb) - \\ &\quad a^2\left(1 - \frac{n^4_{\mathrm{clad}}h^2}{n^4_{\mathrm{core}}p^2}\right)J_{l+1}(ha)\cdot J_{l-1}(ha).\end{aligned} \tag{1.26}$$

Therefore, the normalization constants A^{i} for core and cladding modes are determined by the total power P guided in the corresponding mode via

$$|A^{\mathrm{i}}| = \sqrt{\frac{2\omega\mu_0 P}{\pi\beta D^{\mathrm{i}}}}. \tag{1.27}$$

1.3.4. Coupling between guided modes

As mentioned above, local modes only yield an accurate approximation to the exact fields in the taper transition if the radius changes sufficiently slowly along the fiber axis. In this case, the mode conversion within the taper transition is adiabatic, and loss from the fundamental mode is negligible.

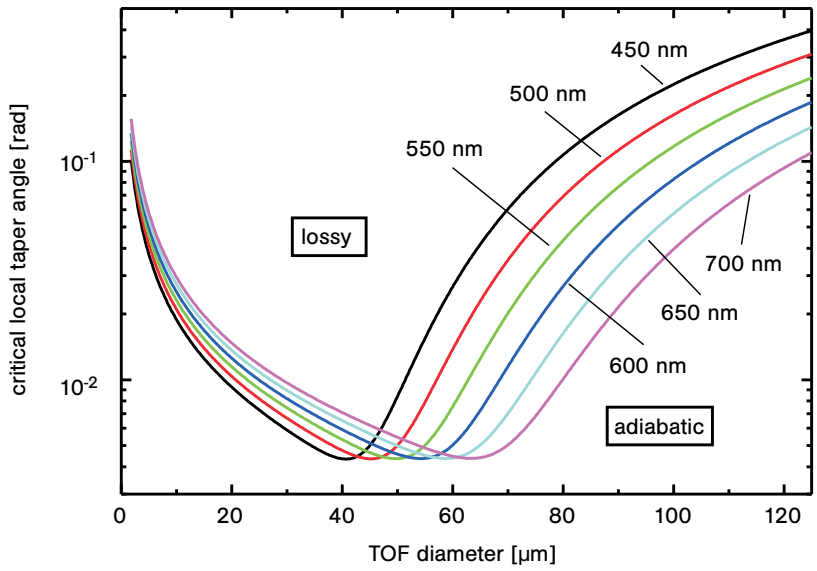

Figure 1.13.: Delineation between adiabatic and lossy tapers for coupling between guided modes calculated for six different wavelengths ranging from 450 nm to 700 nm and a three layer system as defined in Sec. 1.3.1 ($NA_{core/clad} = 0.13$, $a/b = 0.02$).

Length scale criterion

An appropriate adiabaticity condition is expressed by the length-scale criterion derived by Love et al. [46]. It compares the local taper length scale $z_t(b)$ for a given cladding radius b with the beat length $z_b(b, \lambda)$ between the fundamental mode and the dominant coupling mode for power loss [46]:

$$z_b(r, \lambda) = 2\pi/(\beta_1(r, \lambda) - \beta_2(r, \lambda)), \tag{1.28}$$

where $\beta_1(b, \lambda)$ and $\beta_2(b, \lambda)$ are the propagation constants of the two modes. The local taper length scale is defined via the local taper angle $\Omega(b)$ of the cladding and the local cladding radius b according to $z_t(b) = b/\Omega(b)$ [46].

The condition $z_t = z_b$ leads to an approximate delineation between adiabatic and lossy tapers given by [46]

$$\Omega(b) = \frac{b \cdot (\beta_1(b, \lambda) - \beta_2(b, \lambda))}{2\pi}, \tag{1.29}$$

As will be discussed below, the fundamental mode couples predominantly to higher order modes with the same azimuthal symmetry and thus, the LP_{02} mode is considered here. The resulting delineation between adiabatic and lossy tapers for the three layer system defined in Sec. 1.3.1 is shown in Fig. 1.13. The critical local taper angle at which the taper starts to become lossy is plotted as a function of the TOF diameter for six different wavelengths ranging from 450 nm to 700 nm. It is above 4 mrad for all TOF diameters and wavelengths of the guided light. The minimum of the delineation curve shifts to higher TOF diameters for increasing wavelengths with about 9 µm diameter shift per 100 nm wavelength shift. Therefore, for a given taper diameter profile with varying local taper angles, the transmission properties will be wavelength dependent.

Coupled local mode equations

In order to quantify the loss from the fundamental mode due to tapering, a set of coupled local mode equations has to be solved as described in detail in [47]. These coupled mode equations can be derived from the description of the total transverse electric and magnetic fields of the TOF as a superposition of local modes [47]:

$$\begin{aligned} \vec{E}_t &= \sum_j b_j(z)\hat{e}_{tj}(r,\phi,\beta_j(z)), \\ \vec{H}_t &= \sum_j b_j(z)\hat{h}_{tj}(r,\phi,\beta_j(z)), \end{aligned} \tag{1.30}$$

where $\hat{e}_{tj}$ and $\hat{h}_{tj}$ are the orthonormalized transversal field components which only implicitely depend on the axial position via the propagation constant of the local modes and are normalized to the total guided power. The parameter $b_j(z)$ describes the amplitude and phase of the respective mode. Here, only forward-propagating guided modes have been taken into account. Using Maxwell's equations and the orthogonality conditions for local modes, the coupled local mode equations can be derived as [47]

$$\frac{db_j(z)}{dz} - i\beta_j(z)b_j(z) = \sum_p C_{jp}(z)b_p(z), \tag{1.31}$$

for the jth forward-propagating mode. The coupling coefficients C_{jp} are defined by [47]

$$C_{jp}(z) = \frac{1}{4}\int_A \left\{ \hat{h}_j \times \frac{\partial \hat{e}_p}{\partial z} - \hat{e}_j \times \frac{\partial \hat{h}_p}{\partial z} \right\} \cdot \hat{z} dA, \tag{1.32}$$

for $j \neq p$ and with $C_{jj} = 0$. Here, A is the plane perpendicular to the fiber axis, and $\hat{z}$ the unit vector parallel to the fiber axis. The coupling coefficients can also be expressed in terms of the refractive index profile $n(r,z)$ [47]:

$$\begin{aligned} C_{jp}(z) &= \frac{k_0}{4}\left(\frac{\varepsilon_0}{\mu_0}\right)^{1/2} \frac{1}{\beta_j(z) - \beta_p(z)} \\ &\times \int_A \frac{\partial n^2(r,z)}{\partial z} \hat{e_j}^*(r,\phi,\beta_j(z)) \cdot \hat{e_p}(r,\phi,\beta_p(z)) dA. \end{aligned} \tag{1.33}$$

For a three layer system with the parameters introduced in Fig. 1.1, the refractive index profile can be described by

$$n^2(r,z) = n^2_{\text{core}} \cdot [1 - 2\Delta H(r - a(z))] \cdot [1 - 2\tilde{\Delta} H(r - b(z))], \tag{1.34}$$

where H is the Heaviside step function and

$$\begin{aligned} \Delta &= \frac{n^2_{\text{core}} - n^2_{\text{clad}}}{2n^2_{\text{core}}}, \\ \tilde{\Delta} &= \frac{n^2_{\text{clad}} - n^2_{\text{vac}}}{2n^2_{\text{clad}}}, \end{aligned} \tag{1.35}$$

leading to

$$\begin{aligned}\frac{\partial n^2}{\partial z} &= 2\Delta n_{\text{core}}^2 \frac{\partial a}{\partial z}\delta(r-a(z))[1-2\tilde{\Delta}H(r-b(z)] + \\ &+ 2\tilde{\Delta} n_{\text{core}}^2 \frac{\partial b}{\partial z}\delta(r-b(z))[1-2\Delta H(r-a(z)]. \end{aligned} \tag{1.36}$$

Due to the contribution of the Dirac delta function δ, substituting Eq. (1.36) into Eq. (1.33) yields coupling coefficients which only depend on the fields at the interfaces between core and cladding as well as cladding and vacuum, where $r = a(z)$ and $r = b(z)$, respectively:

$$\begin{aligned} C_{jp}(z) &= \frac{k_0}{4}\left(\frac{\varepsilon_0}{\mu_0}\right)^{1/2} \frac{\Omega(z)}{\beta_j(z)-\beta_p(z)} b(z) \times \\ &\times \Big[\left(\frac{a_0}{b_0}\right)^2 (n_{\text{core}}^2 - n_{\text{clad}}^2) \int_0^{2\pi} \hat{e_j}^*(a(z),\phi,\beta_j(z)) \cdot \hat{e_p}(a(z),\phi,\beta_p(z)) d\phi + \\ &+ (n_{\text{clad}}^2 - n_{\text{vac}}^2) \int_0^{2\pi} \hat{e_j}^*(b(z),\phi,\beta_j(z)) \cdot \hat{e_p}(b(z),\phi,\beta_p(z)) d\phi\Big], \end{aligned} \tag{1.37}$$

with the local taper angle $\Omega(z) = \partial b(z)/\partial z$ and the core and cladding radii a_0 and b_0 at the beginning of the taper transition where $z = 0$.

The electric field components at the interfaces are given by Eqs. (A.11) and (A.13), and the coefficients A and B can be expressed via Eqs. (1.27), and (A.23) and (A.24), respectively. Normalization to the total guided power P leads to the orthonormalized electric field components of the local modes. The integration over the azimuthal angle ϕ yields the coupling coefficient $C_{jp}^{\text{tot}}(z)$. For two modes with the same azimuthal symmetry, i. e., $l = 0$, it is given by

$$C_{jp}^{\text{tot}}(z) = C_{jp}^{\text{core},y}(z) + C_{jp}^{\text{core},z}(z) + C_{jp}^{\text{clad},y}(z) + C_{jp}^{\text{clad},z}(z). \tag{1.38}$$

It is the sum of four distinct contributions originating from coupling via either the transverse or the longitudinal electric field components at each of the two interfaces of the three layer system:

$$\begin{aligned} C_{jp}^{\text{core},y}(z) &= \frac{k_0^2}{2\pi\sqrt{\beta_j(z)\beta_p(z)}} \cdot \frac{2\pi\Omega(z)}{b(z)(\beta_j(z)-\beta_p(z))} \cdot D_j^{-1/2} \cdot D_p^{-1/2} \times \\ &\quad a(z)^2 \cdot (n_{\text{core}}^2 - n_{\text{clad}}^2) \cdot J_0(h_j a) \cdot J_0(h_p a), \\ C_{jp}^{\text{core},z}(z) &= \frac{h_j h_p \sqrt{\beta_j(z)\beta_p(z)}}{4\pi n_{\text{core}}^4 k_0^2} \cdot \frac{2\pi\Omega(z)}{b(z)(\beta_j(z)-\beta_p(z))} \cdot D_j^{-1/2} \cdot D_p^{-1/2} \times \\ &\quad a(z)^2 \cdot (n_{\text{core}}^2 - n_{\text{clad}}^2) \cdot J_1(h_j a) \cdot J_1(h_p a), \\ C_{jp}^{\text{clad},y}(z) &= \frac{k_0^2}{2\pi\sqrt{\beta_j(z)\beta_p(z)}} \cdot \frac{2\pi\Omega(z)}{b(z)(\beta_j(z)-\beta_p(z))} \cdot D_j^{-1/2} \cdot D_p^{-1/2} \times \\ &\quad b(z)^2 \cdot (n_{\text{clad}}^2 - n_{\text{vac}}^2) \cdot \frac{B_j}{A_j} \cdot \frac{B_p}{A_p} \cdot K_0(q_j b) \cdot K_0(q_p b), \\ C_{jp}^{\text{clad},z}(z) &= \frac{q_j q_p \sqrt{\beta_j(z)\beta_p(z)}}{4\pi n_{\text{vacuum}}^4 k_0^2} \cdot \frac{2\pi\Omega(z)}{b(z)(\beta_j(z)-\beta_p(z))} \cdot D_j^{-1/2} \cdot D_p^{-1/2} \times \\ &\quad b(z)^2 \cdot (n_{\text{clad}}^2 - n_{\text{vac}}^2) \cdot \frac{B_j}{A_j} \cdot \frac{B_p}{A_p} \cdot K_1(q_j b) \cdot K_1(q_p b). \end{aligned} \tag{1.39}$$

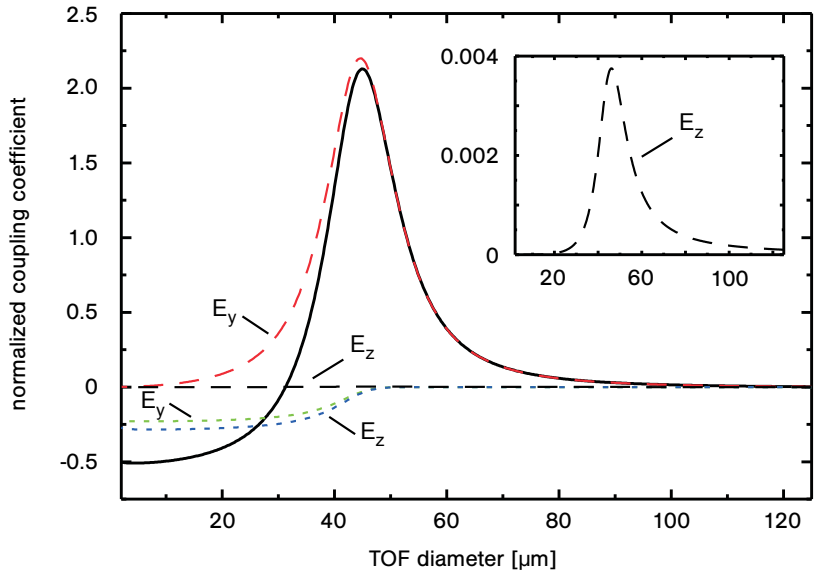

Figure 1.14.: Total normalized coupling coefficient $\bar{C}_{12}$ (solid line) and the contributions due to coupling at the core/cladding (dashed lines) and the cladding/vacuum interface (dotted lines) as a function of TOF diameter. The contributions due to coupling of the transversal and longitudinal components are plotted separately. The inset shows a magnification of the contribution from coupling of the longitudinal field components at the core/cladding interface which is suppressed by about three orders of magnitude.

The coupling between modes depends linearly on the taper angle and increases as the difference between the propagation constants of the modes becomes smaller [62]. Figure 1.14 shows the normalized coupling coefficient $\bar{C}_{12} = C_{12}b/\Omega$ for coupling between the LP_{01} and the LP_{02} modes as a function of the TOF diameter (solid line). It is clearly apparent from the figure that there are two coupling regimes: For higher TOF diameters, where the mode is still mainly confined by the core/cladding interface, the total coupling is dominated by coupling at this interface (dashed lines). Since here, the longitudinal components of the electric fields are negligibly small, also the coupling via these components is suppressed by almost three orders of magnitude, as indicated by the magnification in the inset of Fig. 1.14. For coupling at the core/cladding interface, the coupling coefficient is positive which results in a coupling of light from the LP_{01} mode to the LP_{02} mode for negative taper angles.

As the TOF becomes thinner, the fundamental mode extends more to the surrounding vacuum, causing the coupling to be dominated by the coupling at the cladding/vacuum interface (dotted lines). For small TOF diameters, the longitudinal components of the electric fields become more pronounced, yielding roughly equal contributions to the coupling from the transverse and longitudinal field components. For coupling at the cladding/vacuum interface, the coupling coefficient $\bar{C}_{12}$ is negative, yielding losses from the fundamental LP_{01} mode to the LP_{02} mode for positive taper angles.

Like the delineation between adiabatic and lossy tapers, the coupling coefficient exhibits a significant wavelength dependence as is shown in Fig. 1.15. Here, the normalized coupling coefficient for coupling between the LP_{01} and the LP_{02} modes is plotted as a function of the TOF diameter for six different wavelengths. The coupling coefficient reaches a maximum at

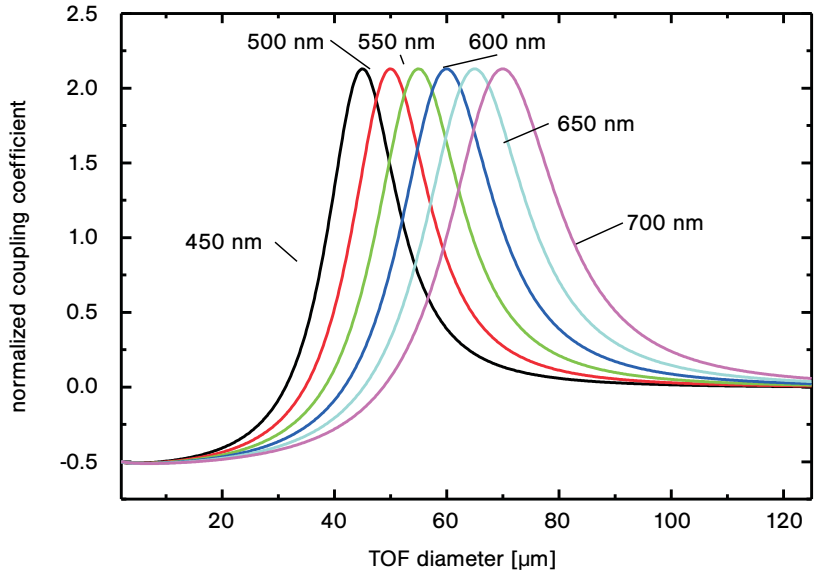

Figure 1.15.: Normalized coupling coefficient as a function of TOF diameter for six different wavelengths ranging from 450 nm to 700 nm.

roughly the same TOF diameter at which the critical local taper angle in the delineation of Fig. 1.13 reaches a minimum. This is due to the fact that the wavelength dependence of the coupling coefficient is dominated by the wavelength dependence of the beat length between the modes, with only small modifications due to the spatial overlap of the electric fields of the modes. The length scale criterion is therefore a good criterion for the design of roughly adiabatic tapers. Calculation of the coupling coefficients and the resulting power transfer can then be used to quantify the residual losses of such a taper.

So far, only coupling between modes with the same azimuthal symmetry has been considered. This is due to the fact that the azimuthal integral for the transverse field components becomes

$$\int_0^{2\pi} exp[i(l_p - lj)\phi]d\phi = 2\pi\delta_{l_p l_j}, \tag{1.40}$$

where $\delta_{l_p l_j}$ is the Kronecker delta function, which is equal to 1, if the z-components of the orbital angular momentum, l_p and l_j, of the two coupling modes coincide, and equal to 0 otherwise. Hence, coupling of the fundamental mode via the transverse electric field components is only possible to modes with the same azimuthal symmetry. For the longitudinal field components, however, the azimuthal integral becomes the sum of three components which include $\delta_{l_p l_j}$, δ_{l_p, l_j-2}, and δ_{l_p, l_j+2}. As a result, coupling of the fundamental mode to modes

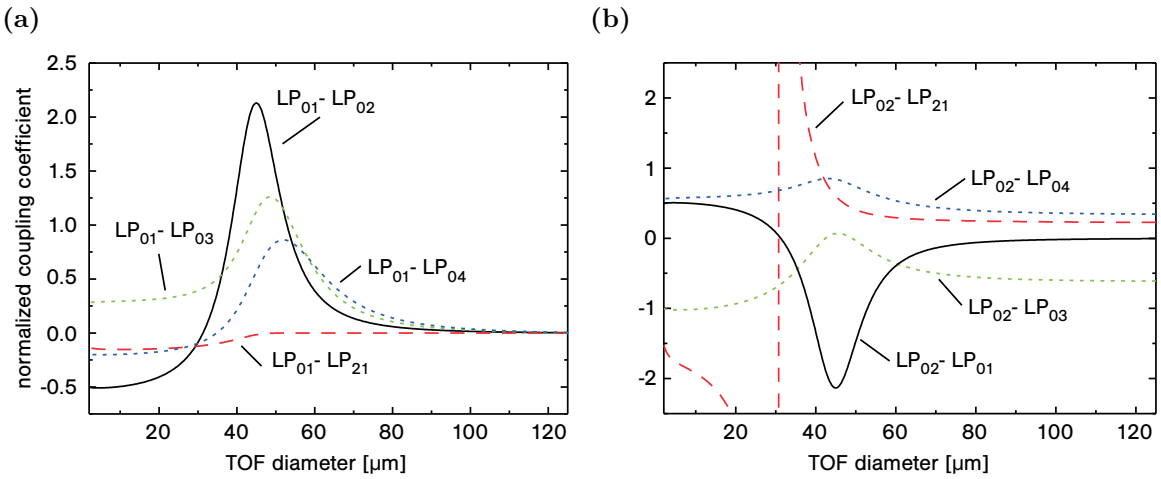

Figure 1.16.: Normalized coupling coefficient for coupling of the LP_{01} (a) and the LP_{02} (b) mode to higher order modes. Coupling to the LP_{21} (dashed line) mode is only possible via the longitudinal electric field components whereas coupling between modes with the same azimuthal symmetry (solid and dotted lines) is dominated by coupling via the transverse field components.

with $l = 2$ is also possible. The according coupling coefficient is given by

$$\begin{aligned} C_{jp}^{l=2}(z)) \quad = \quad & \frac{\sqrt{\beta_j(z)\beta_p(z)}}{8\pi k_0^2} \cdot \frac{2\pi\Omega(z)}{b(z)(\beta_j(z)-\beta_p(z))} \cdot D_j^{-1/2} \cdot D_p^{-1/2} \times \\ & \Big[\frac{h_j h_p}{n_{\text{core}}^4} \cdot a(z)^2 \cdot (n_{\text{core}}^2 - n_{\text{clad}}^2) \cdot J_1(h_j a) \cdot J_1(h_p a) - \\ & \frac{q_j q_p}{n_{\text{vac}}^4} \cdot b(z)^2 \cdot (n_{\text{clad}}^2 - n_{\text{vac}}^2) \cdot \\ & \frac{B_j}{A_j} \cdot \frac{B_p}{A_p} \cdot K_1(q_j b) \cdot K_1(q_p b)\Big]. \end{aligned} \tag{1.41}$$

The normalized coupling coefficients for coupling of the fundamental LP_{01} mode to higher order modes as a function of the TOF diameter are shown in Fig. 1.16(a). Since coupling to the LP_{21} mode is only possible via the longitudinal components of the electric field, the corresponding normalized coupling coefficient (dashed line) only contributes at smaller TOF diameters where coupling predominantly occurs at the cladding/vacuum interface. The normalized coupling coefficients for coupling to higher order modes with the same azimuthal symmetry (dotted lines) exhibit a similar qualitative behavior as that for coupling to the LP_{02} mode (solid line). The sign of the coefficient for low TOF diameters depends on the relative phase between the transverse field components of the fundamental mode and that of the higher order mode at the cladding/vacuum. Therefore, it is negative for coupling to LP_{0m} modes with an even value of m and positive for coupling to modes with an odd value for m. Although the coupling strength decreases with rising order of the modes, the contributions of coupling to these modes are still significant and have to be included into a comprehensive study of the propagation properties of the fundamental mode in a TOF taper transition.

Furthermore, the coupling between higher order modes has to be considered as can be seen from Fig. 1.16(b) on the example of coupling of the LP_{02} mode to the next higher and

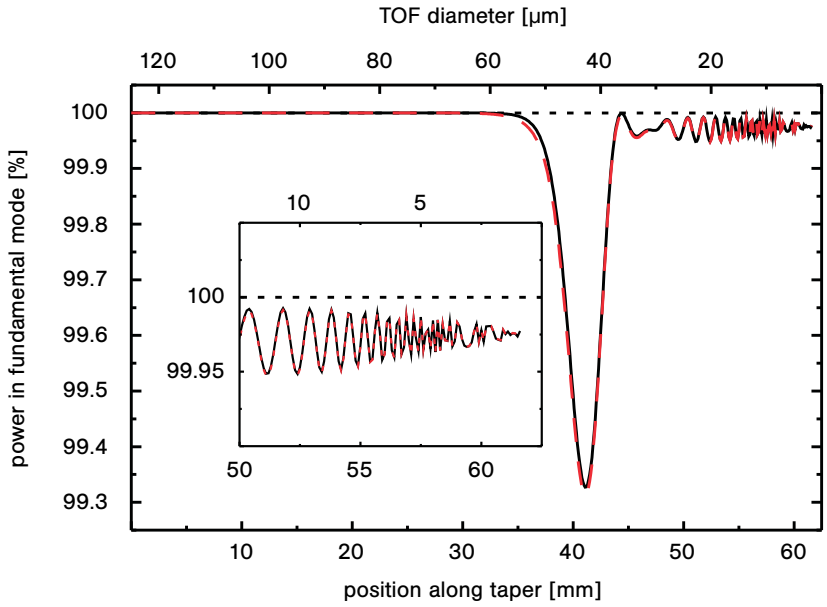

Figure 1.17.: Evolution of the fraction of power guided by the fundamental mode as a function of the position along the TOF for a taper transition with a constant slope of 1 mrad and a wavelength of the guided light of 450 nm. Taking into account the first four higher order modes (dashed line) does not change the evolution significantly as compared to only considering coupling to the LP_{02} mode (solid line). The inset shows a magnification of the power oscillation for small taper diameters and the dotted lines indicate a power fraction of 100 %.

lower order modes. Here, coupling to the LP_{03} and LP_{04} (dotted lines) is weaker but still on the same order of magnitude as the coupling to the fundamental mode (solid line). The coefficient for coupling to the LP_{21} mode (dashed line) diverges for a fiber diameter of about 30 µm since the effective refractive indices, and therefore the propagation constants of the two modes, are equal for this diameter (cf. Fig. 1.8) and the overlap of the axial field components for both modes is finite (cf. Fig. 1.11(d)). This means that a significant amount of the light power coupled from the fundamental mode to the LP_{02} mode can be lost due to the highly efficient coupling to the LP_{21} mode at this fiber diameter. Therefore, the light power cannot be transferred back anymore into the fundamental mode via the beating between the LP_{01} and the LP_{02} mode. This effect makes it even more important to tailor the shape of the taper transitions such that coupling from the fundamental mode to the LP_{02} mode is avoided.

Power loss from the fundamental mode

Once the coupling coefficients are known, the fraction of the guided power propagating along the taper for each mode can be determined by solving the coupled local mode equations given by Eq. (1.31). For each position z along the taper transition, it is given by the modulus squared of the coefficients $b_j(z)$ which describe the amplitude and phase of the corresponding mode. Figure 1.17 shows the evolution of the fraction of the total power guided by the fundamental mode for a downtaper with a constant slope of 1 mrad, taking into account only coupling between the LP_{01} and LP_{02} modes (solid line) as well as coupling between the

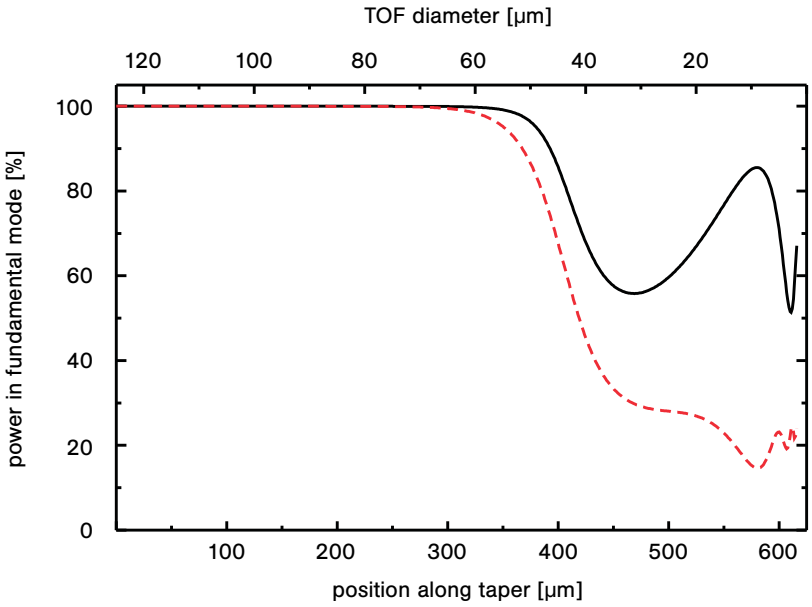

Figure 1.18.: Evolution of the fraction of power guided by the fundamental mode as a function of the position along the TOF for a taper transition with a constant slope of 100 mrad and a wavelength of the guided light of 450 nm. Taking into account the first four higher order modes (dashed line) significantly increases the losses from the fundamental mode as compared to only considering coupling to the LP_{02} mode (solid line).

fundamental mode and the first four higher order modes which can couple to the fundamental mode (LP_{02} to LP_{04} and LP_{21}, dashed line). The data has been calculated for a wavelength of 450 nm, assuming that at the beginning of the taper, for $z = 0$, all the power is guided in the fundamental mode of the TOF. It is clearly apparent from the figure that for a taper slope of 1 mrad, the mode transformation within the taper transition is approximately adiabatic with a transmission above 99.97 % for the whole taper transition. For a TOF diameter of about 43 µm, where the coupling coefficient for coupling between the LP_{01} and LP_{02} modes reaches a maximum, approximately 0.7 % of the guided power are coupled out of the fundamental mode. Due to the beating of the modes, however, the power is transferred back into the fundamental mode directly. The change of sign of the coupling coefficient at a TOF diameter of about 30 µm is clearly visible as a phase shift in the oscillation of the guided power between the fundamental and higher order modes. For small TOF diameters, the amplitude and period of this oscillation decrease yielding a convergence of the power in the fundamental mode to its value at the end of the taper transition, as is shown in detail in the inset of Fig. 1.17. Since the oscillation is very fast for small TOF diameters, the TOF diameter resolution of the simulation of 0.2 µm is not sufficient anymore to reproduce the complete oscillation resulting in the spiky structure visible in Fig. 1.17. For the quasi-adiabatic taper transition discussed here, already the fraction of power lost from the fundamental mode due to coupling to the LP_{02} mode is very small. Thus, coupling to and between higher order modes can be neglected as is apparent from the comparison of the solid and the dashed line depicted in Fig. 1.17.

For a non-adiabatic taper transition, however, taking into account higher order modes significantly changes the simulated results. Figure 1.18 shows the evolution of the fraction of the total power guided by the fundamental mode for a downtaper with a constant slope

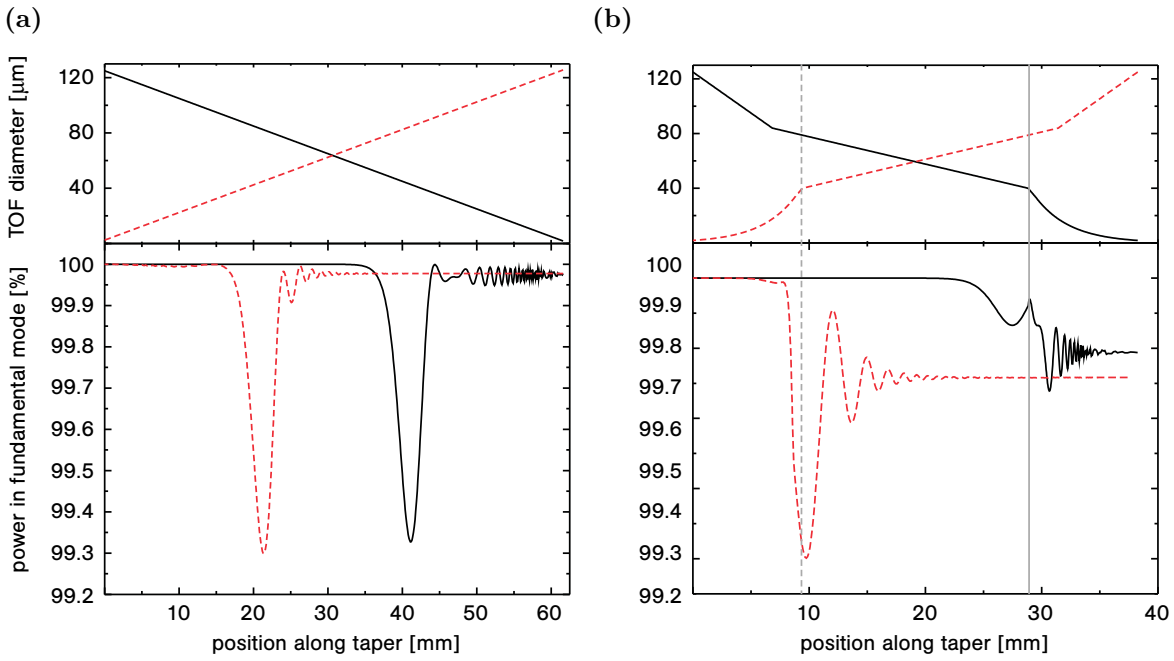

Figure 1.19.: Evolution of the fraction of power guided by the fundamental mode as a function of the position along the TOF for light with a wavelength of 450 nm. For a constant local taper angle (a), the total transmission of the downtaper (solid line) and uptaper (dashed line) is equal, while it differs for a variable local taper angle (b).

of 100 mrad, using the same assumptions as for the 1 mrad slope downtaper before. Since here, the local taper length scale is much smaller than the beat length between the modes, the light coupled out of the fundamental mode around the TOF diameter of about 43 µm cannot be recovered completely before the TOF diameter has changed significantly. As a result, the coupling mechanisms become more complex and a significant fraction of the power can be coupled to higher order modes. Hence, in order to properly predict the transmission properties of non-adiabatic taper transitions, a large number of higher order modes has to be taken into account. Since this thesis concentrates on TOFs with adiabatic or at least quasi-adiabatic taper transitions, the further analysis will be limited to coupling between the LP_{01} and LP_{02} modes.

Every TOF consists of a downtaper and an uptaper where the core guided mode is transformed into a cladding guided mode and back from the cladding guided mode to a core guided mode, respectively. The evolution of the fraction of the total power guided by the fundamental mode will, in principle, be different for each of the two taper transition, as is shown in Fig. 1.19 for two different TOFs. The relation between the local TOF diameter and the position along the taper for the downtaper (solid line) and the uptaper (dashed line) is plotted in the upper part of the figure for both TOFs.

Figure 1.19(a) displays the power in the fundamental mode as a function of the position along the taper for a downtaper (solid line) and an uptaper (dashed line) with constant slopes of 1 mrad. As for the downtaper discussed above, the power evolution in the uptaper is determined by the taper diameter dependence of the coupling coefficient. The fraction of power guided by the fundamental mode reaches a minimum for a TOF diameter of about

43 µm but recovers quickly before the TOF diameter has changed significantly. Due to the decreasing coupling coefficient, the beating amplitude between the two modes decreases with increasing TOF diameter yielding a convergence of the power in the fundamental mode to the same value as for the downtaper.

The transmission properties of taper transition with a variable local taper angle, however, can differ significantly from this behavior, as is shown in Fig. 1.19(b) for a taper transition with three different parts of different slopes and an exponential diameter profile for small TOF radii. The taper transition diameter profile assumed for the simulation will be discussed in detail in Sec. 2.1.1. Up to a position along the taper of approximately 29 mm, the downtaper (solid line) shows the same power evolution in the fundamental mode as the one with the 1 mrad slope, since in the significant diameter range below 84 µm, this taper transition also exhibits a slope of 1 mrad. At a position along the taper of about 29 mm (solid vertical line), however, the taper slope changes to 5 mrad yielding a much shorter local taper length scale which prevents the power from being coupled back completely to the fundamental mode. As a result, the transmission of the whole downtaper is approximately 98.9 %. In the uptaper of the variable local taper angle TOF (dashed line), the taper slope changes from 5 mrad to 1 mrad at a position along the taper of about 9.4 mm (dashed vertical line) where already a significant amount of power has been coupled out of the fundamental mode due to the large taper angle. This power cannot be transferred back to the fundamental mode completely since the coupling coefficient decreases due to the decrease of the local taper angle. Consequently, the total transmission of the uptaper of about 98.6 % is lower than the transmission of the downtaper. Hence, the transmission properties of down- and uptaper have to be calculated separately in order to allow for possible asymmetric coupling behavior. For a TOF with a nanofiber waist which acts as a mode filter only transmitting the fundamental mode, the product of these two values yields the total transmission of the TOF, assuming no other loss channels.

1.3.5. Coupling to radiative modes

In the subwavelength diameter parts of a TOF, a considerable fraction of the guided light travels outside the fiber as shown in Fig. 1.7. As a result, the effective refractive index of the fundamental mode is reduced and its propagation constant approaches the propagation constant of the radiative modes which is given by $\beta_{\mathrm{rad}} = 2\pi/\lambda$. Thus, for TOFs with a subwavelength diameter waist, coupling to radiative modes can become a significant loss mechanism [42, 63]. According to Eq. (1.29), the delineation condition for the coupling between two modes is determined by the local taper length scale and the beat length between the two modes. For coupling of the fundamental guided mode to radiative modes, the beat length increases monotonically with decreasing fiber radius. Therefore, the largest beat length is reached at the nanofiber waist. For the subwavelength diameter parts of the taper transitions of the TOFs discussed within this thesis, the taper length scale is constant, as discussed in Chapter 2 and, thus, the largest coupling occurs at the position along the TOF where the taper transitions adjoin the nanofiber waist. For a given taper length scale z_t, the approximate delineation between adiabatic and lossy tapers only depends on the waist diameter d of the TOF and the wavelength λ of the guided light [63]:

$$\frac{\lambda}{n_{\mathrm{eff}}(d,\lambda) - 1} = z_t. \tag{1.42}$$

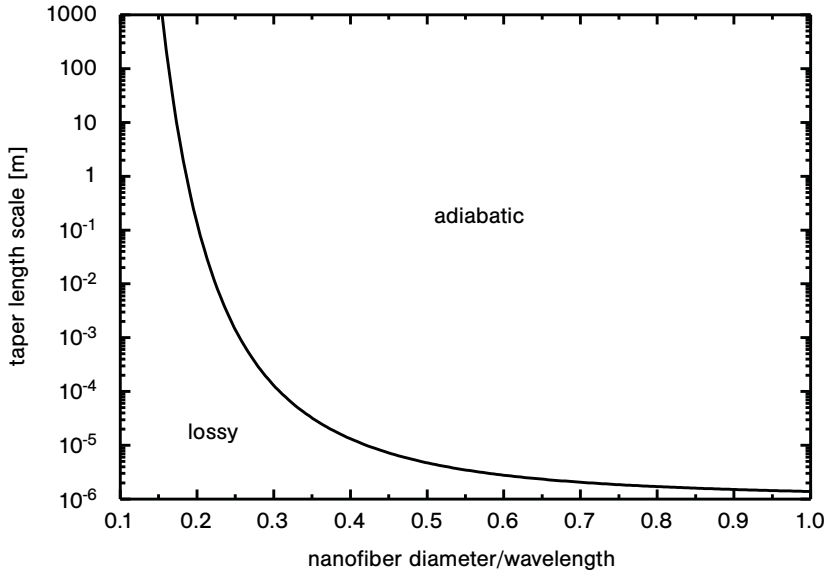

Figure 1.20.: Delineation curve between adiabatic and lossy tapers caused by coupling to radiative modes, calculated for a two layer system with refractive indices of 1.46557 and 1 for the nanofiber and the surrounding vacuum, respectively.

Fig. 1.20 shows the delineation curve between adiabatic and lossy tapers for a local taper length scale range from 1 µm to 1 km and a nanofiber diameter between 0.1λ and λ. It has been calculated for a wavelength of 450 nm and a two layer system assuming a pure silica nanofiber with a refractive index of 1.46557 (Sellmeier formula for 450 nm [64]) surrounded by vacuum with a refractive index of 1. As expected, the adiabaticity criterion for the taper length scale becomes more strict for smaller nanofiber diameters. Apart from small changes due to dispersion of the fiber material, the displayed curve holds universally for all wavelengths.

2. Fabrication and optimization of broadband tapered optical fibers

Since the light propagation properties of a tapered optical fiber (TOF) with a nanofiber waist depend crucially on its geometry, the TOFs used for the experiments presented in this thesis have been fabricated by a carefully designed flame pulling process. This process and the characterization of the resulting fiber diameter profile as well as the nanofiber quality via scanning electron microscopy and transmission measurements are discussed in the first part of this chapter. In the second part, a systematic study of the influence of the fiber profile parameters on the transmission properties of the TOF is presented. The information obtained thereby can be used to tailor and optimize the diameter profile of the TOF to meet the desired transmission properties. Parts of this chapter have been published in [65, 66].

2.1. Fabrication and characterization of tapered optical fibers

Figure 2.1 shows a schematic of the fiber pulling rig developed by F. Warken [67]. A standard optical fiber is inserted into two V-grooves which are precisely aligned to fall in line and in which the fiber is held in place by two magnetic clamps on each holder. The V-groove holders are mounted onto two linear translation stages, the translator and the stretcher, which permit sub-micrometer positioning. A stationary hydrogen/oxygen flame heats a section of the fiber with a length of approximately 1 mm to a temperature of about 1700 °C [68], making it soft and malleable. A mass flow controller ensures a constant laminar gas flow and, thereby, a constant flame profile which is important for a homogeneous nanofiber waist. To avoid contamination of the fiber by carbon and other residuals of the combustion process, very clean gases and pipes are used. The translator moves the fiber back and forth above the flame while the stretcher simultaneously elongates it. Due to volume conservation, the fiber diameter is thus gradually reduced. The motion of the two translation stages is computer controlled in order to obtain a predetermined fiber shape. The trajectories of the translator and of the stretcher used for the control of the pulling process are calculated using an analytic algorithm presented in [67]. In order to avoid pollution of the fiber during the pulling process, the procedure is performed under clean room conditions in a laminar flow box.

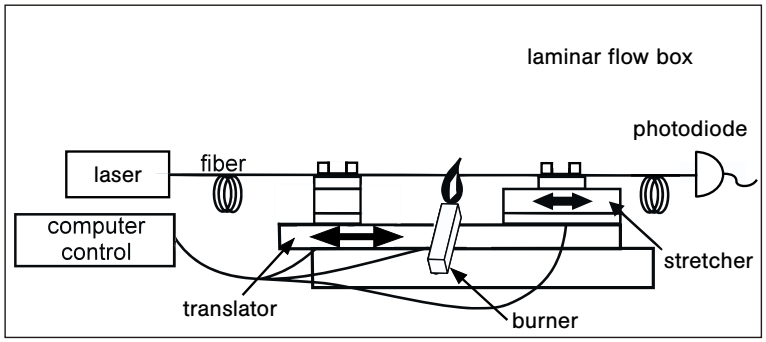

Figure 2.1.: Schematic of the fiber pulling rig. A standard glass fiber is heated by the flame of a stationary gas burner while it is moved and stretched by two stacked translation stages.

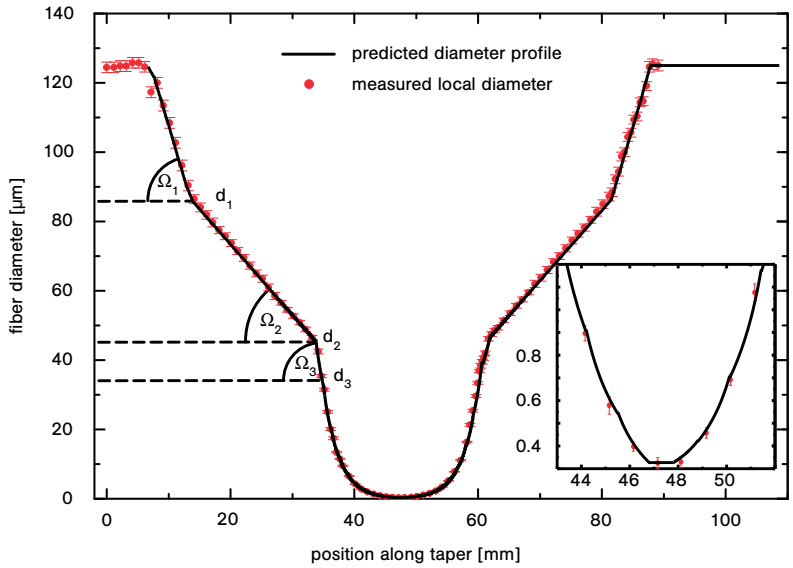

Figure 2.2.: Comparison of the predicted diameter profile (solid line) with the local TOF diameter measured with a scanning electron microscope (data points). The inset shows a magnification of the submicron-diameter region of the profile.

By this technique, any shape of fiber taper with two identical taper transitions and a uniform waist of any length and diameter can, in principle, be produced [69]. Technically, this is limited by the resulting total length of the TOF which in turn is limited to 16 cm by the travel range of the stretcher. The TOFs dicussed in this thesis all exhibit a three-fold linear taper transition, thereby approximating the rotated 's-shape' of the optimal taper transition for adiabatic mode conversion [45].

2.1.1. Characterization of the taper shape via scanning electron microscopy

Figure 2.2 shows the diameter profile of a TOF measured with a scanning electron microscope (SEM) in close collaboration with C. Wuttke. The solid line indicates the fiber diameter profile as predicted by our algorithm. The TOF is characterized by the following preset parameters: a 320 nm-diameter waist of 1 mm length (shown in the inset), local taper angles $\Omega_1 = 3\,\mathrm{mrad}$, $\Omega_2 = 1\,\mathrm{mrad}$ and $\Omega_3 = 5\,\mathrm{mrad}$ for the three linear parts of the taper transition, and a change of the local taper angles at the fiber diameters $d_1 \approx 86\,\mu\mathrm{m}$ and $d_2 \approx 45\,\mu\mathrm{m}$. Note that the d_i denote the diameters of the fiber cladding along the taper, and the Ω_i denote the local taper angles of the fiber cladding for the three linear parts of the taper transition. It has been found empirically from the simulations of the diameter profile that the profile exhibits local deformations if $\Omega(d)/d$ becomes too large. Hence, the local taper angle $\Omega(d)$ is limited to $0.15\,\mathrm{mrad}/\mu\mathrm{m} \cdot d$. For the local taper angle $\Omega_3 = 5\,\mathrm{mrad}$ used for our TOFs, the profile thus has an exponential shape for radii smaller than $d_3 \approx 34\,\mu\mathrm{m}$.

The TOF characterized in Fig. 2.2 was fabricated from a Nufern 460-HP fiber and placed on a gold coated substrate for the SEM measurements. While the fiber is glued to the substrate well outside the taper regions, the van-der-Waals-force between the fiber and the substrate fixes the TOF over its whole length during the acquisition of electron micrographs. The measurements were performed with an electron energy of 2 keV and a current of 53 pA. For

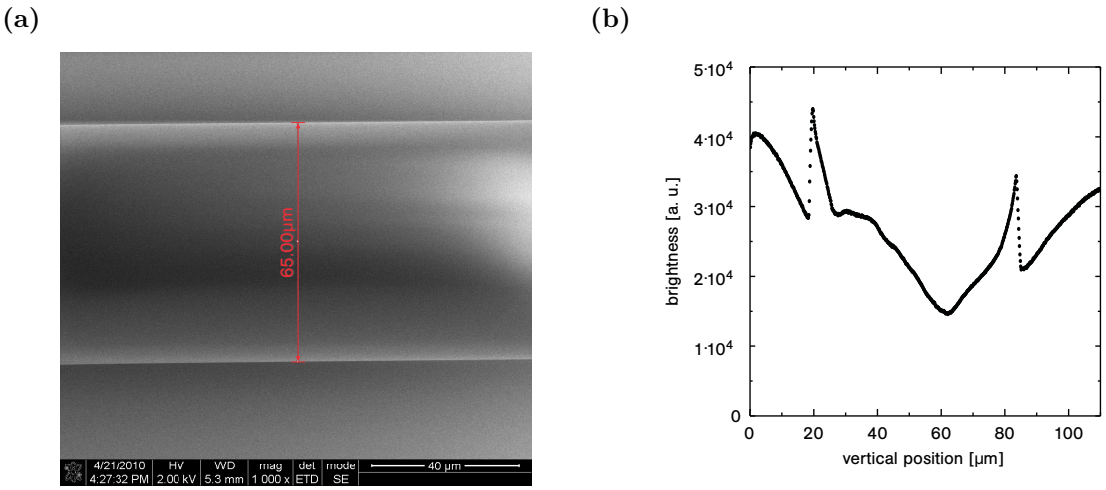

Figure 2.3.: (a) Electron micrograph taken in the taper transition of a TOF where the local diameter is $(65 \pm 1)\,\mu m$ as determined by the measurement tool of the the SEM imaging program. (b) Horizontally binned brightness values of the micrograph. The fiber edges appear as steep increases of the brightness.

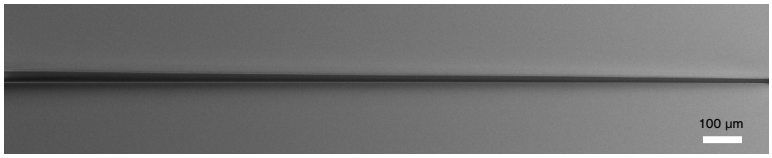

Figure 2.4.: Electron micrograph of the exponential part of the taper transition of a TOF between $d \approx 31\,\mu m$ and $d \approx 12\,\mu m$.

these values, distortions of the electron micrograph due to charges that accumulate on the insulating fiber turned out to be negligible.

In order to determine the local fiber diameter, sucessive electron micrographs were taken along the TOF by shifting the field of view in steps varying between 0.25 mm and 1 mm. An example of such a micrograph taken in the taper transition is shown in Fig. 2.3(a). The diameter has been determined with the measurement tool of the SEM imaging program to be $(65 \pm 1)\,\mu m$. The relative error in the diameter determination due to the slight tilt of the fiber with respect to the picture frame is below 10^{-3} and therefore negligible. in order to further analyze the shown micrograph, the brightness values have been binned horizontally and plotted as a function of the vertical position in Fig. 2.3(b). The edges of the fiber appear as steep increases of the brightness at $(19.1 \pm 0.63)\,\mu m$ and $(84.5 \pm 0.88)\,\mu m$ yielding a fiber diameter of $(65.4 \pm 1.08)\,\mu m$ which agrees well with the value determined directly from the micrograph.

Since Fig. 2.3(a) only shows an approximately 125 µm long piece of the fiber taper, the change in diameter caused by the slope of 1 mrad is as small as 125 nm and therefore invisible in the electron micrograph. In order to visualize the tapering of the fiber, an approximately 2 mm long section of the exponential part of the diameter profile is shown in Fig. 2.4. Here, the decrease of the diameter from about 29 µm down to about 12 µm is clearly visible.

Figure 2.5(a) shows an electron micrograph of the nanofiber waist from which the diameter has been determined to be $(330 \pm 25)\,nm$. The relatively large error is due to the blurred

(a) **(b)**

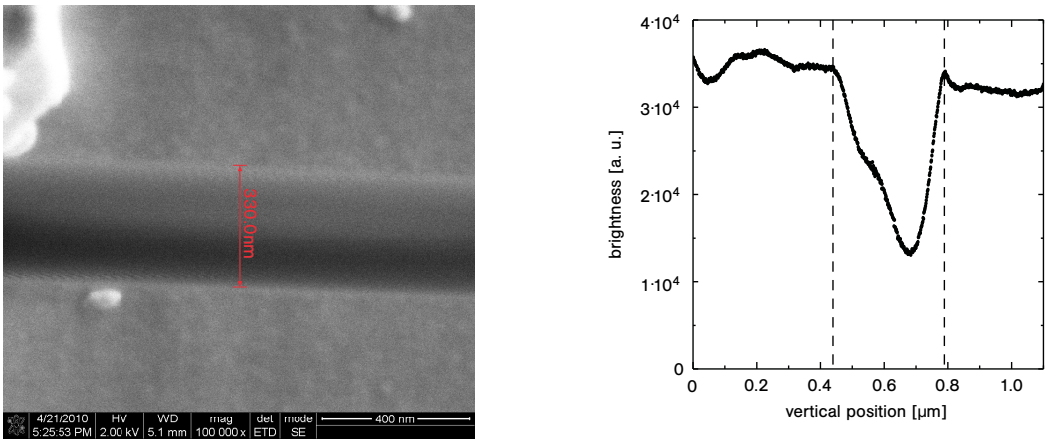

Figure 2.5.: (a) Electron micrograph of the nanofiber waist of a TOF. (b) Horizontally binned brightness values of the micrograph. The vertical dashed lines indicate the middle of the brightness decrease at the fiber edge. The features in the background are due to contaminations of the substrate.

micrograph which makes it difficult to determine the edge of the nanofiber. Compared to this effect, the tilt of the fiber with respect to the picture frame is negligible. The binned data in Fig. 2.5(b) shows the same issue. The brightness only decreases slowly at the nanofiber edges at $440 \pm 10\,\mathrm{nm}$ and $790 \pm 10\,\mathrm{nm}$ indicated by the vertical lines. This yields a relatively large value for the fiber diameter of $(350 \pm 14)\,\mathrm{nm}$. Due to the lack of a steep increase of the brightness at the fiber edges as shown in Fig. 2.3(b), the determination of the nanofiber radius from the binned brightness values is considered a not very reliable method. Thus, the values plotted in Fig. 2.2 have been determined directly from the electron micrograph as described before. The radius and homogeneity of the nanofiber waist of TOFs fabricated with the same fiber pulling rig have been studied in detail by U. Wiedemann et al. [18]. The measurements discussed here have been focussed on the taper transitions rather than on the nanofiber waist.

The measured diameter profile depicted in Fig. 2.2 closely follows the predicted profile. Figure 2.6(b) shows the absolute value of the relative deviations between the measured and simulated diameters. For comparison, the simulated diameter profile and the measurement errors relative to the measured values for the fiber diameter are displayed in Figs. 2.6(a) and (c), respectively. In the two linear sections with local taper angles Ω_1 and Ω_2, the relative deviations between the measured and simulated diameters are below 3 %, which is on the order of the precision of the SEM measurements. For the steep part of the taper transition with $\Omega_3 = 5\,\mathrm{mrad}$ and the exponential part, the relative deviation slightly increases to up to 10 %. This might be due to the finite precision of simulation and measurement owing to the small fiber diameters (cf. Fig. 2.6(a) and Fig. 2.6(c)). From the excellent agreement between the measured and simulated TOF diameters, we conclude that our production procedure for TOFs indeed realizes the predicted profiles, especially for diameters larger than 45 µm where the coupling of the fundamental mode to higher order modes is critical for the visible wavelength range as has been discussed in Sec. 1.3.

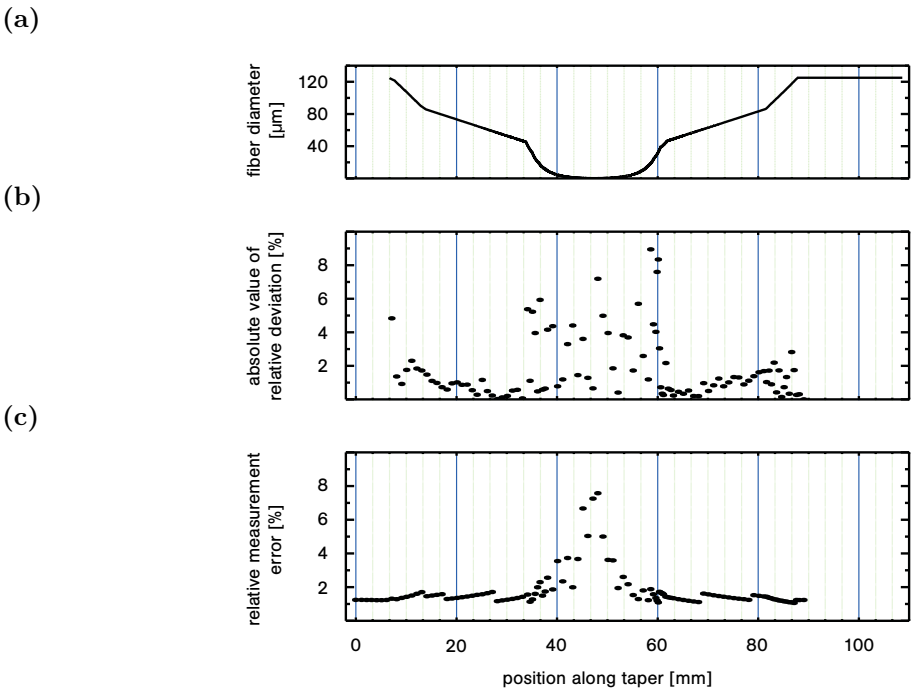

Figure 2.6.: (a) Simulated diameter profile, (b) relative deviation of the measured diameter profile with respect to the simulated profile, (c) and relative SEM measurement error as a function of the position along the taper.

2.1.2. Optical characterization of the TOF quality via transmission measurements

The transmission of light through the TOF is continuously monitored during the pulling process using a tungsten halogen light source (Ando AQ-4303B) and a spectrometer (Avantes AvaSpec-2048-2), yielding valuable information about the quality of the pulling process and the produced TOFs. For monochromatic light of 850 nm wavelength and a 500-nm diameter nanofiber waist, TOFs with a transmission of up to 98.7 % of the initial fiber transmission have been reported by our group [70].

Reproducibility of the pulling process

Figure 2.7 shows the transmission spectra of three different samples with the diameter profile presented in Fig. 2.2 fabricated from a Nufern 460-HP fiber. The measured transmission has been normalized to the transmission spectrum of the untapered fiber. Due to the careful control of the pulling process, the transmission exhibits a very high degree of reproducibility with variations of only $\pm(2\pm1)$ %. The transmission spectrum can be understood qualitatively by considering the wavelength dependence of the coupling to higher order modes discussed in Sec. 1.3. Since the used diameter profile exhibits a diameter dependent local taper angle, light guided in the fundamental mode will experience a variably strong coupling to higher order modes according to its wavelength. It is apparent from the figure that the coupling is rather weak in a wavelength range between 470 and 690 nm, but causes significant losses beyond this spectral band. Within this spectral band, the TOFs have a transmission of over 70 % with a peak transmission of over 90 % around 560 nm. Since the coupling strength and

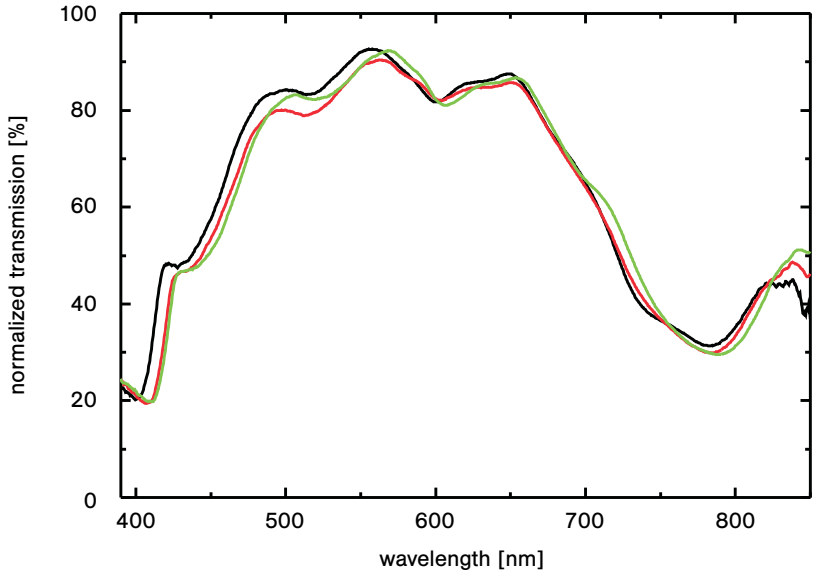

Figure 2.7.: Normalized transmission spectra for three different TOFs with the same radius profile as shown in Fig. 2.2.

the beat length between modes depend on the wavelength (cf. 1.3.4), the transmission shows an undulated modulation, as shown by Cassidy et al. [71].

Quality of the nanofiber waist

It has been suggested that scattering of light by surface contaminants or by surface roughness can cause losses in the nanofiber waist of a TOF which increase with waist length [39]. Figure 2.8(b) shows the normalized transmission spectra of fibers with the diameter profile presented in Fig. 2.2 but with three different waist lengths. The simulated diameter profiles with waist lengths of 1 mm, 5 mm, and 10 mm are depicted in Fig. 2.8(a). Due to the high degree of control over the TOF fabrication process discussed in Sec. 2.1.1 and Sec. 2.1.2 above, the actual diameter profiles of the TOFs can be assumed to coincide with the simulated profiles. Therefore, only the simulated profiles will be considered throughout this chapter. The variations of the transmission shown in Fig. 2.8(b) of $\pm(2\pm1)\,\%$ match those determined from Fig. 2.7. Within this degree of precision and for the waist lengths up to 1 cm considered here, an increase in the nanofiber length does not change the transmission properties. This, in turn, yields losses smaller than about 9 dB/m in this waistlength regime and implies that the surface of the nanofiber waist is very smooth and clean.

2.2. Design and optimization of broadband tapered optical fibers

The controlled fabrication of TOFs with preset diameter profiles permits an a priori design of the transmission properties of the TOFs. The influence of the taper shape on the coupling of the fundamental mode to higher order and radiative modes can be determined either theoretically from the coupled local mode equations (Eq. (1.31)) discussed in Sec. 1.3 or by

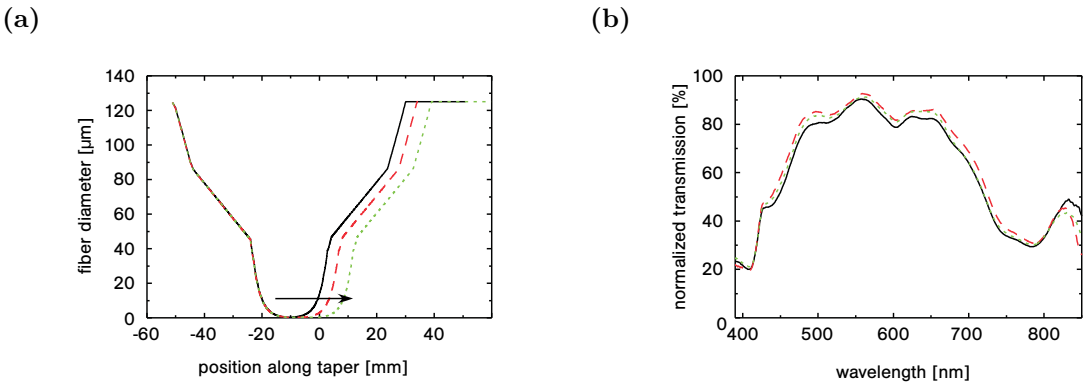

Figure 2.8.: Transmission properties for different waist lengths of 1 mm (solid line), 5 mm (dashed line), and 10 mm (dotted line): fiber taper profiles (a) and corresponding normalized transmission spectra (b).

an empirical study. The resulting knowledge can then be employed to optimize the TOFs according to the desired transmission properties.

2.2.1. Model calculations for TOFs fabricated from different fiber types

In order to investigate the influence of the properties of the fiber type used for tapering, the transmission properties of TOFs with the same diameter profile but fabricated from two different fiber types are studied.

For the experiments presented in this thesis, TOFs fabricated from a Nufern 460-HP fiber are used. This fiber type has a core diameter of 2.5 µm, a cladding diameter of 125 µm, a numerical aperture of 0.13, and a cut-off wavelength of about 430 nm. Assuming a pure silica cladding with a refractive index of $n_{\mathrm{clad}} = 1.46557$ at 450 nm, the refractive index of the core can be calculated to be $n_{\mathrm{core}} = 1.47132$. This refractive index increase is achieved by doping with 6 wt% of Germanium, as specified by the manufacturer. A TOF fabricated from this fiber type which is surrounded by vacuum with a refractive index of $n_{\mathrm{vac}} = 1$ can therefore be described by a three layer system with the parameters used for the calculations presented in Sec. 1.3, provided the refractive indices of core and cladding as well as the ratio of core and cladding diameter stay constant during tapering of the fiber.

A typical diameter profile used for our experiments has been presented and characterized in Sec. 2.1. The theoretically and experimentally determined transmission properties of a TOF with such a diameter profile and the parameters listed above are summarized in Fig. 2.9(a). The figure shows the measured transmission spectrum of a TOF with the diameter profile presented in Sec. 2.1.1 (solid line) together with the TOF transmission expected by considering coupling to higher order modes due to the tapering (dots). The theoretical values have been calculated by solving the coupled local mode equations (Eq. (1.31)) and deducing the power in the fundamental mode at the end of the taper transitions as described in Sec. 1.3.4.

It is clearly apparent from the figure that the theoretically expected transmission of the TOF is much higher than the actually measured value for the whole wavelength range. However, a zoom into the calculated spectrum (inset) shows that the shape of the measured transmission spectrum agrees quite well with the simulated data. This suggests that the measured losses are indeed caused by coupling of the fundamental mode to higher order modes due to the

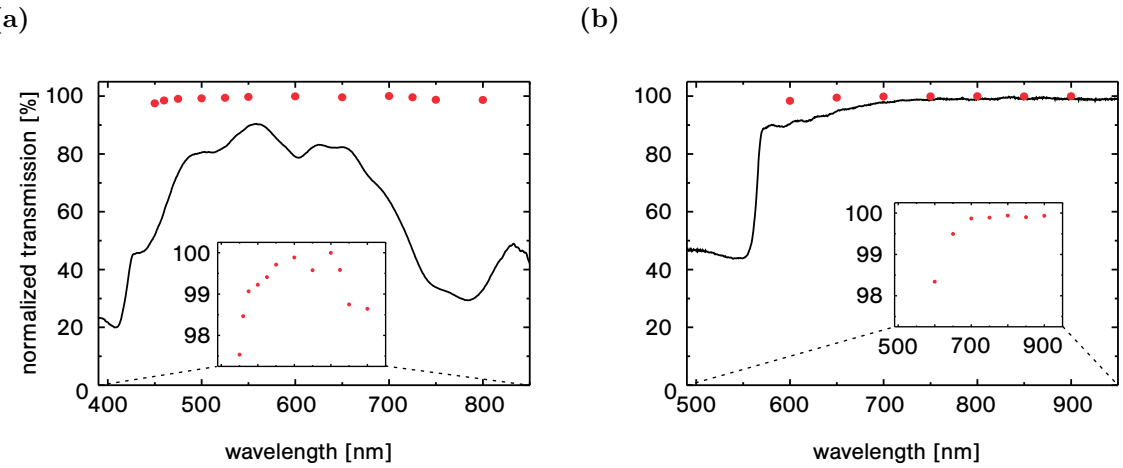

Figure 2.9.: Measured (solid line) and calculated (data points) transmission spectra of two TOFs with the same diameter profile fabricated from two different fiber types: (a) Nufern 460-HP and (b) Fibercore SM600. The insets show a magnification of the calculated data to reveal the spectral shape.

change of the local taper angle, but that the coupling strength is much higher than expected under the assumptions made in Sec. 1.3.1. As mentioned above, these assumptions comprise constant refractive indices for core, cladding, and the surrounding vacuum or air, as well as a constant ratio of core and cladding diameter. Therefore, possible explanations for the observed quantitative discrepancy could be that, due to material properties, the ratio of core and cladding diameter does not stay constant during tapering of the fiber or that the core doping material diffuses due to the heat input. Moreover, slight diameter variations of core and/or cladding of the fiber present already before the pulling process or a minor roughness of the fiber surface can also lead to a stronger coupling to higher order modes.

For comparison of the transmission properties, a TOF with the same diameter profile has been fabricated from a Fibercore SM600 fiber (serial number: 41471/B-00ED). The measured transmission spectrum is shown in Fig. 2.9(b) (solid line). The theoretical values for the transmission of a TOF with this diameter profile (dots) have been calculated for a three layer system with a core/cladding diameter ratio of $a/b = 3.78\,\mu\text{m}/125\,\mu\text{m} \approx 0.03$ and a numerical aperture of 0.12, yielding a refractive index profile of $n_{\text{core}} = 1.47047$, $n_{\text{clad}} = 1.46557$, and $n_{\text{vac}} = 1$ at 450 nm. These parameters match the values specified for the SM600 fiber by the manufacturer. Since the unprocessed fiber has a single mode cut-off wavelength of 592 nm as specified by the manufacturer, the single mode nanofiber waist of the TOF acts as a mode filter [71, 72] resulting in a transmission drop for wavelengths below 592 nm which is clearly visible in the measured spectrum. The calculations have only been performed for wavelengths above the single mode cut-off wavelength because the theoretical transmission values are calculated assuming a fiber with one core guided mode at most. The theoretical data suggests a transmission loss which is about one order of magnitude smaller than the measured transmission loss. A magnification of the calculated data in the inset shows that the qualitative behaviour of the simulated data agrees well with the measured spectrum. Therefore, it can be assumed that also for the TOF fabricated from a Fibercore SM600 fiber, the strength of the coupling to higher order modes is dominated by other effects than the change of the fiber diameter characterized by the local taper angle. These effects seem to be not specific to one certain fiber type used for tapering.

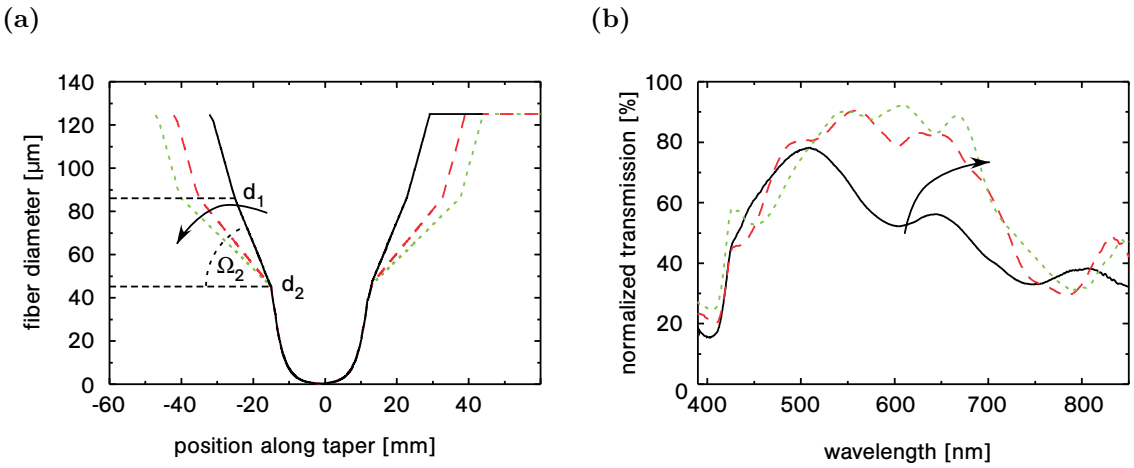

Figure 2.10.: Effect of the central linear slope of the taper profile (a) on the measured transmission spectra (b). The taper angle Ω_2 has been varied from 2 mrad (solid line) to 1 mrad (dashed line) and 0.8 mrad (dotted line).

In order to get a deeper insight into the underlying coupling mechanisms within the taper transitions and the quality of the flame pulling process, further studies can be performed. In the remainder of this chapter, however, I will concentrate on the empirical studied transmission properties of TOFs fabricated from a Nufern 460-HP fiber, since these are the TOFs used for the nanofiber-based spectroscopy experiments presented in this thesis.

2.2.2. Empirical study of coupling to higher order modes

Since the transmission properties of a TOF fabricated from a Nufern 460-HP fiber cannot be predicted sufficiently by the simulations presented in Sec. 1.3.4, their dependence on the taper diameter profile of the TOF has been studied empirically. For a three-fold linear taper shape as fabricated by the fiber pulling rig presented in Sec. 2.1, the local taper angle can be tuned either by changing the slope of the individual linear sections given by the Ω_i or by shifting the boundaries between the linear sections determined by d_1 and d_2.

Fig. 2.10 illustrates the effect of tuning the slope of the central linear section for the taper profile presented in Fig. 2.2. The profiles predicted by the analytic algorithm for three different values of the local taper angle Ω_2 are shown in Fig. 2.10(a). The corresponding measured transmission spectra are displayed in Fig. 2.10(b). As expected from the linear dependence of the mode coupling on the local taper angle, the transmission in the wavelength range between 470 and 690 nm rises if the taper angle Ω_2 is reduced from 1 mrad (dashed line) to 0.8 mrad (dotted line). For an increased taper angle of 2 mrad (solid line) on the other hand, the transmission drops significantly. Moreover, the undulated modulation of the transmission spectrum is compressed for smaller angles and streched for higher angles, as expected from the results presented in [62, 71].

The transmission for wavelengths smaller than 470 nm or larger than 690 nm is almost unaffected by the changes presented in Fig. 2.10(a). This means that the coupling of the fundamental mode to higher order modes for these wavelengths predominantly occurs at TOF diameters below 45 µm or above 86 µm, where the taper angle is unchanged for the taper diameter profiles presented in Fig 2.10(a). Apart from tuning the taper angles Ω_1 and

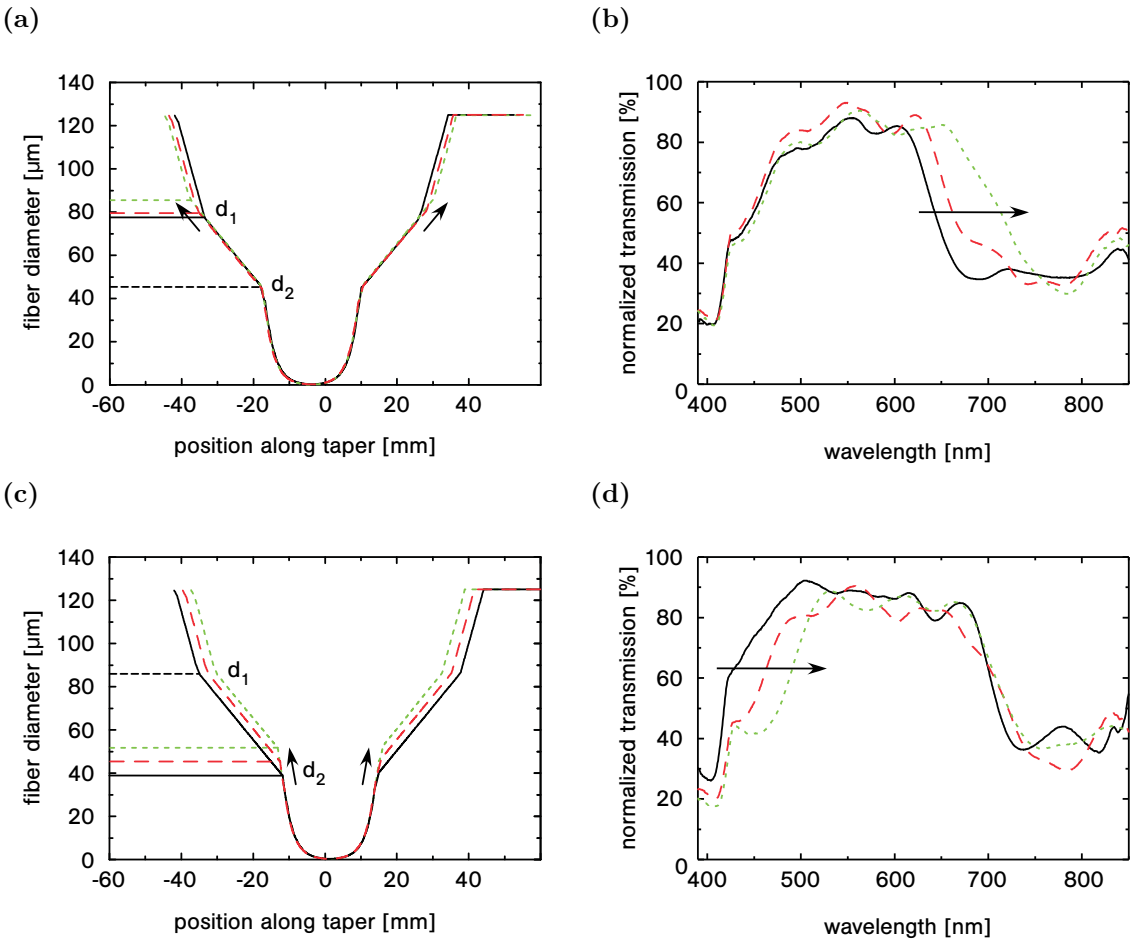

Figure 2.11.: Tuning of the TOF transmission band for long wavelengths ((a) fiber taper profiles, (b) normalized transmission spectra) and short wavelengths ((c) fiber taper profiles, (d) normalized transmission spectra).

Ω_3, the transmission properties for these wavelengths can also be changed by shifting the boundaries of the central linear section. Thereby, the spectral band of high transmission can be shifted, extended, or compressed. The radius profiles shown in Fig. 2.11(a) and (c) exhibit either a shift of the boundary d_1 between the first two linear sections (Fig. 2.11(a)) or a variation of the boundary d_2 between the last two linear sections (Fig. 2.11(c)). The corresponding changes of the measured transmission band are shown in Fig. 2.11(b) and (d), respectively. On the short wavelength side, this tuning is limited by the mode filter character of the nanofiber waist of the TOF. From the observed transmission drop, the single mode cut-off wavelength of the standard fiber used for tapering can be determined to be (430 ± 7) nm which agrees very well with the value of (430 ± 20) nm specified by the manufacturer for the Nufern 460-HP fiber.

Note that all changes of the transmission properties of the TOF also affect the total TOF length which renders a compromise between these two TOF properties necessary. The systematic study of the TOF transmission properties in dependence on the taper diameter profile permits the design of TOFs for different experimental demands. For the experiments pre-

	molecule fiber	cryo fiber
d_1	86 µm	86 µm
d_2	45 µm	45 µm
d_3	34 µm	34 µm
Ω_1	3 mrad	3 mrad
Ω_2	1 mrad	2 mrad
Ω_3	5 mrad	5 mrad
waist length	1 mm	1 mm
TOF length	81.2 mm	61.2 mm

Table 2.1.: Parameters of the TOF types used for the experiments discussed throughout this thesis.

sented in this thesis, two different TOF types have been used. For experiments where the total length of the TOF is less critical, the taper diameter profile presented in Fig. 2.2 with a total TOF length of 81.2 mm has been used. For applications demanding shorter TOFs, the taper angle Ω_2 is increased to 2 mrad, yielding a TOF of 61.2 mm length. The properties of these two types of TOFs, denoted as molecule fiber and cryo fiber, respectively, are summarized in Tab. 2.1.

2.2.3. Coupling to radiative modes

As discussed in Sec. 2.1.1, the TOFs used for the measurements presented in this thesis exhibit a local taper angle which is limited to 0.15 mrad/µm $\cdot 2b$ for all TOF radii b. This typically results in an exponential shape of the radius profile in the subwavelength diameter parts of the TOF, yielding a constant taper length scale of $z_t \approx 3.3$ mm (cf. Sec. 1.3.4). From Fig. 1.20, the nanofiber diameter at which adiabaticity breaks down for such a TOF can be determined as approximately $0.239 \cdot \lambda$.

The dramatic threshold behavior of the transmission loss has already been observed experimentally by Sumetsky et al. [42] and Hartung et al. [63] for biconical tapered fibers fabricated using an indirect laser heating method [69,73]. In order to experimentally verify the predicted behavior for the TOFs used here, three TOFs with the fiber radius profile presented in Fig. 2.2 and waist diameters of 120 nm, 150 nm, and 180 nm have been fabricated. The normalized transmission spectra of these TOFs, together with the normalized transmission spectrum of a TOF with a 320 nm waist diameter for comparison, are shown in Fig. 2.12(a). While losses in the visible wavelength range due to coupling to radiative modes can be assumed to be negligible for the TOF with a 320 nm waist diameter ($320\,\text{nm}/0.239 \approx 1300$ nm), adiabaticity breaks down at a different characteristic threshold wavelength for the other three examined waist diameters.

For clarity, the transmission spectra have been normalized to the transmission spectrum of the TOF with the 320 nm-diameter waist and plotted as a function of the ratio between nanofiber diameter and wavelength as shown in Fig. 2.12(b). As expected from Fig. 1.20, the transmission is reduced to 50 % at values for d/λ of approximately 0.239. The exact values are summarized in Tab. 2.2. They agree very well with the threshold values calculated according to Eq. (1.42) taking into account dispersion of the fiber material which are also shown in Tab. 2.2. However, the measured values lie systematically below the calculated values. This is most likely caused by a slight deviation of the actual value of the nanofiber

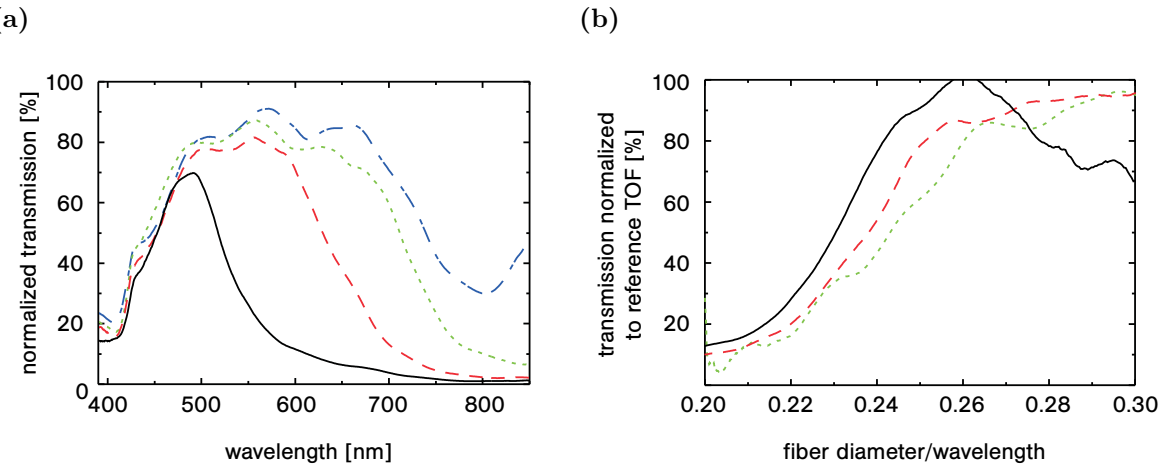

Figure 2.12.: (a) Normalized transmission spectra for different waist diameters of 120 nm (solid line), 150 nm (dashed line), 180 nm (dotted line), and 320 nm (dash-dotted line). (b) Transmission for the three thinner waist diameters normalized to the transmission of the 320 nm-diamter nanofiber waist TOF as a function of the fiber diameter in units of the wavelength of the guided light.

waist diameter [nm]	experimental threshold	calculated threshold
120	0.230	0.241
150	0.238	0.245
180	0.243	0.248

Table 2.2.: Experimentally determined threshold values of d/λ where the transmission is reduced to 50 % in comparison with the calculated threshold values taking into account material dispersion for the TOFs under study.

diameter from the simulated value which has been assumed for the calculations of d/λ. It has been suggested that the gas flow of the flame pushes the fiber perpendicular to the pulling direction and therefore further reduces its diameter [50]. This effect is not included in the simulation of the fiber diameter profile and might cause the actual diameter to lie below the simulated one. Already a deviation of 5 % for the nanofiber diameter would suffice to explain the observed delineation between adiabatic and lossy tapers.

Another explanation for the deviation of the calculated values can be found in the assumed index of refraction for the nanofiber. Possible reasons for a refractive index of the nanofiber waist of the TOF other than that of pure silica are the use of a slightly different material for the fiber cladding by the manufacturer or the residual influence of the core of the unprocessed fiber.

3. Nanofiber-based spectroscopy of organic molecules - theoretical considerations

A comprehensive understanding of nanofiber-based spectroscopy of organic molecules requires not only knowledge about the properties of the nanofiber-guided light mode but also about the molecular system under study. Therefore, in the first part of this chapter, the photophysical properties of organic molecules will be discussed.

The strong radial confinement of the light field over the whole length of a nanofiber is particularly advantageous for highly sensitive spectroscopy of molecules at or near the nanofiber surface. The principles of the interaction between the guided mode of the nanofiber and organic molecules adsorbed on the nanofiber surface will be discussed in the second part of this chapter.

For nanofiber-based single molecule spectroscopy, a dye-doped organic crystal has to be brought into the evanescent field of the optical nanofiber. The interaction of the embedded guest molecules with the guided fiber mode depends critically on the position of the molecules in the evanescent field. This dependence will be analyzed in the third part of this chapter.

3.1. Molecular spectroscopy

The interaction of light with organic molecules is predominantly determined by the internal energy structure of the molecule which depends on the intramolecular interactions as well as on the interactions of the molecule with its environment. Therefore, the form of the measured absorption and emission spectra contains a multitude of information about the molecular structure and about the environment of the molecule.

3.1.1. Energy structure of molecules

In order to describe the energy structure of organic molecules, the complete system of nuclei and electrons interacting via coulomb attraction and repulsion has to be considered. This complex many-body problem is usually solved using the Born-Oppenheimer approximation. It relies on the fact that nuclei are much heavier and therefore move more slowly than electrons. The electrons can thus be assumed to follow the movement of the nuclei instantaneously and the wave function of the molecule can be separated into a nuclear and an electronic component [74]:

$$\Psi = \Psi_{nuc} \cdot \Psi_{el}. \tag{3.1}$$

Consequently, the electronic problem and the nuclear problem can be treated separately. It is the objective of quantum chemistry to find the solution of the electron wave function $\Psi_{el}(\{\vec{r}_i\}, \{\vec{R}_A\})$ for a given set of nuclear coordinates $\{\vec{R}_A\}$ in this approximation, where the $\{\vec{r}_i\}$ are the coordinates of the electrons in the system [75]. Once the electronic problem is solved, it is possible to solve for the motion of the nuclei assuming an average field of the electrons which is obtained from the electronic coordinates averaged over the electronic wave function. This average field, together with the coulomb repulsion between the nuclei, provides a potential for the nuclear motion which describes the vibration, rotation, and translation of

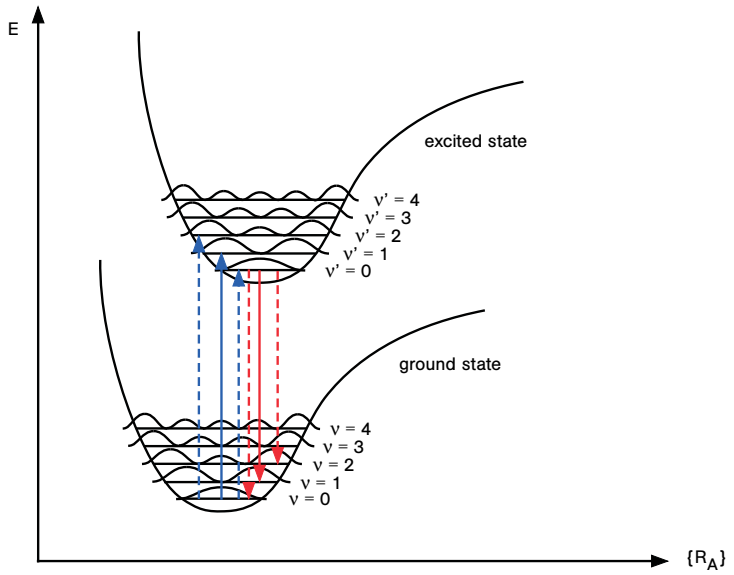

Figure 3.1.: Potential energy hypersurfaces of the electronic ground and excited state as a function of the nuclear coordinates including the vibrational states for one vibrational mode and the corresponding probability density functions. Transitions between the two states are indicated by blue (ground to excited state) and red (excited to ground state) arrows. The solid lines denote the dominating transitions as given by the Franck-Condon factor.

an isolated molecule. Figure 3.1 shows a schematic of the resulting potential energy hypersurfaces of the electronic ground state and an excited electronic state as a function of the nuclear coordinates $\{\vec{R}_A\}$. The possible states of a vibrational mode within these potentials are examplarily identified by the vibrational quantum numbers ν and ν', and the probability density of finding the nuclei at given coordinates is sketched for each vibrational state. Typically, in a molecule which consists of more than two atoms, a multitude of vibrational modes with different vibrational frequencies can be excited, yielding a much more complex level structure than shown in Fig. 3.1.

For the molecules considered in this thesis, which are adsorbed on a dielectric surface or embedded in a host crystal, the relevant quantum-mechanical system does not only consist of the nuclei and electrons and their intramolecular interactions but also of the surrounding matter and the interactions of the molecules with this environment. Within the Born-Oppenheimer approximation, these interactions add to the potential for the nuclear motion yielding additional vibrational states in the energy level structure which, for simplicity, are not shown in Fig. 3.1. Since the surface and lattice modes (phonons) are very numerous and densely spaced with energy quanta in the range of 10 to 100 cm^{-1}, they have continuum character [76].

The transition probability between two different electronic states of a molecule can be determined via Fermi's golden rule [77] and the separability of the molecular wave function [78]:

$$P_{if}(\omega) = \frac{2\pi}{\hbar^2} \left| \left\langle \Psi^f_{nuc} \mid \Psi^i_{nuc} \right\rangle \right|^2 \cdot \left| \left\langle \Psi^f_{el} \mid \vec{E} \cdot \vec{\mu} \mid \Psi^i_{el} \right\rangle \right|^2 \cdot g_{if}(\omega), \tag{3.2}$$

where the indices i and f denote the initial and the final state, respectively, $\vec{E}$ is the electric field vector of the light field, $\vec{\mu}$ is the transition dipole operator, g_{if} is the line shape function of the transition which depends on the angular frequency ω of the light field, and $\hbar$ is the

reduced Planck constant. The line shape function is centered around the transition frequency which is determined by the energy difference ΔE_{if} of the initial and the final state:

$$\omega_{if} = \frac{\Delta E_{if}}{\hbar} = \frac{1}{\hbar}(\Delta E_{el} + \Delta E_{vib}), \tag{3.3}$$

where ΔE_{el} is the energy difference of the electronic states and ΔE_{vib} the energy difference between the excited vibrational quanta for the two states.

Equation (3.2) is only valid if the transition occurs at precisely defined positions of the nuclei which do not change during the transition. This assumption is even more restrictive than the Born-Oppenheimer approximation and is expressed by the Franck-Condon principle. It is based on the fact that the electronic transitions are essentially instantaneous compared with the time scale of the nuclear oscillations [74], which is illustrated by the vertical transitions in the potential energy diagram of Fig. 3.1. If the rotational motion of the molecule can be neglected as it is the case in liquids, solids and on surfaces, the overlap between the inital and the final nuclear wavefunction can be reduced to the vibrational overlap, the square modulus of which is referred to as Franck-Condon factor. Some of the possible transitions from the vibrational ground state of the electronic ground and of the excited state are shown in Fig. 3.1 by blue and red arrows, respectively. For the situation depicted here, the vibrational overlap for an initial state with vibrational quantum number (ν or ν') equal to zero is largest if the vibrational quantum number of the final state equals one. The resulting dominating transitions are indicated by solid arrows as opposed to dashed arrows for the weaker transitions.

The electronic contribution to the transition probability is determined by the transition dipole moment

$$\vec{\mu}_{if} = e \left\langle \Psi^f_{el} \mid \vec{r} \mid \Psi^i_{el} \right\rangle \tag{3.4}$$

which is the expectation value of the transition dipole operator $\vec{\mu} = e\vec{r}$, where e is the elementary charge and $\vec{r}$ is the sum of the coordinates of all electrons. The transition probability further depends on the orientation of the electric field relative to the transition dipole moment of the molecule which enters via the scalar product $\vec{E} \cdot \vec{\mu}_{if}$.

3.1.2. Light absorption and emission

The dynamic processes of light absorption and emission by a molecule can be visualized by a Jablonski diagram. It shows the energy levels of a molecule together with the possible excitation and relaxation mechanisms. Figure 3.2 depicts a simplified Jablonski diagram for the first three electronic states of a typical organic molecule. Usually, the ground state is a singlet state with paired electrons. It is therefore denoted by S_0 and has diamagnetic properties. The next higher electronic state is a triplet state (T_1) with unpaired electrons and paramagnetic properties. Due to conservation of total spin, the transition from S_0 to T_1 is forbidden. Absorption of light thus leads to excitation to the first excited singlet state S_1. This three level structure determines most of the properties of the molecule, and the higher energy singlet and triplet states are therefore not shown in the figure. The possible excitation and relaxation mechanisms will be discussed in detail in the following.

Absorption

The absorption strength of a transition between two states i and f can be characterized by the absorption cross section $\sigma_{if}(\omega)$ which is given by the rate of absorption of energy per

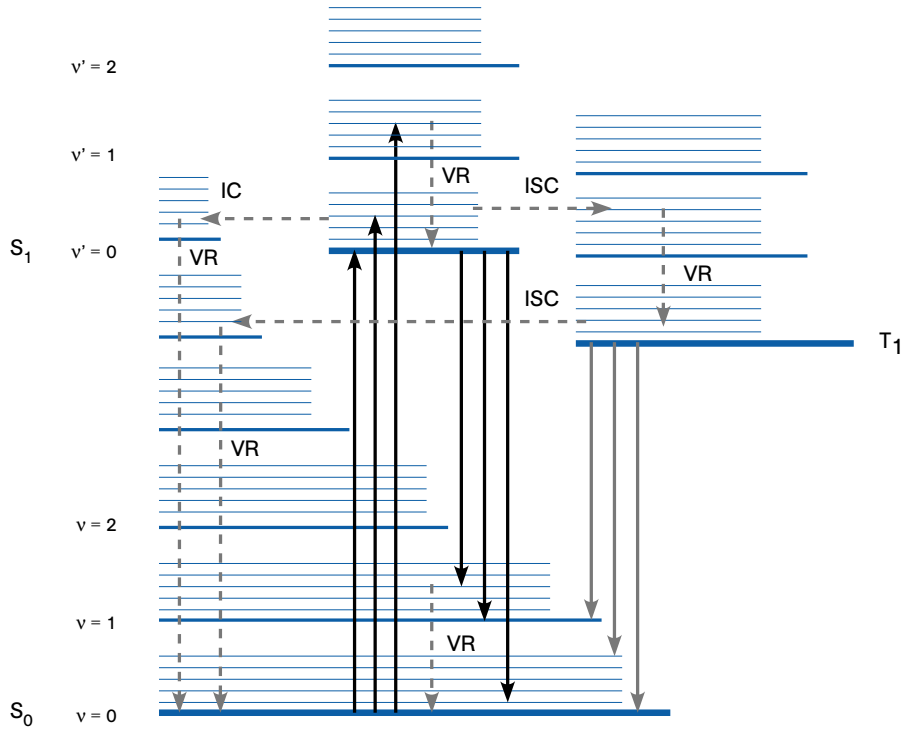

Figure 3.2.: Simplified Jablonski diagram of a typical organic molecule. Absorption is indicated by upward pointing arrows, fluorescence (black) and phosphorescence (gray) by downward pointing arrows. Non-radiative processes including vibrational energy relaxation (VR), internal conversion (IC), and intersystem crossing (ISC) are displayed with dashed arrows. For simplicity, only one intramolecular vibrational mode is shown, while the phonon states of the environment are depicted as a quasi-continuum.

molecule, $P_{if}(\omega) \cdot \hbar\omega$, divided by the intensity of the electric field $\vec{E}_{||} = \vec{E} \cdot \vec{\mu}_{if} / |\vec{\mu}_{if}|$ parallel to the transition dipole moment. The intensity can be expressed by

$$I = \frac{1}{2}\frac{c}{n}\varepsilon \left|\vec{E}_{||}\right|^2, \tag{3.5}$$

where ε and n denote the permittivity and the refractive index of the surrounding medium, respectively, and c is the vacuum speed of light. According to Eq. (3.2), the absorption cross section is therefore related to the transition dipole moment $\vec{\mu}$ via [79]

$$\sigma_{if}(\omega) = \frac{4\pi n\omega}{\hbar c\varepsilon} F_{if} \left|\vec{\mu}_{if}\right|^2 \cdot g_{if}(\omega) \tag{3.6}$$

with the Franck-Condon factor F_{if}. For each excitation frequency ω, the total absorption cross section $\sigma(\omega)$ of a molecule is given by the sum of the cross sections at the frequency ω for all possible transitions. On the other hand, the total strength of each transition between two states i and f can be obtained by integrating $\sigma_{if}(\omega)$ over all frequencies. It is often quantified by the dimensionless oscillator strength [74]

$$f_{if} = \frac{2m_0 c\varepsilon_0}{10\pi e^2 n} \cdot \int \sigma_{if}(\omega)\mathrm{d}\omega, \tag{3.7}$$

where m_0 and e denote the mass and charge of the electron, respectively.

At low temperatures, the majority of the molecules is in the vibrational ground state of the electronic ground state with a negligible population of higher phonon states. The upward pointing arrows in Fig. 3.2 which all originate from the vibrational and phononic ground state of S_0 therefore indicate absorption at low temperatures. Note that in thermal equilibrium at room temperature, however, the thermal energy is sufficient to result in a significant population of higher phonon states while the population of higher intramolecular vibrational states ($\nu \geq 1$) is still negligible.

Experimentally, absorption of light with a wavelength $\lambda = 2\pi c/\omega$ which travels through a medium along the z-axis can be described by the Lambert-Beer law, if saturation is low [80]:

$$I(z, \lambda) = I_0(\lambda) \cdot \exp(-\alpha(\lambda) \cdot z), \tag{3.8}$$

where $I(z, \lambda)$ is the light intensity at position z which decays exponentially with an absorption coefficient $\alpha(\lambda)$, and $I_0(\lambda)$ is the reference intensity at $z = 0$. The absorption coefficient is determined by the properties of the absorbing medium and can be expressed by the product of the molecular absorption cross section $\sigma(\lambda)$ and the number density $\tilde{n}$ of absorbing molecules in the medium: $\alpha(\lambda) = \sigma(\lambda)\tilde{n}$.

For a sample of a fixed length l along the propagation direction of the incident light, the absorption is typically quantified by the absorbance which is defined as the negative decadic logarithm of the intensity of the signal after travelling through the sample, $I(l, \lambda)$, relative to the reference intensity $I_0(\lambda)$:

$$\eta(\lambda) = -\log\left(\frac{I(l, \lambda)}{I_0(\lambda)}\right) = l\varepsilon(\lambda)\tilde{c}. \tag{3.9}$$

Here, the molecule-specific molar decadic absorption coefficient $\varepsilon(\lambda)$ has been introduced which describes the absorbance per molar concentration $\tilde{c}$ of absorbers in the medium. It is related to the absorption coefficient via $\alpha(\lambda) = ln(10) \cdot \varepsilon(\lambda) \cdot \tilde{c}$. The molecular absorption cross section can therefore be obtained from the the molar decadic absorption coefficient by the following relation:

$$\sigma(\lambda) = \frac{\ln 10}{N_\mathrm{A}}\varepsilon(\lambda), \tag{3.10}$$

with Avogadro's number $N_\mathrm{A} = \tilde{n}/\tilde{c} = 6.022 \cdot 10^{23}\,\mathrm{mol}^{-1}$. As a result, the absorbance can be expressed in terms of $\sigma(\lambda)$:

$$\eta(\lambda) = \frac{\sigma(\lambda)N}{\ln 10 \cdot A}, \tag{3.11}$$

with the numer N of molecules and the area A probed by the light beam.

Non-radiative processes

There are three major types of non-radiative transitions: vibrational energy relaxation (VR), internal conversion (IC), and intersystem crossing (ISC).

If a molecule is excited to a higher vibrational state, it is no longer in thermal equilibrium. By interaction with the environment, the vibrational energy of the molecule can be transferred into motional energy of the surrounding matter within picoseconds. Since the spacing of the vibrational levels in a molecule is on the same order of magnitude as the thermal energy at room temperature, this vibrational energy relaxation to thermal equilibrium leads to a

negligibly small population of higher vibrational states. This process is indicated by the vertical dashed arrows in Fig. 3.2.

Internal conversion describes a transition from a lower vibrational state of a higher excited electronic state to a higher vibrational level of a lower electronic state (horizontal dashed arrow in Fig. 3.2). Since higher excited electronic states are more densely spaced than, e. g., the ground and the first excited state, their potential energy surfaces can cross which may result in a large overlap of the vibrational wavefunctions of these excited states. Therefore, internal conversion between higher excited electronic states is highly probable. The energy gap between the ground state and the first excited state, however, is usually too large for efficient internal conversion. Hence, internal conversion in combination with vibrational relaxation leads to an almost instantaneous relaxation of the excited molecule to the vibrational ground state of S_1 which typically decays radiatively to the ground state.

Internal conversion can also occur between singlet and triplet states if the interaction of the electron's spin with its orbital angular momentum, the spin-orbit coupling, is strong enough to induce the spin-flip involved in this transition. This process is called intersystem crossing and leads to emission of photons from the vibrational ground state of T_1 or to a completely radiationless transition from T_1 to the electronic ground state.

The result of these non-radiative processes is formulated by Kasha's rule [81]. It states that light emission by a molecule originates preferably from the vibrational ground state of the first excited singlet or triplet state, independent of the excitation wavelength. This can explain the approximate mirror symmetry between absorption and emission spectra often observed for rigid molecules.

Emission

If the molecule has relaxed to the vibrational ground state of S_1 and does not undergo intersystem crossing to the triplet state, it can decay to the electronic ground state via emission of a photon. This process is called fluorescence and occurs on timescales of a few nanoseconds corresponding to the lifetime of the excited electronic state. The fluorescence photon can have a maximum energy of ΔE_{el} if the molecule decays to the vibrational ground state of S_0. For all other transitions from $\nu' = 0$ to $\nu > 0$, the energy of the emitted photon is lowered by the vibrational energy of the molecule in the ground state: $\Delta E = \Delta E_{el} - \nu \Delta E_{vib}$, as indicated by the downward pointing arrows of different lengths in Fig. 3.2. An important quantity to describe the fluorescence of a molecule is the fluorescence quantum yield η_f. It describes the percentage of absorbed photons which cause a fluorescence photon to be emitted and can be determined via the the rates for the possible decay channels:

$$\eta_f = \frac{k_f}{k_f + k_{nr}}, \tag{3.12}$$

where k_f denotes the fluorescence rate and k_{nr} is the total rate for non-radiative processes.

If, however, the molecule has been transferred to the triplet state by intersystem crossing, there is a small probability of radiative decay to the electronic ground state via spin-orbit coupling. This process is called phosphorescence and is the radiative manifestation of intersystem crossing (gray arrows in Fig. 3.2). Typical timescales of phosphorescence are as long as minutes or hours due to the metastability of T_1. Since the energy of the first excited triplet state is lower than the energy of S_1, the phosphorescence photons have a lower maximum energy than the fluorescence photons.

Population kinetics and saturation

Throughout this thesis, coherences of the molecular states and polarizations of the light field play a minor role. Therefore, the coherences in the density matrix approach can be neglected and it is sufficient to describe the system by the rate equations for the population kinetics of the three level system shown in Fig. 3.2. The time evolution of the population of the three levels can be expressed by the following equations:

$$\begin{aligned} \frac{dN_1}{dt} &= -\frac{\lambda}{hc} \cdot \sigma(\lambda) I_{exc}(\lambda)(N_1 - N_2) + k_{21} N_2 + k_{31} N_3 \\ \frac{dN_2}{dt} &= \frac{\lambda}{hc} \cdot \sigma(\lambda) I_{exc}(\lambda)(N_1 - N_2) - k_{21} N_2 - k_{23} N_2 \\ \frac{dN_3}{dt} &= k_{23} N_2 - k_{31} N_3 \\ 1 &= N_1 + N_2 + N_3, \end{aligned} \tag{3.13}$$

where N_1 and N_2 are the populations of the singlet states S_0 and S_1, respectively, and N_3 is the population of the triplet state T_1. $I_{exc}(\lambda)$ denotes the excitation intensity at a given wavelength λ and the rates k_{21}, k_{31}, and k_{23} describe the transition rates from S_1 to S_0, from T_1 to S_0, and from S_1 to T_1, respectively. From these rate equations, the steady state solution ($dN_i/dt = 0$; $i = 1, 2, 3$) for the population of the excited singlet state and for the population difference between the ground state and the excited singlet state can be derived as

$$\begin{aligned} N_2 &= \frac{\sigma(\lambda) I_{exc}(\lambda) \cdot \lambda / hc}{k_{21} + k_{23} + \sigma(\lambda) I_{exc}(\lambda)(k_{23}/k_{31} + 2) \cdot \lambda / hc} \\ \Delta N = N_1 - N_2 &= \frac{k_{21} + k_{23}}{k_{21} + k_{23} + \sigma(\lambda) I_{exc}(\lambda)(k_{23}/k_{31} + 2) \cdot \lambda / hc}. \end{aligned} \tag{3.14}$$

The intensity absorbed by a molecule is proportional to the product of population difference and excitation intensity $\Delta N \cdot I_{exc}$ and the intensity emitted by a molecule is proportional to the population of the excited state N_2. Therefore, the intensity I_{sig} of both, the absorption and the emission signal, shows the following saturation behaviour with increasing excitation intensity I_{exc}:

$$I_{sig} = I_\infty \frac{I_{exc}}{I_s + I_{exc}}, \tag{3.15}$$

with the saturation intensity

$$I_s = \frac{k_{21} + k_{23}}{\sigma(k_{23}/k_{31} + 2)} \cdot \frac{hc}{\lambda} \tag{3.16}$$

and the saturation value I_∞ for high excitation intensities.

3.1.3. Line shape of molecular transitions

The line shape function g introduced in Eq. (3.2) accounts for the fact that a molecular transition is never strictly monochromatic. Instead, the relative strength of the transition around the mean frequency ω_{if} obeys a distribution $g(\omega)$ determined by several broadening mechanisms.

Homogeneous linewidth

The homogeneous linewidth of the transition contains all broadening mechanisms which apply equally to every molecule in an ensemble.

The most important broadening effect which is inherent in all molecular transitions is a result of the limited lifetime of at least one of the molecular states involved. An excited molecule can be described by a classical model where the electrons oscillate at the resonance frequency ω_{if} of the considered transition [82]. This oscillation is assumed to be damped with a damping constant γ causing the amplitude of the oscillation to decay exponentially with a decay rate of $\gamma/2$ [78]. Due to the decay of the oscillation amplitude, the molecular transition is not strictly monochromatic but shows a frequency spectrum which can be obtained from the Fourier transformation of the time dependent oscillation amplitude. The real squared absolute value of this Fourier spectrum which constitutes the line shape function of the transition is a Lorentzian distribution [83]:

$$g(\omega) = \frac{1}{2\pi} \frac{\gamma}{(\omega - \omega_{if})^2 + (\gamma/2)^2}. \tag{3.17}$$

The homogeneous linewidth of the transition due to the limited lifetime is defined as the full width at half maximum (FWHM) γ of this Lorentzian profile. For a transition between two states with lifetimes τ_i and τ_f of the initial and final state, respectively, the homogeneous linewidth is composed of these two contributions via

$$\gamma = \left(\frac{1}{\tau_i} + \frac{1}{\tau_f} \right). \tag{3.18}$$

If one of the two states is the ground state with infinite lifetime, the linewidth is determined by the lifetime τ of the excited state:

$$\gamma = \frac{1}{\tau}. \tag{3.19}$$

For an isolated molecule, this lifetime is only determined by the radiative and non-radiative decay channels of the molecule itself. It is therefore called natural linewidth and provides a fundamental lower limit for the spectral linewidth of any molecular transition.

Further homogeneous broadening can be induced by interactions with the environment. For the molecules considered in this thesis, which are deposited onto a dielectric surface or embedded into an organic crystal, this interaction is predominantly mediated by phonons.

The coupling of the electrons to phonons may provide additional decay channels yielding a reduction of the excited state lifetime. However, the relaxation to the electronic ground state would require an n-phonon process which is strongly suppressed due to the large energy difference between the electronic states. Thus, this effect only affects the vibrational states as discussed in Sec. 3.1.2.

Moreover, elastic scattering of phonons can lead to perturbations of the phase of the dipole oscillation. This results in phonon-assisted broadening effects which add a dephasing contribution γ_d to the homogeneous linewidth:

$$\Delta\omega_{\mathrm{hom}}(T) = \gamma + \gamma_d(T), \tag{3.20}$$

where $\gamma = 1/\tau$ is the lifetime-limited linewidth due to the lifetime τ of the excited state. The influence of the dephasing effect follows the Arrhenius equation [84, 85]:

$$\gamma_d(T) = \gamma_p \cdot \exp(-\frac{E_a}{k_B T}), \tag{3.21}$$

with an activation energy E_a and the Boltzmann constant k_B. The preexponential factor γ_p relates to the lifetime and energy of the involved phononic modes [86]. The influence of the dephasing effect is strongly temperature-dependent and vanishes for low temperatures where the population of phonon states is negligibly small.

Homogeneous line broadening can also be caused by saturation of the transition. Since the transition strength depends on the detuning from the resonance frequency ω_{if} of the transition, saturation is also frequency-dependent with the strongest effect on the absorption of light on resonance. This leads to a "compression" of the line shape function. The resulting saturation or power broadened line has a Lorentzian shape with an intensity dependent width [83]:

$$\gamma_{sat} = \gamma_0 \sqrt{1 + \frac{I_{exc}}{I_s(\omega_{if})}}, \tag{3.22}$$

determined by the saturation intensity $I_s(\omega_{if})$ on resonance.

Zero-phonon line and phonon sideband

The line shape of molecular transitions is significantly influenced by the phonon states discussed in Sec. 3.1.1 which are caused by interactions of the molecular electrons with the surface or lattice modes of the environment surrounding the molecules. Since these states have continuum character, they offer a multitude of possible transitions in addition to the transitions between purely electronic and vibrational states of the molecules themselves. The mean occupation number $\langle n(E) \rangle$ of a state with phononic energy E is given by Bose-Einstein statistics [76]:

$$\langle n(E) \rangle = \frac{1}{\exp(E/k_B T) - 1} \tag{3.23}$$

and depends strongly on the temperature T of the system.

At high temperatures, quantum effects are negligible and the expected occupation number of a phononic state can be described by Maxwell–Boltzmann statistics [87]. The probability density for a molecule in thermal equilibrium to be in a state with phononic energy E is therefore given by:

$$\langle n(E) \rangle = \frac{\exp(-E/k_B T)}{k_B T}, \tag{3.24}$$

yielding a mean phononic energy of $k_B T$ with a standard deviation of also $k_B T$. At room temperature, the thermal energy of $k_B T \approx 25\,\mathrm{meV}$ is sufficient to excite a large number of phonons. Hence, a multitude of resonance energies for the molecular transition from the electronic ground state to the first excited state (and vice versa) is possible, resulting in a broad absorption (emission) band without sharp lines. The spectra consist mostly of the so called phonon sideband which has a width of a few hundred cm^{-1} at room temperature.

At low temperatures, however, the population of phonon states is significantly reduced, and purely electronic transitions without participation of phonons are much more probable. Such transitions are called zero phonon transitions and are characterized by a very well defined transition frequency which is the same for absorption and emission. The corresponding spectral feature is called zero phonon line (ZPL) and has a Lorentzian shape. At low temperatures close to 0 K, the linewidth of the ZPL is given by the natural linewidth of the transition which lies between 1 and 100 MHz for a typical organic molecule [88].

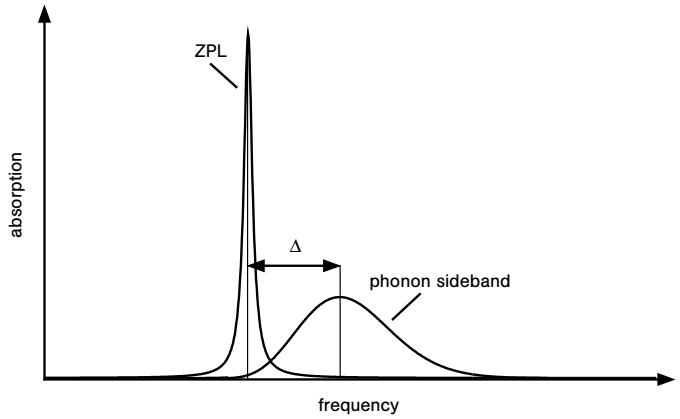

Figure 3.3.: Schematic of a typical absorption band for an electronic transition of a molecule in solid state at low temperature consisting of zero phonon line (ZPL) and phonon sideband.

Even at low temperatures, the ZPL is accompanied by a phonon sideband which results from transitions involving the creation of phonons. The extinction of phonons is strongly suppressed due to the negligible population of phonon states of the initial electronic state in thermal equilibrium. As a result, the phonon wing appears on the low energy side of the ZPL in fluorescence spectra and on the high energy side of the ZPL in absorbance spectra. The line shape of the phonon sideband is determined by the superposition of all phonon modes which corresponds to a Poissonian distribution. The exact structure and width of the phonon sideband depends on the density of phonon states. Since it is composed of many short-lived states, it is much broader than the ZPL with a width of about $100\,\mathrm{cm}^{-1}$. The shift Δ of the maximum of the phonon sideband with respect to the center of the ZPL is typically 30 to $50\,\mathrm{cm}^{-1}$ [88]. It results in the so-called Stokes shift given by 2Δ between the maxima of absorption and fluorescence spectra usually observed in the cases where the intensity of the zero phonon line is small compared to the phonon sideband.

Figure 3.3 shows a typical absorption band for an electronic transition including the phonon sideband. The line shape $g(\omega)$ of such a band can be expressed by

$$g(\omega) = \alpha_D \cdot z(\omega) + (1 - \alpha_D) \cdot p(\omega \pm \Delta), \tag{3.25}$$

where $z(\omega)$ and $p(\omega \pm \Delta)$ denote the contribution of the zero phonon line and the phonon wing, respectively. The Debye-Waller factor α_D gives the relative intensity of the zero phonon line and can be calculated via

$$\alpha_D = \frac{I_{ZPL}}{I_{ZPL} + I_{PSB}}, \tag{3.26}$$

where I_{ZPL} and I_{PSB} are the total intensity of the zero phonon line and the phonon sideband, respectively. A large Debye-Waller factor implies weak electron-phonon coupling as depicted in Fig. 3.3. In this case, the probability to excite phonon states via an electronic transition is low, and the zero phonon line is the dominating feature in the spectrum. If the electron-phonon coupling is strong, the excitation of phonon states is more efficient, resulting in a dominating phonon sideband and, thus, a small Debye-Waller factor. For organic molecules embedded in an organic crystal, the coupling of the electronic states to the crystal lattice depends predominantly on the quality of the crystal structure and on the crystal temperature.

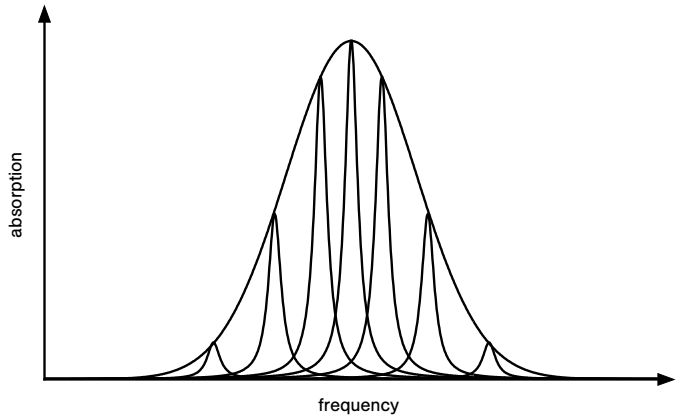

Figure 3.4.: Schematic of an inhomogeneously broadened absorption band caused by the locally varying environment of a molecular ensemble.

Inhomogeneous broadening

In any environment, a molecule can be subject to electrostatic and dipole-dipole or dispersion interactions [89]. These interactions result in a shift of the transition frequency with respect to the transition frequency of a free molecule which is commonly known as solvent shift [90]. This shift can be caused by the interaction with solvent molecules in a solution [89], by the guest-host interactions for crystal-embedded molecules [91], by the surface forces exerted on surface-adsorbed molecules [92], or by other influences of the environment. The size of the solvent shift depends on the properties of the molecules under study as well as on the properties of the local environment of each molecule. Molecules with a permanent dipole moment can cause an electric field, a so-called reaction field, in their environment which acts on the molecules in the same way as an external electric field [89]. For molecules which do not have a permanent dipole moment, the shift is solely determined by the dipole-dipole interactions between the molecules and the environment which always cause a red shift [50,89].

Since the microscopic environment for an ensemble of otherwise identical molecules can vary from molecule to molecule, the transition frequencies obey a statistical distribution which is determined by the nature of the ensemble environment. The absorption spectrum of such an ensemble is schematically shown in Fig. 3.4. It is a superposition of several Lorentzian lines with approximately the same width but different center positions. In contrast to the homogeneous broadening effects discussed before, this effect is different for each molecule, and the resulting broadening is therefore called inhomogeneous broadening.

The exact shape and width of the inhomogeneously broadened spectrum depends critically on the type of environment the molecules are embedded in. In solutions, amorphous materials or on surfaces, the molecules can be oriented arbitrarily with respect to their environment. As a result, the molecular transition frequencies are usually statistically distributed over a large spectral range yielding a Gaussian line shape with a width of a few hundred cm^{-1}. In crystalline host matrices, however, only a limited number of orientations of the guest molecules relative to the crystal structure can be realized. Therefore, the molecular transition frequencies are usually distributed around a few center frequencies with inhomogeneous linewidths of a few GHz. This residual broadening is typically caused by crystal defects like stress, vacancies, and dislocations which can be caused by the guest molecules themselves or by external

perturbations of the crystal structure. The shape of the inhomogeneously broadened lines depends on the defect concentration. Low defect concentrations yield a Lorentzian line shape while higher defect concentrations result in a satellite structure with the resonances of the individual molecules centered around more than one frequency. A Gaussian line shape is only expected for very high crystal defect concentrations [88].

The inhomogeneous broadening does not depend on temperature and dominates the width of the absorption band at low temperatures, while at higher temperatures, the inhomogeneous broadening is usually concealed by the large homogeneous linewidths.

3.1.4. Single molecule spectroscopy

In standard absorption and fluorescence experiments, a whole ensemble of molecules is probed. Although these measurements can render manifold information about the ensemble and its interaction with the environment as well as about the interaction between the molecules within the ensemble, the information about the individual molecules is usually concealed by the inhomogeneous broadening of the spectra. To overcome this effect, several experimental techniques for single molecule spectroscopy (SMS) have been developed. Using these techniques, molecules can be studied as single quantum systems or used as a nanoprobe for a local environment or for the dynamic processes inside a sample like an organic crystal or a cell. Since the methods and experimental techniques for nanofiber-based spectroscopy of organic molecules presented in this thesis can also be applied to single molecules, the requirements and experimental techniques for SMS are briefly discussed in this section.

Due to the spectrally stable behaviour and the narrow spectral lines shown by organic dye molecules embedded in a crystalline matrix [93], they have become the preferred sample system for single molecule spectroscopy. The first absorption spectrum of a single dopant molecule in an organic host crystal has been observed by Moerner and Kador in 1989 using two different double-modulation techniques [94]. In 1990, however, Orrit and Bernard established fluorescence excitation spectroscopy as the preferred technique for SMS owing to the much higher signal to noise ratio (SNR) [95]. In fluorescence excitation spectroscopy, the molecule is excited by a laser beam and its total fluorescence intensity is measured as a function of the excitation wavelength. To separate the fluorescence light from the excitation light, usually, a longpass filter is used. As a result, only the red-shifted part of the emission is detected. If the fluorescence quantum yield and the fluorescence detection efficiency are independent of the excitation wavelength, the resulting fluorescence excitation spectrum corresponds to the absorption spectrum of the sample [83].

In order to select the spectral signature of a single molecule from the inhomogeneously broadened absorption spectrum of a doped-crystal sample, two different approaches can be used, either seperately or in combination. They are commonly referred to as spatial and spectral selection.

Spatial selection

Figure 3.5 shows a schematic of a laser beam probing a dye-doped crystal sample. Usually, the laser beam excites several molecules simultaneously. In order to reduce the number of molecules interacting with the excitation light, the concentration of dye molecules in the sample and/or the interaction volume can be reduced by using very thin samples and/or by focussing the excitation laser beam to a very small volume inside the sample, respectively. The

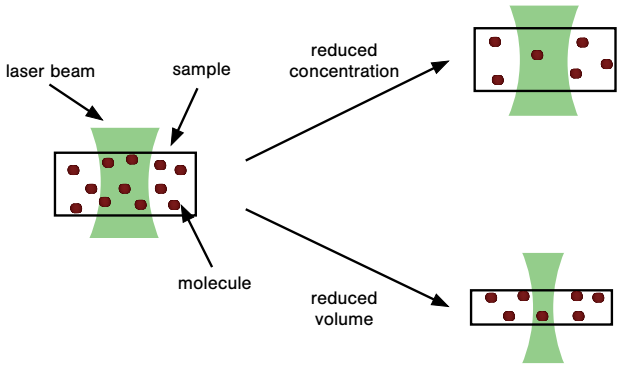

Figure 3.5.: Spatial selection of single molecules: the number of molecules interacting with the excitation light can be reduced by reducing the dopant concentration in the sample and/or by reducing the interaction volume.

reduction of the interaction volume yields the additional advantage that not only the number of dopant molecules but also the number of host molecules interacting with the excitation light field and, thus, the amount of spurious fluorescence decreases which results in an increased signal to noise ratio.

Single molecule spectroscopy is therefore usually performed with doping concentrations on the order of 10^{-9} mol/mol [85, 96] and sample thicknesses down to 80 nm [97]. The smallest interaction volumes can be achieved with optical near field techniques [98]. However, single molecule spectroscopy has also been performed using far field techniques like confocal microscopy [99] and wide field microscopy [100, 101].

Spectral selection

At low temperatures, the dephasing contribution to the homogeneous linewidth goes to zero for molecules in a crystalline matrix and the linewidth is purely determined by the excited state lifetime. As a consequence, the homogeneous linewidth for one molecule is much narrower than the distribution of absorption frequencies in the sample. Hence, the absorption band, which is composed of the absorption lines of a limited number of molecules, cannot be a smooth function but exhibits a "spectral noise" on the overall Gaussian background [102]. Due to the statistically random distribution of the absorption lines, this feature is called statistical fine structure [103]. The root mean square fluctuation of this fine structure scales with the square root $\sqrt{\bar{N}}$ of the mean number $\bar{N}$ of molecules with an absorption frequency within one homogeneous width around the excitation wavelength. Figure 3.6 shows the results of numerical simulations of inhomogeneously broadened absorption bands for different total numbers of absorbing molecules [104]. The relative fluctuations of the absorption signal scales with $1/\sqrt{\bar{N}}$ and thus increases with decreasing total molecule numbers. For the situation shown in the figure, the absorption lines of the single molecules can be distinguished for a total number of 10 molecules. However, even for higher molecule numbers, the absorption lines of individual molecules are apparent in the wings of the inhomogeneously broadenend absorption profile.

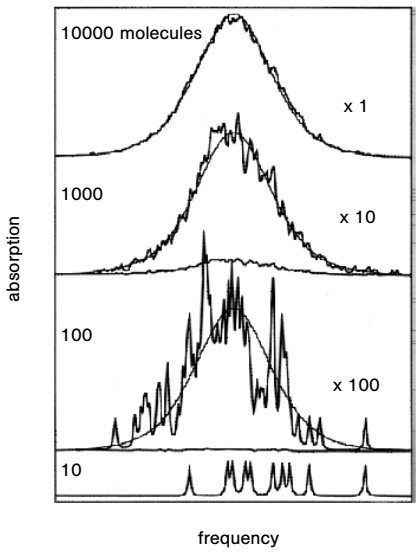

Figure 3.6.: Numerical simulation of inhomogeneously broadened absorption spectra for different total numbers of absorbing molecules. The resonance frequencies of the constituent molecules were picked at random from a nearly Gaussian probability distribution (thin smooth curves). The upper three spectra have been normalized for constant absorption with the factors indicated on the right side of the figure. Adapted from [104].

Requirements for SMS

The need to select a single molecule as well as the small signal provided by a single molecule renders SMS experimentally challenging. This challenge can be met by a careful choice of the sample system and a thorough design of the experimental setup. For organic dye molecules embedded in a crystalline matrix probed by fluorescence excitation spectroscopy, the following requirements have to be considered:

- A high absorption cross section of the dye molecule ensures high excitation efficiencies. In combination with a high fluorescence quantum yield, this provides a fluorescence intensity which is on the same order of magnitude as the excitation intensity. A high saturation intensity of the dye molecule raises the maximum applicable excitation intensity and thus further increases the achievable fluorescence signal.

- Crystalline host matrices which agree well with the dopant structure usually yield the highest photostability of the embedded dye molecules. A high crystal quality is crucial for the stability of the dopant and for a low electron-phonon coupling between dopant and matix, i. e., a strong zero phonon line. It can be improved by careful crystal growth and low dopant concentrations.

- Small crystals with low dopant concentrations facilitate the spectral and spatial selection of single molecules. However, very small crystals are dominated by surface effects which affect the crystal quality.

- Cooling down the sample to cryogenic temperatures ensures small homogeneous linewidths and thus yields high absorption cross sections. This facilitates spectral selection and increases the achievable fluorescence signal.
- A narrow-band excitation source is a crucial requirement for fluorescence excitation spectroscopy and yields a high resolution for spectral selection and spectroscopy.
- A small excitation volume facilitates spatial selection and increases the signal to noise ratio. Moreover, the light power needed to achieve the desired excitation intensity is reduced, resulting in a lower heating of the sample.
- A high collection efficiency for the fluorescence light, low losses in the optical path from the molecule to the detector, a highly sensitive detector with a low dark count rate, and effective shielding of the detector from excitation and background light increase the signal to noise ratio.

Fluorescence autocorrelation

Single molecules can be identified experimentally by autocorrelation measurements. These measurements reveal information about the fluctuations of the fluorescence intensity via its correlation function $g^{(2)}(\tau)$, which is defined by [105]:

$$g^{(2)}(\tau) = \frac{\langle I(t)I(t+\tau)\rangle}{\langle I(t)\rangle^2}, \tag{3.27}$$

where $I(t)$ is the fluorescence intensity and $\langle\rangle$ denotes the average over a much longer time than all characteristic time scales in the system. Note that the correlation function of the intensity is the second order correlation function of the electric field which is expressed by the superscript $^{(2)}$.

A completely uncorrelated light emission results in a $g^{(2)}$-value of 1 while correlated light emission yields values larger than 1 and anticorrelated emission renders values smaller than 1. A single emitter can only emit one photon at a time and has to be excited again before it can emit a second photon. Therefore, the light emission is highly anticorrelated for $\tau = 0$ yielding $g^{(2)}(0) = 0$ [106]. This effect is commonly called antibunching and is a highly non-classical property of the light emitted by an isolated quantum system [105].

Antibunching has first been observed by H. J. Kimble and co-workers in 1977 in experiments with sodium atoms [107]. The observation of antibunching in the emission of single molecules has been achieved with pentacene molecules embedded in a para-terphenyl crystal in 1992 [108], followed by terrylene molecules embedded in para-terphenyl in 2000 [109].

The long lifetimes of the triplet state of organic molecules lead to bright and dark periods in their fluorescence emission. As a result, the photons form bunches on these timescales, and the autocorrelation function shows an exponential decay with a timescale given by the lifetime of the triplet state and the ISC-rates [110]. Hence, autocorrelation measurements can provide important information about the photophysical properties of a molecular sample system.

3.2. Nanofiber-based surface spectroscopy

Due to their unique properties, optical nanofibers are a highly efficient tool for molecular surface spectroscopy. The pronounced intensity of the evanescent field at the surface yields a

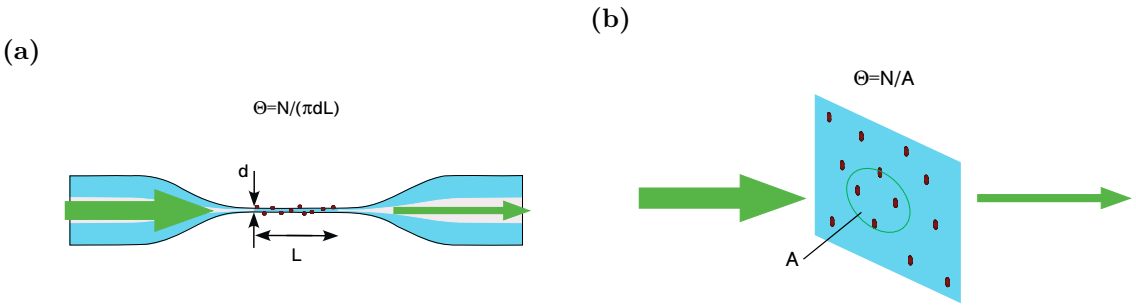

Figure 3.7.: Probed surfaces in nanofiber-based (a) and free-beam (b) surface absorption spectroscopy. For the nanofiber-based technique, the whole nanofiber surface is probed, whereas in free-beam techniques, the probed surface is determined by the size of the light beam.

strong interaction of surface-adsorbed molecules with the nanofiber-guided mode. Moreover, the special geometry of this system makes it possible to probe comparatively large surfaces with very high intensities. Therefore, this method yields the possibility to study the interaction of the molecules with a dielectric surface and their dynamics on the surface with a very high sensitivity.

3.2.1. Absorption of light from the fiber mode

For a thin film of surface-adsorbed molecules covering a nanofiber, the absorbance at a wavelength λ defined by Eq. 3.9 can be measured by comparison of the transmitted powers $P_{\mathrm{sig}}(\lambda)$ and $P_{\mathrm{ref}}(\lambda)$ in the presence and absence of molecules, respectively:

$$\eta(\lambda) = -\log\left(\frac{P_{\mathrm{sig}}(\lambda)}{P_{\mathrm{ref}}(\lambda)}\right). \tag{3.28}$$

The power $P_{\mathrm{abs}}(\lambda, z)$ absorbed by a molecule at a position z along the nanofiber is given by the product of the molecular absorption cross section $\sigma(\lambda)$ and the surface intensity $I_{\mathrm{surf}}(\lambda, z)$ of the electric field components of the guided light which are parallel to the molecular transition dipole moment at this position. Introducing the effective area of the guided mode A_{eff} which is defined by [27]

$$A_{\mathrm{eff}}(\lambda) = P_{\mathrm{exc}}(\lambda, z)/I_{\mathrm{surf}}(\lambda, z), \tag{3.29}$$

the absorbed power can be expressed by

$$P_{\mathrm{abs}}(\lambda, z) = \frac{\sigma(\lambda)}{A_{\mathrm{eff}}(\lambda)} P_{\mathrm{exc}}(\lambda, z), \tag{3.30}$$

where $P_{\mathrm{exc}}(\lambda, z)$ is the guided power of the excitation light at a wavelength λ and a position z along the nanofiber. In the limit of weak absorption, the guided power of the excitation light is roughly equal to $P_{\mathrm{ref}}(\lambda)$ at all positions along the nanofiber, and each molecule absorbes approximately the same power. The absorbance of the thin film can therefore be approximated as [27]

$$\eta(\lambda) \approx \frac{P_{\mathrm{abs}}^{\mathrm{tot}}(\lambda)}{\ln 10 \cdot P_{\mathrm{ref}}(\lambda)} \approx \frac{N\sigma(\lambda)}{\ln 10 \cdot A_{\mathrm{eff}}(\lambda)}, \tag{3.31}$$

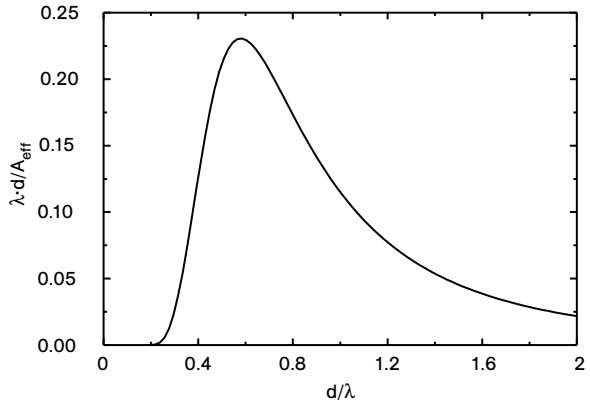

Figure 3.8.: Plot of he quantity d/A_{eff} in units of $1/\lambda$ as a function of the fiber diameter d in units of the wavelength λ of the guided light. A_{eff} is calculated taking into account the azimuthal and axial components of the electric field of the fundamental HE_{11} mode. Assuming a refractive index of 1.46 and ignoring material dispersion, the plot holds universally for any wavelength λ.

where the total absorbed power $P_{\text{abs}}^{\text{tot}}(\lambda) = P_{\text{ref}}(\lambda) - P_{\text{sig}}(\lambda)$ is given by the sum of the power absorbed by each of the N molecules covering the nanofiber surface.

For a nanofiber with diameter d and length L uniformly covered with N molecules, the whole cylindrical surface of the nanofiber is probed by the guided light yielding a surface coverage, i. e., number of molecules per surface area, of $\Theta = N/(\pi dL)$ (cf. Fig. 3.7(a)). Hence, for a fixed surface coverage Θ, the absorbance signal measured by nanofiber-based spectroscopy is

$$\eta(\lambda) \approx \frac{\theta\sigma(\lambda)}{\ln 10} \frac{\pi dL}{A_{\text{eff}}(\lambda)}. \tag{3.32}$$

The situation is completely different for free beam techniques where the absorbance is proportional to the number of molecules N per area A probed by the light beam (cf. Eq. (3.11)). As can be seen from Fig. 3.7(b), the surface coverage for an evenly covered surface in this case is simply given by $\Theta = N/A$, yielding an absorbance of $\eta_{\text{free}} = \Theta\sigma(\lambda)/\ln 10$. For a given surface coverage Θ, the absorbance obtained in nanofiber-based surface spectroscopy is therefore enhanced by a factor $\xi(\lambda) = \pi dL/A_{\text{eff}}$:

$$\eta(\lambda) = \eta_{\text{free}}(\lambda)\xi(\lambda). \tag{3.33}$$

With a length of the nanofiber L on the order of millimeters and a diameter d in the submicron range, the sensitivity can thus be increased by four orders of magnitude compared to methods using freely propagating beams [27].

The enhancement is proportional to the length L and the quantity d/A_{eff}, which should therefore be maximized. In order to determine the effective area of the guided fiber mode relevant for the interaction with surface adsorbed molecules, the orientation of the transition dipole moment has to be taken into consideration. The planar molecules studied in this thesis can be assumed to lie flat on the fiber surface [111] resulting in a transition dipole moment oriented perpendicularly to the radial electric field component of the guided fiber mode. Further assuming that there is no preferred orientation of the flat lying molecules on the fiber surface and that the molecules are distributed evenly over the whole surface,

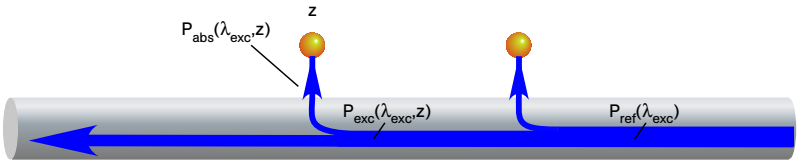

Figure 3.9.: Schematic of the absorption of the guided light of a nanofiber by a molecule at position z along the nanofiber, taking into account the attenuation of the light due to circumjacent molecules on the nanofiber surface.

the axial and azimuthal components of the electric field contribute equally to $I_{\mathrm{surf}}(\lambda)$ and therefore to $A_{\mathrm{eff}}(\lambda)$.

The quantity d/A_{eff} relevant for the interaction with surface-adsorbed planar molecules is plotted in Fig. 3.8 in units of $1/\lambda$ as a function of d/λ. It has been calculated for the circularly or unpolarized fundamental mode and a refractive index of $n_{\mathrm{silica}} = 1.46$. It reaches a maximum for $d_{\mathrm{max}} = 0.584 \cdot \lambda$ which is below the cut-off for the next higher nanofiber mode of $d/\lambda \approx 0.72$, thus ensuring single mode operation of the nanofiber. The nanofibers used for the results presented in this thesis exhibit a diameter of 320 nm resulting in a maximum sensitivity for surface spectroscopy at a wavelength of about 550 nm.

In order to correct for this wavelength dependence of the sensitivity, the total sample absorption cross section $\sigma_{\mathrm{tot}}(\lambda) \approx \ln 10 \cdot A_{\mathrm{eff}}(\lambda) \cdot \eta(\lambda)$ is shown in the surface absorption spectra presented throughout this thesis.

For the tapered optical fibers (TOFs) used in the experiments presented in this thesis, the fiber diameter increases exponentially in the taper transitions close to the nanofiber waist as discussed in Sec. 2.1. Since the surface intensity and, hence, the sensitivity decreases rapidly for increasing fiber diameters, the contribution of surface-adsorbed molecules in the transitions to the total absorbance signal can be assumed to be negligible.

3.2.2. Emission of light into the fiber mode

In order to understand the fluorescence signal of surface-adsorbed molecules measured at the fiber output upon excitation with a monochromatic light source, multiple processes of absorption from and emission into the guided fiber mode have to be taken into account. The considerations discussed in this section have been published in [112].

As stated in Sec. 3.2.1, a molecule at position z along the nanofiber waist absorbs the fraction $\sigma(\lambda_{\mathrm{exc}})/A_{\mathrm{eff}}(\lambda_{\mathrm{exc}})$ of the guided power $P_{\mathrm{exc}}(\lambda_{\mathrm{exc}}, z)$ of the excitation light at a wavelength λ_{exc}, as schematically shown in Fig. 3.9. According to the Lambert-Beer law (Eq. (3.8)), the guided power at position z is given by $P_{\mathrm{ref}}(\lambda_{\mathrm{exc}}) \cdot e^{-\alpha(\lambda_{\mathrm{exc}})z}$ which can be transformed into

$$P_{\mathrm{exc}}(\lambda_{\mathrm{exc}}, z) = P_{\mathrm{ref}}(\lambda_{\mathrm{exc}}) \cdot 10^{-\eta(\lambda_{\mathrm{exc}}) \cdot z/L} \tag{3.34}$$

for a nanofiber with length L. The power absorbed by a molecule at position z can therefore be expressed as

$$P_{\mathrm{abs}}(\lambda_{\mathrm{exc}}, z) = \frac{\sigma(\lambda_{\mathrm{exc}})}{A_{\mathrm{eff}}(\lambda_{\mathrm{exc}})} P_{\mathrm{ref}}(\lambda_{\mathrm{exc}}) \cdot 10^{-\eta(\lambda_{\mathrm{exc}}) \cdot z/L}. \tag{3.35}$$

For the nanofiber diameters and the wavelengths considered here, about 20% of the fluorescence of a single dipole emitter on the fiber surface is expected to be coupled back into the

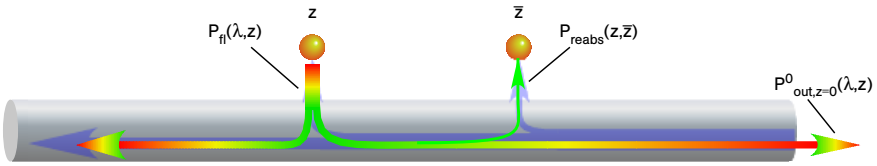

Figure 3.10.: Schematic of the emission into the nanofiber by a molecule at position z and the reabsorption of a fraction of this light by a molecule at position $\bar{z}$ along the nanofiber. The fluorescence from the molecule at position z exiting the fiber at $z = 0$ is denoted by $P^0_{\mathrm{out},z=0}(\lambda, z)$.

fundamental guided mode of the fiber, 10% in each direction of the fiber [31]. As a result, the fluorescence emitted into the fiber mode by a molecule at position z along the fiber waist is proportional to the absorbed power:

$$P_{\mathrm{fl}}(\lambda, z) = C(\lambda) \cdot P_{\mathrm{abs}}(\lambda_{\mathrm{exc}}, z), \tag{3.36}$$

where the proportionality factor $C(\lambda) \propto q(\lambda)/A_{\mathrm{eff}}(\lambda)$ includes the wavelength dependent fluorescence quantum yield of the molecule $q(\lambda)$ and the average fractional emission of the molecule into the guided fiber mode. The latter is an average over all possible orientations of the molecule on the fiber surface and is determined by the intensity of the evanescent field at the fiber surface which is proportional to $1/A_{\mathrm{eff}}$, (cf. Eq. (3.29)). The wavelength dependent fluorescence quantum yield is connected to the total fluorescence quantum yield of the molecule defined in Eq. (3.12) via $\eta_f = \int_\lambda q(\lambda) d\lambda$.

The spectral overlap between the absorption and emission spectra typical for most molecular species results in a partial reabsorption of the emitted fluorescence by circumjacent molecules before it reaches the output of the fiber as schematically shown in Fig. 3.10. The broad spectral bandwidth of the emission is indicated by the arrows of changing color in the figure. Again using the Lambert-Beer law (Eq. (3.8)), the fluorescence from a molecule at position z along the nanofiber exiting the fiber including the lowest order correction for reabsorption can be expressed by

$$P^0_{\mathrm{out},z=0}(\lambda, z) = P_{\mathrm{fl}}(\lambda, z) \cdot 10^{-\eta(\lambda)\cdot z/L} \tag{3.37}$$

for the fiber end where $z = 0$, and by

$$P^0_{\mathrm{out},z=L}(\lambda, z) = P_{\mathrm{fl}}(\lambda, z) \cdot 10^{-\eta(\lambda)\cdot (L-z)/L} \tag{3.38}$$

for the fiber end where $z = L$. Concentrating on the fiber end where $z = 0$ for the remainder of this section, the power $P^0_{\mathrm{out}}(\lambda)$ of the total fluorescence signal exiting the fiber output can be calculated by integrating the power $P^0_{\mathrm{out},z=0}(\lambda, z)$ over all N molecules adsorbed on the fiber waist:

$$\begin{aligned} P^0_{\mathrm{out}}(\lambda) &= \int_0^N P^0_{\mathrm{out},z=0}(\lambda, z)\mathrm{d}N \\ &= \int_0^L \pi \cdot d \cdot \theta \cdot C(\lambda) \cdot \frac{\sigma(\lambda_{\mathrm{exc}})}{A_{\mathrm{eff}}(\lambda_{\mathrm{exc}})} P_{\mathrm{ref}}(\lambda_{\mathrm{exc}}) \cdot 10^{-(\eta(\lambda_{\mathrm{exc}})+\eta(\lambda))\cdot z/L}\mathrm{d}z \\ &= C(\lambda) \cdot \frac{\eta(\lambda_{\mathrm{exc}})}{\eta(\lambda)+\eta(\lambda_{\mathrm{exc}})} \cdot \left(1 - 10^{-(\eta(\lambda)+\eta(\lambda_{\mathrm{exc}}))}\right) \cdot P_{\mathrm{ref}}(\lambda_{\mathrm{exc}}). \end{aligned} \tag{3.39}$$

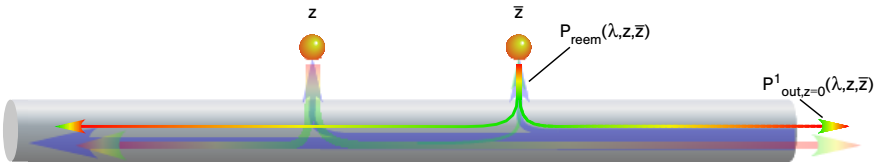

Figure 3.11.: Schematic of the reemission from a molecule at position $\bar{z}$ which has been excited by the emission from a molecule at position z along the nanofiber. The fraction of the reemission resulting from this process which reaches the fiber output at $z = 0$ is denoted by $P^1_{\mathrm{out},z=0}(\lambda, z)$.

For small surface coverages, i. e. $\eta(\lambda) + \eta(\lambda_{\mathrm{exc}}) \ll 1$, this equation can be approximated by

$$P^0_{\mathrm{out}}(\lambda) \approx C(\lambda) \cdot \eta(\lambda_{\mathrm{exc}}) \cdot \ln(10) \cdot P_{\mathrm{ref}}(\lambda_{\mathrm{exc}}) \ . \tag{3.40}$$

Hence, if the reabsorption is small enough to be neglected, the wavelength dependence of the fluorescence quantum yield of the molecules under study can be inferred directly from the measured signal, provided the signal has been corrected for the known wavelength dependent coupling to the fiber mode characterized by $1/A_{\mathrm{eff}}(\lambda)$. For higher surface coverages, however, reabsorption will become important and the spectral shape of the output signal will change according to Eq. (3.39).

For even higher surface coverages, multiple processes of emission and reabsorption may become significant and can inflict additional changes upon the spectral shape of the output signal. The next higher order process following the reabsorption of the emitted fluorescence is the reemission due to the excitation of molecules by reabsorbed fluorescence light. For each wavelength $\bar{\lambda}$, a molecule at position $\bar{z}$ reabsorbs a fraction $\sigma(\bar{\lambda})/A_{\mathrm{eff}}(\bar{\lambda})$ of the power $P_{\mathrm{fl}}(\bar{\lambda}, z, \bar{z})$ originating from the fluorescence emitted by a molecule at position z, which is determined by the Lambert-Beer law (Eq. (3.8)):

$$P_{\mathrm{fl}}(\bar{\lambda}, z, \bar{z}) = P_{\mathrm{fl}}(\bar{\lambda}, z) \cdot 10^{-\eta(\bar{\lambda}) \cdot |z-\bar{z}|/L}. \tag{3.41}$$

The total power $P_{\mathrm{reabs}}(z, \bar{z})$ which the molecule at position $\bar{z}$ reabsorbs from the fluorescence emitted by a molecule at position z can be obtained by integration over all wavelengths $\bar{\lambda}$:

$$P_{\mathrm{reabs}}(z, \bar{z}) = \int_0^\infty \frac{\sigma(\bar{\lambda})}{A_{\mathrm{eff}}(\bar{\lambda})} \cdot P_{\mathrm{fl}}(\bar{\lambda}, z) \cdot 10^{-\eta(\bar{\lambda}) \cdot |z-\bar{z}|/L} \mathrm{d}\bar{\lambda}. \tag{3.42}$$

The reemission of this molecule can be calculated in analogy to Eq. (3.36):

$$P_{\mathrm{reem}}(\lambda, z, \bar{z}) = C(\lambda) \cdot P_{\mathrm{reabs}}(z, \bar{z}), \tag{3.43}$$

and the reemission from a molecule at position $\bar{z}$ along the nanofiber, which exits the fiber at the end where $z = 0$, can be expressed in analogy to Eq. (3.37):

$$P^1_{\mathrm{out},z=0}(\lambda, z, \bar{z}) = P_{\mathrm{reem}}(\lambda, z, \bar{z}) \cdot 10^{-\eta(\lambda) \cdot \bar{z}/L}. \tag{3.44}$$

The reemission process is schematically depicted in Fig. 3.11. The power of the total reemission signal exiting the fiber output at $z = 0$, $P^1_{\mathrm{out}}(\lambda)$, can be calculated by integrating the power $P^1_{\mathrm{out},z=0}(\lambda, z, \bar{z})$ over all N molecules emitting and reemitting:

$$P^1_{\mathrm{out}}(\lambda) = \int_0^L \int_0^L (\pi d\theta)^2 \cdot P^1_{\mathrm{out},z=0}(\lambda, z, \bar{z}) \mathrm{d}\bar{z} \mathrm{d}z. \tag{3.45}$$

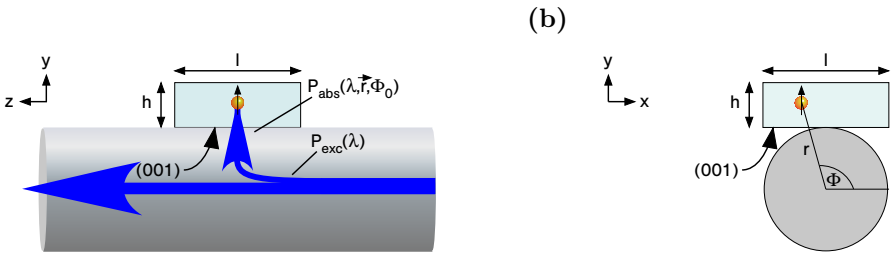

Figure 3.12.: Schematic of a terrylene-doped p-terphenyl crystal with a constant thickness h and a quadratic face with side length l which is attached to the nanofiber with its (001) face parallel to the surface. The position of a dopant molecule in the nanocrystal is defined with respect to the nanofiber center and the nanofiber end while the orientation of its dipole moment is assumed to be perpendicular to the crystal face and is indicated by an arrow. (a) Side view perpendicular to the fiber axis showing the absorption of light from the fiber mode. (b) View along the fiber axis.

Due to its complexity, the integration has to be solved numerically once the absorbance for a certain surface coverage has been measured.

For low surface coverages as considered within this thesis, higher order processes beyond the reemission in first order are, in general, negligible, and the fluorescence signal at the fiber output $P_{\text{out}}^{\text{tot}}(\lambda)$ can be approximated by:

$$P_{\text{out}}^{\text{tot}}(\lambda) \approx P_{\text{out}}^{0}(\lambda) + P_{\text{out}}^{1}(\lambda). \tag{3.46}$$

3.3. Nanofiber-based spectroscopy of molecules in organic crystals

For the nanofiber-based spectroscopic measurements on crystal-embedded molecules presented in this thesis, a terrylene-doped para-terphenyl (p-terphenyl) crystal is attached to the nanofiber surface (cf. Sec. 6.2.1) as schematically shown in Fig. 3.12. P-terphenyl forms platy crystals with (001) faces [113] and the transition dipole moment of a terrylene molecule embedded in such a crystal forms an angle α between 99.8 ° and 103.6 ° with respect to the a-axis of the crystal, where the exact orientation depends on the insertion site [114]. For the considerations in the following, a platy crystal with constant thickness h and a quadratic face (side length l) oriented in parallel to the nanofiber surface (x-z-plane) is assumed. Furthermore, the orientation of the dipole moment $\vec{\mu}$ of the embedded terrylene molecules is approximated by an orientation perpendicular to the crystal face. It is indicated by the arrow in the figure. The position of a molecule in the crystal with respect to the fiber center is determined by the coordinates r and ϕ, while its position along the nanofiber is determined by the coordinate z.

The geometric situation depicted in Fig. 3.12 strongly determines the coupling strength of the dopant molecules to the evanescent field of the guided nanofiber-mode. The non-uniform distribution of the crystal and, therefore, of the dopant molecules around the nanofiber in combination with the uniform orientation of the molecular dipole moment with respect to the crystal face results in a strong dependence on the polarization of the nanofiber-guided mode with respect to the position of the crystal on the nanofiber surface. Moreover, for a uniform distribution of dye molecules in the host crystal, the dopant molecules have distances from the fiber surface which can range between a few nanometers and several micrometers for a large crystal. Therefore, the coupling strength to the evanescent for individual molecules in a

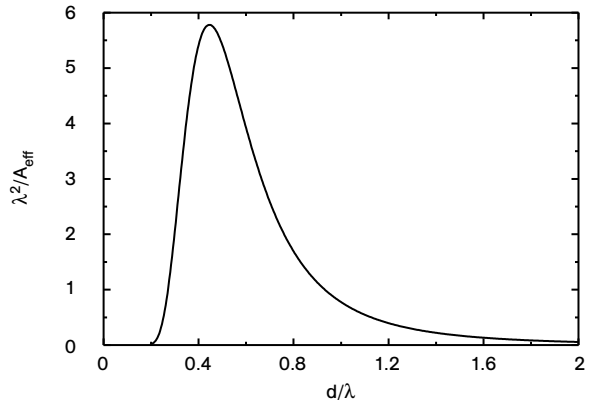

Figure 3.13.: Plot of the quantity $1/A_{\text{eff}}^{\max}(d/\lambda)$ in units of $1/\lambda^2$ as a function of the fiber diameter d in units of the wavelength λ of the guided light. Assuming a refractive index of 1.46 for the nanofiber and ignoring material dispersion, the plot holds universally for any wavelength λ.

crystal can vary by several orders of magnitude and the mean coupling strength for a sample depends critically on the crystal size and the orientation of the crystal with respect to the polarization of the nanofiber-guided mode.

The absorption of light by a dopant molecule in the host crystal is indicated in Fig. 3.12(a). Due to the orientation of the molecular dipole moment, the dopant molecules interact only with the y-component of the electric field. The power absorbed by a molecule at position $\vec{r}$ upon excitation with quasi-linearly polarized light with wavelength λ and a polarization determined by the angle ϕ_0 as discussed in Sec. 1.2 can therefore be expressed by

$$\begin{aligned} P_{\text{abs}}(\lambda, \vec{r}, \phi_0) &= \sigma(\lambda) \cdot \frac{n_{\text{c}} c \varepsilon_0}{2} \cdot \left| E_y(\lambda, \vec{r}, \phi_0) \right|^2 \\ &= \frac{\sigma(\lambda)}{A_{\text{eff}}(\lambda, \vec{r}, \varphi_0)} P_{\text{exc}}(\lambda), \end{aligned} \tag{3.47}$$

where n_{c} denotes the refractive index of the host material, $\sigma(\lambda)$ is the molecular absorption cross section, ε_0 the vacuum permittivity, and c the vacuum speed of light. For a rough estimation of the excitation efficiency of the crystal embedded molecules via the nanofiber-guided mode, the influence of the crystal on the propagation properties of the nanofiber mode is assumed to be negligible and the electric field at the position of an embedded molecule is approximated by the evanescent field of the nanofiber at this position. The effective mode area $A_{\text{eff}}(\lambda, \vec{r}, \phi_0)$ for each position in the evanescent field and each orientation of the molecular dipole moment is introduced as a measure for the excitation efficiency in analogy to the discussion of nanofiber-based surface spectroscopy in Sec. 3.2:

$$A_{\text{eff}}(\lambda, \vec{r}, \phi_0) = \frac{2}{n_{\text{c}} c \varepsilon_0} \cdot \frac{P_{\text{exc}}(\lambda)}{\left| E_y(\lambda, \vec{r}, \phi_0) \right|^2}. \tag{3.48}$$

Since the evanescent field along the polarization axis of the nanofiber-guided mode is dominated by the radial electric field component, the strongest interaction is expected for a molecule positioned on the polarization axis of the electric field ($\phi = \phi_0$) with its dipole

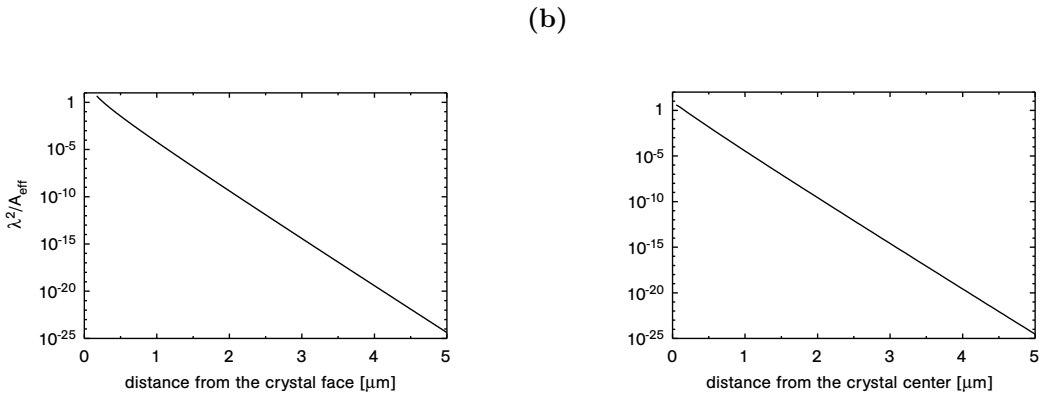

Figure 3.14.: Plot of the quantity $1/A_{\text{eff}}$ in units of $1/\lambda$ for a fixed polarization of the electric field of $\phi_0 = 90\,^\circ$, a wavelength of $\lambda = 580\,\text{nm}$ and a nanofiber diameter of $d = 320\,\text{nm}$. (a) Logarithmic plot as a function of the distance to the crystal face along the y-direction for a fixed angular position of $\phi = 90\,^\circ$. (b) Logarithmic plot as a function of the distance to the crystal center along the x-direction for a fixed distance to the crystal face of $\Delta = 10\,\text{nm}$. The effective mode area is calculated for a refractive index of p-terphenyl of 2.

moment oriented along the radial electric field component ($\phi = 90\,^\circ$). Although the interaction strength decreases quickly with increasing distance from the fiber surface, a minimum distance to the crystal face of $\Delta = 10\,\text{nm}$ is assumed for properly embedded dye molecules. The resulting maximum value of the interaction strength given by the quantity $1/A_{\text{eff}}^{\max}(d/\lambda) = 1/A_{\text{eff}}(\lambda, d/2+\Delta, 90\,^\circ, 90\,^\circ)$ is shown in Fig. 3.13 in units of $1/\lambda^2$ as a function of the fiber diameter d in units of the wavelength λ of the guided light. It has been calculated for refractive indeces of 1.46 and 2 for the nanofiber and p-terphenyl [115], respectively, and reaches a maximum for $d_{\max} = 0.450 \cdot \lambda$. The nanofibers used for the results presented in this thesis exhibit a diameter of 320 nm resulting in a maximum sensitivity at a wavelength of about 710 nm with a value for the quantity $1/A_{\text{eff}}^{\max}(d/\lambda)$ of about $5.78/\lambda^2$. For the resonance frequency of terrylene molecules in p-terphenyl between approximately 577.9 nm and 580.4 nm [116], the inverse effective mode area is 20 % smaller with a value of about $4.7/\lambda^2$.

The strongest interaction possible for a crystal embedded molecule with the nanofiber-guided mode is therefore more than one order of magnitude bigger than the mean interaction for surface absorbed molecules. However, due to the decay of the evanescent field with increasing distance from the nanofiber surface and the decrease of the y-component of the electric field with increasing distance from the crystal center, most crystal-embedded molecules exhibit a much weaker coupling strength to the nanofiber-guided mode.

Figure 3.14 shows the dependence of the interaction strength given by the quantity $1/A_{\text{eff}}$ in units of $1/\lambda^2$ on the position of the embedded molecule in the host crystal for light polarized along the y-axis ($\phi_0 = 90\,^\circ$) with a wavelength of $\lambda = 580\,\text{nm}$ and a nanofiber diameter of $d = 320\,\text{nm}$. The interaction strength decreases by about ten orders of magnitude for a distance of 2 µm from the crystal face along the y-axis (Figure 3.14(a)) as well as from the crystal center along the x-axis (Figure 3.14(b)). For the ensemble measurements on large crystals with dimensions of several micrometers which are presented in this thesis, this broad distribution of coupling strengths can significantly influence the properties of light absorption and emission from and into the nanofiber mode.

Note that the influence of the crystal on the propagation properties of the nanofiber mode have been neglected in the considerations above. Due to the disturbance of the mode by a large organic crystal, the nanofiber-guided light can be scattered out of the fiber mode, and, consequently, the molecules embedded in the crystal cannot be assumed to couple to the evanescent field of the nanofiber but to a "'random"' field generated by the presence of the crystal. In this case, the local strength and polarization of the resulting field cannot be predicted theoretically yielding light absorption and emission properties which cannot be predicted theoretically either.

4. Experimental setup

The setup used for the experiments presented in this thesis can be divided in three parts: a setup for deposition and in situ surface spectroscopy of molecules at ambient conditions, a vacuum setup for measurements in an air-free environment, and a low temperature setup with a cryostat for spectroscopic measurements on dye-doped organic crystals at low temperatures. Since all three setup parts for nanofiber-based spectroscopy of organic molecules are, by nature, fiber-coupled, they can easily be connected to the same optical setup. Although the parts of the setup mainly follow well-known concepts, the unique properties of the optical nanofiber and the nanofiber-based method yield additional benefits and challenges which are discussed in detail.

4.1. Optical setup

The optical setup is the same for all experiments and offers a high amount of flexibility. It can be used for absorption and fluorescence spectroscopy on a variety of molecular systems with different transition wavelengths.

Figure 4.1 shows a schematic of the optical setup. It includes optics for the light from three different laser sources and a white light source for excitation of molecules via the fiber mode. A spectrograph and a Hanbury-Brown and Twiss (HBT) setup can be used for detection of the light emitted by the molecules into the fiber mode and the light transmitted through the fiber in absorption measurements.

For fluorescence measurements, a fraction of the incident laser light is coupled into the tapered optical fiber (TOF) after reflection from a glass plate, as indicated in the figure by the orange, green, and blue lines. The counterpropagating part of the fluorescence emitted by the molecules into the fiber mode (red line) is collected in transmission through the glass plate. This configuration avoids direct incidence of the excitation laser light on the detectors. The residual backscattered and reflected excitation laser light is suppressed by means of long pass filters in front of the detectors. The cut-off wavelength of the longpass filters is chosen according to the laser wavelength used. The choice between the two detection paths is realized by a removable mirror.

For absorption measurements, white light can be coupled into the other end of the TOF. The transmitted light is coupled out of the TOF and detected along the same optical path as the fluorescence signal, indicated by the rainbow-colored line in Fig. 4.1. In order to automatically perform subsequent absorption and fluorescence measurements with fixed time intervals on the order of seconds, two alternating shutters open the path of the white light and the laser light. The shutter blocking the laser light is mounted at the position of the focus of a 1:1-telescope while the shutter blocking the white light is positioned in the filter slot of the fiber-coupled white light source. The shutters are controlled by a custom-made push-pull output amplifier which provides the electrical power needed to operate the shutters and allows one to switch with frequencies between 0.5 and 5.0 Hz and amplitudes between 0.0 and 5.0 V. This signal generator also triggers the spectrograph, thus synchronizing the data aquisition.

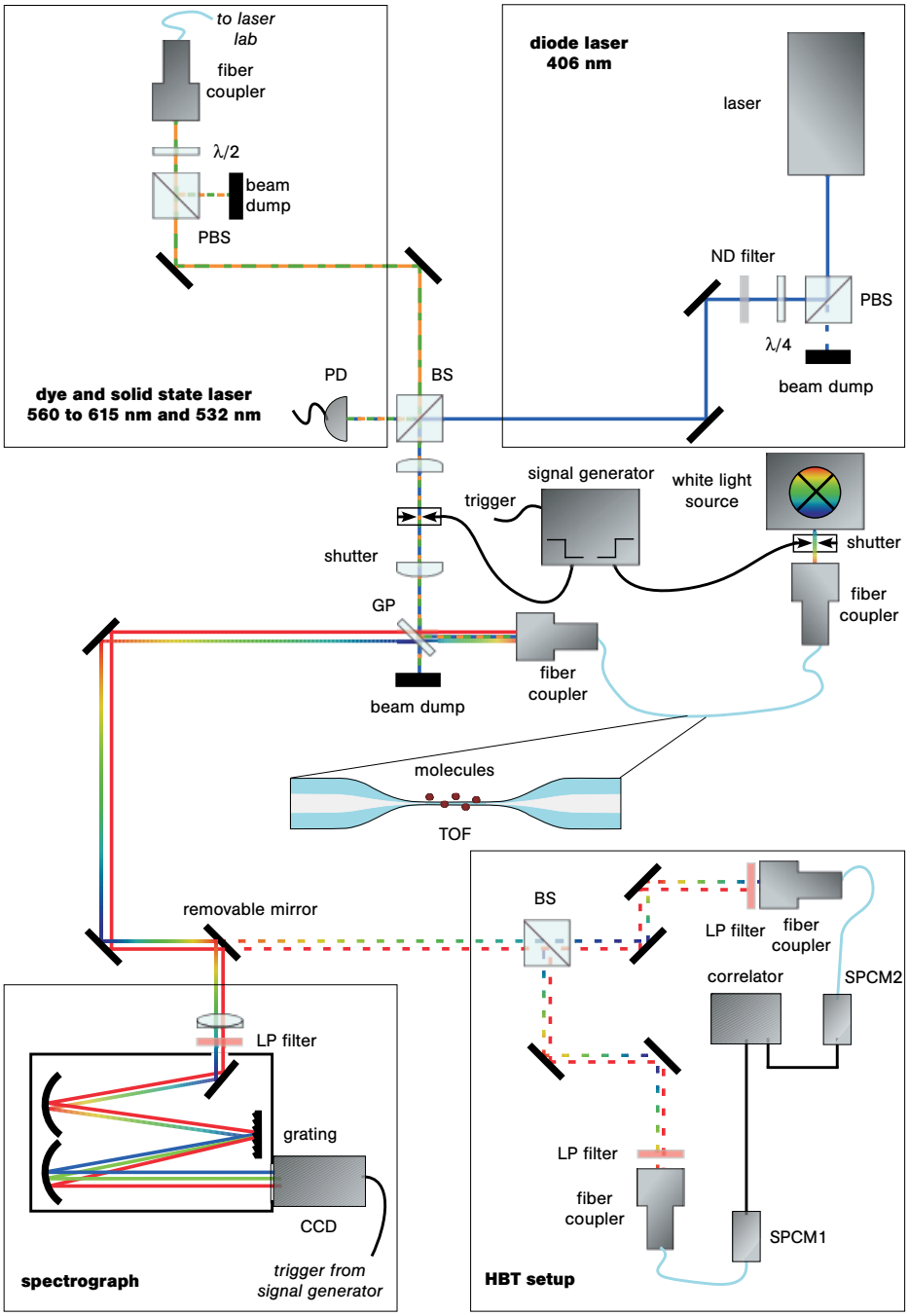

Figure 4.1.: Schematic of the optical setup. $\lambda/4$ and $\lambda/2$: quarter- and half-wave plate, respectively, PBS and BS: polarizing and non-polarizing beam splitter, respectively, PD: photodiode, ND and LP filter: neutral density and longpass filter, respectively, GP: glass plate, TOF: tapered optical fiber, CCD: charge coupled device camera, SPCM: single photon counting module, HBT: Hanbury-Brown and Twiss.

The properties of the different parts of the optical setup will be discussed in detail in the following.

4.1.1. Laser sources

The results presented in this thesis were obtained by studying different molecular systems with different transition wavelengths. Moreover, due to the homogeneuos and inhomogeneous broadening effects discussed in Sec. 3.1.3, a given molecular system can be excited with light covering a large range of wavelengths. Probing the system with two or more different wavelengths can thus yield valuable information about the underlying broadening mechanisms. Therefore, the optical setup presented in Fig. 4.1 was designed to offer a high flexibility in the choice of excitation wavelengths and currently provides the option to use three different laser sources for excitation.

Diode laser

For excitation at the high energy edge of the visible spectrum, a freely running laser diode (Sharp GH04020B2A) with a wavelength of 406 nm and a maximum output power of 20 mW is used (upper right of Fig. 4.1). The output power of the laser diode can be adjusted by a laser controller (Sacher PilotPC 3000) via the diode current. The laser controller is also employed to stabilize the temperature of the laser diode to 25 °C using a negative temperature coefficient (NTC) thermistor and a thermoelectric cooler (TEC).

Backreflections from the setup into the laser diode are reduced by a combination of a polarizing beam splitter (PBS) and a quarter-wave plate. The PBS reflects the vertically polarized fraction of the light into the beam path, whereas the horizontally polarized part is blocked by a beam dump. The quarter-wave plate transforms the vertical polarization into circular polarization. Ideally, any backreflected light from the setup will pass through the quater-wave plate a second time which transforms the circular polarization to horizontal polarization which causes the light to be transmitted through the PBS and blocked by a beam dump (not shown in the figure). Since the backreflected light is not purely circularly polarized due to the reflections from further optical components in the setup, the backreflected light is only reduced and not completly extinguished. The resulting stability of the diode laser is, however, sufficient for the requirements of spectroscopic experiments with integration times on the order of seconds.

In order to reduce the light power to a few microwatts for nanofiber-based surface spectroscopy, the diode laser beam can be additionally attenuated by a neutral density (ND) filter. The laser light is coupled into the setup by two mirrors and a non-polarizing beam splitter (BS). For fluorescence measurements with excitation at a wavelength of 406 nm, a long pass filter with an edge at 418 nm (BLP01-405R-25, Semrock) is placed directly in front of the spectrometer entrance slit in order to suppress the background due to the excitation laser light. The filter exhibits a transition width of 10.3 nm, a transmission band with more than 93 % transmission between 421.5 nm and 900 nm, and a blocking band with an optical density higher than 6 between 324 nm and 410 nm. This yields a suppression of the background due to excitation laser light to a level on the order of the dark counts of the spectrograph, which can easily be substracted from the measured signal.

Dye laser

The spectral selection of single molecules with narrow linewidths on the order of a few ten megahertz from a molecular ensemble requires a narrow-band tunable laser source, as discussed in Sec. 3.1.4. Here, a ring dye laser (Matisse DS, Sirah) which is pumped by a frequency-douled diode-pumped solid state laser (Verdi V10, Coherent, described below) is used. The dye laser is operated with Rhodamine 6G yielding a wavelength tuning range from 560 nm to 615 nm and a specified maximum output power of 1.8 W at 575 nm [117]. The dye has been dissolved in ethylene glycol with a mixing ratio of 0.75 g/l. Single-mode operation of the laser and tuning of the wavelength are realized by the design of the laser resonator and the introduction of additional frequency-selective optical elements, as discussed in detail in [117].

The laser frequency is stabilized to an external reference cavity, yielding a linewidth of the dye laser of 250 kHz root mean square (rms) within 100 ms relative to the reference cavity, which is small compared to the typical linewidths of crystal embedded organic molecules at low temperatures of a few ten megahertz. Since the reference cavity is not actively stabilized, its resonance frequency can drift yielding a drift of the laser frequency which could be measured to be tyically below 1 MHz/s. This value limits the velocity of the slow frequency scans which are used in low temperature studies on organic molecules in order to increase the signal to noise ratio of the measurement. A custom-made plug-in to the laser control software allows for external triggering of these frequency scans.

The dye laser is clamped to a vibration isolated optical table in a temperature stabilized clean room environment in order to ensure stable operation. The laser wavelength can be determined by means of a fiber-coupled wavelength meter (WS-6/600, High Finesse) using a reflex inside the ring resonator. The emitted laser light is attenuated by a neutral density filter and a combination of a rotating half-wave plate and a polarizing beam splitter. This allows stable operation of the dye laser with sufficiently high pump power even if only a few milliwatts of laser power are needed for the experiment. The attenuated laser beam is then coupled into a polarization-maintaining fiber (PM460-HP, Nufern) which guides the light from the laser laboratory to the experiment table shown in Fig. 4.1. The polarization of the laser light is adjusted to the axis of the polarization-maintaining fiber by means of an achromatic half-wave plate. Since there is a residual wavelength dependence of the polarization rotation by the achromatic wave plate, fluctuations of the polarization induced by the 47-meter long fiber connection cannot be avoided completely. To compensate for this effect, the laser light is collimated by a fiber coupler (60FC-4-M12-33, Schäfter + Kirchhoff), and a combintaion of a half-wave plate and a polarizing beam splitter is used to obtain a stable polarization as shown in the upper left corner of Fig. 4.1. The part of the light with perpendicular polarization is reflected by the PBS and blocked by a beam dump. For the experiments presented in this thesis, the intensity fluctuations introduced by the PBS are monitored with a photodiode for each measurement.

If the dye laser light is used for excitation of molecules on the nanofiber waist of the TOF, a long pass filter with an edge wavelength of 600 nm (NT62-985, Edmund Optics) is used for suppression of the background from the excitation light. The filter has an optical density larger than 6 in the blocking band between 200 nm and 588 nm and a transmission of more than 91 % in a band between 610 nm and 1650 nm. As a result, the background from the excitation laser light is suppressed down to the level given by the dark counts of the spectrograph.

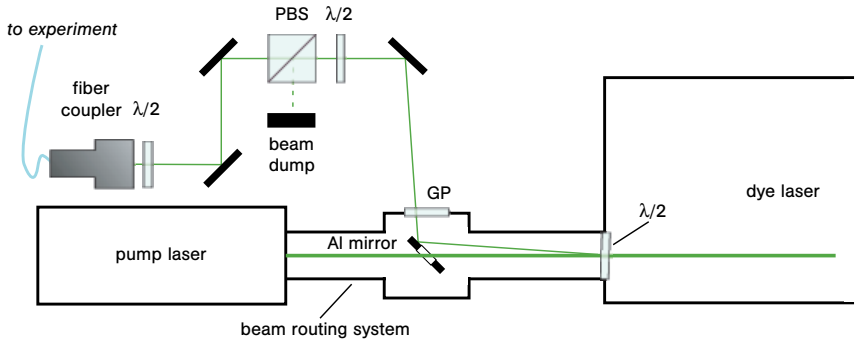

Figure 4.2.: Schematic of the optical setup for branching off pump laser light to the experiment. $\lambda/2$: half-wave plate, PBS: polarizing beam splitter, GP: glass plate, Al mirror: aluminum substrate mirror with aluminum coating and concentric hole.

Pump laser

The dye laser is pumped by a diode-pumped frequency-doubled neodymium-doped yttrium orthovanadate ($Nd : YVO_4$) laser (Verdi V10, Coherent). It emits single-frequency laser light at a wavelength of 532 nm with a maximum power of 10 W and a laser linewidth below 5 MHz within 50 ms [118].

The pump laser is aligned collinearly with the dye laser, and the pump beam path between the two lasers is protected by a tubing system to avoid fluctuations of the pump power. As a result, the pump laser light is usually not accessible for spectroscopic studies during dye laser operation. Figure 4.2 shows the modified setup for branching off pump laser light without disturbing the dye laser operation. The pump laser head is mechanically connected to the dye laser by a beam routing system (Aegis Qube, Newport). Inside a qubic enclosure between the laser heads, an aluminum substrate mirror (diameter 1 ") with aluminum coating (NT47-113, Edmund Optics) and a concentric hole of 15 mm diameter is mounted at an angle of about 45 °. The pump beam has a diameter of 2.25 mm and can therefore pass through the hole without significant diffraction. It enters the dye laser head through a half-wave plate which is slightly tilted in order to avoid backreflection into the pump laser. The small fraction of the pump light which is reflected from the half-wave plate is incident on the remaining rim of the mirror. It is then reflected out of the beam routing system through a glass window. For the maximum pump laser power of 10 W, a fraction of 180 mW is branched off by this technique which is more than enough power for nanofiber-based excitation of organic molecules for which powers on the order of microwatts are applied. The power of the resulting light beam can be adjusted by a combination of a half-wave plate and a polarizing beam splitter and is then coupled into a polarization-maintaining fiber (PM460-HP, Nufern) which guides the light to the experiment table shown in Fig. 4.1. The polarization of the light is adjusted to the axis of the polarization-maintaining fiber by a zero order half-wave plate for 532 nm in front of the fiber coupler which leads to negligible polarization fluctuations on the experiment table.

4.1.2. White light source

For absorption measurements with the optical setup shown in Fig. 4.1, a tungsten halogen light source (AvaLight-HAL, Avantes) is used. The lamp is fan-cooled and actively intensity stabilized via its supply current. The output light is fiber coupled by focussing optics and a ferrule connector (FC) fiber adapter, separated by a 3 mm-thick filter slot. This slot allows to block the beam path with a shutter before the light is coupled into the TOF, as shown in Fig. 4.1. The light bulb is operated at a temperature of 2850 K yielding an spectral output determined by Planck's law with a maximum output power at around 1000 nm. The total output power of the white light source transmitted through a TOF with about 30 % transmission has been measured with an optical spectrum analyzer (AQ-6315A, Ando) to be 2.6 ± 0.2 nW in a wavelength range between 400 nm and 600 nm. This wavelength range is of special interest because it covers the spectral absorption range of the organic molecules studied in this thesis.

As discussed in Sec. 3.2.1, for nanofiber-based absorption measurements, the absorbance is approximately proportional to the ratio of the absorbed light power to a reference power (Eq. (3.31)). If the power of the light source fluctuates with respect to the reference power, the absorbance signal fluctuates accordingly which can mask small signals from molecular absorption. Therefore, the stability of the white light source is crucial for high-sensitivity absorption measurements. In order to determine the power fluctuations of the AvaLight-HAL light source, the output power of the white light source in a spectral interval with a width of 0.6 nm around 517.6 nm has been measured with a temporal resolution of 0.1 s over a total time of about 4 hours. An ideal way to quantify the stability of the output power is the Allan variance which is defined as [119]

$$\sigma_A^2(\tau) = \frac{1}{m} \sum_{n=1}^{m} \frac{(\bar{P}_{n+1,\tau} - \bar{P}_{n,\tau})^2}{2\bar{P}^2}, \tag{4.1}$$

where $\bar{P}_{n,\tau}$ denotes the mean of the measured power values in the time interval n of length τ, and $\bar{P}$ is the power averaged over the entire data set. The Allan deviation $\sigma_A(\tau)$ expresses the instability of the output power between two observations separated by the time τ. This instability will cause fluctuations in the absorbance signal which can be calculated by

$$\sigma_A^{\eta}(\tau) = \frac{\sigma_A(\tau)}{ln10}. \tag{4.2}$$

Figure 4.3(a) exemplarily shows the Allan deviation of the absorbance for averaging times ranging from 0.1 to 300 s. The fluctuations in the absorbance signal due to fluctuations of the white light source are below 0.001 for all time scales shown in the figure. For a typical molecular absorption cross section on the order of $\sigma = 1 \cdot 10^{-16}\,\mathrm{cm}^2$ [27] and an effective mode area on the order of $A_{\mathrm{eff}} = 1 \cdot 10^{-13}\,\mathrm{m}^2$ (cf. Sec. 3.2.1), an absorbance of 0.001 corresponds to approximately 20000 molecules on the fiber waist (cf. Sec 3.2.1). This is the technical detection limit due to fluctuations of the white light source. By averaging over several seconds, the detection limit can be lowered by about one order of magnitude to a few thousand molecules. Figure 4.3(b) displays the Allan deviation of the absorbance in the same wavelength interval around 517.6 nm for the same time range for two other white light sources (WLS100, Bentham, black dots, and AQ-4303B, Ando, red dots). The output of these white light sources has been measured with a resolution of 0.5 s over a time of about 4 hours causing

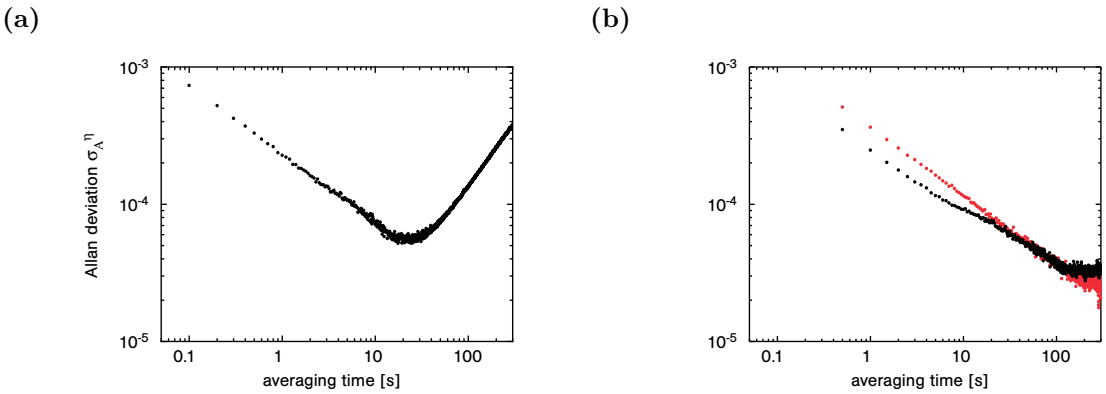

Figure 4.3.: Allan deviation of the absorbance at 517.6 nm due to fluctuations of three different light sources. (a) AvaSpec-2048 (Avantes). (b) WLS100 (Bentham, black dots) and AQ-4303B (Ando, red dots).

the lowest possible averaging time to be 0.5 s. Both light sources yield very similar technical limitations for the detection sensitivity as the light source described before. Therefore, the majority of measurements has been performed with the AvaLight-HAL light source which is less costly.

4.1.3. Spectrograph

A schematic of the spectrograph (Shamrock SR-303i, Andor Technology) used for measuring fluorescence and absorption spectra is shown in the lower left of Fig. 4.1. It exhibits a Czerny-Turner arrangement with imaging toroidal optics and an entrance slit with variable width (10 µm to 3 mm). Optionally, the entrance slit can be replaced by an FC fiber adapter. A triple grating turret allows to choose from three different gratings to vary the spectral resolution of the spectrograph: grating 1 (SR3-GRT-0300-0500) with 300 l/mm blazed for 500 nm yielding a reciprocal dispersion of 10.6 nm/mm, grating 2 (SR3-GRT-0600-0500) with 600 l/mm blazed for 500 nm yielding a reciprocal dispersion of 5.2 nm/mm, and a holographic grating (SR3-GRT-1800-FH) with 1800 l/mm and a resulting reciprocal dispersion of 1.5 nm/mm. The grating turret can be turned in order to adjust the wavelength range incident on the exit window. A CCD camera (Newton DU920N-BR-DD, Andor Technologies) is attached directly to the exit window of the spectrograph. It features a CCD chip with 1024×256 pixels with a size of $26 \times 26\,\mu m^2$ and an anti-reflection coated (AR) entrance window. For a slit width smaller than the size of a CCD pixel, the resulting spectral resolution is below 0.9 nm for grating 1, about 0.4 nm for grating 2, and below 0.1 nm for the holographic grating.

The CCD chip can be thermoelectrically cooled to a minimum temperature of −80 °C without additional water cooling, thereby reducing the dark current to below 0.1 electrons per pixel and second. The readout noise varies between 12 and 36 electrons for full vertical binning of the pixels depending on the readout rate. For a conversion rate of about 12 electrons per count and typical integration times of up to 60 s, the spectrometer noise limits the sensitivity to about 3.5 detected photons, if a signal-to-noise ratio of 1 is employed as detection limit. Higher integration times are impractical due to cosmic radiation incident on the CCD chip. The CCD exhibits a quantum efficiency of about 40 to 90 % in the wavelength range between 400 nm and 1000 nm with a maximum around 750 nm.

The spectrograph has been calibrated spectrally using a fiber-coupled mercury argon calibration source (AvaLight-CAL, Avantes) either connected directly to the fiber adapter of the spectrometer or replacing the white light source in the setup shown in Fig. 4.1. For the two configurations, the calibration turned out to be mutually offset by about 7 pixels. A possible reason for this discrepancy could be that the incidence angle of the light into the spectrograph differs for the two configurations. This result makes it important to employ the right calibration for the used measurement configuration.

Due to the working principle of the spectrograph, the spectra $\Im(\lambda) \approx I(\lambda) \cdot \Delta\lambda$ are measured over equidistant wavelength intervals $\Delta\lambda$, where $I(\lambda)$ is the intensity at the center wavelength of the interval. Since the width of such an interval in units of energy E depends on the center energy of the interval, an additional energy dependence has to be taken into account if the spectra are displayed as a function of energy. The intensity at the center energy of the interval $I(E)$ is given by the relation

$$\int_{\lambda} I(\lambda) d\lambda = \int_{E} I(E) dE. \tag{4.3}$$

This yields

$$I(E) = I(\frac{hc}{\lambda}) = -\frac{d\lambda}{dE} I(\lambda) = \frac{\lambda^2}{hc} I(\lambda). \tag{4.4}$$

The spectrum over equidistant energy intervals ΔE is then given by $\Im(E) \approx I(E) \cdot \Delta E = \lambda^2/(hc) \cdot \Im(\lambda) \cdot \Delta E/\Delta\lambda$. The same holds for displaying spectra as a function of wavenumber $\bar{\nu} = 1/\lambda$ or frequency $\nu = c/\lambda$, where $d\lambda/dE$ has to be replaced by $d\lambda/d\bar{\nu}$ or $d\lambda/d\nu$, respectively, and ΔE has to be substituted by $\Delta\bar{\nu}$ or $\Delta\nu$, respectively.

4.1.4. Hanbury-Brown and Twiss setup

A schematic of the Hanbury-Brown and Twiss (HBT) setup for measuring the intensity correlations of the light is displayed in the lower right corner of Fig. 4.1. The incoming light is split by a non-polarizing beam splitter and coupled into two single mode fibers (460HP, Nufern). Two identical long pass filters are placed directly in front of the fiber couplers in order to suppress background light. The single mode fibers guide the light to APD-operated photon counting devices (SPCM-AQHR-14-FC, Excelitas Technologies) The correlator is based on a field programmable gate array (FPGA) which provides time tags for each detection event with sub-nanosecond precision. The data can then be read out and processed by a computer. By using two detection channels, the dead time of the counters can be overcome.

For the experiments presented in this thesis, the setup is used for coupling the fluorescence light into the spectrometer. For this purpose, one of the single mode fibers is connected to the fiber adapter of the spectrometer instead of the SPCM as indicated by the dashed light blue line in Fig. 4.1.

4.1.5. Transmission characteristics of the setup

The spectral characteristics and the absolute height of the signal measured by the detector depends strongly on the transmission properties of the setup. For absorption measurements, where spectra are obtained by comparison of the measured signal with a reference spectrum which has been transmitted through the same components, this dependence cancels out. It can, however, significantly influence the spectral shape and total strength of the measured fluorescence signal.

In Fig. 4.1, the two possible detection paths for measuring fluorescence spectra are shown: one via the entrance slit of the spectrometer and the other via one port of the HBT setup and the FC fiber adapter of the spectrometer. The total detection efficiency for the fluorescence signal which is coupled into the nanofiber waist of a TOF is determined by several factors and can be expressed by

$$\eta_{slit}(\lambda) = \eta_{taper}(\lambda) \cdot \eta_{optic1}(\lambda) \cdot \eta_{coll1}(\lambda) \cdot \eta_{CCD}(\lambda) \tag{4.5}$$

for detection via the entrance slit and by

$$\eta_{FC}(\lambda) = \eta_{taper}(\lambda) \cdot \eta_{optic2}(\lambda) \cdot \eta_{fiber}(\lambda) \cdot \eta_{coll2}(\lambda) \cdot \eta_{CCD}(\lambda) \tag{4.6}$$

for detection via the FC fiber adapter. Here, $\eta_{taper}(\lambda)$ denotes the transmission efficiency of the fiber uptaper which has been determined in Sec. 2.2.2 for different taper diameter profiles. The transmission probability through all optical components in the detection beam path is summed up in $\eta_{optic1}(\lambda)$ for the beam path from the TOF end to the entrance slit of the spectrometer and in $\eta_{optic2}(\lambda)$ for the beam path from the TOF end to the fiber coupler of the HBT setup. They are mainly determined by the transmission of the glass plate and the non-polarizing beam splitter and are roughly wavelength independent with values of $\eta_{optic1}(\lambda) \approx 0.5$ and $\eta_{optic2}(\lambda) \approx 0.25$. The coupling efficiency into the single mode fiber, denoted by $\eta_{fiber}(\lambda)$, can be up to 0.9 around 655 nm due to the good mode matching between the mode coupled out of the TOF and the mode of the single mode fiber of the HBT setup. However, the lens of the fiber coupler (60FC-4-M12-33, Schäfter + Kirchhoff) exhibits a wavelength dependent focal position and an antireflection coating for the wavelength range of $390 - 670$ nm causing the collection efficiency to peak around 640 nm with a full width at half maximum of about 110 nm. The coupling efficiency into the spectrometer via the entrance slit or the fiber adapter including the transmission of the light through the optical components of the spectrometer is denoted by $\eta_{coll1}(\lambda)$ or $\eta_{coll2}(\lambda)$, respectively, and the CCD has a quantum efficiency of $\eta_{CCD}(\lambda)$.

The total detection efficiency for both paths has been measured using a NIST traceable calibrated tungsten halogen light source (AvaLight-HAL-CAL, Avantes) and a cosine corrector (CC-UV/VIS, Avantes) connected to a multimode fiber (AFS50/125Y, Fiberguide). A cosine corrector is a diffuser used to increase the field of view of the attached fiber to 180 °. For the measurement, the cosine corrector/fiber/spectrometer-system has first been calibrated by means of the known spectrum of the calibrated light source. Then, the calibrated system has been used to measure the power of the light emerging from the end of the TOF when light from a standard white light source was coupled into the other end of the TOF. This way, the absolute power transmitted through the TOF can be determined. Subsequently, the cosine corrector has been removed from the beam path, and the same signal has been measured via both detection paths, yielding the detection efficiency for the light coupled out of the TOF for both detection paths. Multiplying these with the transmission properties of the uptaper of the TOF, renders the total detection efficiencies $\eta_{slit}(\lambda)$ and $\eta_{FC}(\lambda)$.

Figure 4.4 shows the number of photons per second and per spectral interval detected on the CCD chip of the spectrometer per microwatts power of light within this spectral interval guided in the nanofiber waist as a function of wavelength. It is depicted for both detection paths and both TOFs used for the experiments presented in this thesis. The detection efficiency for the beam path via the entrance slit of the spectrometer presented in Fig. 4.4(a) is dominated by the properties of the spectrometer, namely the grating which is blazed at

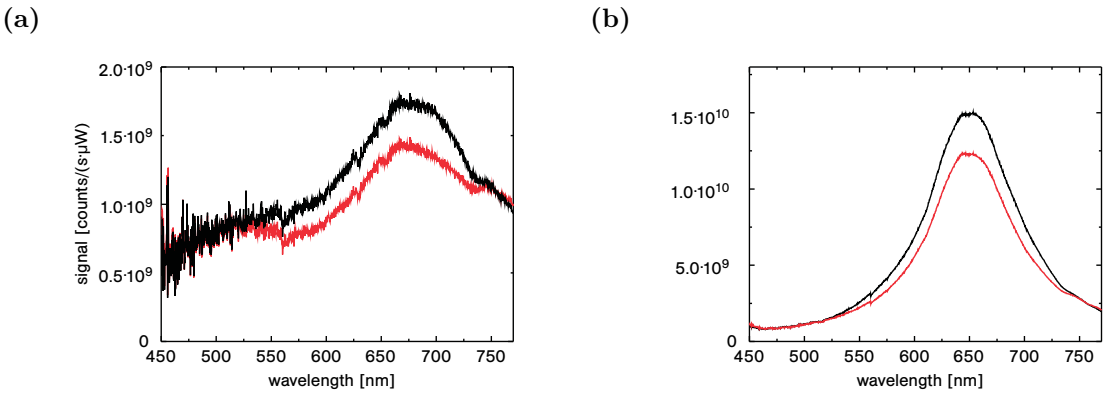

Figure 4.4.: Detection efficiency as a function of wavelength using the entrance slit (a) and the FC fiber adapter of the spectrometer (b). The black curves indicate the efficiency using a molecule fiber, and for the red curves, a cryo fiber has been used (cf. Sec. 2.2.2).

500 nm and the CCD which has its maximum quantum efficiency around 750 nm. For the detection efficiency via the FC fiber adapter of the spectrometer displayed in Fig. 4.4(b), these effects become negligible compared to the wavelength dependence of the fiber collection efficiency discussed above.

Assuming a wavelength of 600 nm, a microwatt power corresponds to about $3 \cdot 10^{12}$ photons. This yields a total detection efficiency of about 0.1 % and 1.0 % for detection via the entrance slit and the FC fiber adapter of the spectrometer, respectively. Taking into account the different contributions to the total detection efficiency discussed above, these results are clearly dominated by the collection efficiency of the spectrometer with an incoupling efficiency about one order of magnitude smaller for coupling via the entrance slit. The origin of these low efficiencies has yet to be determined. The knowledge of the transmission characteristics for the optical setup can be used to determine the collection efficiency of nanofiber-based fluorescence spectroscopy and to correct the measured fluorescence spectra for the spectral sensitivity of the setup in order to recover the spectral shape of the molecular emission.

4.2. Deposition of molecules at ambient conditions

In order to use the nanofiber waist of a TOF as a tool for molecular surface spectroscopy, molecules have to be deposited on the nanofiber surface. At ambient conditions, this can be implemented by a very simple setup as schematically shown in Fig. 4.5.

The TOF (not to scale in the figure) is fixed to an aluminum holder with a drop of UV-curable glue (Optic-Fix) on each end outside the taper region. For depositing molecules onto the nanofiber waist, a boron nitride crucible can be moved under the TOF with a manual positioning stage from the left side. Using a crucible for evaporation of material offers the advantage of complete isolation of the evaporant from the heater, facilitating a homogeneous temperature of the material and, thus, ensuring a constant deposition rate (cf. [120]). Due to its high purity and chemical stability, boron nitride is well suited for sublimation of material [121], especially for the deposition of small amounts of material on a device as sensitive as an optical nanofiber. It is further a very good electric insulator and exhibits a high thermal conductivity of up to $120\,\mathrm{W/(m \cdot K)}$ and a high specific heat of up to $1610\,\mathrm{J/(kg \cdot K)}$ which ensures a uniform heating of the crucible material by the heater element [122].

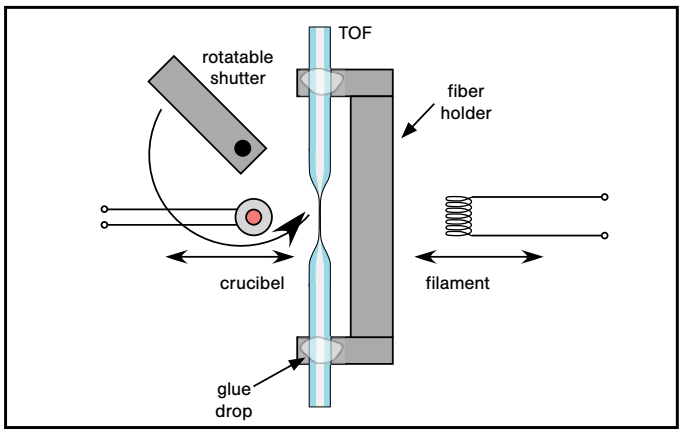

Figure 4.5.: Schematic topview of the setup for deposition of molecules at ambient conditions.

The boron nitride crucible is heated by a current flowing through a platinum wire which is wound around the crucible. The high electrical resistivity of platinum of $1.06 \cdot 10^{-7}\,\Omega$m [123] renders it a highly efficient heater while degassing is strongly reduced in comparison to, e. g., tungsten. The molecules inside the crucible, indicated by the red color, are sublimated and carried to the nanofiber surface by convection. For the model compound Perylene-3,4,9,10-tetracarboxylic dianhydride (PTCDA) used here, heating currents between 2.35 A and 2.45 A have been employed. These currents have been measured to correspond to a temperature of about 300 °C at the bottom of the crucible and, therefore, ensure low deposition rates for PTCDA which has a melting point above 300 °C [124].

A rotatable aluminum shutter can be used to interrupt the air flow from the crucible to the nanofiber waist of the TOF, thereby stopping the molecule deposition onto the nanofiber surface and instantaneously changing the nanofiber temperature, as discussed below. In order to clean the fiber after a measurement, a platinum wire filament can be moved under the TOF with a second translation stage from the right side. By sending a current through the filament, the fiber is convectively heated resulting in a desorption of the molecules from the nanofiber surface. For PTCDA, a current of about 3.0 A is applied which has been measured to yield a nanofiber temperature of about 300 °C and, therefore, results in an efficient desorption of PTCDA from the surface.

The deposition is performed in a closed box in order to shield the TOF and the setup from air turbulences, as discussed in Appendix C.1. This ensures, as much as possible, a constant flow of molecules from the crucible to the nanofiber waist as well as a stable temperature evolution of the TOF.

4.2.1. TOF temperature

Due to convection, heat can be transferred to the TOF from the crucible beneath it. Since the effect of the nanofiber surface on the optical spectra of surface-adsorbed molecules depends on the nanofiber temperature (cf. Sec. 3.1.3), it is important to study the temperature change of the nanofiber caused by the deposition process. Moreover, the mobility of molecules on the nanofiber surface is influenced by the surface temperature, making the temperature an important parameter for measurements of molecular dynamics.

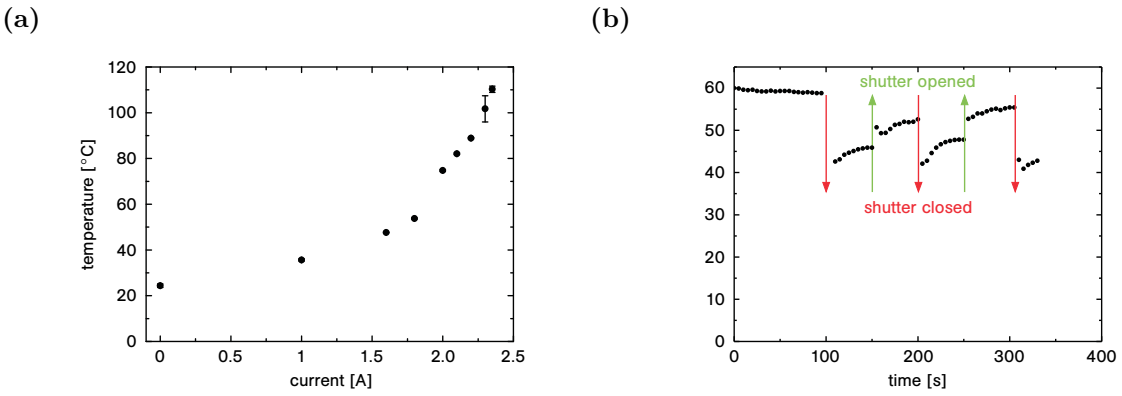

Figure 4.6.: (a) Equilibrium temperature at the position of the TOF as a function of heating current. (b) Temperature change at the position of the TOF due to the introduction (red downward pointing arrows) and removal (green upward pointing arrows) of the aluminum shutter.

Because of the small dimensions of the nanofiber, it can be assumed that it immediately thermalizes with the air surrounding it. Therefore, the nanofiber temperature can be measured by replacing the TOF in the setup shown in Fig. 4.5 with a horizontally oriented thermocouple. Fig. 4.6(a) shows the equilibrium temperature at the position of the TOF after a few minutes of thermalization averaged over several measurements as a function of the current through the crucible heater. This result can be used to determine the nanofiber temperature for surface spectroscopy measurements performed at ambient conditions with the setup shown in Fig. 4.5.

The temperature of the TOF can also be changed by interrupting the air flow from the crucible to the TOF with the rotatable aluminum shutter. Since the shutter is initially positioned far away from the crucible as sketched in Fig. 4.5, it is not affected by the hot air flow from the crucible and is approximately at room temperature. Once it is inserted between the hot crucible and the TOF, the temperature of the TOF is reduced instantaneously. Figure 4.6(b) shows the time evolution of the measured temperature at the position of the TOF for a repeated introduction of the shutter into the air flow. The crucible is heated with a current of 1.8 A through its heater, initially yielding a temperature of 60 °C at the position of the TOF. The introduction of the shutter between crucible and TOF, indicated by the red downward pointing arrows in the figure, causes an immediate temperature drop to about 40 °C. While the shutter is kept over the crucible, the temperature at the position of the TOF slowly rises, because the shutter heats up by the air flow from the crucible beneath. The removal of the shutter, indicated by the green upward pointing arrows, results in an instantaneous increase in temperature because the heated rising air from the crucible can reach the TOF directly. While the shutter is open, the system rethermalizes to the initial temperature of 60 °C at the position of the TOF. Hence, the rotatable aluminum shutter can be used to induce an instantaneous and quantifiable change of the nanofiber temperature in order to study the temperature dependent dynamics of molecules adsorbed on the nanofiber surface.

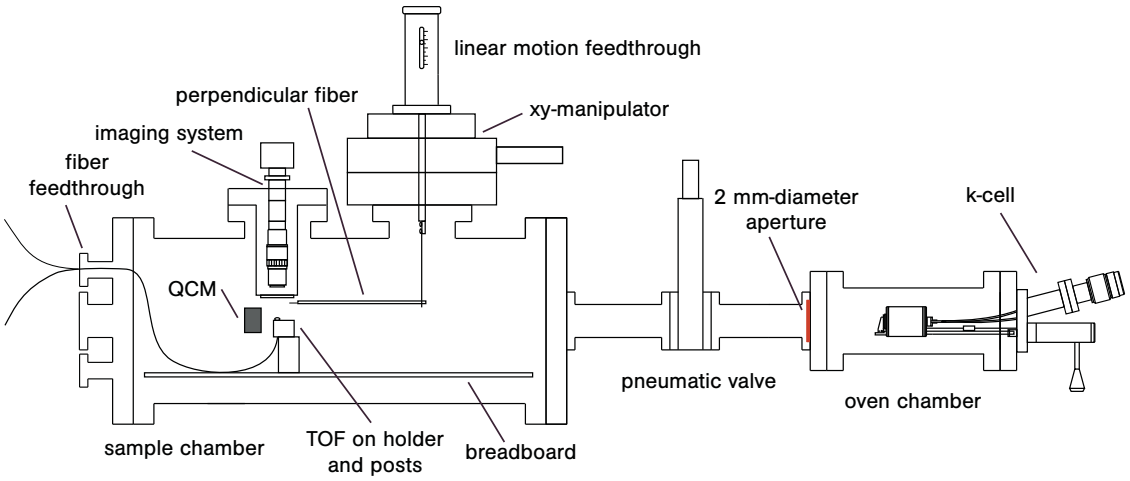

Figure 4.7.: Schematic of the vacuum chamber, divided into sample chamber (left) and oven chamber (right) by a differential pumping aperture and a pneumatic valve.

4.3. Vacuum setup

For the deposition of molecular layers and the growth of crystals from compounds which can react with the components of air, mainly water or oxygen, an air-free environment is required. An ultra-high vacuum (UHV) chamber provides such an environment which also facilitates the desorption of water and other pollutants from the sample surface. These pollutants can induce impurities during crystal growth, modify the interactions of the molecules with the surface, and change the characteristics of molecular layers due to unwanted interactions with the pollutants. An additional advantage of UHV conditions is the possibilty to implement molecular beam deposition which yields a homogeneous and controllable flux of molecules to the sample.

The vacuum setup used for the experiments presented in this thesis is schematically shown in Fig. 4.7. A detailed description can be found in [120]. The vacuum setup consists of two vacuum chambers, the sample chamber (left) and the oven chamber (right). A pneumatic valve (Vacom 11223-0154R) between the two chambers allows for separate venting and opening of the two chambers. If the pneumatic valve is open, a 2 mm-diameter aperture modifies the conductance between the chambers such that the pressure in the sample chamber does not exceed $3 \cdot 10^{-9}$ mbar even if the pressure inside the oven chamber rises to $1 \cdot 10^{-6}$ mbar due to heating of the oven.

4.3.1. Sample chamber

The custom-made cylindrical sample chamber with a length of 489 mm and an inner diameter of 200 mm comprises 13 conFlat flanges and a breadboard in the bottom for clamping components on the vacuum side. A TOF, glued to a holder as described in Sec. 4.2, is screwed to two posts which are clamped to the breadboard and raise the position of the TOF to the height of the molecular beam. The unprocessed ends of the TOF are led out of the vacuum chamber via a fiber feedthrough. This feedthrough consists of a Swagelok connector (SS-400-1-2RS) welded to a conFlat flange with the metal ferrule substituted by a custom-made teflon

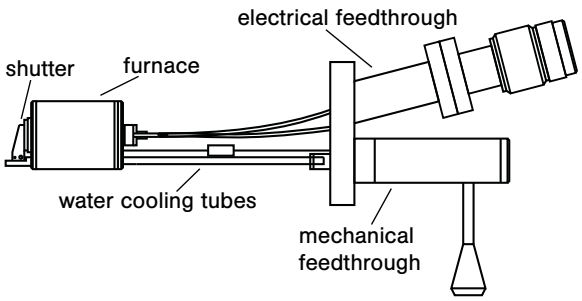

Figure 4.8.: Schematic of the Knudsen cell with a furnace containing crucible, heater element, and heat shields.

ferrule with two off-axis holes for the fiber. Tightening the nut of the Swagelok connector seals the vacuum chamber and makes it possible to reach UHV conditions [50, 125]. A quartz crystal microbalance (QCM, Sigma Instruments) behind the TOF is used for monitoring the deposition rate with a resolution of 0.01 Å/s (rate monitor SQM-160).

In order to either excite molecules on the TOF with freely propagating light or to collect their emission into free space, an additional fiber, which is glued to a stainless steel tube, can be positioned perpendicularly to the nanofiber waist. The vertical position of this fiber can be adjusted by a linear motion feedthrough (LewVac) and the horizontal position can be aligned by an xy-manipulator (Mewasa Flex). The relative distance of the perpendicular fiber to the nanofiber waist of the TOF can be determined by an imaging system from the outside of the vacuum chamber. The system consists of a microscope objective (G Plan Apo 20x, Mitutoyo), a tube (InfiniTube Standard, Infinity Photo-Optical Company), and a monochrome CCD camera (Guppy F-046B, Allied Vision Technologies) and exhibits a resolution of 2.4 µm (see [120] for details).

The sample chamber is evacuated by a combination of a scroll pump (SCROLLVAC SC 15D, Oerlikon Leybold Vacuum) and a turbomolecular pump (HiPace 300, Pfeiffer Vacuum). The pressure inside the sample chamber has been measured by a cold-cathode ionization gauge (IKR 270, 0.01 mbar to $5 \cdot 10^{-9}$ mbar, Pfeiffer Vacuum) to be $1 \cdot 10^{-8}$ mbar for the measurements presented in this thesis.

4.3.2. Oven chamber

The oven chamber is composed of a tee whose upper part is axially aligned with the sample chamber and whose base is used to mount the vacuum pumps and gauges (not shown in Fig. 4.7). The chamber is evacuated by a scroll pump (SCROLLVAC SC 5D, Oerlikon Leybold Vacuum) and a turbomolecular pump (HiPace 80, Pfeiffer Vacuum). The oven, a Knudsen cell (Miniature K-cell, Chell instruments), is located at the right end of the upper part of the tee and is also axially aligned with the sample chamber.

A Knudsen cell (K-cell) is based on the principle of molecular effusion, i. e., individual molecules leave the oven without collisions between molecules. This occurs if the aperture of the oven is considerably smaller than the mean free path of the molecules [126]. Molecular effusion provides a directed molecular beam which is required for a controlled layer deposition and crystal growth. A schematic of the K-cell is shown in Figure 4.8. The furnace consists of a water cooled housing and a removable cartridge containing a graphite crucible, the heater

element, and heat shields. It is heated by a tantalum foil element wrapped around the crucible and isolated with pyrolytic boron nitride (PBN) shields. A removable PBN crucible can be fitted into the graphite crucible to facilitate filling of the oven with the material to be deposited. Additionally, the output beam can be defined by removable apertures. The furnace temperature is measured by a thermocouple (PtRh, Type R) connected to the graphite crucible. Thermocouple and heater are connected to the outside via an electrical feedthrough on a conFlat flange. The flange also comprises a mechanical feedthrough for the furnace shutter. A microprocessor-based PID (proportional, integral, differential) controller (Eurotherm 2216E) is used for regulation of the input power to the heater and should maintain the operating temperature within $\pm 2.0\,^{\circ}\mathrm{C}$ or $\pm 0.3\,\%$ of the target temperature.

4.4. Cryostat

In order to perform spectroscopic measurements on molecules with narrow linewidths, the samples have to be cooled to cryogenic temperatures. For this purpose, a bath cryostat is used which accounts for the technical challenges posed by the pronounced evanescent field (disturbances of the guided mode by thermal contacting or pollutants) and the small dimensions (sensitivity to meachnical stress) of the optical nanofiber. Parts of this chapter have been adapted from [127, 128].

4.4.1. Bath cryostat

The experimental setup is based on a bath cryostat, a schematic of which is shown in Fig. 4.9(a). In a bath cryostat, the sample is immersed in a liquid helium bath. In order to minimize heat transfer from the environment via convection and thermal conduction, the liquid helium bath is surrounded by a concentric evacuated shielding layer. According to the Stefan-Boltzmann law, the heat transfer via radiation between the environment and the helium bath is proportional to the forth power of the temperature of the environment [123]. Therefore, the temperature of the environment is lowered by an additional heat shield that is cooled by liquid nitrogen. With a boiling temperature at standard pressure of 77.35 K for liquid nitrogen and of 4.23 K for liquid helium(^{4}He) [123], the heat exchange rate can be reduced by a factor of about 270 in comparison to a room temperature environment. The liquid nitrogen bath is shielded by a second evacuated layer. Both isolating layers are evacuated by a rotary vane pump (Alcatel 1012A) connected via a valve at the bottom of the cryostat. The liquid helium level can be measured by a liquid helium level sensor (Cryomagnetics 3DA-60-100, monitored with Cryomagnetics LM-500).

Figure 4.9(b) shows the sample rod with the sample chamber which is immersed into the liquid helium bath. To reduce heat transfer to the bath via the rod, it consists of stainless steel which exhibits a low thermal conductiviy. Heat transfer by radiation is reduced by three heat shields, and the liquid helium bath is sealed by a Klein flange (KF) attached to the sample rod. The tapered optical fiber is located in a sample chamber made of oxygen-free copper. Due to the high thermal conductivity of the material, the sample chamber thermalizes efficiently with the liquid helium bath. The sample chamber can be connected to the sample rod via a stainless steel flange on its top. The connection is sealed with indium wire yielding an ultra-high vacuum-proof connection even at cryogenic temperatures. The temperature of the sample chamber is measured by a silicon diode temperature sensor (Lake Shore DT-670-CU-1.4L) attached to the stainless steel flange and monitored by a temperature monitor (Lake

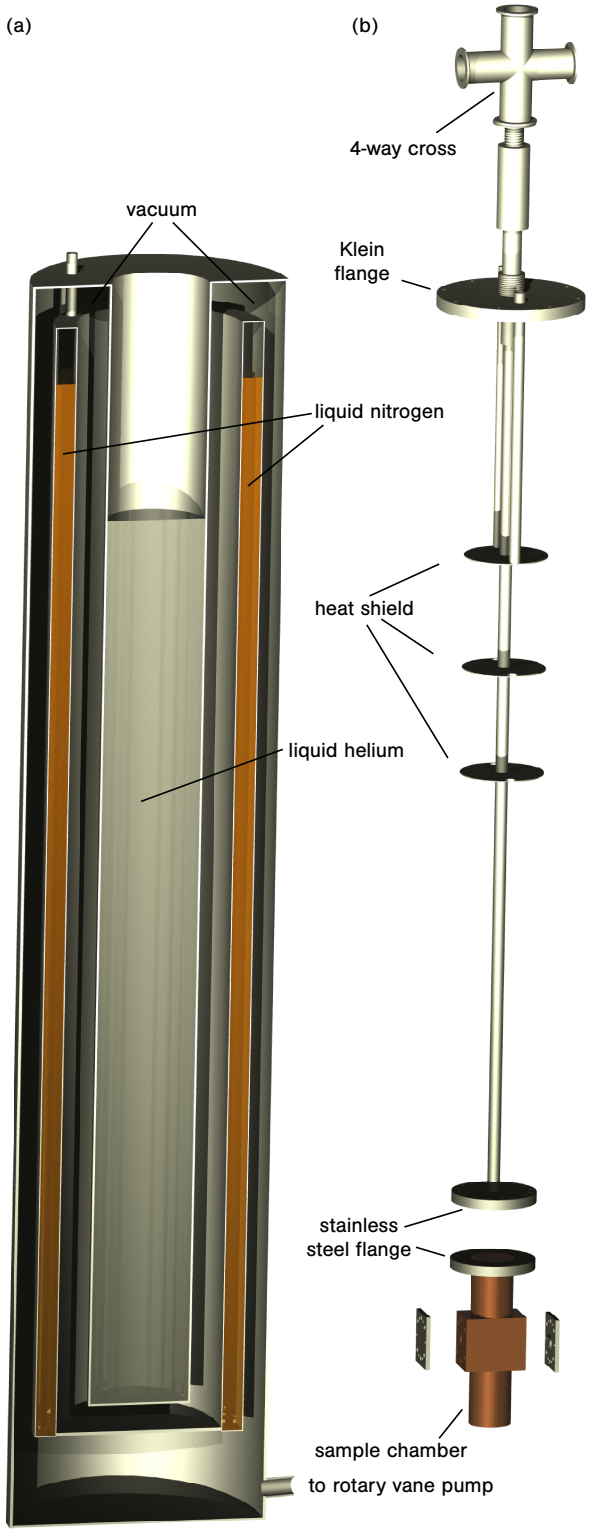

Figure 4.9.: Schematic of the bath cryostat (a) and sample rod with sample chamber (b).

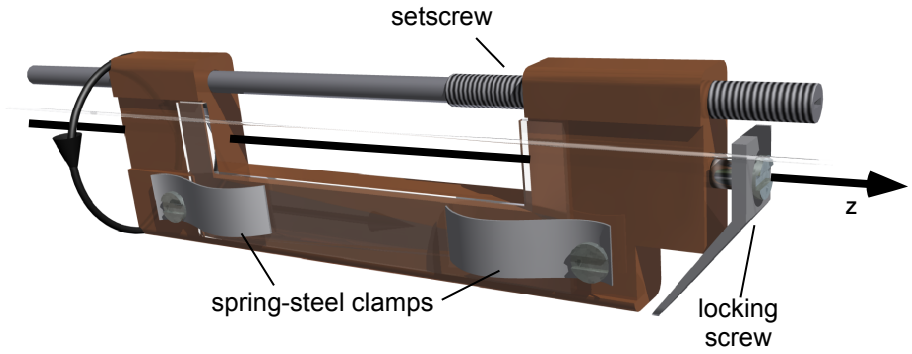

Figure 4.10.: Copper mount with a glass fiber holder fixed with two spring steel clamps, a setscrew for vertical positioning (z-direction), and a locking screw for fastening inside the sample chamber.

Shore 211). At the upper end of the sample rod, a 4-way cross comprises flanges with an electrical feedthrough for the temperature sensor, a fiber feedthrough as described in Sec. 4.3, a pressure relief valve, a pressure gauge, and a valve for evacuating and venting the sample rod and chamber (components not shown in the figure).

Although the isotope ^{4}He usually used in bath cryostats has a boiling point of 4.23 K at standard pressure, the sample chamber thermalizes to a minimum temperature of about 4.4 K. This is most likely due to the residual heat transfer from the environment to the sample chamber via the sample rod. The liquid helium hold time of the bath cryostat with sample rod and sample chamber can significantly exceed 24 hours, provided that the liquid nitrogen bath is full during this period and there is no additional heat input by, e. g., light transmitted through the fiber inside the sample chamber.

4.4.2. Fiber mount

Inside the sample chamber, the TOF is positioned with the copper mount displayed in Fig. 4.10. The mount is inserted into the sample chamber along the negative z-direction, and its vertical position can be adjusted by a setscrew. After the adjustment, the mount can be fastened inside the sample chamber by a locking screw. An U-shaped fiber holder of a few millimeters thickness is fixed to the mount with two spring-steel clamps to allow for movement of the holder against the mount due to thermal contraction and expansion. This is especially important if a glass holder is used as shown in the figure since glass is a brittle material which can easily crack under thermally induced stress.

In order to minimize the amount of thermally induced stress on the TOF during the cooling process and at cryogenic temperatures, two different fiber holder designs have been developed and tested especially for this purpose. Figure 4.11 shows a schematic of the two fiber holders and the applied techniques for fixing the TOF to the holder. For simplicity, the taper of the TOF is not shown in the figure. The first fiber holder is made out of a standard microscopy slide (soda-lime glass) to which the TOF can be glued with an UV-curable glue (Optic-Fix) as schematically depicted in Fig. 4.11(a). Here, a second glass holder is glued on top of the first holder and the TOF. The resulting sandwich construction is additionally fixed by the spring

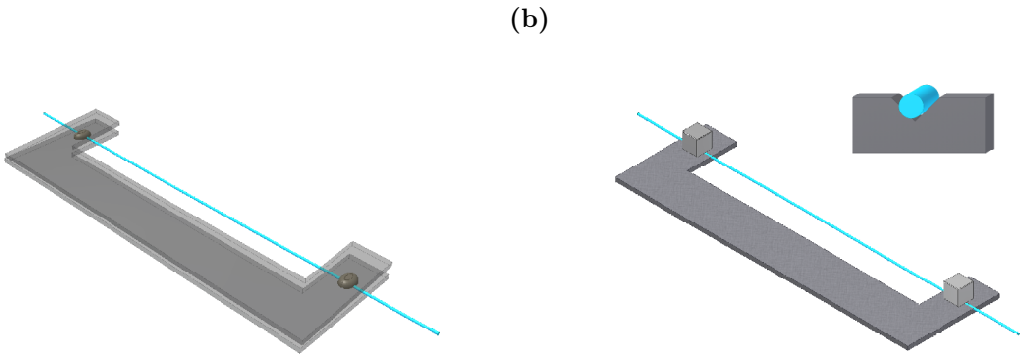

Figure 4.11.: Schematic of the fiber glued between two stacked glass holders (a) and fixed by magnets inside V-grooves on a steel holder (b).

steel clamps of the fiber mount in order to keep the TOF in place even if the glue separates from the glass surface due to thermal contraction. The second fiber holder approach relies on fixing the TOF with magnets on a steel holder as sketched in Fig. 4.11(b). In order to avoid transmission losses due to deformations of the TOF by the magnets, the fiber is inserted into V-grooves on both sides of the holder as shown in the inset of Fig. 4.11(b) [128]. The depth of the V-grooves is 120 µm causing the fiber to be embedded in the grooves by three quarters of its height.

In order to determine the stress on the TOF due to the different thermal expansion of fiber and holder, the total relative length change of both parts has to be determined. The total realative length change of a material due to thermal expansion can be expressed by [123]

$$\frac{\Delta L}{L} = \int_{T_1}^{T_2} \alpha(T) dT, \tag{4.7}$$

where T_1 and T_2 denote the initial and final temperature, respectively, and $\alpha(T)$ is the temperature dependent linear coefficient of thermal expansion.

The TOFs used for the experiments presented in this thesis are produced from a pure silica fiber with a germanium doped core (460HP, Nufern). Due to the small size of the core compared to the cladding, the TOF can be assumed to consist of pure silica. The linear coefficient of thermal expansion for silica has been measured to be below $0.5 \cdot 10^{-6}\,\mathrm{K}^{-1}$ for the whole temperature range between 10 and 300 K, with negative values for temperatures below approximately 140 K [129]. Therefore, an upper limit for the relative length change of the TOF can be estimated to be about $-1.45 \cdot 10^{-4}$ over this temperature range. For a TOF of 80 mm total length, this results in a contraction of about 12 µm. This length change is much less than the length change usually introduced by stretching the TOF after the pulling process which is typically on the order of 200 µm. The length change by thermal contraction can therefore easily be compensated by stretching the fiber less before cooling it.

As a result, the fiber holder material is only relevant for the determination of the stress on the TOF, if it expands significantly during the cooling process (negative thermal expansion coefficient), which is usually not the case for standard materials. For steel, the linear thermal expansion coefficient is positive for all temperatures with values ranging from about $12 \cdot 10^{-6}\,\mathrm{K}^{-1}$ to $5.5 \cdot 10^{-6}\,\mathrm{K}^{-1}$ in a temperature range from 283 to 103 K [123, 130]. Soda-lime glass has a linear coefficient of thermal expansion between $9 \cdot 10^{-6}\,\mathrm{K}^{-1}$ and $5 \cdot 10^{-6}\,\mathrm{K}^{-1}$ in

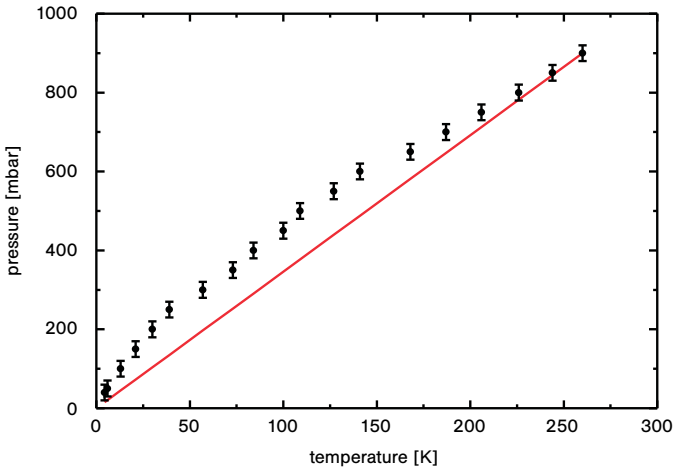

Figure 4.12.: Helium gas pressure in the sample chamber as a function of the chamber temperature measured with a pressure gauge at room temperature (black dots) and predicted by the ideal gas law assuming that the helium gas is thermalized with the sample chamber (red line).

this temperature range which only becomes negative at very low temperatures [130]. As a result, both materials contract more than the TOF when cooled and therefore only lower the already negligible stress on the TOF due to thermal contraction.

In contrast, the applied technique for fixing the TOF to the holder can greatly influence the stress on the TOF due to cooling. During the cooling process, a glue drop can contract and change its inner structure which exerts a significant amount of stress on the TOF. Depending on the experimental conditions like drop size, curing time or cooling speed, this stress can cause fracture of the TOF. Early experiments have been performed with this fiber holder approach. However, fixing the TOF with magnets on a steel holder has proven to be a much more reliable approach. Since the TOF is fixed to V-grooves, a shift of the TOF by thermally induced stress at these points which can lead to fracture at the nanofiber waist is precluded. Hence, the glass holder approach has been replaced by the steel holder technique for present and future experiments.

4.4.3. Cooling of the nanofiber

The nanofiber waist of the TOF is cooled by heat transfer to the walls of the sample chamber. However, it cannot be brought into direct physical contact with a coldplate or a coldfinger, which is the typical approach for cooling of samples in a bath cryostat, without disturbing the guided mode. Moreover, the heat transfer from the nanofiber waist to the environment by thermal conduction along the TOF can be assumed to be negligible, which also renders cooling via physical contact of the untapered part of the TOF with a coldplate/coldfinger impractical. As an alternative approach, helium buffer gas (Alphagaz 1, Air Liquide) is introduced into the sample chamber to ensure the heat transfer from the nanofiber to the walls of the sample chamber.

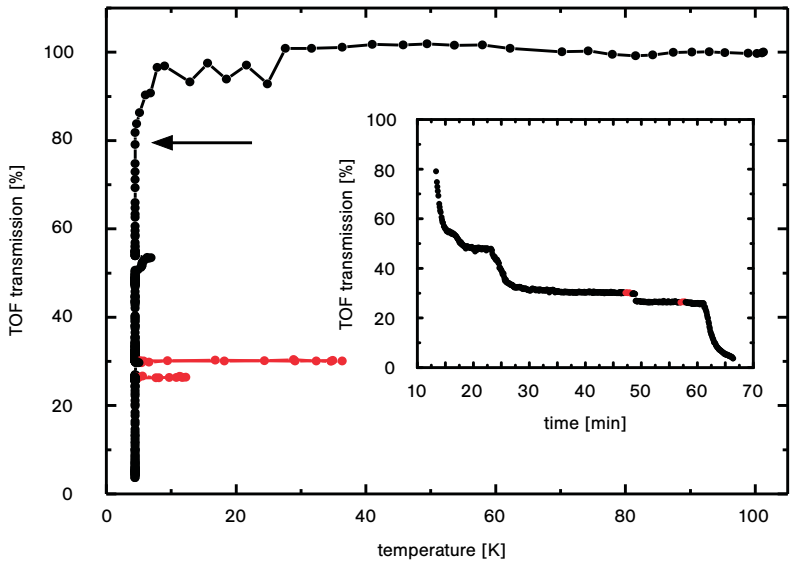

Figure 4.13.: Transmission of a TOF in a helium buffer gas atmosphere (1.27 bar at room temperature) during the cooling process as a function of sensor temperature with connecting lines as a guide to the eye. The horizontal lines marked in red are caused by additional liquid helium fillings of the cryostat, and the arrow indicates the point where the sensor has reached a minimum temperature of about 4.4 K. The inset shows the time evolution of the transmission after the sensor has reached its minimum temperature with the additional liquid helium fillings again marked in red.

In order to ensure an efficient heat transfer between the nanofiber and the sample chamber walls even at low temperatures, an initial buffer gas pressure of about $p_1 = 1\,\text{bar}$ at room temperature (T_1) is chosen. Figure 4.12 shows the helium buffer gas pressure measured by the pressure gauge at the upper end of the sample rod as a function of sample chamber temperature during cooling of the sample chamber. For comparison, the behavior predicted by the ideal gas law is indicated by the red line. The figure shows that the measured pressure is higher than the theoretically expected pressure. This is due to the fact that the differential pumping via the sample rod causes the pressure at the upper end of the sample rod to be higher than the pressure inside the sample chamber. Hence, the actual behavior of the pressure inside the sample chamber is described better by the ideal gas law than by the measurement at the upper end of the sample rod. However, due to the large relative error, the measured pressure of $40 \pm 25\,\text{mbar}$ for a sample chamber temperature of 4.4 K agrees well with the theoretically predicted value of $p_2 = p_1 \cdot T_2/T_1 \approx 15\,\text{mbar}$ at $T_2 = 4.4\,\text{K}$. In any case, the initial pressure of about 1 bar at room temperature has been shown to yield a significant helium pressure and, thus, an efficient heat transfer even at 4.4 K.

4.4.4. Influence of the buffer gas on the fiber transmission

It has been observed that the cooling process can affect the transmission properties of the TOF significantly. This effect is described in detail in the following. Figure 4.13 shows the typical evolution of the transmission properties during the cooling process as a function of sensor temperature for a TOF fixed to a steel holder with magnets as discussed in Sec. 4.4.2.

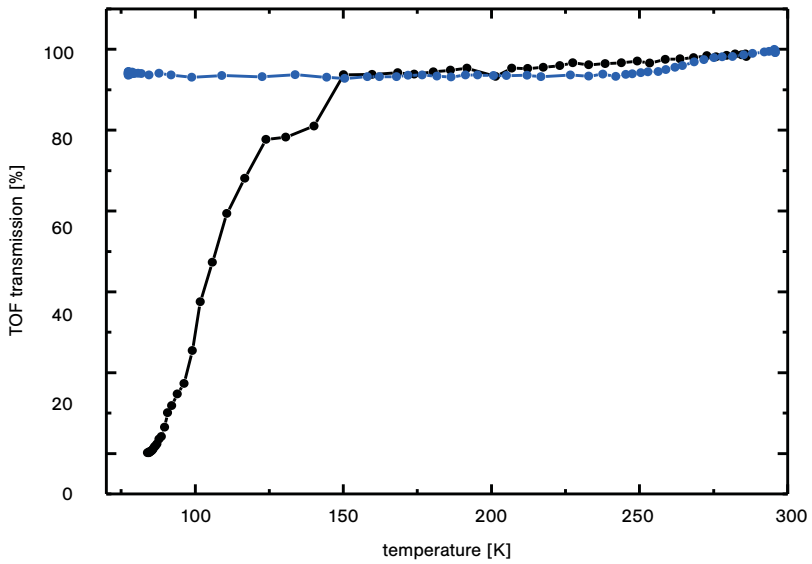

Figure 4.14.: Transmision properties of a TOF in a nitrogen buffer gas atmosphere (1.27 bar at room temperature) during the cooling process as a function of sensor temperature (black dots with connecting lines as a guide to the eye). For comparison, the behavior of the same fiber in a helium buffer gas atmosphere with the same initial pressure is shown (blue dots with connecting lines as a guide to the eye).

The transmission has been measured using a tungsten halogen light source and a fiber optic spectrometer. It is displayed exemplarily for a wavelength of 523.67 nm, since the observed behavior proved to be wavelength independent for all practical purposes (cf. [128]). Before cooling in the bath cryostat, the sample chamber has been vented with 1.27 bar of helium gas (Alphagaz 1, Air Liquide) and precooled to 77 K in a liquid nitrogen dewar. Transferring the sample rod to the bath cryostat and filling the cryostat with liquid helium causes the temperature to rise to about 100 K. The figure shows the evolution of the TOF transmission from the point where the cooling by the liquid helium becomes effective.

The transmission stays roughly constant for a large temperature range, until it starts to drop rapidly around a sensor temperature of 8 K. The temperature rises marked in red are caused by refilling the cryostat with liquid helium and the arrow marks the point where the sensor has reached a minimum temperature of about 4.4 K. The inset shows the time evolution of the transmission after this point. The transmission drops in steps and vanishes completely after about one hour. Again, the time periods of temperature rise due to refilling the cryostat are marked in red. It is clearly visible that the refilling does not affect the transmission of the TOF. Upon warming up the sample chamber and the TOF by taking it out of the cryostat, the transmission rises instantaneously to about 100 % at a sensor temperature of about 70 K.

A similar behavior has been observed for nitrogen buffer gas (Air Liquide). However, here, the transmission drops at much higher temperatures. The typical evolution of the transmission properties of a TOF during cooling to liquid nitrogen temperatures as a function of sensor temperature is shown in Fig. 4.14. For this measurement, the sample chamber was vented with 1.27 bar of nitrogen gas and subsequently immersed in a dewar filled with liquid nitrogen. The TOF transmission has been determined in the same way as described above. The transmission stays roughly constant up to a temperature of about 150 K and then slowly starts to decrease

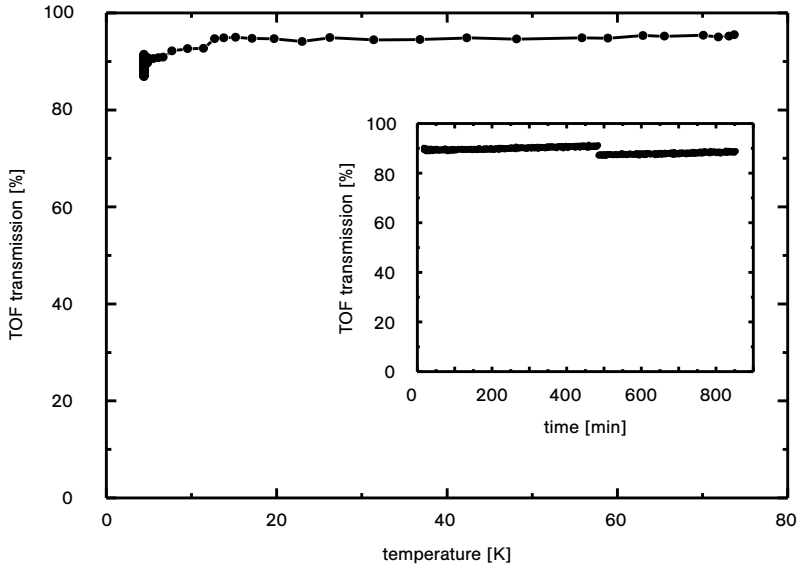

Figure 4.15.: Transmission properties of a TOF in a low pressure (10 mbar) helium buffer gas atmosphere during the cooling process as a function of temperature with connecting lines as a guide to the eye. The inset shows the time evolution of the transmission at about 4.4 K.

to zero at liquid nitrogen temperatures. If the sample chamber is taken out of the dewar, the temperature rises and the full transmission is reestablished at a sensor temperature of around 291 K.

For comparison, the behavior of the same TOF during exactly the same process but with helium buffer gas instead of nitrogen buffer gas is also shown in Fig. 4.14. The transmission is unchanged over the whole temperature range, clearly indicating that the observed break-down of TOF transmission is directly connected to the type of buffer gas and its properties.

Another important factor influencing the transmission properties of the fiber is the buffer gas pressure. Figure 4.15 shows the typical behavior of a TOF cooled in a helium buffer gas atmosphere of a constant pressure of 10 mbar at all temperatures. This has been achieved by constantly refilling the sample chamber with buffer gas during the cooling process. The cooling procedure and the transmission measurement have been performed in the same way as for the measurement with a buffer gas pressure of 1.27 bar. For the lower buffer gas pressure, however, the transmission of the TOF never drops below 85 % for the whole temperature range. The inset of the figure shows the time evolution of the TOF transmission at about 4.4 K for an observation time of almost 15 hours. Over the whole time period, the transmission exhibits only one small drop of about 4 % while it shows a very small but constant upward slope otherwise.

Due to the pronounced evanescent field of the nanofiber waist of a TOF, the transmission properties of the TOF a very sensitive to the surrounding medium and to scatterers on the nanofiber surface. The observed behavior suggests that the cooling of the used buffer gas results in significant changes of the surrounding medium in close proximity to the nanofiber surface where the evanescent field is especially strong. These changes could possibly be induced by the adsorption of buffer gas molecules on the nanofiber surface. A thin film of adsorbed buffer gas molecules might influence the nanofiber-guided light via Brillouin scattering of the guided light from the density waves within the thin film [131]. Here, the

propagation direction of the scattered light forms an angle with original propagation direction of the guided light which is given by the Bragg condition [38, 132]. However, independent of the exact scattering direction, the light would be scattered out of the nanofiber by a possible interaction with density waves in the surface-adsorbed thin film which could explain the observed transmission drop. The adsorption of buffer gas molecules on the nanofiber surface depends strongly on the temperatures of the buffer gas and the nanofiber surface, on the buffer gas pressure, and on the type buffer gas [133]. This could explain the observed behaviour described above.

Another possible explanation could be given by the surface assisted formation of buffer gas clusters, although it is unlikely for such clusters to be big enough to act as serious scatterers in the visible wavelength range. To resolve this issue, the observed effect has to be further investigated. For the measurements presented in this thesis, the buffer gas pressure has been kept low enough to avoid a complete break-down of TOF transmission.

5. In-situ spectroscopy of surface adsorbed molecules

Due to the strong radial confinement of the light field over the whole length of a nanofiber, optical nanofibers are a highly efficient tool for surface absorption and fluorescence spectroscopy, as theoretically discussed in Sec. 3.2. As an experimental demonstration of the numerous effects which can be measured by nanofiber-based surface spectroscopy, various measurements on the model system 3,4,9,10-perylene-tetracarboxylic dianhydride (PTCDA) have been performed.

PTCDA molecules feature a low vapor pressure and a high thermal stability which makes them well suited for molecuar vapor deposition at UHV condition as well as at ambient conditions [134]. These organic molecules are further especially attractive as a model system for sensitivity studies, since they significantly change their spectral properties depending on their arrangement on the surface [135]. The properties of the model system PTCDA will be discussd in detail in the first part of this chapter.

The absorption and fluorescence spectroscopy measurements on ultra-thin molecular layers on the dielectric surface of the nanofiber presented in the second and third part of this chapter reveal the high sensitivity of nanofiber-based surface spectroscopy. The method is used to study surface effects like homogeneous and inhomogeneous broadening, the formation of crystalline films and excimers on the surface, and the interaction of PTCDA molecules with localized surface defects, as well as ensemble effects like self-absorption. Moreover, the collection efficiency of the molecular emission by the guided fiber mode is determined by interlaced measurements of absorption and fluorescence spectra. Parts of this chapter have been published in [66, 112, 120].

Note that all measurements presented in this chapter have been performed with a 320-nanometer diameter nanofiber with a length of 1 mm fabricated from a Nufern 460-HP fiber (molecule fiber, cf. Sec. 2.2.2).

5.1. Model system PTCDA

Perylene-3,4,9,10-tetracarboxylic dianhydride (PTCDA) is an organic dye frequently used as a pigment and for organic semiconductor devices. Due to its many applications, the compound has been studied extensively (cf., e. g., [136]). PTCDA ($C_{24}H_8O_6$) is a perylene derivative and therefore belongs to the rylene homologous series which exhibits large fluorescence quantum yields and high photostabilities [137]. It has a planar structure and consists of two naphthalene ($C_{10}H_8$) units connected at the peri-position and four carboxyl groups as substituents at the 3, 4, 9, and 10 positions. The Lewis structure formula of PTCDA is shown in Fig. 5.1. Taking into account the van der Waals radii of the outer atoms, the molecular dimensions of PTCDA can be estimated as $1.42\,\mathrm{nm} \times 0.92\,\mathrm{nm}$ [138]. As for most organic dye molecules, the optical properties of PTCDA are mainly determined by π-electrons which are highly delocalized along the backbone of the molecule [139]. Therefore, they are basically independent of the outer constituents and similar to the optical properties of perylene and other perylene derivatives. The absorption and fluorescence spectrum of PTCDA dissolved in dichloromethane (DCM, CH_2Cl_2) for the $S_0 \leftrightarrow S_1$ transition at room temperature are shown in Fig. 5.2. The dipole

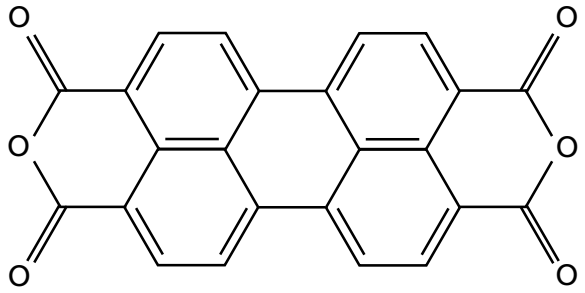

Figure 5.1.: Lewis structure formula of PTCDA.

moment of this transition is oriented along the long molecular axis [140] and has a gas phase value of about 7.4 D as derived from the solution spectra in dimethyl sulfoxide (DMSO, $(CH_3)_2SO$) [141]. The spectra exhibit the typical mirror symmetry which results from Kasha's rule [81] (cf. Sec. 3.1.2) with a Stokes shift of about 40 meV. Due to the fact that for the $S_0 \leftrightarrow S_1$ transition in PTCDA, only a few vibronic modes at close frequencies contribute to the spectrum with significant oscillator strengths [142], the spectrum can be described by coupling to one effective vibronic mode with a spacing of $E_{\text{eff}} \approx 0.17\,\text{eV}$. The $\nu = 0 \rightarrow \nu' = 0$ peak of the absorption spectrum at about 2.4 eV has a molar absorption coefficient of $\varepsilon_{DCM} \approx 7 \cdot 10^4\,\text{l}/(\text{mol} \cdot \text{cm})$. Since the molecules can be randomly orientated within the solution, the absorption can be assumed to be a factor 3 higher for molecules with their transition dipole moment aligned along the electric field vector. Using Eq. (3.10), this yields a peak absorption cross section of $\sigma_{\text{peak}}^{\text{DCM}} = \ln(10)/\text{N}_\text{A} \cdot 3 \cdot \varepsilon(\lambda) \approx 8 \cdot 10^{-16}\,\text{cm}^2$.

The next higher absorption band for PTCDA in DCM at room temperature occurs between approximately 3.35 eV and 3.70 eV and has been attributed to the $S_0 \rightarrow S_3$ transition [140]. It is polarized along the short in-plane axis of the PTCDA molecule and is much weaker than the $S_0 \rightarrow S_1$ transition [141].

The gas phase spectra of PTCDA are not known, but they are expected to largely agree with the fluorescence excitation spectra measured in helium nanodroplets [143]. Indeed, the energy of the $S_0, \nu = 0 \rightarrow S_1, \nu' = 0$ transition in helium nanodroplets has been measured to be about 2.6 eV [143] which is close to the calculated value of about 2.65 eV for an isolated PTCDA molecule [140].

5.1.1. Thin films

PTCDA forms highly ordered layers on a large range of substrates (cf. [136] and references therein). On strongly interacting substrates like silver surfaces (Ag(110)), the PTCDA molecules are arranged in a brickwall structure which is commensurate with the crystal structure of the substrate [144]. On all other substrates, the arrangement on the surface is predominantely determined by the interaction between the PTCDA molecules rather than by the interaction of the molecules with the surface. This is due to the electrostatic interaction of the strong quadrupole moments of the PTCDA molecules [145] and results in an arrangement of the molecules in a herringbone structure. Even for amorphous substrates like glass, it has been shown that PTCDA molecules tend to be deposited parallel to the substrate surface, if cluster formation of the molecules before they reach the substrate surface is prevented [111].

Figure 5.3 shows the monoclinic unit cell of a PTCDA crystal which contains two PTCDA

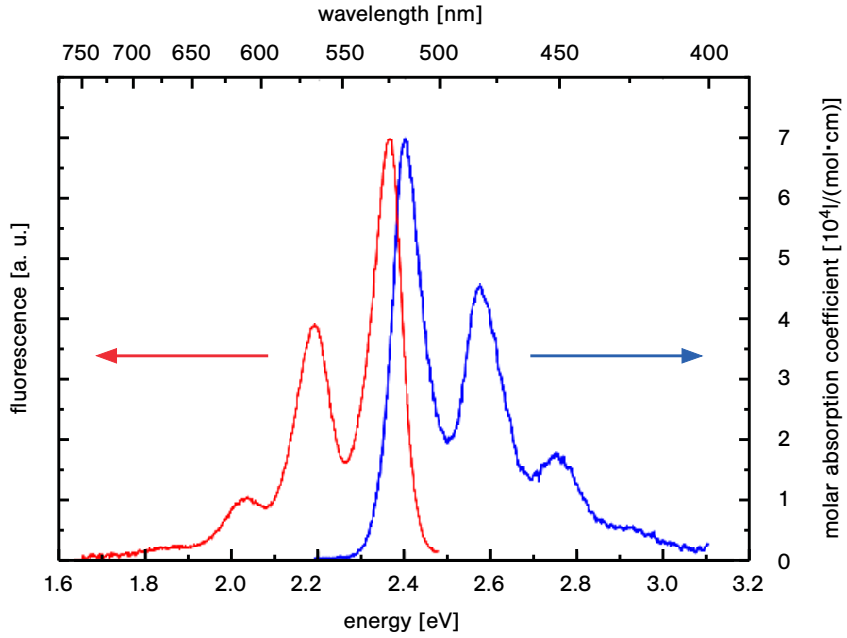

Figure 5.2.: Absorption (blue) and fluorescence (red) spectrum of PTCDA in dichloromethane (DCM) at room temperature, adapted from [28].

molecules. The arrangement in a heringbone structure on the surface occurs parallely to the lattice plane (102) which is indicated in gray in the figure. Due to the small extension of the unit cell along the [001] direction, the crystal layers are closely packed with a separation of only 0.34 nm between the molecular layers [135]. This leads to a strong overlap of the delocalized π electron systems yielding a strong interlayer interaction. Within a molecular plane, however, the separation between the molecules is about 1.2 to 1.5 nm, and the overlap of the electron wavefunctions is much weaker in this direction. Therefore, the intralayer interaction between the PTCDA molecules is very weak resulting in a quasi-one-dimensional crystal structure [135].

Depending on their strength, the interactions within the PTCDA crystal can significantly alter the spectral properties of the system. The relatively weak intralayer interactions do not influence the shape of the optical spectra but only result in a shift of the spectrum to lower energies (redshift) by up to 30 meV [134, 135, 146]. In contrast, interlayer interactions cause a significant modification of the spectral shape. During the formation of physical dimers along the stacking direction, the ratio of the heights of the two lowest energy absorption peaks changes, accompanied by a significant broadening of the spectrum [135]. Further increase of the film thickness results in a strong redshift of the lowest energy peak and a splitting of the broadened second lowest energy peak into two bands [135, 146]. From a surface coverage of four compact monolayers (ML) onwards, the spectral shape stays almost constant up to film thicknesses of at least 100 nm [136]. Even though the spectra of PTCDA in the crystalline phase differ significantly from the monomer spectra, the spectral signature is not destroyed completely because the interactions between the molecules are still much weaker than the intramolecular interactions yielding a similar electronic structure for isolated molecules and molecules in a crystal.

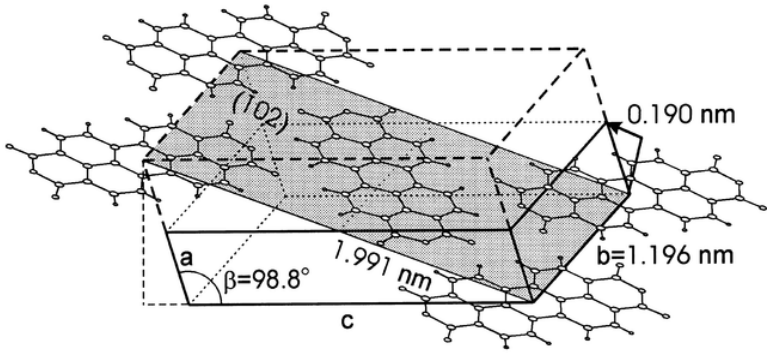

Figure 5.3.: Monoclinic unit cell of a PTCDA crystal with $a = 0.372\,\text{nm}$, $b = 1.196\,\text{nm}$, $c = 1.734\,\text{nm}$ and $\beta = 98.8\,^\circ$ (adapted from [147]).

5.2. Surface absorption spectroscopy

The absorption spectrum of PTCDA molecules adsorbed on the nanofiber surface at room temperature is shown in Fig. 5.4. It has been measured via the mode of the nanofiber using the simple optical setup described in Sec. 2.1.2 with an effective spectral resolution of 6 nm. The power coupled into the TOF from the white light source of about 3 nW within the spectral interval between 400 and 600 nm is low enough not to saturate the molecules. For the determination of the molecular absorbance, a reference spectrum is recorded before deposition. The measurement has been performed under ultra-high vacuum conditions provided by the vacuum chamber introduced in Sec. 4.3. For comparison, the absorption spectrum of PTCDA dissolved in DCM at room temperature from Fig. 5.2 is shown in blue in Fig. 5.4. The surface absorption spectrum exhibits the same vibronic progression as the solution spectrum with a spacing of approximately 0.17 eV. However, it is shifted by about 10 meV and broadened with respect to the solution spectrum. This suggests that the interaction of the molecules with the fiber surface is more inhomogeneous but slightly weaker than their interaction with DCM, as discussed in Sec. 3.1.3.

The number N of molecules covering the nanofiber surface can be determined from the measured peak value of the total sample absorption cross section of $\sigma_{\text{peak}}^{\text{tot}} \approx 14.4 \times 10^{-9}\,\text{cm}^2$ via division by the peak absorption cross section $\sigma_{\text{peak}}^{\text{DCM}} \approx 8 \cdot 10^{-16}\,\text{cm}^2$ measured in DCM. Since the molecules can be assumed to be orientated randomly within the surface plane (cf. Sec. 3.2.1), on average, only half of the molecules have a transition dipole moment aligned along the electric field vector yielding

$$N \approx 2 \cdot \frac{\sigma_{\text{peak}}^{\text{tot}}}{\sigma_{\text{peak}}^{\text{DCM}}}. \tag{5.1}$$

Therefore, it can be deduced that the nanofiber surface is covered by approximately 36 million PTCDA molecules.

This corresponds to a surface coverage of $\Theta = N/(\pi d L) \approx 3.6 \cdot 10^{12}\,\text{cm}^{-2}$ for the nanofiber parameters used here. From the values given in Fig. 5.3, the area in the lattice plane (102) which is occupied by the two PTCDA molecules in the monoclinic unit cell of the PTCDA crystal can be determined to be about $2.4 \cdot 10^{-14}\,\text{cm}^2$. A surface coverage of $\Theta = 3.5 \cdot 10^{12}\,\text{cm}^{-2}$ therefore corresponds to 4.3 % of a compact monolayer.

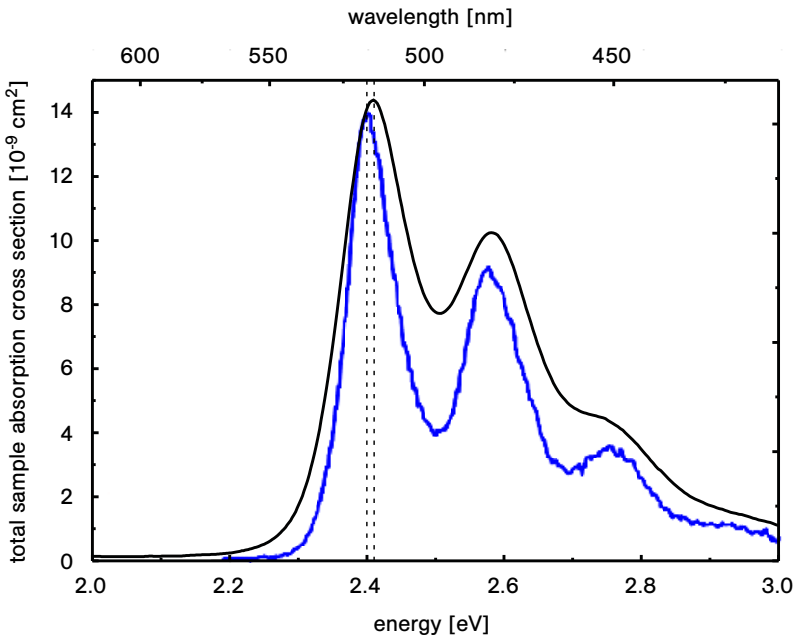

Figure 5.4.: Absorption spectrum of an ultra-thin layer of PTCDA molecules adsorbed on a nanofiber surface at room temperature and under UHV conditions (black line). The solution spectrum from Fig. 5.2 is shown in blue for comparison. The dashed lines mark the absorbance maximum of each spectrum in order to illustrate the shift of the surface spectrum by about 10 meV with respect to the solution spectrum.

Since the surface absorption spectrum is broadened with respect to the solution spectrum, the same peak absorbance corresponds to a higher oscillator strength in the case of the surface absorbance spectra. Therefore, the values determined above are only a lower bound for the molecule number and the resulting surface coverage. However, the broadening is small enough to lead to a change determined by a factor on the order of 1 which still yields the above values to be a good estimate.

It has been shown in earlier work that surface coverages as low as 0.12 % [27] or even 0.02 % [120] can be resolved by nanofiber-based surface absorption spectroscopy. The corresponding sensitivity is more than two orders of magnitude higher than the sensitivity reported for, e. g., differential reflectance spectroscopy [146].

5.2.1. Temperature dependence of surface absorption spectra

Since in the vacuum setup, the nanofiber in the sample chamber is well seperated from the K-cell in the oven chamber (cf. Sec. 4.3), the nanofiber is not heated up during deposition of the PTCDA molecules but stays at a constant temperature of approximately room temperature. If, however, the molecules are deposited onto the nanofiber at ambient conditions, the crucible used for evaporating the molecules is placed directly underneath the nanofiber waist of the TOF, yielding a nanofiber temperature which depends on the heating current as discussed in Sec. 4.2.

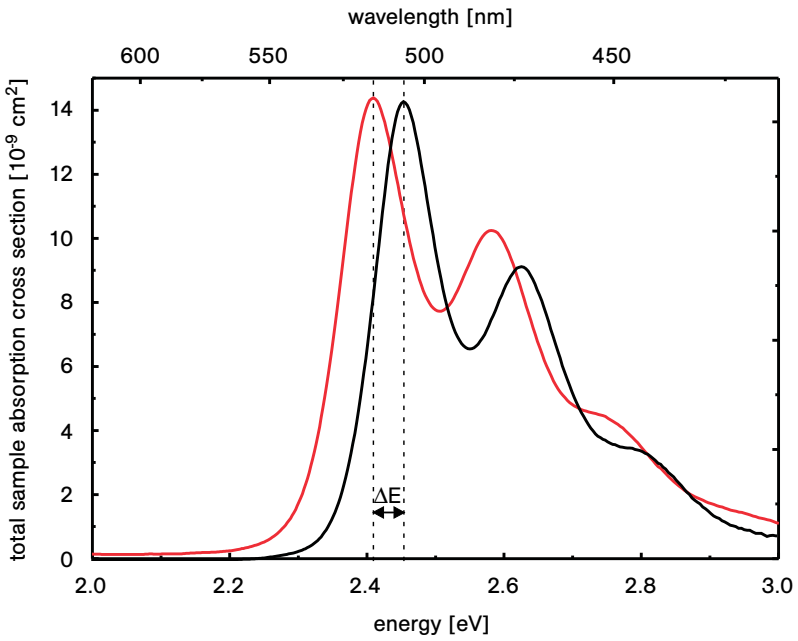

Figure 5.5.: Absorption spectrum of an ultra-thin layer of PTCDA molecules adsorbed on a nanofiber surface at ambient conditions (black line). The nanofiber is heated by the crucible used for evaporating the molecules causing a shift of the spectrum by $\Delta E \approx 47\,\text{meV}$ with respect to the room temperature spectrum from Fig. 5.4 shown in red. The dashed lines mark the absorbance maximum of each spectrum in order to illustrate this shift.

Figure 5.5 shows an absorption spectrum of surface adsorbed PTCDA molecules measured at ambient conditions, with a heating current of 2.35 A which corresponds to a nanofiber temperature of roughly 110 °C as discussed in Sec. 4.2.1. It exhibits the same vibronic progression as the spectrum measured with the vacuum setup (Fig. 5.4) which is shown in red for comparison. However, the maxima are shifted by $\Delta E \approx 47\,\text{meV}$ to higher energies. This blue shift originates from the fact that the PTCDA molecules experience a different solvent shift at ambient conditions as compared to UHV conditions (cf. Sec. 3.1.3). A blue shift with increasing temperature has already been observed for thin film spectra of PTCDA by V. Bulović and co-workers and can be attributed to the redistribution of occupied phonon levels [148].

The influence of the surface temperature on the absorption band width is studied in detail by changing the temperature of the nanofiber surface via the crucible heating current. For this purpose, PTCDA molecules are deposited onto the nanofiber surface with a heating current of 2.35 A in three consecutive measurements. In each measurement, the current is reduced to a value between 1.6 and 2.0 A after 150 s of deposition in order to stop the deposition of PTCDA molecules and reach an equilibrium state. Note that the deposition is only reduced to a negligible rate if the heating current is 2.0 A or lower. At the same time, for heating currents lower than 1.6 A, the absorption spectra are not stable due to the adsorption of water on the nanofiber surface as discussed in Sec. 5.2.2 below.

Table 5.1 shows the width (FWHM) of the strongest absorption band for four different heating currents of the crucible as obtained from Gaussian fits to the spectra. The values for

heating current [A]	temperature [°C]	FWHM [meV]
1.6	47.6 ± 0.1	114.0 ± 0.2
1.8	53.8 ± 0.3	114.7 ± 0.6
2	74.7 ± 0.4	117.3 ± 0.1
2.35	110.3 ± 1.4	121.9 ± 0.8

Table 5.1.: Temperature dependent width of the strongest absorption band of PTCDA molecules adsorbed on a nanofiber surface.

heating currents of 1.6, 1.8, and 2.0 A have been averaged over the values from five consecutive spectra after 250 s of thermalization of the nanonfiber. For the heating current of 2.35 A, the given value is the mean of six values obtained during deposition for the three measurements, two values from each measurement. The temperature values are taken from the measurement presented in Sec. 4.2.1.

As discussed in Sec. 3.1.3, the standard deviation σ of the mean phononic energy of the system is given by $k_B T$, yielding a width (FWHM) of the molecular transition of $w = \sigma \cdot \sqrt{8 \ln 2} = k_B T \cdot \sqrt{8 \ln 2}$. As expected from this relation, the width listed in Tab. 5.1 increases with increasing temperature. However, the increase is not proportional to the temperature increase. This is due to the fact that the strongest absorption band of PTCDA does not consist of a single transition. The PTCDA spectrum exhibits an effective vibronic progression which originates from the Gaussian convolution of a more complex energy structure [143]. The derivation of the width of the resulting absorption bands as a function of temperature can be found in Appendix B.1 and will not be explicitly given here.

Assuming that the homogeneous width of each spectral line contributing to an absorption band is dominated by the thermal excitation of phonons ($\sigma_{\mathrm{hom}} = k_B T$), Eq. (B.6) for the squared $1/e$-width of the absorption band can be simplified to:

$$\sigma_{\mathrm{tot}}^2 = k_B^2 T^2 + C, \tag{5.2}$$

where $k_B^2 T^2$ accounts for the homogeneous broadening of each individual transition, and the temperature independent paramter C sums up the influence of the inhomogeneous broadening as well as the spectral position and relative strength of the individual transitions contributing to the specific absorption band.

The squared $1/e$-width of the strongest absorption band of PTCDA adsorbed on the nanofiber surface is plotted in Fig. 5.6 as a function of the squared temperature of the nanofiber (data points). The red line shows a linear fit to the data which yields an intercept of $1570 \pm 6\,\mathrm{meV}^2$. The slope of $(7.55 \pm 0.05) \times 10^{-9}\,\mathrm{eV}^2/\mathrm{K}^2$ agrees well with the expected value of the squared Boltzmann constant of $k_B^2 \approx 7.44 \times 10^{-9}\,\mathrm{eV}^2/\mathrm{K}^2$.

5.2.2. Mobility of surface-adsorbed molecules

Due to the high sensitivity of nanofiber-based surface spectroscopy, dynamic processes involving the adsorbed molecules on a seconds to minutes time scale can readily be studied with this method. On a weakly interacting surface like the glass nanofiber surface, the thermal energy of adsorbed molecules at room temperature is sufficient to enable a certain mobility of the molecules on the surface [134]. As discussed in Sec. 5.1, this mobility allows PTCDA molecules to form crystalline films on the surface which yields significantly altered spectral

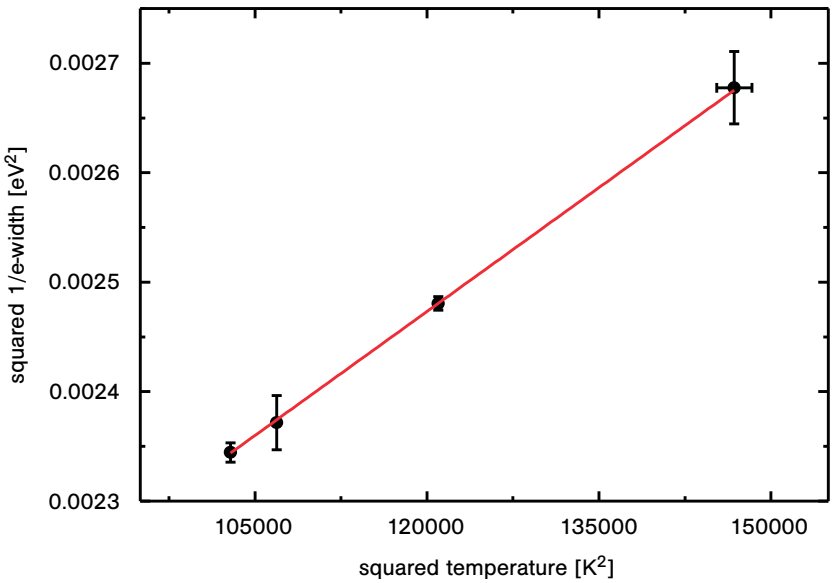

Figure 5.6.: Squared $1/e$-width of the strongest absorption band of an ultra-thin layer of PTCDA molecules adsorbed on a nanofiber surface. The black data points have been calculated from the width given in Tab. 5.1 and the red line is a linear fit to the data with a slope of $(7.55 \pm 0.05) \times 10^{-9}\,\mathrm{eV}^2/\mathrm{K}^2 \approx k_B^2$.

properties of the system. Moreover, the reorganization of the molecules on the surface leads to an increased interaction of the molecules with localized surface defects of the nanofiber, which can also be captured by the resulting spectral signature.

Agglomeration

Agglomeration of PTCDA molecules on the nanofiber surface leads to the formation of a crystalline film, which can be observed by the accompanying change in the spectral properties. Figure 5.7 shows absorption spectra measured during the ripening of the film after the molecular deposition has been stopped and the nanofiber surface has thermalized back to room temperature. In order to accelerate the thermalization from typically a few hundred seconds (cf. Sec. 4.2.1) to below one minute, the heated crucible has been removed from underneath the nanofiber instantly after the deposition has been stopped. Once the nanofiber has thermalized to room temperature, a continuous change of the shape of the spectra can be observed. It exhibits the change of the height ratio of the lowest energy absorption peaks and the accompanying broadening characteristic for the formation of stacked dimers. At the beginning of this process (up to 23 min), the absorbance remains constant at the energies of about 2.34 eV and 2.67 eV. These so-called isosbestic points result from the fact that, at these energies, the monomer and the dimer phase of PTCDA have the same molar absorptivity. This observation thus indicates that the total number of molecules remains nearly constant during the ripening. For times larger than 23 min, the absorbance at the isosbestic points starts to deviate from the value determined by the monomeric and dimeric contributions, indicating the formation of higher oligomers on the nanofiber surface. Details about the ripening process of PTCDA on a nanofiber surface at ambient conditions can be found in [27, 67].

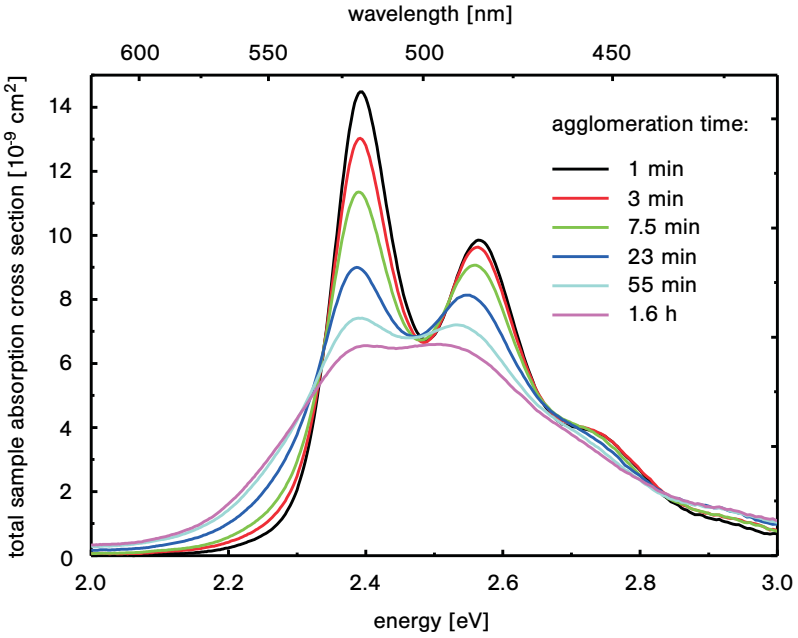

Figure 5.7.: Time evolution of the spectral absorption of a constant number of PTCDA molecules adsorbed on the nanofiber surface at ambient conditions. The agglomeration of the molecules from isolated monomers to a crystalline film is clearly visible.

Reordering of monomeric PTCDA molecules to a crystalline film at ambient conditions has also been observed on a mica surface [146]. However, the agglomeration process was not resolved in time. This reordering is attributed to a film of adsorbed water on the surface which increases the mobility of the PTCDA molecules and thus catalyzes their reordering. The surface coverage θ of water adsorbed from the atmospheric moisture to a surface can be derived from the Langmuir equation [133, 149]:

$$\theta = \frac{Np}{\sqrt{2\pi MRT_{\text{air}}}}\tau_0 exp\left[\frac{E_a}{k_B T_{\text{surf}}}\right], \tag{5.3}$$

where N is Avogadro's number, M the molecular mass of water, R the universal gas constant, k_B the Boltzmann constant, and τ_0 the water molecule–wall collision time. The thickness of the film of adsorbed water is therefore determined by the partial pressure p of water vapor in the surrounding air, the absolute temperature T_{air} of the surrounding air, the absolute temperature T_{surf} of the surface, and the adsorption energy E_a of water on the surface. For a thermalized system, the temperatures T_{air} and T_{surf} of the surrounding air and the surface can be assumed to be equal. For nanofiber-adsorbed molecules, this results in an increased mobility for high water vapor concentrations, high water adsorption energies of the surface, and low temperatures.

The effect of reduced water vapor concentration in the surroundings of the nanofiber can best be studied in an UHV environment. Hence, the agglomeration of surface-adsorbed PTCDA molecules has been studied using the vaccum setup presented in Sec. 4.3. The absorption spectra measured during the reordering process at a background pressure of about $1 \cdot 10^{-8}$ mbar are displayed in Fig. 5.8. The molecular deposition has been stopped at about

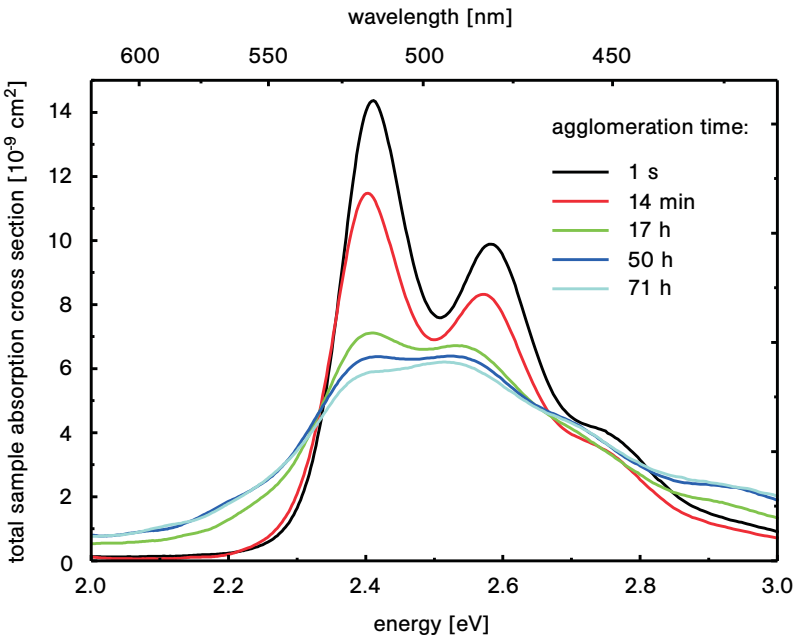

Figure 5.8.: Time evolution of the spectral absorption of a constant number of PTCDA molecules adsorbed on the nanofiber surface at UHV conditions and room temperature. The agglomeration process is slowed down due to the much lower concentration of water vapor in the surroundings of the nanofiber as compared to ambient conditions.

the same surface coverage as for the measurements at ambient conditions shown in Fig. 5.7, and a nanofiber with the same geometry has been used. Qualitatively, the agglomeration process at UHV conditions shows the same dynamics as the process at ambient conditions. It is, however, slowed down by about two orders of magnitude due to the much lower atmospheric moisture at UHV conditions as compared to ambient conditions. At pressures as low as $1 \cdot 10^{-8}$ mbar, the partial pressure of water vapor in the vacuum setup can be assumed to be negligible. Thus, the agglomeration dynamics are dominated by the uncatalyzed mobility of the molecules due to their thermal energy resulting in a total agglomeration time of several days instead of a few hours.

The adsorption energy E_a of water on the surface is determined by the properties of the nanofiber surface. The main contributions to the surface properties are the material properties of the silica glass and the nanofiber geometry which are very similar for every nanofiber. However, the adsorption energy can differ from nanofiber to nanofiber due to random effects like slight radius variations, contaminations on the surface or a varying surface roughness. Figure 5.9 shows the agglomeration behavior for a different nanofiber than the one used for the measurements presented in Fig. 5.7. The nanofiber has the same geometry as the one used for the measurements at ambient conditions shown in Fig. 5.7. The spectra displayed in Fig. 5.9(a) are measured during the reordering of PTCDA molecules on the surface of this nanofiber at ambient conditions and room temperature. In contrast to the measurement presented in Fig. 5.7, the heated crucible has not been removed from underneath the nanofiber after the deposition has been stopped, but the heating current has been reduced to 0.0 A. Consequently, the nanofiber has not yet thermalized back to room temperature after one

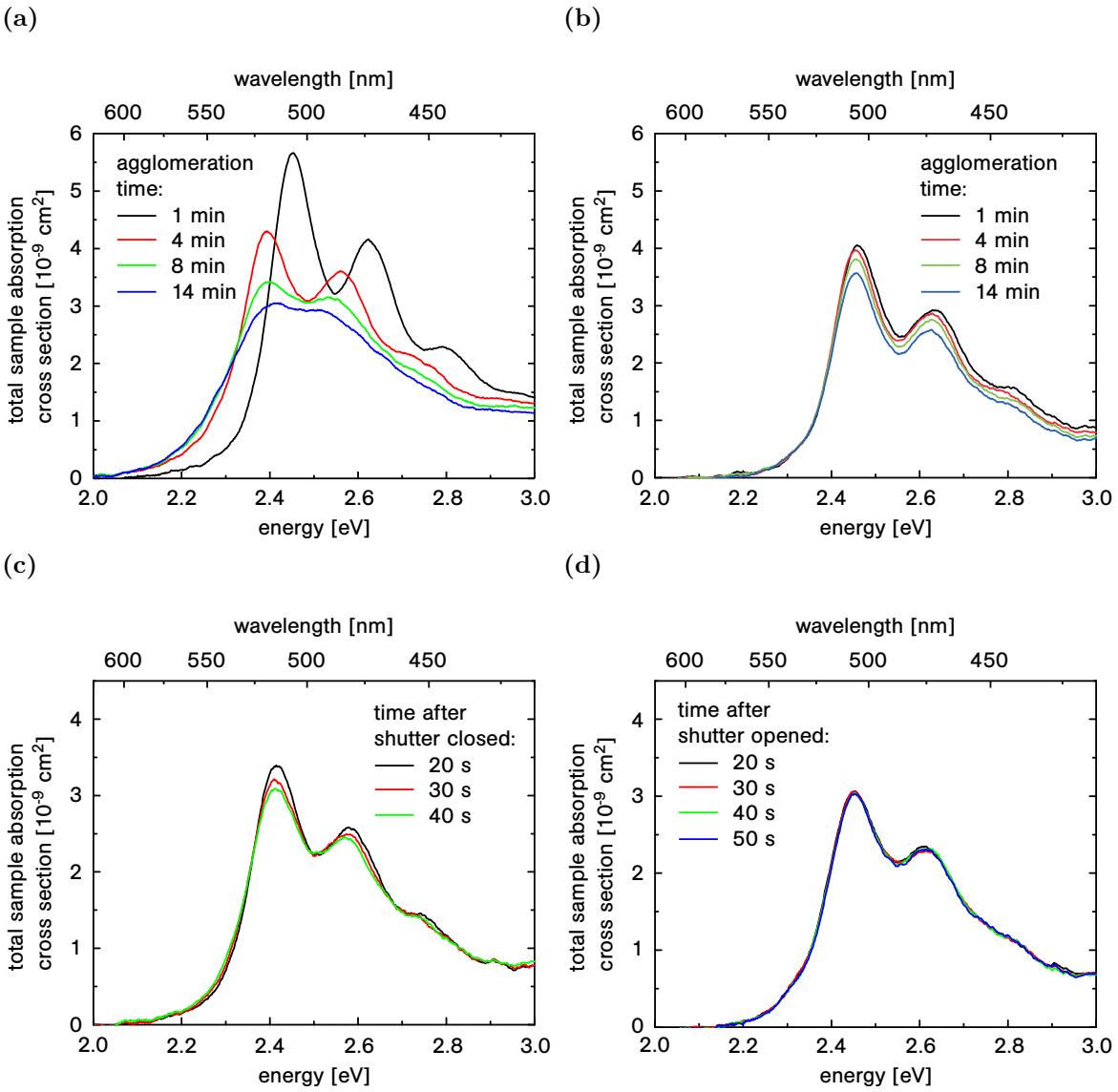

Figure 5.9.: Time evolution of the spectral absorption during the agglomeration of PTCDA molecules adsorbed on the surface of one specific nanofiber at ambient conditions. After the deposition of molecules, the nanofiber and the surrounding air is cooled down to (a) room temperature and (b) 50 °C. At higher nanofiber tempeartures, the adsorption of atmosheric moisture on the nanofiber surface is reduced, causing a much slower agglomeration process. By rotating an aluminum shutter underneath the nanofiber (closed), the agglomeration process is (c) accelerated as compared to the situation where the shutter is (d) removed (opened) again.

minute and, as a result, the first spectrum taken after one minute of agglomeration exhibits a small blue shift compared to the room temperature spectrum. Moreover, the reordering process is accelerated by about one order of magnitude as compared to the measurement presented in Fig. 5.7. This can be caused by both, a higher water vapor concentration in the air surrounding the nanofiber, which contributes linearly to the thickness of the water film on the surface, or a slightly different nanofiber surface, which can favor the surface-adsorption of water via the exponential influence of the adsorption energy.

The influence of the nanofiber surface temperature and, therefore, the temperature of the surrounding air is studied in a subsequent measurement using the same nanofiber as for the measurements shown in Fig. 5.9(a). For this purpose, the heating current of the crucible has been reduced to 1.8 A instead of 0.0 A after the deposition has been stopped. As discussed in Sec. 4.2.1, this yields a nanofiber and air temperature of approximately 50 °C after thermalization which leads to a weaker adsorption of atmosheric moisture on the nanofiber surface according to Eq. (5.3). The spectral signature of the reordering process at about 50 °C is displayed in Fig. 5.9(b). The molecular deposition has been stopped after the same time as for the measurements shown in Fig. 5.9(a), yielding a very similar initial surface coverage for both measurements. In contrast to the agglomeration process at room temperature, the shape of the absorption spectrum hardly changes for the first 14 minutes if the temperature is kept at 50 °C. The slight decrease of the absorption at all energies simultaneously can be attributed to a gradual desorption of molecules from the nanofiber surface. Note that, in a separate measurement, it has been shown that a heating current of 1.8 A yields a deposition rate of molecules onto the nanofiber waist which is smaller than the desorption rate of molecules from the fiber surface. The same has been observed for heating currents of 1.6 A and 2.0 A. Therefore, these heating currents can be used to heat the nanofiber without significantly changing the surface coverage by PTCDA molecules.

After about 14 minutes, the aluminum shutter is rotated between the crucible and the nanofiber, thereby instantaneously reducing the temperature of the nanofiber due to the interrupted airflow from the hot crucible to the nanofiber, as shown in Fig. 4.6(b). Figure 5.9(c) displays the evolution of the spectral absorption after the shutter has been closed and the spectrum has shifted slightly to lower energies as a result of the reduced temperature of the nanofiber. Even during the short period of time that the shutter is closed, a change of the height ratio of the lowest energy absorption peaks and a slight broadening is clearly visible, indicating the formation of stacked dimers. After 50 s, the shutter is opened again, resulting in a rise of temperature and an accompanying shift of the absorption spectrum to higher energies. Moreover, the continuous change of the spectral shape observed while the shutter is closed is slowed down to an extend where it is not visible anymore during the observation time of about one minute, as shown in Fig. 5.9(d).

The measurements presented in Fig. 5.9 suggest that the temperature of nanaofiber and surrounding air significantly influences the amount of water adsorbed on the nanofiber surface and, therefore, also the catalyzing effect of the water on the reordering of the surface adsorbed molecules. In particular, the influence of the reduced water film on the surface is much stronger than the effect of the increased thermal energy at higher temperatures which also yields an increased mobility.

Charge-transfer complex

In addition to the increased interaction between PTCDA molecules on the nanofiber surface, the mobility of the molecules on the nanofiber surface can also yield an increased interaction with localized surface effects. Figure 5.10 shows the time evolution of the spectral absorption from the measurement at UHV conditions and room temperature presented in Fig. 5.8 for an extended spectral range and the first 48 minutes after the deposition has been stopped. While the main spectrum between 2.2 and 3.0 eV changes continously from monomer to dimer spectrum, an additional spectral feature appears between 1.7 and 2.0 eV. As shown in the inset, this additional spectral feature exhibits an internal structure with maxima at

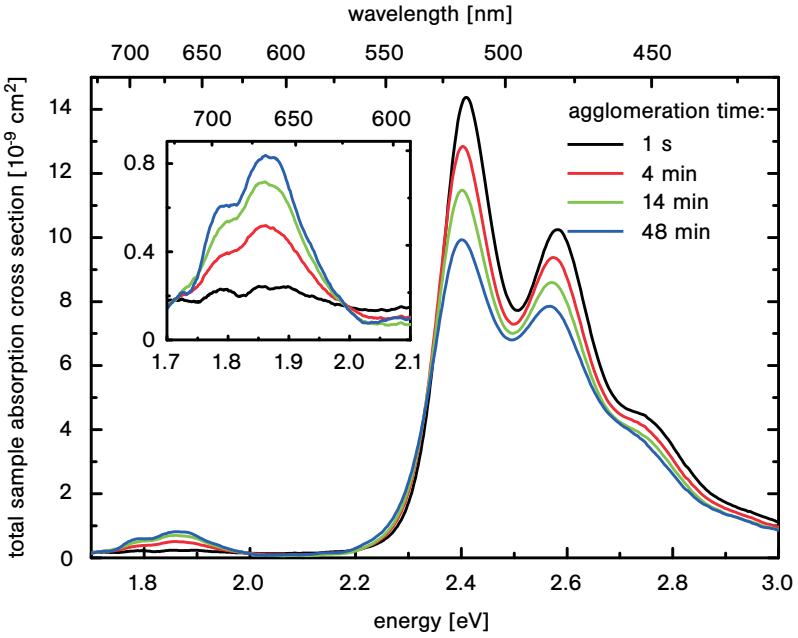

Figure 5.10.: Time evolution of the spectral absorption from the measurement at UHV conditions and room temperature presented in Fig. 5.8 for an extended spectral range, including the spectral signature of a charge-transfer complex between 1.7 and 2.0 eV. The inset shows a magnification of this spectral feature, revealing its internal structure.

around 1.79, 1.85, and 1.89 eV. This spectral signature has already been observed by Bulović et al. for PTCDA dissolved in N-methylpyrrolidone (NMP) [148] and by Proehl et al. for PTCDA molecules adsorbed on a mica surface [146]. In these previous works, it was attributed to a charge-transfer (CT) complex arising from interactions of PTCDA molecules with the highly polar solvent molecules and mica surface, respectively. It can be shown by quantum chemical calculations that the observed spectral signature is compatible with the transition energies of the PTCDA anion (2.02 eV) as well as the cation (1.68 eV) [28]. Due to the strong electronegativity of the oxygen atoms in the carbonyl groups of PTCDA molecules, however, the existance of partially negatively charged $\mathrm{PTCDA}^{-\delta}$ is much more likely [136]. These cations result from the interaction of the adsorbed PTCDA moelcules with a large number of ionic O^{-} ions on the surface [28].

In contrast to mica, a glass surface does not exhibit a large number of ionic molecules. It is typically fully hydroxylated by silanol groups which results in a much weaker polarity [150]. However, similar to pure silicon, localized defects can occur where the surface atoms are not terminated leaving an unpaired electron [151]. These defects are referred to as immobilized free radicals or dangling bonds. They can accept electrons and thus become negatively charged [152]. The interaction of surface adsorbed PTCDA molecules with these localized dangling bonds might thus result in a charge-transfer complex yielding the observed spectral signature.

As shown in Fig. 5.10, the absorption signal of the CT complex increases with agglomeration time. This might be explained by the thermal movement of PTCDA molecules on the fiber surfaces which can cause an increasing number of molecules to couple to dangling bonds

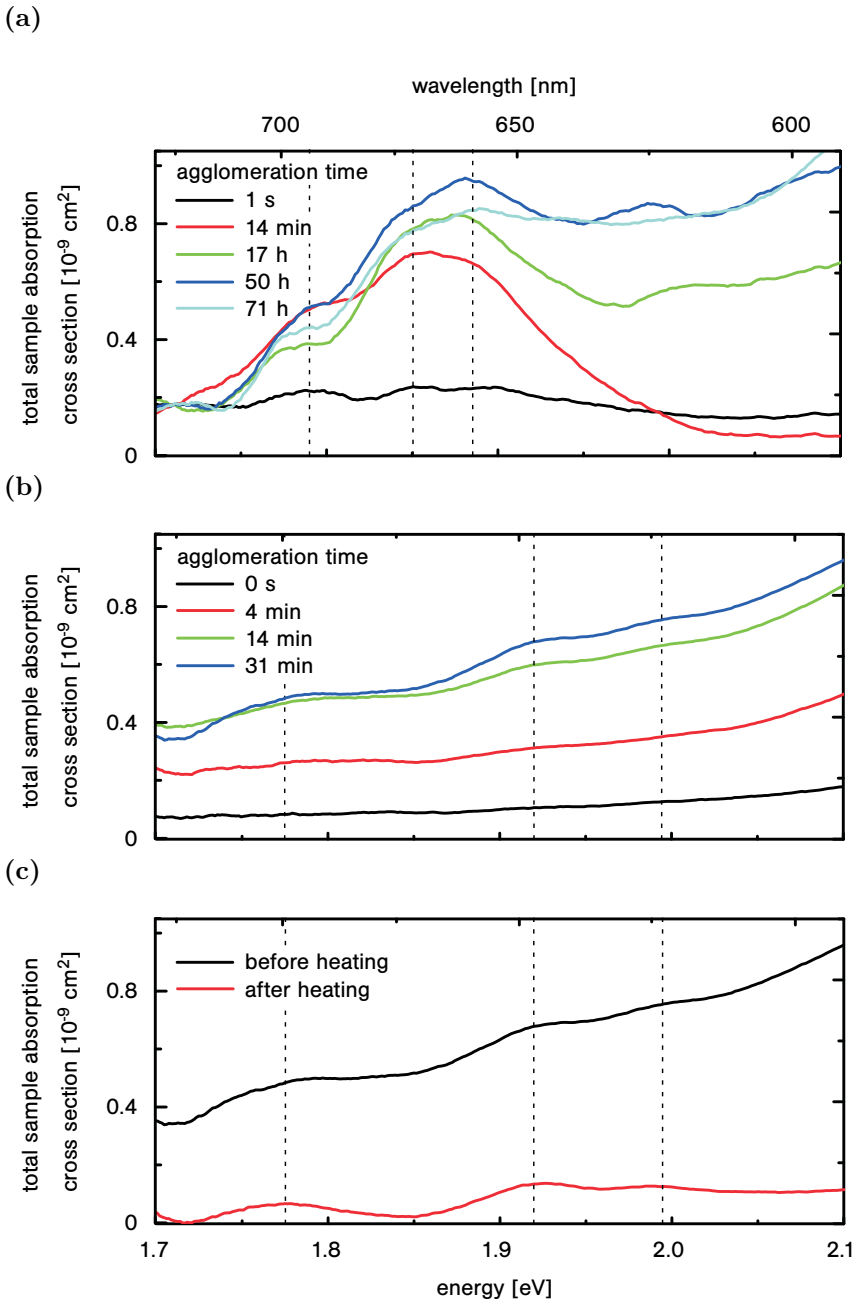

Figure 5.11.: Behavior of the spectral absorption caused by the charge-transfer at (a) UHV conditions, (b) ambient conditions, and (c) after heating of the nanofiber at ambient condition to 300 °C. The black line in (c) corresponds to the blue line in (b).

and to form charge-transfer complexes. However, it can be seen from Fig. 5.11(a) that the absorption signal of the CT complex saturates for longer agglomeration times on the order of days. This can be attributed to the limited number of dangling bonds on the nanofiber surface which can couple to adsorbed PTCDA molecules and form CT complexes. It can further be assumed that the interaction between PTCDA molecules and dangling bonds on the nanofiber surface is strong enough to capture the molecules at the position of the localized surface effects. Note that the shape of the spectral signature is significantly influenced by the broadening of the main spectrum for the shown agglomeration times of 17 hours and more.

Figure 5.11(b) shows the time evolution of the charge-transfer complex signature at ambient conditions as compared to UHV conditions displayed in Fig. 5.11(a). All shown spectra have been recorded after the deposition of approximately the same number of PTCDA molecules onto the nanofiber surface. Since at ambient conditions the mobility of the molecules on the surface is increased by about two orders of magnitude as compared to UHV conditions, the shape of the CT complex signature is already influenced by the broadening of the main spectrum after 4 minutes of agglomeration time. However, the signal strength is much weaker as compared to the measurement at UHV conditions. This suggests a signifiant influence of surface-adsorbed water on the number of immobilized free radicals on the nanofiber surface. A similar effect has also been observed for the surface charge distribution of mica surfaces which have not been heated before deposition of PTCDA molecules [28]. Moreover, the spectral signature of the CT complex exhibits a slightly different structure as compared to the vacuum spectra with maxima shifted by some ten millielectronvolts. A possible explanation for this shift is a different charge state of the surface at ambient conditions yielding a changed spectral signature. Further investigations of the exact shape of the CT complex spectral signature can therefore give deeper insight into the properties of the nanofiber surface under different conditions.

The assumption that the interaction between PTCDA molecules and dangling bonds on the nanofiber surface is strong enough to capture the molecules at the position of the localized surface effects can be further supported by heating the nanofiber surface with the filament described in Sec. 4.2. Figure 5.11(c) displays the CT complex spectral signature before and after heating the nanofiber to about 300 °C with a filament current of about 3.0 A. While the neutral PTCDA molecules are desorbed from the nanofiber surface at this temperature causing the main spectrum to dissappear, the spectral signature of the CT complex is still visible after heating. This suggests that the binding energy of the CT complex is much higher than the binding energy of neutral PTCDA molecules to the nanofiber surface.

5.3. Fluorescence of surface-adsorbed molecules

Figure 5.12 displays a series of fluorescence spectra of PTCDA molecules adsorbed on the nanofiber surface, recorded during the deposition at ambient conditions with a heating current of 2.35 A which heats the nanofiber to roughly 110 °C, as discussed in Sec. 4.2.1. The spectra have been measured at the fiber output using the optical setup described in Sec. 4.1 which provides an effective spectral resolution of 6 nm. All shown fluorescence spectra have been corrected for the wavelength dependent coupling to the fiber mode and for the spectral response of the setup shown in Fig. 4.4(a). For excitation, a power of about 8 µW of laser light transmitted through the nanofiber at 406 nm has been used. Since the excitation wavelength corresponds to the high energy edge of the absorption spectrum, the absorption cross section at this wavelength is reduced by a factor of about 20 in comparison to the cross

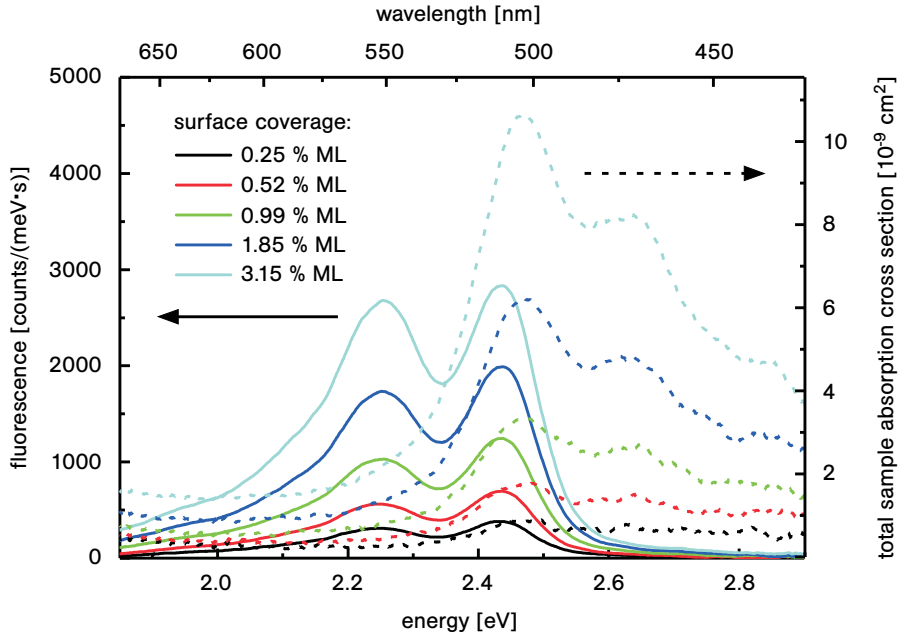

Figure 5.12.: Fluorescence (left) and corresponding absorption (right) spectra of surface-adsorbed PTCDA molecules during deposition at ambient conditions. Five representative spectra within a range of surface coverages between 0.25 and 3.15 % ML are shown.

section in the absorption maximum. Hence, the excitation power is low enough not to saturate the molecules which ensures a linear relationship between the fluorescence signal and the excitation power.

In order to determine the surface coverages underlying the measured fluorescence spectra, absorption spectra have been recorded alternatingly with the fluorescence spectra as described in Sec. 4.1. The absorption spectra shown in Fig. 5.12 are the mean of two consecutive spectra, one recorded 420 ms before and the other 420 ms after the corresponding fluorescence spectrum. Within this time interval, the deposition rate remains roughly constant, thus rendering the average a good estimate for the absorption spectrum actually corresponding to the shown fluorescence spectrum. Note that the signal to noise ratio of the shown absorption spectra is worse than for the spectra presented in Sec. 5.2 because, for the measurements presented here, the white light is coupled into the spectrometer via the entrance slit instead of using the FC fiber adapter. This yields a coupling efficiency which is about one order of magnitude smaller (cf. Sec. 4.1.5).

Using Eq. (5.1), the measured peak values for the total sample absorption cross section ranging from 0.84 to $10.7 \times 10^{-9}\,\mathrm{cm}^2$ correspond to about 2 to 27 million molecules covering the nanofiber surface. This corresponds to surface coverages between $2.1 \cdot 10^{11}\,\mathrm{cm}^{-2}$ and $2.7 \cdot 10^{12}\,\mathrm{cm}^{-2}$ or between 0.25 % and 3.2 % of a compact monolayer (ML) of flat lying PTCDA molecules arranged in the herringbone structure of the (102) plane of the PTCDA crystal. With respect to the luminescence spectra of perrylene derivatives at room temperature reported in [153], the smallest surface coverage for which spectra could be detected is about two orders of magnitude smaller for nanofiber-based surface spectroscopy.

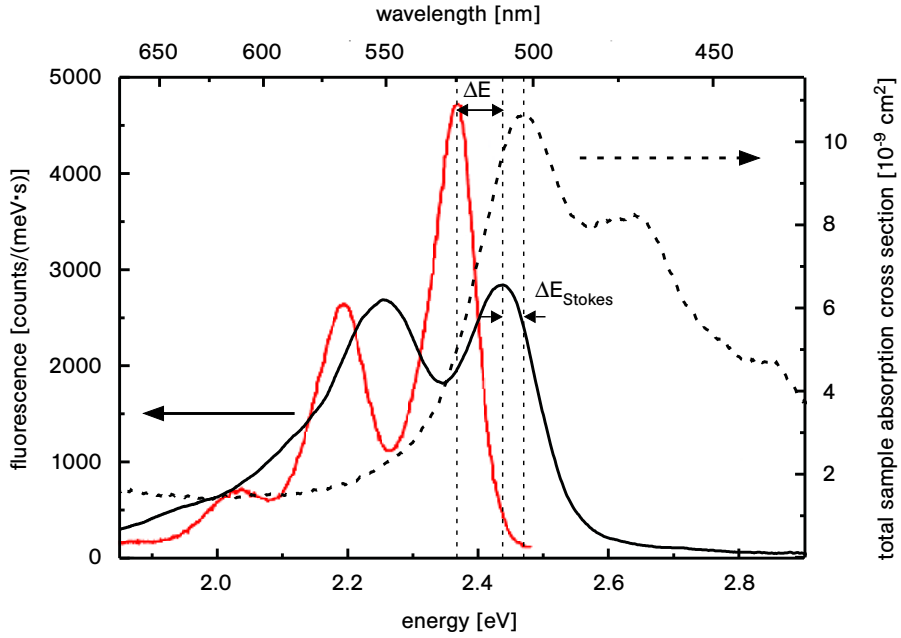

Figure 5.13.: Comparison of the fluorescence spectrum for a surface coverage of 3.15 % ML from Fig. 5.12 (black) with the solution spectrum from Fig. 5.2 (red). The corresponding absorption spectrum (dashed) is shown for complementary information. The dashed lines mark the fluorescence/absorbance maximum of each spectrum in order to illustrate the shift of the surface spectrum by $\Delta E \approx 75\,\mathrm{meV}$ with respect to the solution spectrum and the Stokes shift of the fluorescence $\Delta E_{\mathrm{Stokes}} \approx 35\,\mathrm{meV}$.

The spectral shape of the measured fluorescence is determined by the nanofiber temperature as well as by the mulitple interaction of the nanofiber-guided fluorescence light with the surface-adsorbed molecules as discussed in Sec. 3.2.2.

Figure 5.13 shows a comparison of the fluorescence spectrum for a surface coverage of 3.15 % ML with the fluorescence spectrum of PTCDA dissolved in DCM at room temperature from Fig. 5.2. The fluorescence spectrum of surface adsorbed molecules exhibits the same vibronic progression as the solution spectrum with a spacing of approximately 0.17 eV. It is further shifted by about $\Delta E \approx 75\,\mathrm{meV}$ to higher energies and broadened with respect to the solution spectrum due to interactions of the molecules with the nanofiber surface. The absorption spectrum corresponding to the nanofiber-based fluorescence spectrum exhibits a comparable blue shift with respect to the absorption spectrum of PTCDA dissolved in DCM at room temperature. This shift is larger than the one found in pure absorption spectroscopy measurements at ambient conditions as shown in Fig. 5.5 (approx. 60 meV) which can be attributed to additional heating of the nanofiber by the laser light. The Stokes shift of the fluorescence of approximately 35 meV is slightly smaller than the one measured in solution, which indicates a weaker polarization effect of the molecular dipole moment on the environment for the nanofiber surface as compared to DCM.

According to the considerations discussed in Sec. 3.2.2, the fluorescence signal measured at the fiber output can be approximated by the sum of two contributions, the primary fluorescence signal exiting the fiber output and the reemission signal exiting the fiber output

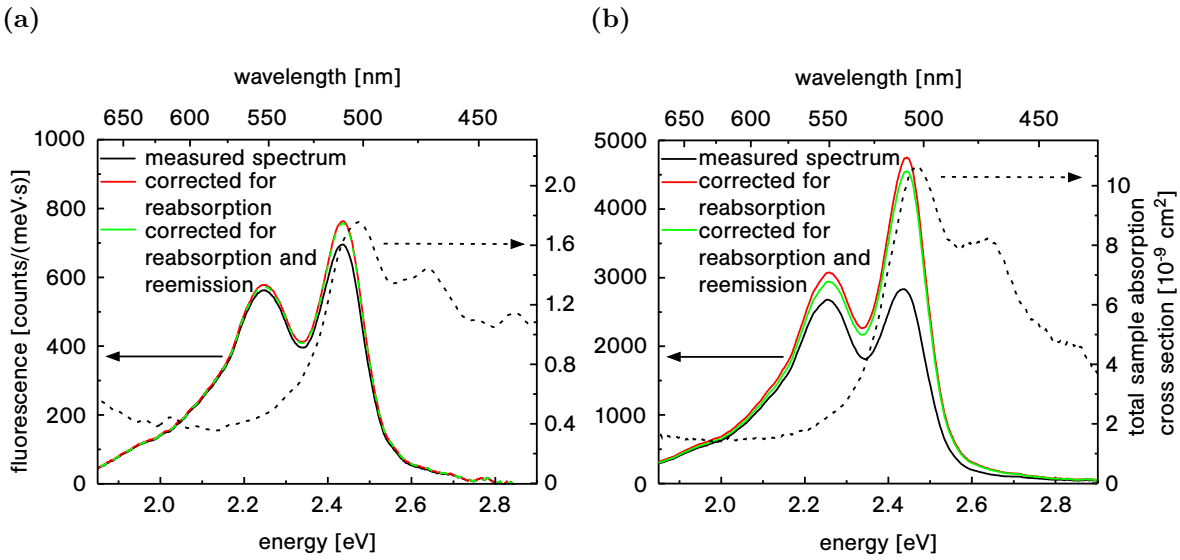

Figure 5.14.: Influence of the self-absorption effect on the measured fluorescence signal for (a) 0.52 % and (b) 3.1 % of a ML. For 0.52 % of a ML, the effect on the signal is small, while for 3.1 % of a ML, the signal corrected for self-absorption differs significantly from the measured spectrum. The correction for reemission does not have a significant influence on the spectral shape for neither of the two surface coverages. The corresponding absorption spectra (dashed) are shown for comparison of the spectral shape.

(cf. Eq. (3.46)). Both contributions are affected by a partial reabsorption by circumjacent molecules before the emitted fluorescence light reaches the output of the fiber. Due to the considerable spectral overlap between the absorption and emission spectra, this self-absorption effect significantly changes the spectral shape of the fluorescence signal measured at the fiber output, which is clearly visible in Fig. 5.13.

The typical mirror symmetry which results from Kasha's rule [81] is retrieved after correction for the self-absorption effect. Figure 5.14 displays two of the spectra from Fig. 5.12 for about 0.52 % and 3.1 % of a monolayer as compared to the ones corrected for self-absorption considering only reabsorption and subsequent reemission.

For lower surface coverages like 0.52 % of a ML (Fig. 5.14(a)), the reabsorption has only a minor effect while reemission is completely negligible. Hence, for surface coverages below 0.52 % of a ML, the directly measured fluorescence signal according to Eq. (3.40) can only give a rough estimate for the spectral fluorescence quantum yield. The exact values for the spectral fluorescence quantum yield of the molecule, however, have to be calculated according to Eq. (3.39). Due to the reduced efficiency of multiple coupling of the fluorescence back into the fiber, reemission has only a minor effect for small surface coverages and higher order processes do not have to be taken into account. Fig. 5.14(b) shows the spectra for a surface coverage of 3.1 % of a ML, where the reabsorption of fluorescence light significantly changes the spectrum. Only after correction for this effect, the mirror symmetry between the fluorescence and absorption spectra can be retrieved. Therefore, even for a rough estimate for the spectral fluorescence quantum yield of the molecule under study, the values have to be calculated according to Eq. (3.39) and cannot be deducecd directly from the measured spectrum. To take into account the small but visible effect of reemission, the spectral fluorescence quantum yield has to be determined according to Eq. (3.46).

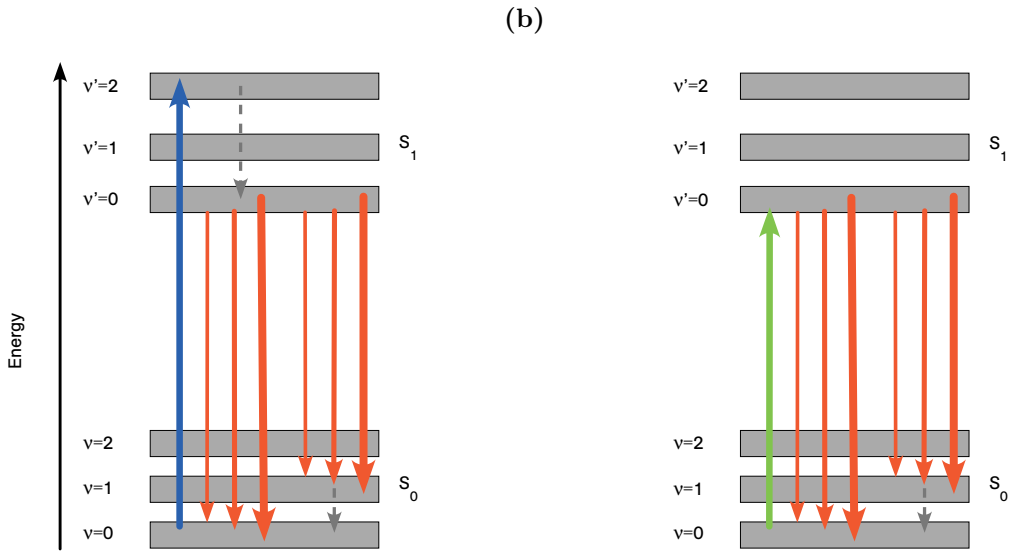

Figure 5.15.: Excitation and decay of a molecule with phononically broadened vibronic states for excitation at the high (a) and low (b) energy edge of the absorption spectrum. Depending on the energy, the molecule is excited to higher vibrational states or the vibrational ground state of the first excited electronic state (blue/green upward pointing arrow). Radiative decay (downward pointing arrows) preferably originates from the vibrational ground state of the first excited electronic state. This can result in energy deposition in the system via vibrational energy relaxation (dashed arrows). On the other hand, hot band absorption and subsequent thermalization can yield anti-Stokes fluorescence and removal of energy from the system.

5.3.1. Anti-Stokes fluorescence

In the measurements presented so far, the PTCDA molecules are excited at the high energy edge of the absorption spectrum. As illustrated in Fig. 5.15(a), this means that the molecules are excited to a higher vibrational level of the first excited electronic state S_1. Following Kasha's rule [81], however, the radiative decay preferably originates from the vibrational ground state of the first excited state, i. e., from a vibrational level below the one that is excited directly. The difference in energy is typically called Stokes loss and is taken up by the rapid vibrational energy relaxation, in the excited as well as the ground state [154]. This can result in a substantial heating effect in addition to the direct heating of the nanofiber by the excitation laser light.

The situation is completely different for excitation in the low energy tail of the absorption spectrum as shown in Fig. 5.15(b), where a significant part of the fluorescence is anti-Stokes shifted with respect to the excitation energy (cf. Fig. 5.2). Here, the broadening of the vibrational levels due to phononic interactions with the environment plays an important role. For simplicity, the phononically broadened vibrational levels are depicted as a continuous band in the figure. Excitation in the low energy tail of the absorption spectrum allows only molecules populating higher phononic states of the electronic and vibrational ground state to absorb. This effect is commonly termed hot band absorption [154]. The excited molecule can then thermalize with the environment, yielding a fluorescence emission at higher energies than the excitation energy. The difference in energy is compensated for by thermal energy which

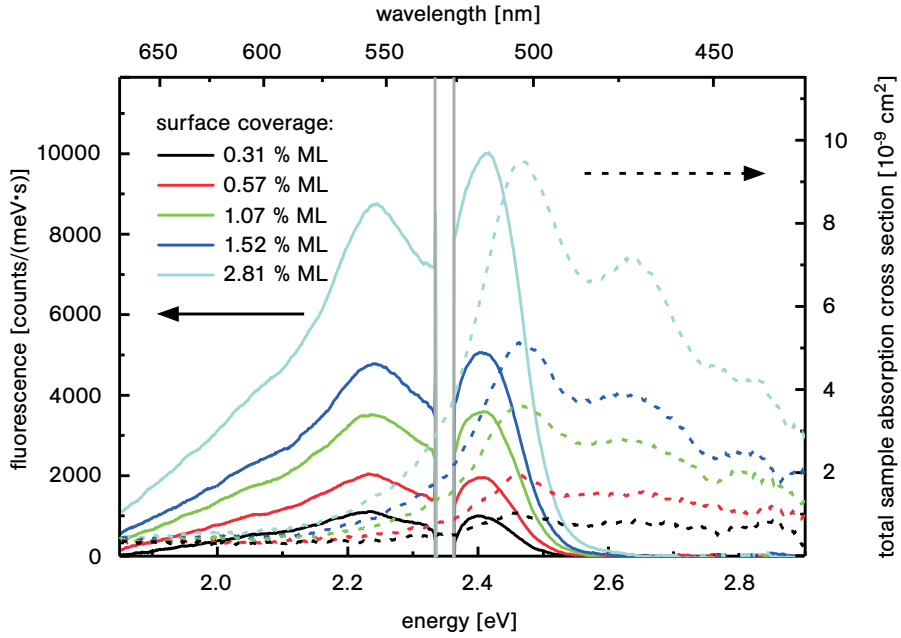

Figure 5.16.: Fluorescence (left) and corresponding absorption (right) spectra of surface-adsorbed PTCDA molecules during deposition at ambient conditions. Five representative spectra within a range of surface coverages between 0.31 and 2.81 % ML are shown. The fluorescence spectra have been obtained upon excitation with a power of about 500 nW of laser light transmitted through the nanofiber at 532 nm. The grey perpendicaular lines indicate the part of the spectrum between 2.33 eV and 2.36 eV which is influenced by the backscattered and reflected excitation light and has thus been removed in the post-processing of the spectra.

can lead to cooling of the whole system. For molecules with vibrational modes, however, radiative decay to higher vibrational levels of the electronic ground state is also possible. The subsequent relaxation to the vibrational ground state results in a heating effect which can dominate over the cooling. Whether the system is heated or cooled depends strongly on the Franck-Condon factors for the different transitions and the exact excitation energy [154].

Figure 5.16 shows a series of fluorescence spectra measured in the same way as the spectra shown in Fig. 5.12, but obtained upon excitation with a power of about 500 nW of laser light transmitted through the nanofiber at 532 nm, i. e., the low energy tail of the absorption spectrum. The fluorescence spectra have been corrected for the wavelength dependent coupling to the fiber mode, for the spectral response of the setup, and for the effect of reabsorption. As discussed above, reemission has only a minor effect for the low surface coverages considered here and therefore has not been corrected for in the spectra shown in Fig. 5.16. The grey perpendicular lines in the figure indicate the part of the spectrum between 2.33 eV and 2.36 eV which is influenced by the backscattered and reflected excitation light. Due to the spectral position of the excitation energy with respect to the fluorescence spectrum, this residual excitation light cannot be suppressed by a long pass filter in front of the spectrometer. Therefore, the influenced part of the spectrum has been removed in the post-processing of the spectra. As for the spectra shown in Fig. 5.12, the underlying surface coverages of the fluorescence spectra have been determined from the corresponding absorption spectra also shown in the figure.

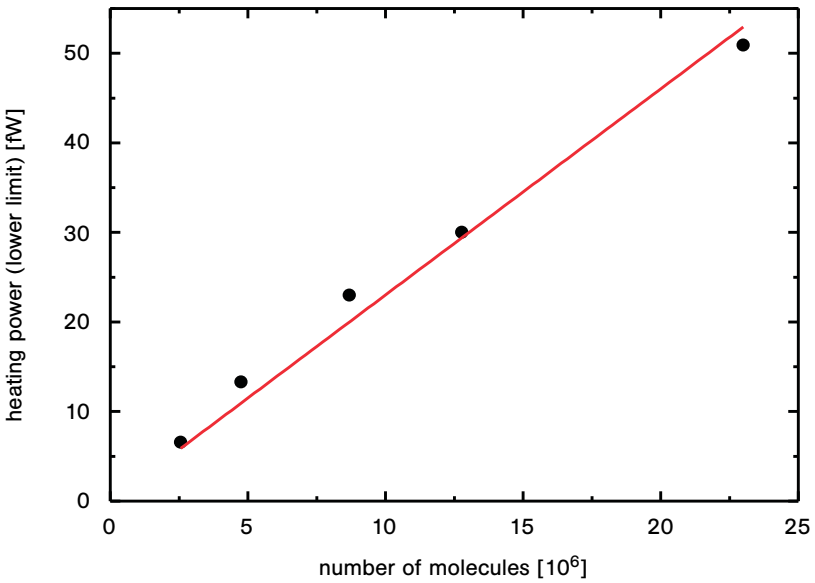

Figure 5.17.: Lower limit to the heating power applied to the sample as a function of the number of molecules covering the nanofiber surface. The black data points have been calculated by multiplication of the difference between the excitation energy and the average emission energy with the total number of detected photons. The red line is a linear fit to the data with a fixed intercept of zero.

The spectra shown in Fig. 5.16 only partially exhibit anti-Stokes character. This is mainly due to the fact that radiative decay to higher vibrational levels of the electronic ground state is also possible and results in a second effective vibrational band at low energy. As mentioned above, the subsequent relaxation to the vibrational ground state results in a deposition of thermal energy in the system. According to [154], the total power applied to the sample is proportional to the difference between the excitation energy and the average emission energy. The average emission energy E_{ave} for the spectra shown in Fig. 5.16 has been calculated via

$$E_{\mathrm{ave}} = \frac{\sum_i N_i E_i}{\sum_i N_i}, \tag{5.4}$$

where E_i are the center energies of the energy intervals of the measured fluorescence spectrum and N_i is the number of measured counts for each interval. Figure 5.17 shows the resulting heating power as a function of the number of molecules covering the nanofiber surface. It has been calculated by multiplication of the difference between the excitation energy and the average emission energy with the total number of detected photons $\sum_i N_i$. Since the detection efficiency of the setup is much smaller than unity (cf. Sec. 4.1.5), these results can be used to qualitatively describe the heating of the sample but only give a lower limit to the actual power applied to the sample. As expected from the proportion of anti-Stokes to Stokes fluorescence shown in Fig. 5.16, the heating power is positive for all surface coverages. It further increases roughly linearly with the number of molecules as shown by the linear fit to the data with a fixed intercept of zero. This suggests that the spectral shape and the proportion of anti-Stokes and Stokes fluorescence does not depend on the number of molecules.

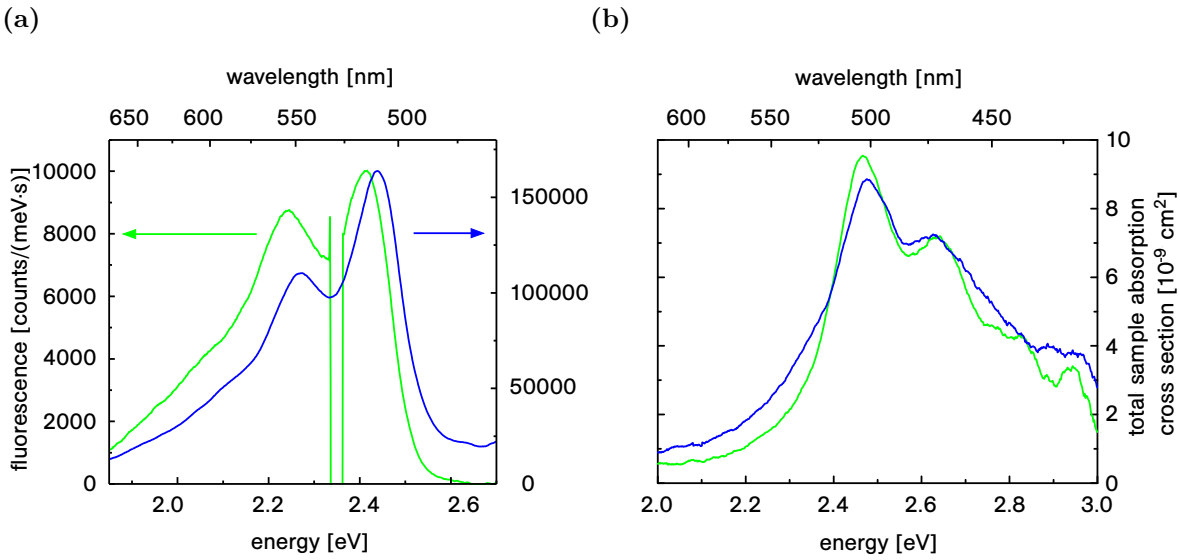

Figure 5.18.: Comparison between (a) a partial anti-Stokes fluorescence spectrum (green) and a pure Stokes fluorescence spectrum (blue) and (b) the corresponding absorption spectra, originating from roughly the same number of about 23 million surface-adsorbed PTCDA molecules or approximately 2.8 % of a compact monolayer.

In order to use the occurance of anti-Stokes fluorescence for optical cooling of the sample as already observed for several systems [155–158], the molecules have to be excited even further in the low energy wing of the absorption spectrum, yielding a negative total power applied to the system. Moreover, the additional heating due to the non-unity fluorescence quantum yield of the molecules as well as the counteracting heat load from the sample surroundings as discussed in [154] have to be taken into account.

Figure 5.18 shows a comparison between a partial anti-Stokes fluorescence spectrum from Fig. 5.16(a) and a pure Stokes fluorescence spectrum as well as the corresponding absorption spectra (b). The pure Stokes spectra have been recorded upon excitation with a power of about 13 µW of laser light transmitted through the nanofiber at 406 nm. Both measurements were performed using the same nanofiber and the same alignment of the optical setup, and the same post-processing has been performed for both spectra for comparability.

From the absorption spectra in Fig. 5.18(b), it can be deduced that the two fluorescence spectra originate from roughly the same number of about 23 million surface-adsorbed PTCDA molecules or approximately 2.8 % of a compact monolayer. Moreover, the absorption spectrum measured alternatingly with excitation at the high energy edge of the absorption spectrum (blue line) is significantly broadened with respect to the absorption spectrum measured alternatingly with excitation at the low energy edge of the absorption spectrum (green line). This broadening effect as well as the slight blue shift is likely due to the higher nanofiber temperature due to two different heating effects: the stronger heating of the nanofiber due to the higher excitation power and the resulting stronger absorption of blue light by the TOF as well as the stronger heating due to the conversion of radiation energy into vibrational, i. e. thermal, energy as discussed above.

The fluorescence spectra in Fig. 5.18(a), however, show much bigger differences than the corresponding absorption spectra. In addition to a red shift of about 28 meV, the spectrum

with an anti-Stokes part clearly exhibits a different shape as compared to the pure Stokes fluorescence spectrum. These effects can be attributed to the inhomogeneous broadening of the spectra and the resulting dependence of excitation efficiencies for different molecule classes on the excitation energy.

The shape of the fluorescence spectrum of a molecular ensemble subject to inhomogeneous broadening effects as a function of excitation energy E_{exc} is derived in Appendix B.2 and is given by Eq. (B.12):

$$\begin{aligned} S_{\mathrm{em}}^{\mathrm{tot}}(E, E_{\mathrm{exc}}) &= \frac{1}{\sqrt{2\pi}\sqrt{\sigma_{\mathrm{hom}}^2+\sigma_{\mathrm{inhom}}^2}} \cdot \frac{1}{\sqrt{2\pi}\sigma_{\mathrm{hom}}\sqrt{1+\frac{\sigma_{\mathrm{inhom}}^2}{\sigma_{\mathrm{hom}}^2+\sigma_{\mathrm{inhom}}^2}}} \\ &\quad \times \sum_{i,l} B_i A_l \cdot \exp\left(\frac{-(E_{\mathrm{exc}}-\mu_l)^2}{2(\sigma_{\mathrm{hom}}^2+\sigma_{\mathrm{inhom}}^2)}\right) \\ &\quad \times \exp\left(\frac{-(E-\tilde{\mu}_i-\frac{\sigma_{\mathrm{inhom}}^2}{\sigma_{\mathrm{inhom}}^2+\sigma_{\mathrm{hom}}^2}\cdot(E_{\mathrm{exc}}-\mu_l))^2}{2\sigma_{\mathrm{hom}}^2(1+\frac{\sigma_{\mathrm{inhom}}^2}{\sigma_{\mathrm{hom}}^2+\sigma_{\mathrm{inhom}}^2})}\right), \end{aligned} \tag{5.5}$$

where B_i and A_l are the amplitudes of the characteristic emission and absorption lines at energies $\tilde{\mu}_i$ and μ_l, respectively. The spectrum is further determined by the homogeneous and inhomogeneous linewidths given by σ_{hom} and σ_{inhom}, respectively.

As can be seen from the expression in Eq. (5.5), the fluorescence spectrum is not only a Gaussian convolution of the characteristic emission spectrum given by $\sum_i B_i \delta(E-\tilde{\mu}_i)$, but also the sum of contributions from different absorption lines l which are shifted by the difference between the excitation energy E_{exc} and the characteristic absorption energies μ_l of the molecule.

Assuming that the absorption upon excitation in the wings of the absorption spectrum is dominated by a single transition, Eq. 5.5 can be simplified to

$$\begin{aligned} S_{\mathrm{em}}^{\mathrm{wing}}(E, E_{\mathrm{exc}}) &\approx \frac{1}{\sqrt{2\pi}\sqrt{\sigma_{\mathrm{hom}}^2+\sigma_{\mathrm{inhom}}^2}} \cdot \frac{1}{\sqrt{2\pi}\sigma_{\mathrm{hom}}\sqrt{1+\frac{\sigma_{\mathrm{inhom}}^2}{\sigma_{\mathrm{hom}}^2+\sigma_{\mathrm{inhom}}^2}}} \\ &\quad \times A_{\mathrm{high/low}} \cdot \exp\left(\frac{-(E_{\mathrm{exc}}-\mu_{\mathrm{high/low}})^2}{2(\sigma_{\mathrm{hom}}^2+\sigma_{\mathrm{inhom}}^2)}\right) \\ &\quad \times \sum_i B_i \exp\left(\frac{-(E-\tilde{\mu}_i-\frac{\sigma_{\mathrm{inhom}}^2}{\sigma_{\mathrm{inhom}}^2+\sigma_{\mathrm{hom}}^2}\cdot(E_{\mathrm{exc}}-\mu_{\mathrm{high/low}}))^2}{2\sigma_{\mathrm{hom}}^2(1+\frac{\sigma_{\mathrm{inhom}}^2}{\sigma_{\mathrm{hom}}^2+\sigma_{\mathrm{inhom}}^2})}\right), \end{aligned} \tag{5.6}$$

where A_{low} and A_{high} are the amplitudes of the characteristic absorption lines with the lowest and highest energies μ_{low} and μ_{high}, respectively. As a result, the spectra yield a shift of $\sigma_{\mathrm{inhom}}^2/(\sigma_{\mathrm{inhom}}^2+\sigma_{\mathrm{hom}}^2)\cdot(E_{\mathrm{exc}}-\mu_{\mathrm{high/low}})$ with respect to the characteristic emission spectrum of PTCDA.

The absorption line of PTCDA with the lowest energy is the 0-0 transition with an absorption energy which coincides approximately with the center of the first absorption band

at $\mu_{\mathrm{low}} \approx 2.466\,\mathrm{eV}$ [143]. The absorption line with the highest energy measured in helium nanodroplets is blue-shifted by $2370\,\mathrm{cm}^{-1} \approx 294\,\mathrm{meV}$ with respect to the 0-0 transition [143], yielding $\mu_{\mathrm{high}} \approx 2.76\,\mathrm{eV}$. For excitation at 532 nm ($E_{\mathrm{low}} = 2.335\,\mathrm{eV}$) and 406 nm ($E_{\mathrm{high}} = 3.06\,\mathrm{eV}$), the expected shift between the two resulting fluorescence spectra can thus be calculated via

$$\begin{aligned} \Delta E &\approx \frac{\sigma^2_{\mathrm{inhom}}}{\sigma^2_{\mathrm{inhom}} + \sigma^2_{\mathrm{hom}}} \cdot (E_{\mathrm{high}} - \mu_{\mathrm{high}} - E_{\mathrm{low}} + \mu_{\mathrm{low}}) \\ &\approx \frac{\sigma^2_{\mathrm{inhom}}}{\sigma^2_{\mathrm{inhom}} + \sigma^2_{\mathrm{hom}}} \cdot 431\,\mathrm{meV}. \end{aligned} \tag{5.7}$$

Assuming that the homogeneous width of each spectral line contributing to an absorption band is dominated by the thermal excitation of phonons, it can be estimated as $\sigma_{\mathrm{hom}} \approx k_B T \approx 33\,\mathrm{meV}$ for a temperature of about 100 °C. Therefore, the measured spectral shift of $\Delta E \approx 28\,\mathrm{meV}$ yields an inhomogeneous linewidth of $w_{\mathrm{inhom}} = \sigma_{\mathrm{inhom}} \cdot \sqrt{8 \ln 2} \approx 19.2\,\mathrm{meV} \approx 155\,\mathrm{cm}^{-1}$. This agrees well with the typical inhomogeneous linewidths of molecules in solutions, in amorphous materials or on surfaces of a few hundred cm^{-1} [88].

The different shape of the two fluorescence spectra shown in Fig. 5.18(a) can be attributed to contributions of emission caused by absorption via other vibronic transitions than the ones considered so far. For excitation in the high energy wing, these contributions exhibit a shift to higher energies, while for excitation in the low energy wing, they exhibit a red shift with respect to the dominating spectrum caused by absorption on the 0-0 transition of PTCDA. Since these additional contributions are suppressed due to the even further shift of the absorption energies with respect to the excitation energies, they will not significantly influence the shift of the overall fluorescence spectrum. However, the summation of all contributions can result in a distortion of the overall fluorescence spectrum, yielding a more pronounced first effective vibronic band for excitation in the high energy wing and and more pronounced second effective vibronic band for excitation in the low energy wing, as is clearly visible in Fig. 5.18.

5.3.2. Collection efficiency

In order to determine the collection efficiency of nanofiber-based fluorescence spectroscopy of surface-adsorbed molecules, the total number of measured fluoresence counts has to be compared to the number of absorbed photons. The total number of measured fluorescence counts can be obtained by integration over the whole fluorescence spectrum, while the number of absorbed photons N_{abs} can be calculated from the total absorbed power $P^{\mathrm{tot}}_{\mathrm{abs}}(\lambda)$ via $N_{\mathrm{abs}} = P^{\mathrm{tot}}_{\mathrm{abs}}(\lambda) \cdot \lambda/(hc)$.

Using Eq. (3.31) for the total absorbed power $P^{\mathrm{tot}}_{\mathrm{abs}}(\lambda_{\mathrm{exc}})$ at the excitation wavelength λ_{exc}, the number of absorbed photons can therefore be calculated via

$$N_{\mathrm{abs}} \approx \frac{\sigma^{\mathrm{tot}}(\lambda_{\mathrm{exc}}) \cdot P_{\mathrm{exc}}(\lambda_{\mathrm{exc}}) \cdot \lambda_{\mathrm{exc}}}{A_{\mathrm{eff}}(\lambda_{\mathrm{exc}}) \cdot hc}, \tag{5.8}$$

where $P_{\mathrm{exc}}(\lambda_{\mathrm{exc}})$ denotes the excitation power. For the measurements shown in Sec. 5.3.1, the signal to noise ratio of the simultaneously measured absorption spectra at the excitation wavelengths of 406 nm and 532 nm is not sufficiently high to determine $\sigma^{\mathrm{tot}}(\lambda_{\mathrm{exc}})$ with a high accuracy. As mentioned above, this is due to the reduced sensitivity for absorption

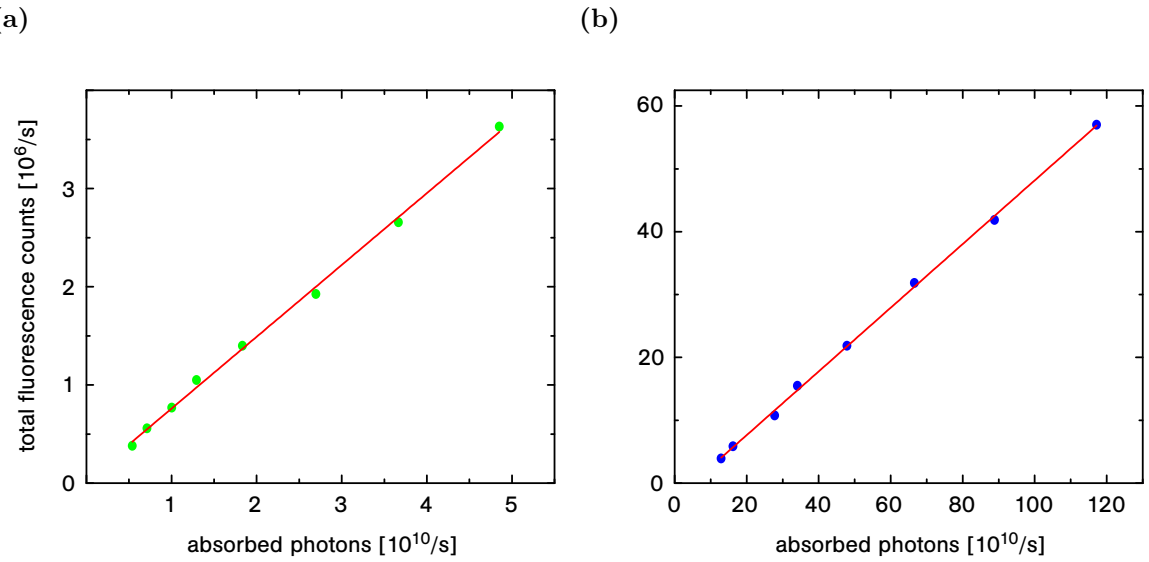

Figure 5.19.: Number of total measured fluorescence counts as a function of the number of absorbed photons for excitation with (a) a power of about 500 nW of laser light transmitted through the nanofiber at 532 nm and (b) a power of about 13 µW of laser light transmitted through the nanofiber at 406 nm. The red lines indicate a linear fit to the data.

measurements in the experimental configuration for fluorescence spectroscopy as compared to pure absorption measurements. However, from the spectrum presented in Fig. 5.5 it can be deduced that the total sample absorption cross section at these wavelengths is about 4.5 % and 3.5 %, respectively, of the peak value $\sigma_{\text{peak}}^{\text{tot}}$ which can be measured with a good signal to noise ratio for all spectra shown in Fig. 5.12.

In Fig. 5.19, the number of total measured fluorescence counts as a function of the number of absorbed photons for both measurements discussed in Sec. 5.3.1 are displayed. The red lines indicate a linear fit to the data. For excitation with a power of about 500 nW of laser light transmitted through the nanofiber at 532 nm (Fig. 5.19(a)), the linear fit yields a slope of $(7.3 \pm 0.1) \cdot 10^{-5}$ fluorescence counts per absorbed photon. Figure 5.19(b) shows that the slope is reduced to $(5.07 \pm 0.06) \cdot 10^{-5}$ fluorescence counts per absorbed photon for excitation with a power of about 13 µW of laser light transmitted through the nanofiber at 406 nm.

The measured slope yields a value for the total efficiency η_{tot} which is influenced by the fluorescence quantum yield η_{Q} of the PTCDA molecules, the collection efficiency η_{col} of the molecular emission by the guided fiber mode, and the detection efficiency η_{setup} of the optical setup:

$$\eta_{\text{tot}} = \eta_{\text{Q}} \cdot \eta_{\text{col}} \cdot \eta_{\text{setup}}. \tag{5.9}$$

As discussed in Sec. 4.1.5, the detection efficiency via the entrance slit of the spectrometer for a photon guided in the nanofiber waist of the TOF is about 0.1 %. The fluorescence quantum yield of PTCDA in solution has been determined to be 77 ± 10 % [159]. From these values, the collection efficiency can be estimated to be $\eta_{\text{col}} \approx 9.5\,\%$ for excitation at 532 nm and $\eta_{\text{col}} \approx 6.6\,\%$ for excitation at 406 nm. Considering that the value for the detection efficiency via the entrance slit used here is only a rough estimate, the results for the collection efficiency agree well with the theoretically expected value of about 10 % in each direction of the fiber [31].

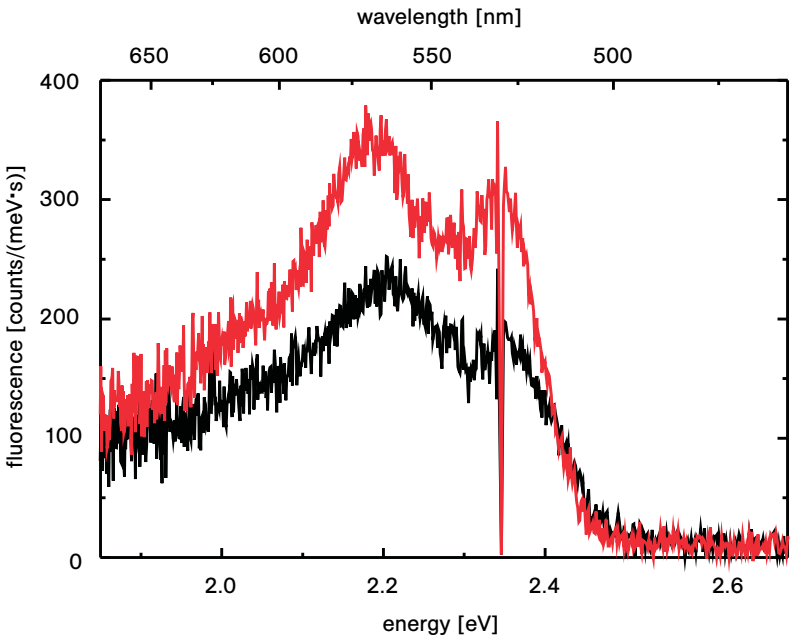

Figure 5.20.: Fluorescence spectra of surface-adsorbed PTCDA molecules before (black) and after (red) reduction of the nanofiber temperature by rotating the the aluminum shutter between the crucible and the nanofiber. The number of total fluorescence counts increases by about 35 %. The spectral feature at an energy of about 2.34 eV can be attributed to the influence of the backscattered and reflected excitation light.

The difference in the collection efficiency values for excitation at 532 nm and at 406 nm of about a factor of 0.7, however, indicates that the fluorescence quantum yield of PTCDA on a nanofiber surface differs from the one in solution and varies for different experimental conditions [148]. On a surface, the fluorescence can be significantly quenched due to non-radiative decay channels added by the presence of the surface as discussed in Sec. 3.1.2. This fluorescence quenching is typically temperature dependent because of the thermal activation energy needed for opening up the competing non-radiative relaxation channels [160]. Therefore, the fluorescence quantum yield for excitation at 406 nm can be significantly reduced as compared to excitation at 532 nm due to the heating effects discussed above.

For a further investigation of the influence of the fiber temperature on the fluorescence quantum yield of surface-adsorbed PTCDA molecules, the aluminum shutter in the deposition setup can be used. Figure 5.20 shows two fluorescence spectra obtained upon excitation with a power of about 500 nW of laser light transmitted through the nanofiber at 532 nm using the same nanofiber as for the measurements shown in Fig. 5.9(a). After the deposition of PTCDA molecules has been stopped, the heating current of the crucible has been reduced to 2.0 A and, after about 18 minutes, the aluminum shutter is rotated between the crucible and the nanofiber, thereby instantaneously reducing the temperature of the nanofiber. The two spectra shown in the figure have been recorded directly before and after rotating the aluminum shutter with a time of just one second between them. Not taking into account the heating of the nanofiber due to the excitation laser light, the roation of the shutter yields a temperature drop of about 20 °C within this time (cf. Fig. 4.6(b)). As a result, the

fluorescence signal increases from about 110000 to about 150000 total fluorescence counts, yielding an increase by about 35 % and therefore revealing a significant amount of thermal quenching. After removing the shutter from underneath the fiber and, thereby, raising the nanofiber temperature again to the original value, the total number of fluorescence counts is reduced again to the original number (not shown in the figure). This indicates, that the reduction is indeed caused by thermal quenching and not by another irreversible effect.

Note that for this measurement, no absorption spectra have been recorded alternatingly with the fluorescence spectra to determine the underlying surface coverages. Thus, the spectra have not been corrected for the effect of reabsorption. Since, however, the number of molecules contributing to the fluorescence spectrum is the same for both measurements, the effect of reabsorption on the spectra can also assumed to be the same. For the comparison of the number of total fluorescence counts, the uncorrected spectra are therefore also suitable. The underlying surface coverages can be estimated from the measurements shown in Fig. 5.9(b), since the molecular deposition has been performed under the same conditions and has been stopped after the same time. From the measured total sample absorption cross section of about $4.2 \times 10^{-9}\,\mathrm{cm}^2$, the surface coverage can be estimated to be about 1.2 % of a compact monolayer of PTCDA molecules. Moreover, the spectra have been measured with a higher spectral resolution of about 0.3 nm, yielding a higher noise on the spectrum and a less pronounced influence of the backscattered and reflected excitation light.

Taking into account thermal quenching, the measured collection efficiencies for both excitation modi agree well with the expected value of about 10 % [31]. Compared to confocal microscopy, where the collection efficiency can be determined to be about 2.5 to 4.2 % without taking into account the detector efficiency [88], this is an improvement of a factor of about 3 for detection on only one end of the fiber. For detection on both ends of the fiber, this factor can be improved even further.

5.3.3. Excimer formation

As discussed in Sec. 5.2.2, the mobility of PTCDA molecules on the nanofiber surface allows them to form crystalline films on the surface which yields significantly altered spectral properties of the system. In order to study the effect of this mobility on the properties of the fluorescence spectrum, the measurement discussed in Sec. 5.3.2 (Fig. 5.20) can be used. As mentioned above, no absorption spectra have been recorded alternatingly with the fluorescence spectra, but the underlying surface coverages can be estimated to be about 1.8 % of a compact monolayer of PTCDA molecules from the measurements shown in Fig. 5.9(b).

After the deposition of PTCDA molecules has been stopped, the heating current of the crucible has been reduced to 2.0 A, thereby ensuring a nanofiber temperature which is high enough to reduce the amount of water adsorbed on the nanofiber surface and, therefore, to suppress the catalyzing effect of the water on the reordering of the surface adsorbed molecules. Like the absorption spectrum, the fluorescence spectrum hardly changes its shape for the first 18 minutes during which the nanofiber surface is kept at a temperature above 70 °C by heating the crucible with a current of 2.0 A.

Figure 5.21 displays the evolution of the fluorescence spectrum after the aluminum shutter has been rotated between the crucible and the nanofiber, thereby instantaneously reducing the temperature of the nanofiber. This temperature reduction causes a red shift of the spectrum as compared to the fluorescence spectra shown so far which have been measured during deposition, i. e., at a higher nanofiber temperature. While the shutter is situated

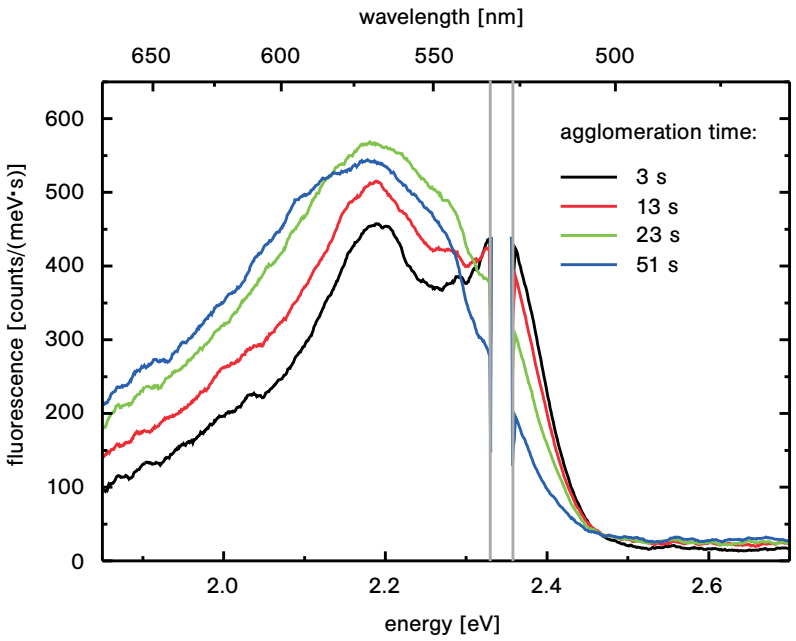

Figure 5.21.: Time evolution of the fluorescence spectrum of PTCDA molecules adsorbed on the nanofiber surface. After the deposition of molecules, the nanofiber is kept at a temperature above 70 °C and an aluminum shutter is rotated underneath the nanofiber. The shift and broadening of the spectrum can be attributed to an increased excimer formation. The grey perpendicular lines indicate the part of the spectrum between 2.33 eV and 2.36 eV which is influenced by the backscattered and reflected excitation light and has thus been removed in the post-processing of the spectra.

between the crucible and the nanofiber, a continuous change of the spectral shape can be observed. However, the time scale on which this change occurs is much shorter than for the absorption spectrum. As shown in Fig. 5.9(c), the absorption spectrum for a similar surface coverage hardly changes its shape within 40 s when the shutter is closed. Therefore, the change of the spectral shape observed for the fluorescence spectrum within the first 50 s cannot be attributed to the formation of stacked dimers. It can, however, be explained by the formation of excited dimers (excimers) already observed for amorphous films of PTCDA which exhibit a monomeric absorption spectrum [134]. Excimers are formed when one of the dimer components is in the excited state and are dissociated into their components after returning to the ground state. The emission of an excimer formed by PTCDA molecules has been measured to be red-shifted with respect to the $S_1, \nu' = 0 \rightarrow S_0, \nu = 0$ transition by about 0.4 eV [134]. An increasing excimer formation due to the mobility of the molecules on the fiber surface can therefore lead to a shift and broadening of the fluorescence spectrum as displayed in Fig. 5.21.

6. Spectroscopy of molecules in a solid state matrix

The strong radial confinement of the light guided by an optical nanofiber yields high efficiencies for the excitation of particles near or on the nanofiber surface and for the fluorescence collection from these particles, as theoretically discussed in Chapter 3. This makes optical nanofibers a well-suited tool for experiments with dye molecules embedded in small organic crystals that are deposited on the nanofiber surface. For a first experimental realization of this approach, terrylene-doped para-terphenyl crystals have been attached to 320-nm diameter nanofibers with a length of 1 mm fabricated from a Nufern 460-HP fiber (cf. Sec. 2.2.2).

In the first part of this chapter, the properties of terrylene in p-terphenyl will be discussed. The preparation of samples with high-quality micro- or nanocrystals which are attached to the nanofiber surface is a challenging task and will be treated in the second part of the chapter. Moreover, the crystal properties like the degree of crystallinity and the amount of crystal defects are studied via their influence on the spectral properties of the embedded terrylene molecules.

In order to achieve stable and narrow spectral lines, the samples are cooled down to cryogenic temperatures, as described in the third part of this chapter. In the last two parts of this chapter, the nanofiber-based method is used to study the properties of terrylene-doped crystals at low temperature via fluorescence and fluorescence excitation spectroscopy. In particular, the statistical fine structure of the fluorescence excitation spectrum is observed which can be used to give an estimate for the average number of molecule that resonate, within their homogeneous linewidth, with the laser frequency and for the homogeneous linewidth of the transition. Parts of this chapter have been adapted from [127, 128].

6.1. Sample characteristics

Terrylene doped p-terphenyl crystals were prepared and studied for the first time by Kummer et al. [116]. The high fluorescence count rate makes this system particularly advantageous for single molecule spectroscopy, and numerous experiments have been performed at different temperatures. To rerview all experimental studies and all the information which is available about this system is beyond the scope of this thesis. Therefore, only the properties relevant for the measurements presented here will be discussed below. Detailed informationcan be found in the literature [88, 161, 162].

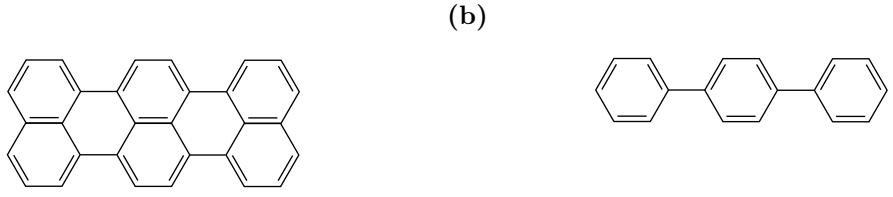

Figure 6.1.: Lewis structure formula of (a) terrylene and (b) p-terphenyl

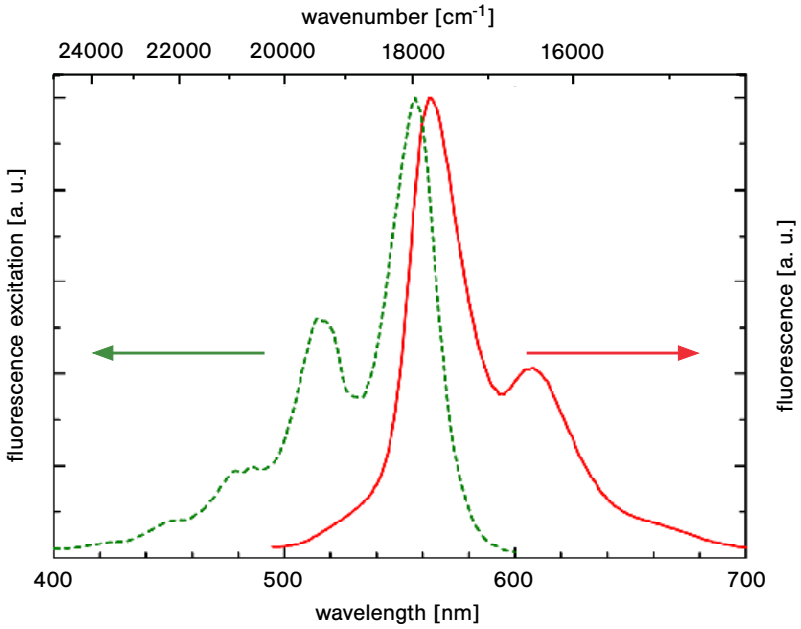

Figure 6.2.: Fluorescence (red solid line) and fluorescence excitation (green dashed line) spectrum of terrylene in dichlormethane (DCM) at room temperature, adapted from [164]

6.1.1. Terrylene

Terrylene ($C_{30}H_{16}$) is an aromatic hydrocarbon consisting of three naphthalene ($C_{10}H_8$) units connected at the peri-position. It is the third molecule in the rylene homologous series after naphthalene and perylene ($C_{20}H_{12}$) and therefore also exhibits a high photostability and a large fluorescence quantum yield of 0.7 [163]. Figure 6.1(a) shows the Lewis structure formula of terrylene. Terrylene has a planar structure with the transition dipole moment of the $S_0 \leftrightarrow S_1$ transition oriented along the long molecular axis [165].

The first synthesis of terrylene has been published in 1956 by Clar et al. [166]. They determined the absorption maxima for the $S_0 \rightarrow S_1$ transition of terrylene in benzene to be at 560 nm, 519 nm, and 483 nm. As expected from the higher position of terrylene in the homologous series, the transition is redshifted with respect to the perylene spectrum [167] which essentially coincides with the PTCDA spectrum discussed in Sec. 5.1. Figure 6.2 shows the fluorescence and fluorescence excitation spectrum of terrylene dissolved in DCM which exhibit a slightly smaller solvent shift to lower energies compared to the benzene spectra. Similar to PTCDA, the spectrum can be described by coupling to one effective vibronic mode with a spacing of $E_{\text{eff}} \approx 0.18\,\text{eV}$ (approx. $1450\,\text{cm}^{-1}$). The Stokes shift of about $200\,\text{cm}^{-1}$ (25 meV) yields fluorescence maxima at 563 nm and 607 nm.

The first electronic transition of the free terrylene molecule has been estimated by extrapolation of the data for terrylene in argon and neon matrices [168] by Hoheisel and Hese in 2006 to be at $19203\,\text{cm}^{-1}$ (521 nm) [169]. They also measured the transition energy of jet-cooled terrylene molecules to be around $19238\,\text{cm}^{-1}$ which agrees well with the extrapolated value for a free molecule.

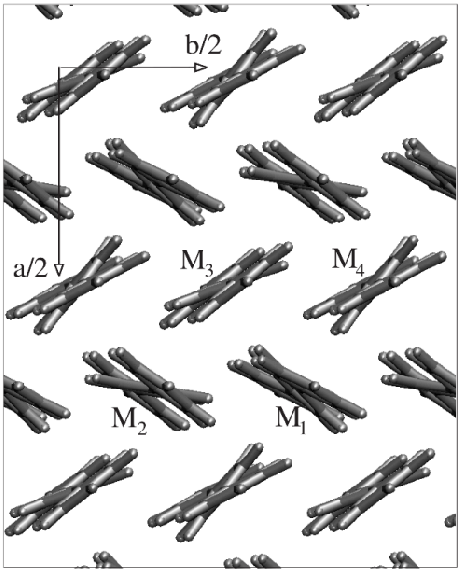

Figure 6.3.: Low temperature crystal structure of p-terphenyl, taken from [175]. The c-axis of the crystal (not shown) forms an angle of 92.1 ° with the a-b-plane. The four non-equivalent molecular equilibrium geometries are labeled with M_1 to M_4.

6.1.2. p-Terphenyl

As a model system for molecular crystals, p-terphenyl and its crystal structure have been studied extensively (cf., e. g., [170]). The molecule consists of a central benzene ring substituted with two phenyl groups at the para-positions as is shown in Fig. 6.1(b).

Although the delocalized π-electrons favor a planar molecular structure, the repulsive interaction between the ortho-hydrogen atoms causes the central ring to twist [171] for a free molecule. In a room temperature crystal, additional intermolecular forces result in a flipping of the central ring between two states with a torsion of $\pm 13.3\,^\circ$ [172], yielding a planar equilibrium structure of the p-terphenyl molecule. The crystal structure has been found to be monoclinic with a unit cell with lattice constants $a = 8.1\,\text{Å}$, $b = 5.6\,\text{Å}$, and $c = 13.6\,\text{Å}$ containing two identical molecules [170]. At a temperature of approximately 193 K, the p-terphenyl crystal undergoes a phase transition and the flipping of the central ring is frozen out [172]. The resulting crystal structure can be described by a pseudo-monoclinic lattice with a unit cell containing eight molecules at four non-equivalent sites (M_1–M_4) which differ by the out of plane twist of the central ring [173] as shown in Fig. 6.3.

p-Terphenyl forms platy crystals with (001) faces with the long molecular axis oriented at an angle of approximately 16 ° with respect to the c-axis of the crystal [113]. Since the polarizability of p-terphenyl is much larger along the long molecular axis, the crystal is highly birefringent with refractive indices of $n_a \approx 1.6$ and $n_b \approx 1.7$ within the a-b-plane and $n_c \approx 2$ perpendicular to the crystal face [115]. Although p-terphenyl is used as a laser dye in the ultraviolet spectral region, it is transparent in the visible range and is therefore a well-suited host material for experiments with terrylene molecules [174].

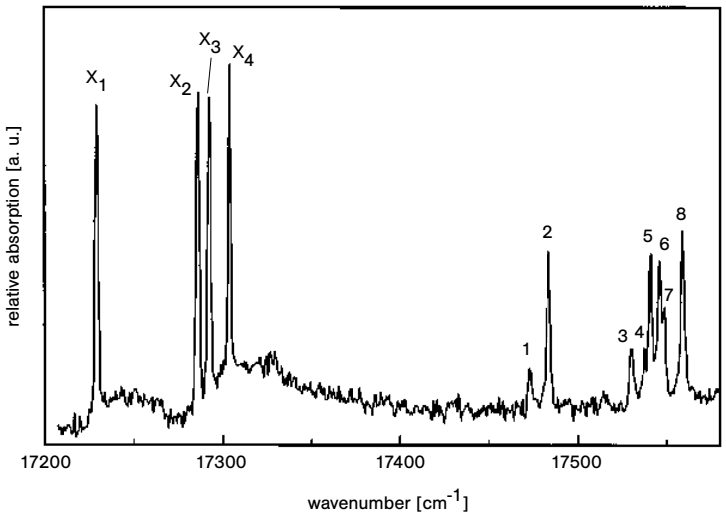

Figure 6.4.: Ensemble absorption spectrum of terrylene in p-terphenyl at $T = 4.2\,\mathrm{K}$, taken from [85].

6.1.3. Terrylene in p-terphenyl

In terrylene doped p-terphenyl crystals, individual dopant molecules are inserted into lattice sites of the host crystal. Although the terrylene molecule is almost twice as big as the p-terphenyl molecule (cf. Fig. 6.1), it could be shown by comparison of quantum chemical calculations to the experimental results that predominantly only one p-terphenyl molecule is replaced by a terrylene molecule [114, 175]. Disubstituted sites can also occur in a real crystal as has been observed experimentally by Kummer et al. [85], but replacement of one molecule of the host material is much more favorable [114]. Hence, at low temperatures, a terrylene molecule is most likely located at one of the four non-equivalent sites M_1–M_4. Since the optical properties of single molecules depend strongly on the local environment, the terrylene molecules substituted into a p-terhenyl crystal thus exhibit four discrete site-specific transition frequencies for the first electronic transition. Figure 6.4 shows the ensemble absorption spectrum of terrylene in a p-terphenyl crystal, grown from the melt by the Bridgman technique [176], measured at 4.2 K by Kummer et al. [85]. Four strong absorption bands can be clearly distinguished at the low energy side of the spectrum which have been assigned to the purely electronic transitions of terrylene molecules occupying four different crystal sites. They are denoted by X_1 to X_4 and located at $17230\,\mathrm{cm}^{-1}$ (580.4 nm, X_1), $17286\,\mathrm{cm}^{-1}$ (578.5 nm, X_2), $17293\,\mathrm{cm}^{-1}$ (578.3 nm, X_3), and $17304\,\mathrm{cm}^{-1}$ (577.9 nm, X_4) [85, 116]. The weaker absorption bands at the high energy side of the shown spectrum have been attributed to higher vibronic transitions of terrylene molecules occupying the four crystal sites. They are shifted with respect to the purely electronic transitions X_1 to X_4 by about $245\,\mathrm{cm}^{-1}$ (lines 1,3,4, and 7) and $255\,\mathrm{cm}^{-1}$ (lines 2,5,6, and 8). The four crystal sites differ greatly in the photostability of molecules occupying them. While molecules with purely electronic transitions X_2 and X_4 exhibit a very high photostability, molecules with transitions X_1 and X_3 readily undergo photo-induced transition frequency jumps. The tendency to photo-induced transition frequency jumps for a guest molecule is directly connected to the number of possible conformations of the surrounding host molecules which affect the transition frequency

via electrostatic and van der Waals interaction as welll as Pauli repulsion [177]. For doping the p-terphenyl crystal at the M_1 and M_4 sites, the local geometry at the site has only one possible conformation, and these sites have therefore been associted with the X_4 and X_2 transitions, respectively [175]. Single molecules in these sites can undergo about 10^{12} emission cycles without experiencing photobleaching or spectral shifts [85]. Substitution at the sites M_2 (X_3) and M_3 (X_1), however, yields several possible conformations of the local geometry and light-induced switching between these conformations is possible [178]. Note that, for historical reasons, the numbering for the crystal sites M_1–M_4 does not coincide with the numbering for the transitions X_1–X_4.

The long axis of a substituted terrylene molecule is aligned roughly parallely to the long axis of the p-terphenyl molecule it replaces. Consequently, the transition dipole moment of terrylene in a p-terphenyl crystal has been found to be aligned at an angle between 99.8 ° and 103.6 ° with respect to the a-axis of the crystal, where the exact orientation depends on the insertion site [114].

For temperatures below 2 K and ideal conditions, the linewidth of terrylene ein p-terphenyl has been found to be lifetime-limited with values between 30 MHz and 55 MHz [162].

6.2. Sample preparation

Organic crystals of high optical quality can be prepared from solution, from the melt, and from the gas phase. For single molecule spectroscopy, terrylene-doped p-terphenyl crystals are typically prepared by co-sublimation [116] or spin-coating [97]. Co-sublimation of p-terphenyl and terrylene in an inert gas atmosphere with a high temperature gradient yields extremely clean and ordered crystals of several micrometers thickness. The spectra of molecules in a sublimated crystal are stable and narrow, but the molecules are usually located a few micrometers away from the surface [161]. By spin-coating, thin crystalline films can be grown on a substrate from solution. If these films are heated up to moderate temperatures [162], they break up and form nanocrystals with thicknesses down to 80 nm. It has been shown that molecules embedded in such a nanocrystal exhibit as stable and narrow spectra as those in larger crystals even though the molecules in the nanocrystal are located much closer to the surface than for the case where the crystals are grown by sublimation [97].

Due to the small dimensions and the curved surface of an optical nanofiber, the deterministic placement of nanocrystals onto the nanofiber surface is a challenging task. Recently, a highly accurate nanomanipulation technique for picking and placing single nanocrystals has been introduced [34, 179]. Alternatively, the crystals can be grown directly on the fiber surface via co-sublimation or molecular beam epitaxy. However, this demands a highly controlled growth process, and the growth of high quality mixed crystals on the nanofiber surface has not yet been achieved. The results presented in this thesis have been obtained with samples prepared from solution.

6.2.1. Crystal growth from solution

For the preparation of samples from solution, a precursor mixture of terrylene and p-terphenyl is dissolved in toluene ($C_6H_5CH_3$, Merck Uvasol). The terrylene concentration relative to the p-terphenyl concentration can be further reduced by admixing pure zone-refined p-terphenyl to the solution. The zone-refined p-terphenyl and two precursor mixtures of terrylene in zone-refined p-terphenyl have been kindly provided by the group of Th. Basché (Institute

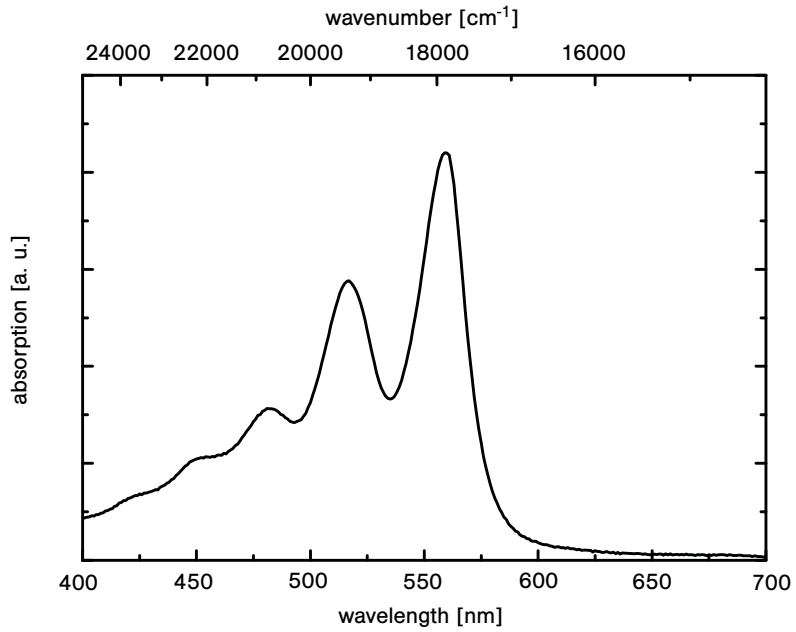

Figure 6.5.: UV/Vis spectrum of a solution with 2.3 mg/ml p-terphenyl and 46 ng/ml terrylene dissolved in toluene.

of physical chemistry, Johannes Gutenberg-Universität Mainz). In order to minimize contamination of the solution, the cuvettes used are first ultrasonically cleaned with an aqueous detergent (Extran MA02 neutral, Merck), followed by successive rinsing steps with acetone and toluene.

Crystallization from solution only occurs if the solution is oversaturated, i. e., if the solute concentration is so high that not all the material can be dissolved by the solvent. For p-terphenyl in toluene, saturation is reached for a concentration of about 5 mg/ml [180]. Figure 6.5 shows the absorption spectrum of a solution with a p-terphenyl concentration of 2.3 mg/ml and a terrylene concentration of 46 ng/ml (solution A). It has been measured with a UV/Vis photometer [181] by W. Scholdei at the Max Planck Institute for Polymer Research in Mainz with a spectral resolution of 1 nm. The spectral characteristics agree very well with the spectral features of terrylene in DCM displayed in Fig. 6.2 with a difference in the solvent shift of about 2 nm, and there is no spectral signature of terrylene-doped p-terphenyl crystals. This indicates that the material is indeed completely dissolved in this solution as is expected from the fact that the concentration is clearly below the saturation concentration. Note that the dissolved p-terphenyl molecules cannot be identified in the spectrum because they do not absorb in the visible spectral range as discussed in Sec. 6.1.2.

If a drop of this undersaturated solution is brought into contact with the surface of the nanofiber waist of a TOF, the solvent will start to evaporate resulting in an increase of the solute concentration. When the concentration comes close to its saturation value, the solute starts to precipitate and p-terphenyl crystals form in the drop and stick to the fiber surface [182]. Figure 6.6 shows a typical absorption spectrum with an effective spectral resolution of 6 nm measured via the nanofiber mode after bringing a drop of solution A into contact with the nanofiber surface (solid line). For comparison, the process was repeated with a solution of pure zone-refined p-terphenyl with a concentration of 7.25 mg/ml resulting

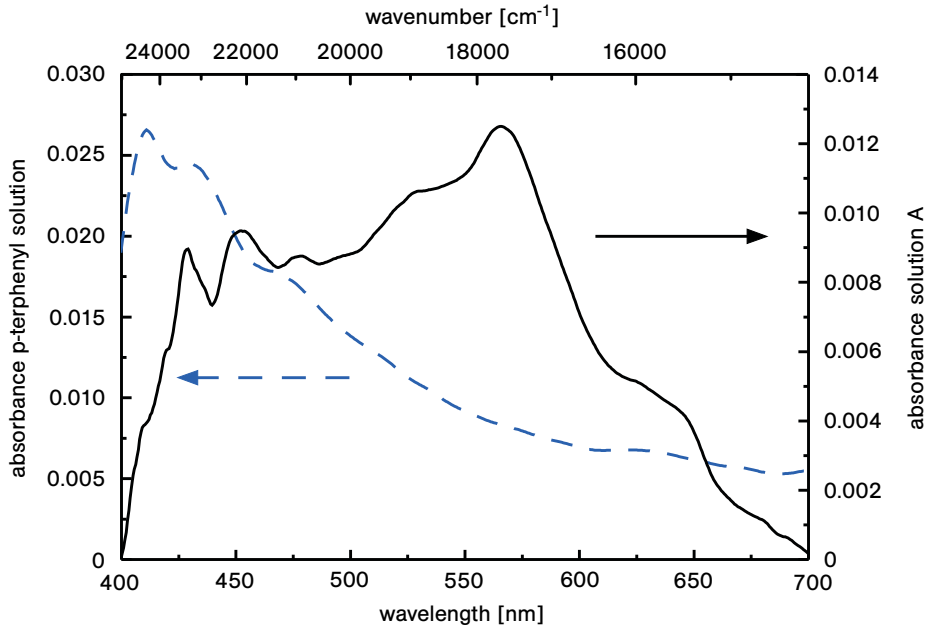

Figure 6.6.: Absorption spectra obtained from bringing a drop of solution A (solid line) or a drop of a pure p-terphenyl solution (dashed line) into contact with the nanofiber surface.

in the absorption spectrum indicated by the dashed line. The spectral features below 500 nm and around 630 nm as well as the overall slope of the spectrum are visible in both absorption spectra. They can be attributed to disturbances of the TOF mode due to p-terphenyl crystals on the fiber surface which influence the transmission properties of the TOF and hence modify the absorption spectrum. Since the distribution of p-terphenyl crystals on the fiber surface is not entirely reproducible, also the absorption spectra can differ slightly from measurement to measurement. However, the absorption signal for these features is about a factor of 3 higher for the sample prepared from the solution of pure p-terphenyl as compared the one prepared from solution A. This increase qualitatively agrees well with the increased concentration of the pure p-terphenyl solution. The admixture of terrylene to the solution results in two spectral bands with maxima around 530 and 565 nm which are significantly broadened and shifted with respect to the UV/VIS spectrum shown in Fig. 6.5. Note that such a shift was also found for surface adsorbed PTCDA molecules, cf. Sec. 5.2. Together with the observed decay on a time scale of about 20 minutes [127], this indicates that the terrylene molecules are not embedded into the crystal properly, since embedded molecules are expected to exhibit stable absorption lines significantly narrower than those of the solution spectrum [93]. A possible reason for the insufficient incorporation of terrylene molecules into the p-terphenyl matrix is the slow crystal growth caused by the slow increase of solute concentration due to evaporation of the solvent. A slow crystal growth usually results in a self-cleaning effect, i. e., the terrylene molecules are pushed to the crystal surface or not incorporated into the crystal at all [183].

Since the fluorescence of terrylene molecules is mainly emitted at wavelengths above 550 nm, the fluorescence signal is not as strongly affected by the disturbances of the TOF mode due to p-terphenyl crystals as the absorption signal. The fluorescence spectrum of a sample prepared from solution A is displayed in Fig. 6.7. It has been measured at the fiber output using the optical setup described in Sec. 4.1 with an excitation power of about 380 nW in the nanofiber

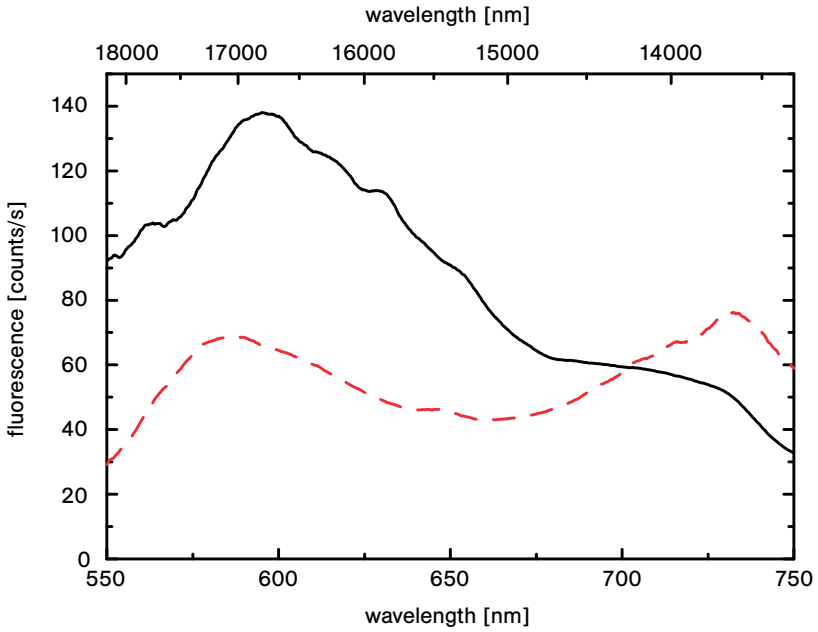

Figure 6.7.: Fluorescence spectra of a sample prepared from solution A (solid line) and a pure terrylene solution (dashed line) for an excitation wavelength of 532 nm. For better comparability, both signals have been normalized to 1 µW excitation power. The spectra below 550 nm are influenced by the backscattered and reflected excitation light and therefore not shown here.

waist of the TOF at a wavelength of 532 nm and an effective spectral resolution of about 14 nm.

For comparison, a fluorescence spectrum obtained from a solution of pure terrylene (Henrychem Science) in toluene with a concentration of 28 µg/ml is included in the figure (dashed line). It has been recorded with the same effective spectral resolution but with an excitation power of about 44 nW at 532 nm. Both spectra have been corrected for the wavelength dependent coupling to the fiber mode as well as the spectral response of the setup and normalized to 1 µW excitation power for better comparability. This normalization is possible because the excitation powers for both measurements of are low enough not to saturate the transitions and, hence, a linear relation between the signal strength and the excitation power can be assumed. Since the backscattered and reflected excitation light has not been suppressed by a long pass filter for these measurements, the spectra below 550 nm are influenced by the residual excitation light and therefore not shown in the figure. Neither spectrum has been corrected for possible self-absorption effects, since due to the nature of the sample preparation procedure, a sufficiently reliable assumption about the arrangement of absorbers along the fiber surface cannot be made.

The spectrum of the sample prepared from solution A (solid line) is dominated by a broad feature with a maximum around 595 nm. In comparison to the broadened absorption spectrum shown in Fig. 6.6, an approximate mirror symmetry between absorption and fluorescence spectrum can be observed. This feature is also visible in the spectrum of pure terrylene with the maximum at about 587 nm slightly shifted to higher energies. The blue shift can be attributed to an additional solvent shift in solution A due by the admixture of p-terphenyl.

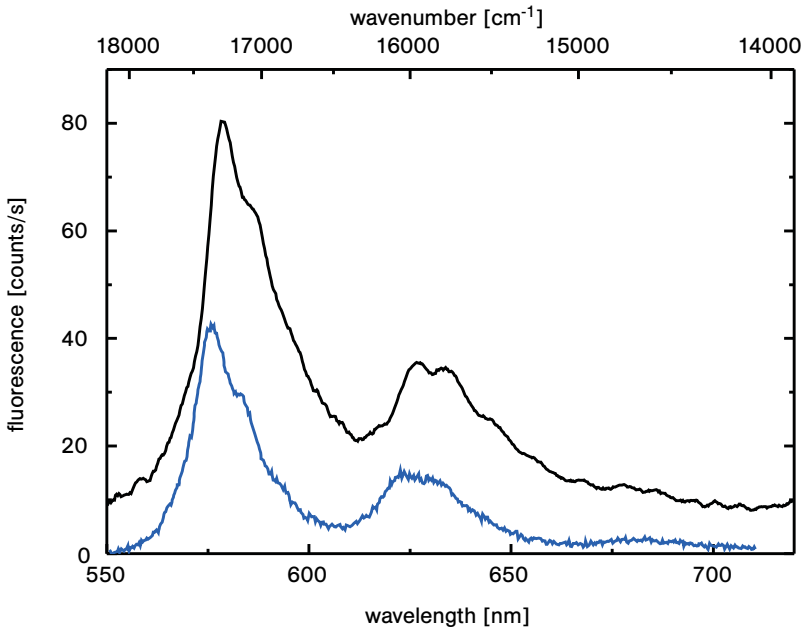

Figure 6.8.: Fluorescence spectrum of terrylene molecules embedded in a crystal on the nanofiber surface, obtained from a sample prepared from solution B for an excitation wavelength of 532 nm (upper trace). The spectrum bears a close resemblance to the single molecule room temperature spectrum of terrylene in p-terphenyl digitized from [184] and shown for comparison in the lower trace.

The fluorescence spectrum obtained from the solution of pure terrylene exhibits a second maximum around 733 nm. This second maximum could originate from the coexistance of excimer states on the fiber surface typically yielding a red-shifted fluorescence with respect to the monomeric emission [134] as has also been observed for PTCDA (cf. Sec. 5.3.3). The suppression of such an excimeric emission in the mixed crystal spectrum might be explained by the interaction with the p-terphenyl crystal as well as by the fact that the absolute terrylene concentration in solution A is almost three orders of magnitude lower than in the pure terrylene solution which renders the formation of excimers much less probable.

In order to speed up the crystallization process and consequently improve the incorporation of terrylene molecules into the p-terphenyl crystals on the fiber surface, an alternative approach to sample preparation can be employed. Instead of slowly approaching oversaturation of the solution by solvent evaporation on the fiber surface, crystals can be prepared directly from an oversaturated solution. For this purpose, a solution with a concentration clearly above the saturation concentration of about 5 mg/ml is heated to approximately 70 °C in an ultrasonic bath until all solute material has been dissolved. If a small amount of the solution is extracted with a pipette, it is cooled down to room temperature rapidly, resulting in a strong oversaturation of the solution which yields a fast crystal growth inside the pipette. Subsequently, a drop of this solution with rapidly grown crystals is brought into contact with the nanofiber waist of a TOF, thereby placing individual crystals on the fiber surface.

The fluorescence spectrum of terrylene molecules embedded in a crystal on the nanofiber surface is shown in Fig. 6.8. The crystal has been prepared by the procedure described above using a solution with a p-terphenyl concentration of 14 mg/ml and a terrylene concentration of 0.83 µg/ml (solution B). The fluorescence spectrum was obtained upon excitation with a

power of about 516 nW in the nanofiber waist of the TOF at a wavelength of 532 nm and it has been corrected for the spectral response of the setup. Due to the insufficient knowledge about the crystal properties (cf. Sec. 3.3), however, a reliable correction for the wavelength dependent coupling to the fiber mode and for self-absorption effects is not possible.

For comparison, a single molecule room temperature spectrum of terrylene in p-terphenyl digitized from [184] has been included in Fig. 6.8 (lower trace). The spectrum obtained from solution B closely resembles the single molecule spectrum, indicating that the terrylene molecules are embedded properly into the p-terphenyl crystal. Both spectra are characterized by three broad bands centered at about 580 nm, 630 nm, and 685 nm. These bands correspond to the vibrational lines observed in low-temperature fluorescence spectra as discussed in detail in [184]. The spectrum obtained from solution B exhibits a slight broadening and a shift of about 3 nm to lower wavelengths with respect to the single molecule spectrum which possibly indicates an inferior crystal quality. The discrepancy in the ratio between the height of the first peak and the height of the second peak can be attributed to residual self-absorption caused by the rather high terrylene density in the crystal.

6.2.2. Determination of crystal quality

In order to determine the quality of crystals obtained from solution processing, four samples prepared from different oversaturated solutions have been studied. The p-terphenyl and terrylene concentrations, c_{pterph} and c_{terr}, of the solutions used as well as the terrylene concentration relative to the p-terphenyl concentration $\tilde{c} = c_{\mathrm{terr}}/c_{\mathrm{pterph}}$ are listed in Tab. 6.1.

Figure 6.9 shows the corresponding fluorescence spectra as a function of the wavenumber. Samples A and B have been excited off-resonantly at a wavelength of 532 nm while samples C and D have been excited resonantly at 578.5 nm. The excitation powers P_{exc} in the nanofiber waist employed for each measurement are also shown in the figure. The power of the excitation light has not been stabilized for any of the measurements, yielding significant fluctuations for the power at 578.5 nm as discussed in Sec. 4.1.1. For the measurements on sample C, the long pass filter for suppression of the background from the excitation light introduced in Sec. 4.1.1 has been omitted, causing a distortion of the spectrum for wavenumbers above approximately 16300 cm^{-1}. For the studies on sample D on the other hand, the cut-on wavelength of 600 nm yields a cut-off of the spectrum at about 16650 cm^{-1}. All spectra were recorded with an effective spectral resolution of about 45 cm^{-1} and have been corrected for the spectral response of the setup shown in Fig. 4.4(a).

The fluorescence signal obtained from sample B is more than twice as high as the one obtained from sample A, even though sample B is excited with only about 75 % of the excitation power of sample A. Since both samples have been prepared from the same solution,

sample	solution	c_{pterph}[mg/ml]	c_{terr} [µg/ml]	$\tilde{c}$
A	B	14	0.83	$59 \cdot 10^{-6}$
B	B	14	0.83	$59 \cdot 10^{-6}$
C	C	14.9	1.19	$79 \cdot 10^{-6}$
D	D	13.9	1.34	$96 \cdot 10^{-6}$

Table 6.1.: P-terphenyl and terrylene concentrations, c_{pterph} and c_{terr}, and relative terrylene concentrations $\tilde{c}$ of the solutions used for the preparation of samples A - D.

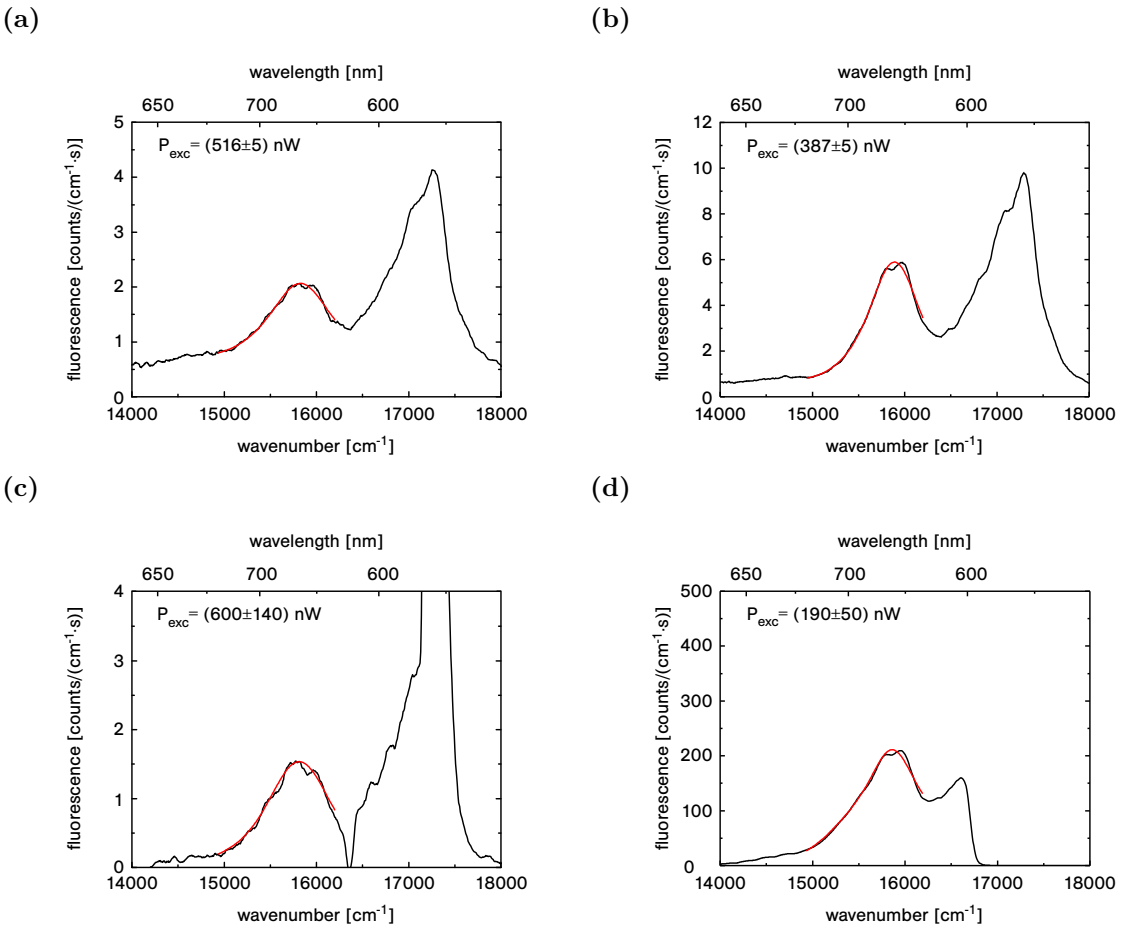

Figure 6.9.: Fluorescence spectra obtained from samples A - D ((a) - (d)) upon excitation with laser light at (a), (b) 532 nm and (c), (d) 578.5 nm with the excitation powers P_{exc} given in the figure. A multiple-peak Gaussian fit to the low-energy emission band is indicated by the red line for each spectrum.

a similar terrylene concentration in the p-terphenyl crystals can be assumed. Therefore, the much higher signal obtained from sample B can be attributed to a bigger crystal or a higher number of crystals on the fiber surface. Moreover, the different height ratio between the two effective vibronic bands visible in the fluorescence spectra of samples A and B could be caused by the stronger effect of self-absorption in sample B due to the higher number of molecules interacting with the guided fiber mode.

The fluorescence signal obtained from sample C is even lower than the one obtained from sample A. Since, within the uncertainty of the power measurement, the excitation power of sample C is comparable to the excitation power of sample A and since the excitation efficiency for sample C is much higher due to the resonant excitation at 578.5 nm, the small fluorescence spectrum indicates a much lower number of molecules interacting with the excitation light in sample C as compared to sample A and B. Moreover, the relative terrylene concentration in solution C is about 30 % higher than in solution B. This suggests that for sample C, the probed crystal is even smaller with a higher dopant concentration, possibly yielding a reduced crystal quality as compared to samples A and B.

For sample D, the fluorescence signal is about two orders of magnitude higher than for the other samples, even though the excitation power is much smaller than the one applied to sample C. Although the relative terrylene concentration in solution D is almost twice as high as in solution C, the strong increase in signal strength cannot be explained by the different terrylene concentrations alone. Instead, it can be concluded that sample D is composed of a very large crystal or several crystals attached to the nanofiber. This means that, most likely, the molecules embedded in the crystal do not couple to the evanescent field of the nanofiber but to a random field generated by the presence of the crystal, as discussed in Sec. 3.3. The pronounced structure of the second spectral band of sample D suggests a high crystal quality which is compatible with the assumption of a large crystal. However, the fluorescence spectrum also exhibits a rather broad wing to smaller wavenumbers. This broad wing possibly indicates an additional contribution to the spectrum from broadened surface molecules or from terrylene molecules embedded in another crystal of lower quality.

In order to further study the crystal quality, a Gaussian fit has been applied to the second emission band centered at approximately $15900\,\mathrm{cm}^{-1}$ for all four samples, as shown in red in Fig. 6.9. The possibilty of a second contribution to the spectra by terrylene molecules with a different environment has been accounted for by a multiple-peak fit with two contributions comprising a uniform center wavenumber.

For all samples, the resulting Gaussian shape agrees well with the wing of the spectral bands and their basic shape around the center. However, the structure around the center of the bands cannot be reproduced by the Gaussian fit. This deviation is due to the fact that a Gaussian distribution is only a rough approximation to the real shape of the emission bands. The shape of the emission bands is rather determined by a Gaussian convolution of the characteristic vibronic emission lines, as discussed in Appendix B.2. For small widths of the Gaussian convolution, i. e., high crystal qualities, the structure of the emission band which stems from the characteristic vibronic spectrum of terrylene is still visible. For convolution with a broad Gaussian, i. e., low crystal qualities, on the other hand, the result is one single structureless effective spectral band. Nevertheless, in both cases, the overall width of the band, which increases with increasing width of the Gaussian convolution, can be approximated by the width of a fitted Gaussian.

The resulting Gaussian widths (FWHM) w_1 and w_2 of both contributing peaks as well as their amplitudes A_1 and A_2 are given in Tab. 6.2. All values exhibit large errors which can be attributed to the very rough approximation by a pure Gaussian distribution and by the assumption of only two distinct molecule classes. Nevertheless, it can be clearly seen that all spectra exhibit a strongly broadened contribution. The fraction of molecules which are embedded properly into a p-terphenyl crystal can be estimated by the value $A_1 \cdot w_1/(A_1 \cdot w_1 + A_2 \cdot w_2)$ given in the last column of Tab. 6.2. For sample D only about 4 % of the signal

sample	w_1 [cm^{-1}]	w_2 [cm^{-1}]	A_1	A_2	$w_1A_1/(w_1A_1 + w_2A_2)$[%]
A	490 ± 101	952 ± 181	221 ± 195	939 ± 83	11 ± 9
B	452 ± 41	868 ± 81	1026 ± 370	2823 ± 242	16 ± 5
C	617 ± 53	1198 ± 126	513 ± 170	928 ± 154	22 ± 7
D	398 ± 26	1168 ± 83	24800 ± 4400	189200 ± 15600	4 ± 1

Table 6.2.: Gaussian widths w_i and amplitudes A_i resulting from a two-peak fit to the low-energy emission band of the spectra obtained from samples A - D.

can be assumed to originate from well-embedded terrylene molecules, while for sample C, the fit results suggest that more than 20 % of the molecules are embedded properly into a p-terphenyl crystal. However, the spectral signature of these molecules is not as narrow as for the other samples.

In conclusion, it has been shown that an increased relative terrylene concentration as in solutions C and D can either lead to a low crystal quality as in sample C or yield a large background signal from molecules excluded from a high quality crystal as in sample D. The high quality of the crystal in sample D may result from a lower growth velocity due to th reduced p-terphenyl concentration in solution D. The lower relative terrylene concentration in solution B yields a high crystal quality, but still only around 30 % of the terrylene molecules interacting with the nanofiber-guided mode can be assumed to be embedded properly in this high-quality crystal. Therefore, to further improve the sample quality, overaturated solutions with a relative terrylene concentration below $\tilde{c} = 59 \cdot 10^{-6}$ should be used.

6.3. Cooling of the sample

For the measurements presented in this thesis, the sample chamber is cooled in the two-stage process described in Sec. 4.4.4, using two different buffer gas pressures during the cooling process. Samples B and C have been cooled with an initial helium buffer gas pressure just below 1.27 bar which results in an almost instantaneous thermalization of the nanofiber with the sample chamber walls and therefore provides the possibility to observe the evolution of the fluorescence spectra as a function of the nanofiber temperature. In order to reduce the probability of a complete breakdown of the TOF transmission during the cooling process as discussed in Sec. 4.4.4, sample D has first been placed inside an evacuated sample chamber which has then been cooled to cryogenic temperatures. After thermalization of the sample chamber with the liquid helium bath, a small amount of helium buffer gas has been inserted into the sample chamber in order to ensure thermalization of the nanofiber with the sample chamber walls. With this method, the influence of the buffer gas on the TOF transmission during the cooling process can be controlled, and it is possible to avoid a complete breakdown of the TOF transmission.

6.3.1. Evolution of the fluorescence spectra with temperature

Figure 6.10 shows two fluorescence spectra measured during the precooling of sample B in the liquid nitrogen dewar. The spectra have been obtained using the same excitation wavelength and power as for the spectrum shown in Fig. 6.9(b).

At a temperature of 257 K (fig. 6.10(a)), the fluorescence spectrum exhibits two broad emission bands around 15900 cm^{-1} and 17200 cm^{-1} with a slight substructure comparable to the room temperature spectrum shown in Fig. 6.9(b). Cooling the sample further to 94 K (fig. 6.10(b)) results in a splitting of the two emission bands into a clearly visible substructure. This can be attributed to the reduction of the homogeneous linewidth which strongly depends on the sample temperature (cf. 3.1.3). As a result, the spectral bands become narrower with a higher peak value.

This narrowing of the spectral bands also causes the effciency of the off-resonant excitation at 532 nm to decrease. Therefore, after precooling of the sample in the liquid nitrogen dewar, fluorescence spectra could only be obtained upon resonant excitation. Figure 6.11 shows two fluorescence spectra measured during the cooling of sample C to liquid helium temperatures

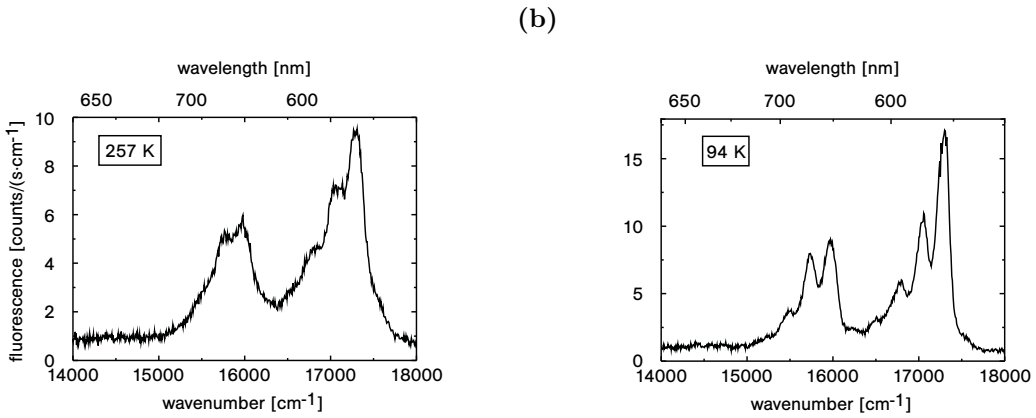

Figure 6.10.: Fluorescence spectra measured during the precooling of sample B in the liquid nitrogen dewar at (a) 257 K and (b) 94 K upon excitation at a wavelength of 532 nm.

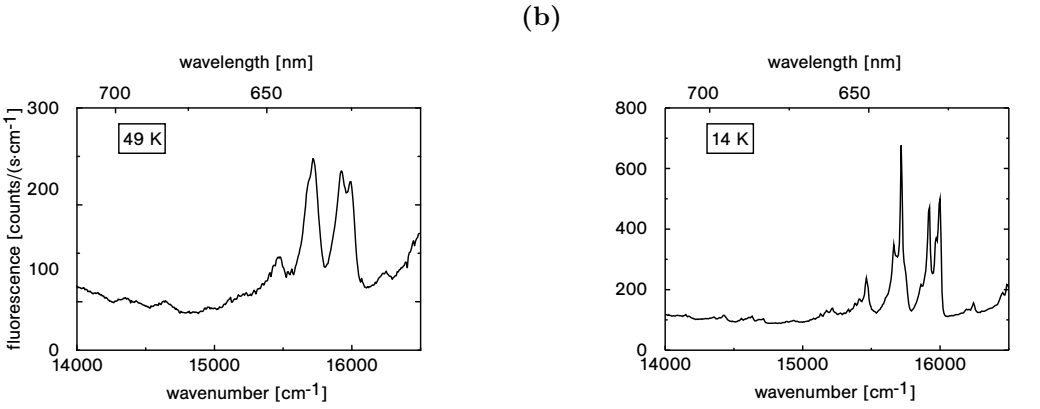

Figure 6.11.: Fluorescence spectra measured during the cooling of sample C to liquid helium temperatures in the bath cryostat at (a) 49 K and (b) 14 K upon excitation at a wavelength of about 578.5 nm.

in the bath cryostat with an effective spectral resolution of about 0.9 nm. The spectra have been obtained upon excitation with a power of about $(129 \pm 13)\,\mu W$ at 578.5 nm and have been corrected for the spectral response of the setup. Note that, in order to increase the signal to noise ratio of the fluorescence measurements with respect to the spectrum shown in Fig. 6.9(c), the excitation power has been increased by about three orders of magnitude.

Due to the influence of the backscattered and reflected excitation light, only the emission at wavenumbers below $16500\,cm^{-1}$ is shown in the figure, which corresponds to the low-energy emission band at $15900\,cm^{-1}$ measured at room temperature. The substructure of this emission band, which is already visible in Fig. 6.10(a), becomes more pronounced with decreasing sample temperature. The resulting narrow spectral lines will be studied in detail in Sec. 6.4.

As discussed above, the thermalization of sample D with the sample chamber walls is slowed down considerably in the evacuated sample chamber. As a result, the fluorescence spectrum obtained from sample D at a measured sample chamber temperature of 4.4 K still exhibits significant broadening, as shown in Fig. 6.12(a). The further evolution of the fluorescence

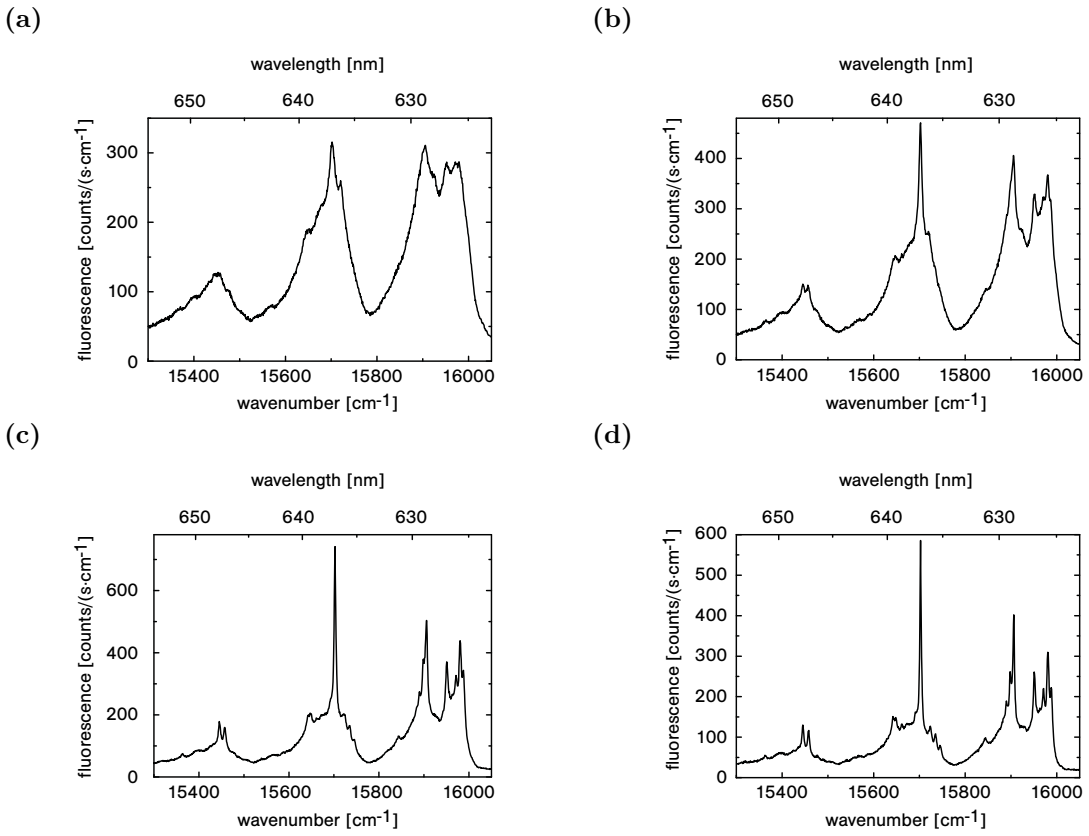

Figure 6.12.: Fluorescence spectrum of sample D (a) before, (b)&(c) during and (d) after the insertion of helium buffer gas into the sample chamber.

spectrum obtained from sample D during the insertion of helium buffer gas into the precooled sample chamber is shown in Fig. 6.12(b) - (d). The spectra have been measured upon excitation with a power of about (117 ± 15) nW at approximately 578.5 nm. In order to resolve the narrow vibronic lines expected for a sample temperature of 4.4 K, the holographic grating of the spectrograph with 1800 l/mm and a resulting effective resolution of about 0.1 nm was used. The efficiency of this grating is reduced by about 15 % as compared to the grating with 300 l/mm used for measurements with a lower resolution [185]. For this grating, no measurement of the spectral response of the setup has been performed. Therefore, the spectra have not been corrected for this effect.

While continuously inserting helium buffer gas, a more and more pronounced substructure of the fluorescence spectrum can be observed (Fig. 6.12(b) and (c)), until a further increase of the pressure does not cause a reduction of the spectral linewidth anymore. The valve at the upper end of the sample rod was closed once the fluorescence signal started to decrease, indicating a sufficient thermal contact between the sample chamber walls and the nanofiber to cool the nanofiber to 4.4 K and to cause the nanofiber transmission to be affected by the effects discussed in Sec. 4.4.4. Figure 6.11(d) shows the fluorescence spectrum with a closed valve and for a buffer gas pressure which is still too low to be measured by the pressure gauge at the upper end of the sample rod. The signal already dropped by about 25 % before the valve could be closed.

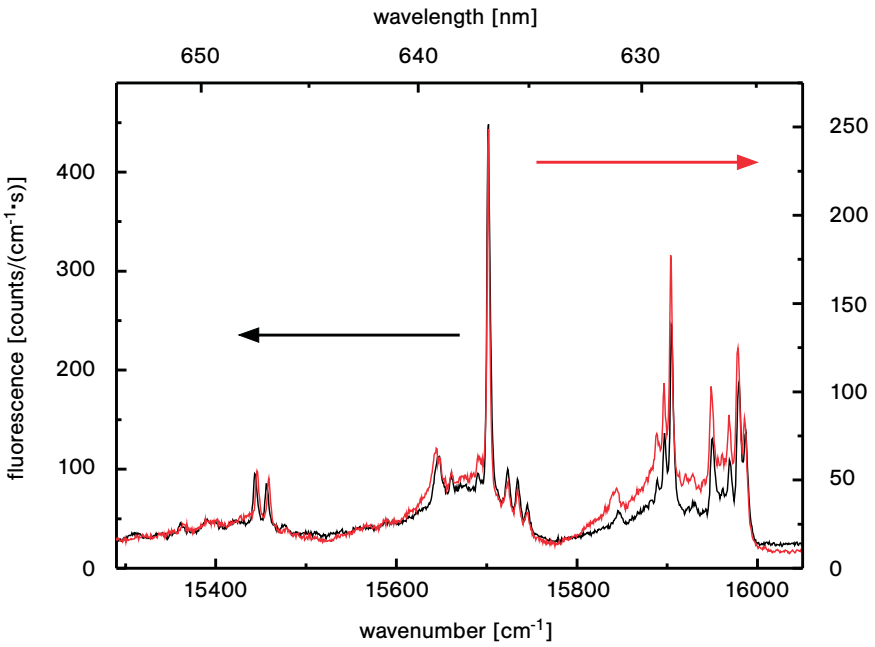

Figure 6.13.: Fluorescence spectra of sample C (black line) and D (red line) at 4.5 K. The typical vibronic transitions are accompanied by phonon sidebands, which are considerably stronger for sample D.

6.4. Low temperature fluorescence spectroscopy

Figure 6.13 shows the fluorescence spectra of sample C and D at a temperature of 4.5 K with an effective spectral resolution of about 0.1 nm (approx. 2.5 cm^{-1}). The spectra have been measured upon excitation with a power of about $((116 \pm 12))\,\mu\mathrm{W}$ and $(117 \pm 15)\,\mathrm{nW}$ at 578.536 nm, respectively. Note that the excitation powers differ by about three orders of magnitude because the excitation power for sample C has been increased in order to increase the signal to noise ratio, as mentioned above. Since sample C was destroyed by a rapid increase of temperature due to technical problems shortly after the measurements presented here, no experiments with lower excitation powers at low temperatures could be performed.

Both spectra exhibit pronounced peaks with vibrational frequencies and intensities very similar to the ones observed by Kummer et al. for terrylene in p-terphenyl [85] and by Myers et al. for terrylene in polyethylene [186]. These vibronic transitions can be assigned to normal modes of the terrylene molecule or the combination of these normal modes [88, 186].

The vibronic transitions are accompanied by clearly visible phonon sidebands which are considerably stronger for sample D. These phonon sidebands can be attributed to a significant excitation of phonon states which can either be caused by saturation of the zero phonon resonances or by a small Debye-Waller factor due to a strong electron-phonon coupling as discussed in Sec. 3.1.3. The likelihood of these two possible explanations will be discussed in the following.

Since the excitation power for sample D is much lower than for sample C, a higher degree of saturation of the zero phonon line of sample D can only be explained by a significantly weaker interaction of the embedded terrylene molecules in sample C with the excitation

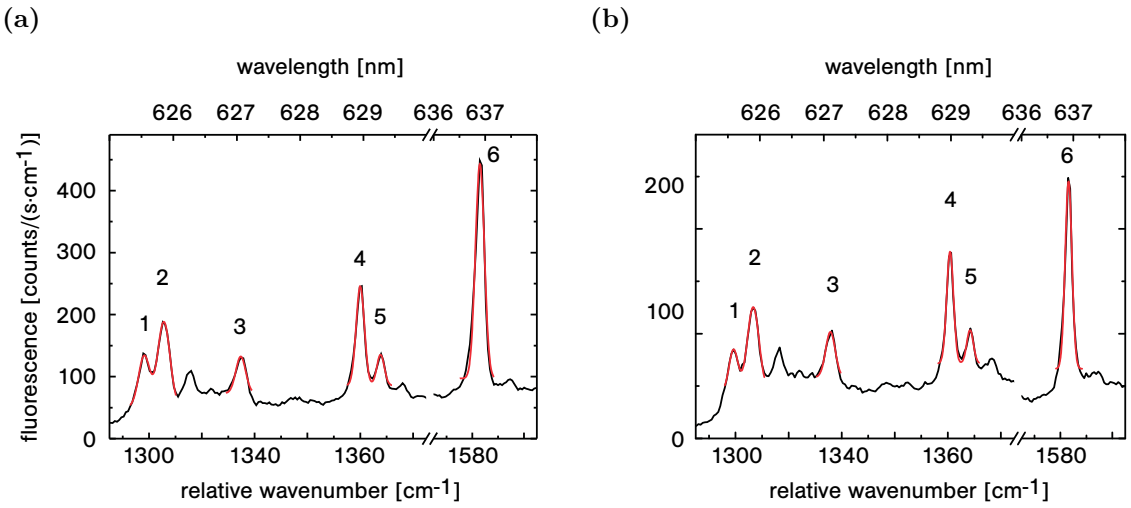

Figure 6.14.: Magnification of the fluorescence spectra from (a) sample C and (b) sample D as a function of the detuning with respect to the purely electronic transition. The Gaussian fits to the vibronic transitions 1 - 6 are indicated by red lines.

light. Such a weaker interaction for sample C can be caused by a disadvantageous position and/or orientation of the p-terphenyl crystal on the nanofiber surface or by a reduction of the excitation light power in the nanofiber due to the negative influence of the cooling process on the TOF transmission (cf. Sec. 4.4.4). To further investigate this possibility, the saturation behaviour of sample D will be studied in the following.

A small Debye-Waller factor can be caused by low crystal quality. Since the coupling of the electronic states of the terrylene molecules to the p-terphenyl crystal lattice depends predominantly on the quality of the crystal structure, a lower crystal quality for sample D as compared to sample C can yield a higher relative strength of the phonon sideband (cf. Sec. 3.1.3).

In order to investigate the observed vibronic transisitions, Fig. 6.14 shows a magnification of the two fluorescence spectra as a function of the detuning with respect to the purely electronic transition at 17285 cm^{-1} (578.536 nm). The six peaks originating from a single vibronic mode are denoted by numbers from 1 to 6 and the Gaussian fits to the peaks are indicated in red.

The spectral positions of the vibronic transitions resulting from the Gaussian fit for both samples are summarized in Tab. 6.3. According to [186], all peaks originate from carbon-carbon stretch vibrations at different positions within the terrylene molecule (last column of Tab. 6.3). Taking into account the spectral resolution of $\pm 2.5\,\mathrm{cm}^{-1}$, the values for samples C and D agree well with each other. The shift of 11 to 14 cm^{-1} to higher energies with respect to the single molecule (SM) spectrum excited at X_2 measured by Kummer et al. [85] (column 4) is possibly due to a slightly different influence of the crystal environment on the vibrational energies of the terrylene molecules. As shown by a comparison with the calculated vibrational energies of a twisted terrylene geometry (column 5), the influence of the crystal environment is slightly weaker for sample C and D than for the measurements presented by Kummer et al. [85].

line #	sample C	sample D	SM X_2 [85]	calculated [85]	description [186]
1	$1298\,\mathrm{cm}^{-1}$	$1299\,\mathrm{cm}^{-1}$	$1285\,\mathrm{cm}^{-1}$	$1345\,\mathrm{cm}^{-1}$	CC stretch of bond parallel to long axis, mainly on end units
2	$1306\,\mathrm{cm}^{-1}$	$1307\,\mathrm{cm}^{-1}$	$1293\,\mathrm{cm}^{-1}$	$1407\,\mathrm{cm}^{-1}$	CC stretch of bond parallel to long axis, mainly on middle units
3	$1335\,\mathrm{cm}^{-1}$	$1336\,\mathrm{cm}^{-1}$	$1324\,\mathrm{cm}^{-1}$	$1474\,\mathrm{cm}^{-1}$	CC stretch
4	$1380\,\mathrm{cm}^{-1}$	$1381\,\mathrm{cm}^{-1}$	$1368\,\mathrm{cm}^{-1}$	$1530\,\mathrm{cm}^{-1}$	CC stretch of outer CC bond adjacent to middle CC bond in end units and of CC outer bonds parallel to long axis
5	$1388\,\mathrm{cm}^{-1}$	$1388\,\mathrm{cm}^{-1}$	$1376\,\mathrm{cm}^{-1}$	$1587\,\mathrm{cm}^{-1}$	-
6	$1583\,\mathrm{cm}^{-1}$	$1583\,\mathrm{cm}^{-1}$	$1574\,\mathrm{cm}^{-1}$	$1597\,\mathrm{cm}^{-1}$	stretch of CC bonds parallel to long axis; end units out of phase relative to center naphtalene

Table 6.3.: Spectral positions of the vibronic transitions for sample C (Column 2) and sample D (column 3). For comparison, the measured and calculated position from [85] for a single molecule (SM) excited at X_2 are shown in column 4 and 5. The origin of the vibrational transition is described in column 6 [186].

6.4.1. Saturation of the zero phonon line

The saturation intensity of terrylene molecules in a p-terphenyl crystal has been calculated by S. Kummer from the measured transition rates of the molecules [88]. The obtained values range between $81\,\mathrm{mW/cm^2}$ and $94\,\mathrm{mW/cm^2}$ at a temperature of 1.4 K. The saturation intensity at 4.5 K can be deduced from these values by taking into account the temperature dependence of the homogeneous linewidth [85], the linewidth dependence of the peak absorption cross section (Eq. (3.17)) and the dependence of the saturation intensity on the absorption cross section (Eq. (3.16)):

$$I_s(4.5\,\mathrm{K}) = I_s(1.4\,\mathrm{K}) \cdot \frac{\gamma_0 + \gamma_p \cdot \exp(-\frac{E_a}{k_B \cdot 4.5\,\mathrm{K}})}{\gamma_0 + \gamma_p \cdot \exp(-\frac{E_a}{k_B \cdot 1.4\,\mathrm{K}})} \approx 5.6 \cdot I_s(1.4\,\mathrm{K}), \tag{6.1}$$

where the temperature independent linewidth of terrylene embedded in p-terphenyl, γ_0, is assumed to be approximately 50 MHz, while $\gamma_p \approx 60000\,\mathrm{MHz}$ and $E_a \approx h \cdot c \cdot 17\,\mathrm{cm}^{-1}$ [85,88]. This results in a saturation intensity between approximately $500\,\mathrm{mW/cm^2}$ and $580\,\mathrm{mW/cm^2}$ at 4.5 K. As discussed in Sec. 3.3, for the crystal-embedded molecules most strongly interacting with the nanofiber-guided mode, the inverse effective mode area is $4.7/\lambda^2$ for a nanofiber diameter of 320 nm and an excitation wavelength of 578.5 nm. Hence, the nanofiber-guided light power needed to saturate the most strongly interacting molecules embedded in the crystal is about 400 pW assuming a polarization of the light field parallel to the dipole moment of the molecules.

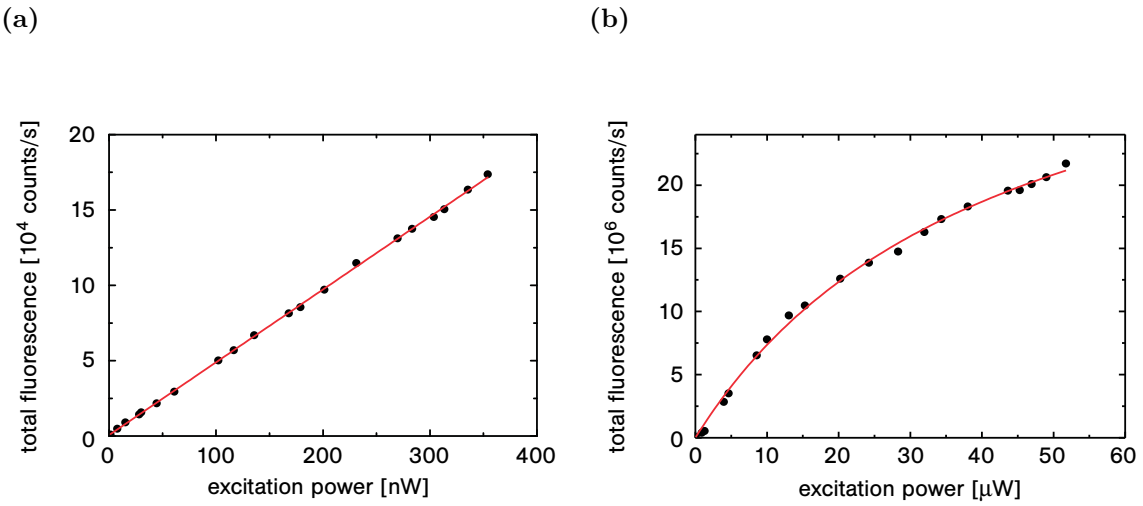

Figure 6.15.: Dependence of the measured fluorescence signal obtained from sample D on the nanofiber-guided light power at 4.5 K. (a) Linear behaviour indicated by the linear fit to the data (red line). (b) A fit to the data (red line) yields a saturation power of (42 ± 3) µW and a saturation count rate of $(3.8 \pm 0.1) \times 10^7$.

Figure 6.15 shows the dependence of the total measured fluorescence signal obtained from sample D on the nanofiber-guided light power. For powers of a few hundred nanowatts as used for the experiments presented here, the fluorescence exhibits a linear dependence on the excitation power, see the linear fit to the data in Fig. 6.15(a). A significant saturation behaviour of sample D can only be observed for higher nanofiber-guided light powers as shown in Fig. 6.15(b). A fit to the data yields a saturation power of (42 ± 3) µW and a measured saturation count rate of $(3.8 \pm 0.1) \times 10^7$. The measured saturation power is therefore about five orders of magnitude higher than the one expected for an ideal coupling of all molecules to the nanofiber-guided mode. This is most likely due to the size of the crystal attached to the nanofiber in sample D. As discussed in Sec. 3.3, large organic crystals can disturb the guided nanofiber mode such that the light is scattered out of the fiber mode and, therefore, the molecules embedded in the crystal couple to a random field generated by the presence of the crystal rather than to the evanescent field of the nanofiber.

The measurements presented in Fig. 6.15 indicate that for an excitation power of 117 nW used to obtain the fluorescence spectrum from sample D shown in Fig. 6.13, the zero phonon transistion does not exhibit significant saturation. Figure 6.16 examplarily shows the fluorescence spectra normalized to the excitation power for three different power values on the order of a few hundres nanowatts. The spectra qualitatively agree well with each other and no saturation is visible in either the zero phonon line or the phonon wings. The pronounced phonon sideband in the fluorescence spectrum of sample D can therefore be predominantly attributed to a strong electron-phonon coupling due to a low quality of the crystal structure.

6.5. Fluorescence excitation spectroscopy

Figure 6.17 shows the long wavelength part of the fluorescence excitation spectrum of sample D at a temperature of 4.5 K. To obtain this spectrum, the total measured fluorescence counts in a wavelength range between 623 and 655 nm (15263 - 16050 cm^{-1}) were normalized to

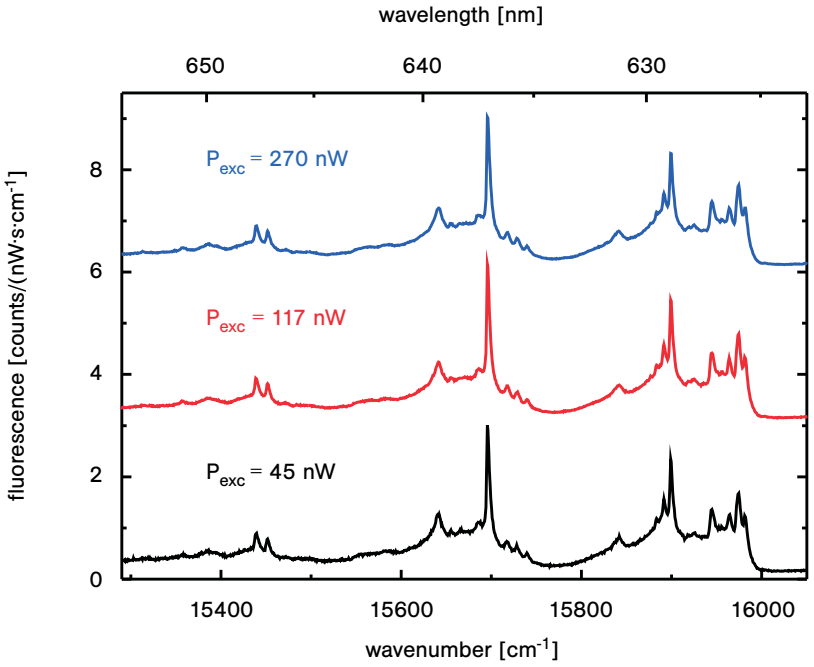

Figure 6.16.: Qualitative comparison of fluorescence spectra for different excitation powers of a few hundres nanowatts. The spectra have been normalized to the nanofiber-guided power.

an excitation power of 1 nW and plotted as a function of the excitation wavenumber. This normalization is possible because the excitation powers between approximately 80 and 230 nW used here ensure a linear relation between the fluorescence signal and the excitation power, as discussed in Sec. 6.4.1.

In Fig. 6.17, some of the characteristic spectral transitions of terrylene molecules embedded in a p-terphenyl crystal measured by Kummer et al. (cf. 6.4) are clearly visible. As already observed in the fluorescence spectra shown in Fig. 6.13, the narrow spectral lines are accompanied by a large phononic background which further supports the assumption that the crystal quality is low for sample D. In [85], the purely electronic transitions X_1 and X_3 of terrylene molecules have been shown to exhibit a low photostability. This possibly explains the fact that they are not visible in the fluorescence excitation spectrum of sample D. Moreover, the signal to noise ratio in view of the large background is probably not high enough to distinguish the higher vibronic transitions which are shifted with respect to the purely electronic transitions X_1 to X_4 by about 245 cm^{-1} (lines 1,3,4, and 7 in Fig. 6.4) and have been observed in absorption by Kummer et al. [85] from the background noise.

Figure 6.18 shows a comparison of the fluorescence excitation spectra obtained from sample D and C around the purely electronic transitions at X_1 to X_4 at 4.5 K. The spectrum displayed in Fig. 6.18(a) is a magnification of the spectrum shown in Fig. 6.17 while the spectrum displayed in Fig. 6.18(b) has been obtained from sample C upon excitation with powers between 70 and 150 µW. The total measured fluorescence counts for each excitation wavelength have been normalized to an excitation power of 1 µW, assuming negligible satu-

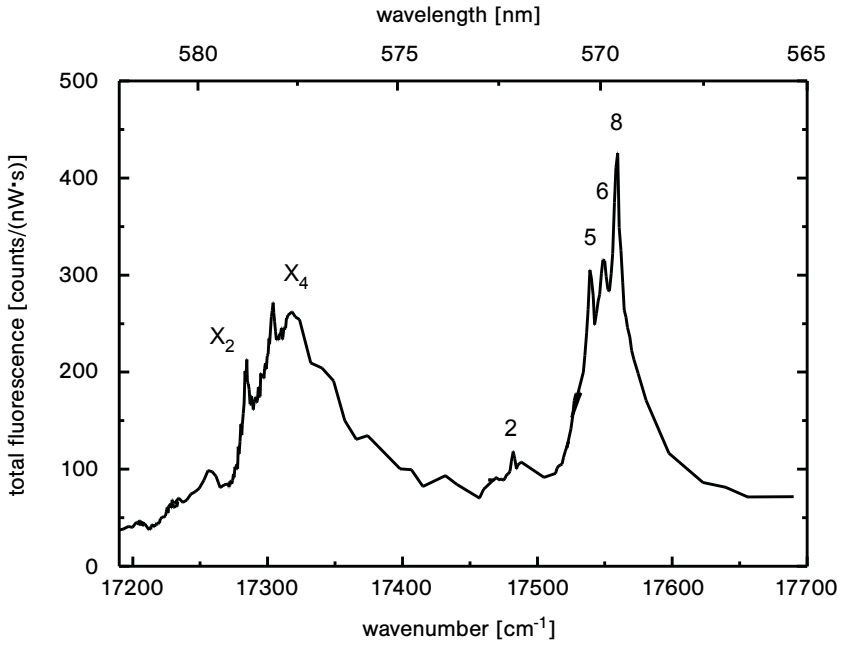

Figure 6.17.: Fluorescence excitation spectrum of sample D at 4.5 K. The visible purely electronic and vibronic transitions are denoted by X_2, X_4, and the numbers 2, 5, 6, and 8 according to the nomenclature in Fig. 6.4.

ration for these excitation powers. Note that the saturation power for sample C could not be measured because the sample was destroyed shortly after the measurements presented here (cf. Sec. 6.4). Nevertheless, the spectrum obtained from sample C exhibits much less pronounced phonon sidebands as compared to the spectrum obtained from sample D, indicating a higher crystal quality as already suggested by the comparison of the fluorescence spectra in Sec. 6.4. Moreover, the purely electronic transition X_1 is clearly visible for sample C. This can be attributed to the much higher intensity of the zero phonon lines relative to the phonon sidebands for sample C as compared to sample D.

crystal site	sample C	sample D	Bridgman crystal [85]
X_1	$(17230.0 \pm 0.2)\,\mathrm{cm}^{-1}$	-	$17230\,\mathrm{cm}^{-1}$
X_2	$(17285.9 \pm 0.1)\,\mathrm{cm}^{-1}$	$(17284.2 \pm 0.2)\,\mathrm{cm}^{-1}$	$17286\,\mathrm{cm}^{-1}$
X_4	$(17304.3 \pm 0.1)\,\mathrm{cm}^{-1}$	$(17303.7 \pm 0.1)\,\mathrm{cm}^{-1}$	$17304\,\mathrm{cm}^{-1}$

Table 6.4.: Comparison of the spectral position of the purely electronic transitions in sample C and D with the values obtained from a Bridgman crystal by Kummer et al. [85].

In order to determine the position of the the purely electronic transitions in sample C and D, a Gaussian fit to the data has been performed. For sample D, a second much broader Gaussian shifted to higher wavenumbers has been included in the fit to account for the large phononic background. A comparison of the results with the values obtained from a Bridgman crystal by Kummer et al. [85] is given in Tab. 6.4. Within the precision of the fit results, the measured values for sample C agree well with the literature values. However, for sample D, the measured spectral positions of the purely electronic transitions deviate from the spectral

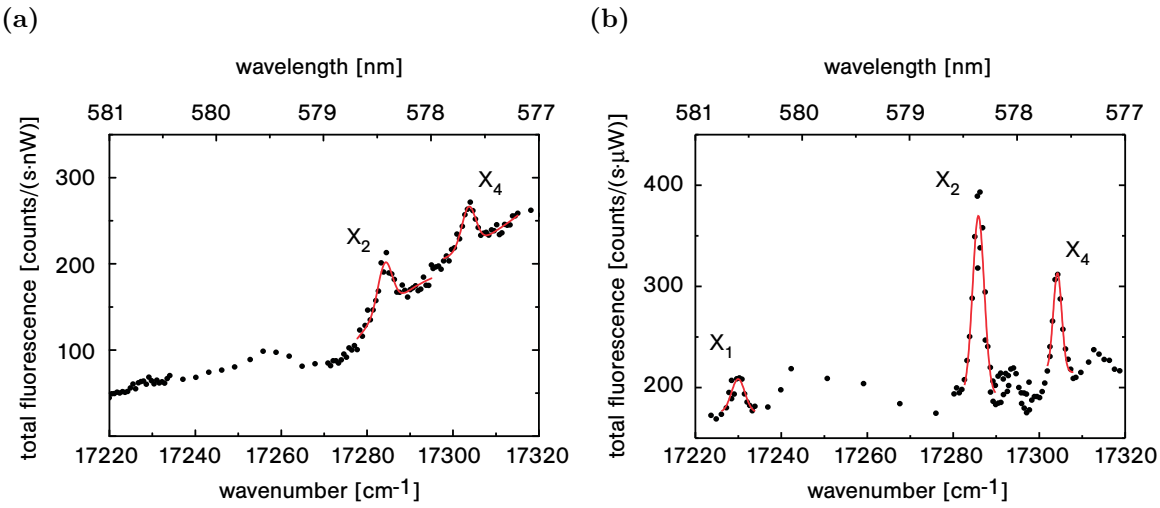

Figure 6.18.: Comparison of the fluorescence excitation spectra obtained from (a) sample D and (b) sample C around the purely electronic transitions X_1 to X_4 at 4.5 K. The position of the visible lines are determined by Gaussian fits to the data (red lines).

positions in the Bridgman crystal and sample C. This could possibly be due to the lower crystal quality of sample D. In [85], it has been shown that the transition frequencies for terrylene embedded in the amorphous host polyethylene are red-shifted with respect to the transition frequencies for terrylene in the crystalline matrix p-terphenyl. Hence, the red shift of the transition frequencies for sample D might be due to amorphous regions in the crystal of sample D.

6.5.1. Inhomogeneous broadening

Figure 6.19 shows a zoom into the purely electronic transition X_2 for sample D with a spectral resolution of 500 MHz. The measurement has been performed with excitation powers ranging between 43 and 166 nW which are small compared to the saturation power determined in Sec. 6.4.1, and, therefore, a normalization of the measured fluorescence counts to an excitation power of 135 nW as desribed above could be performed. In contrast to the fluorescence excitation spectrum shown in Fig. 6.17, the fluorescence has been measured via the entrance slit of the spectrometer and not via the FC fiber adapter of the spectrometer, yielding a lower measured count rate for the same excitation power.

The inhomogeneous broadening of the purely electronic transition shown in Fig. 6.19 is clearly visible. As above, the peak has been fitted with a Gaussian and a second underlying much broader Gaussian shifted to higher wavenumbers, indicated by the red line. The spectral linewidth obtained from the fit of (78 ± 2) GHz ($(2.6 \pm 0.1)\,\mathrm{cm}^{-1}$) is close to the inewidths of the crystals used by Kummer et al. for single molecule experiments of a few GHz [85, 88].

Moreover, Fig. 6.19 clearly shows the pronounced statistical fine structure (SFS) of the X_2 transition. The second trace shown in Fig. 6.19 and taken a few hours after the first trace illustrates the reproducibility of the structure. It is vertically displaced with respect to the first trace for clarity. It has been shown that this structure is stable for days [128]. It arises from statistical variations in the spectral density of absorbing molecules and allows to determine the mean number $\bar{N}$ of molecules with an absorption frequency within one

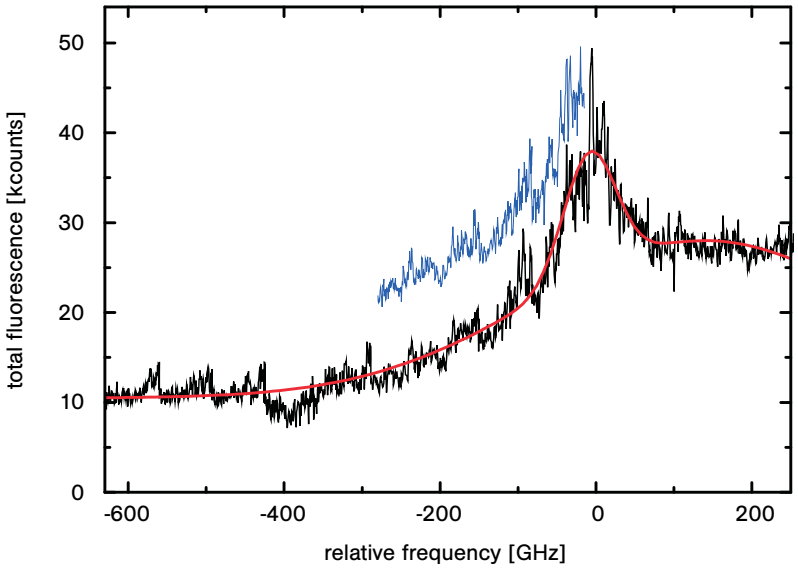

Figure 6.19.: Inhomogeneously broadened fluorescence excitation spectrum around the purely electronic transition X_2 (zero detuning) for sample D at 4.5 K for two subsequent measurements (with the upper trace displaced from the lower). For these measurements, the integration time was 5 s and the measured counts have been normalized to an exitation power of 135 nW. The Lorentzian fit to the data (red line) yields an inhomogeneous linewidth of (78 ± 2) GHz.

homogeneous linewidth of the excitation wavelength via the scaling of the root mean square (rms) amplitude of the statistical fine structure spectra, as well as the homogeneous linewidth γ of the transition via the spectral content of the SFS signal [96, 103].

Determination of molecule number

For zero-background techniques, the rms fluctuations of the statistical fine structure scales with the square root $\sqrt{\bar{N}}$ of the mean number $\bar{N}$ of molecules with an absorption frequency within one homogeneous width of the excitation wavelength [102, 103]. Taking into account the background counts N_{bg}, for each part i of the fluorescence excitation spectrum of sample D shown in Fig. 6.19, the mean number of fluorescence counts $\bar{N}^i_{fl}$ can be expressed by

$$\bar{N}^i_{fl} = \bar{N}^i \cdot N_{1mol} + \bar{N}^i_{bg}, \tag{6.2}$$

where N_{1mol} is the emission rate of one molecule averaged over all detunings within one homogeneous linewidth. The magnitudes $\bar{N}^i_{bg}$ and $\bar{N}^i$ denote the mean number of background counts and the average number of molecules with an absorption frequency within one homogeneous width of the excitation frequency, respectively, for the section i of the fluorescence excitation spectrum. Assuming Poissonian statistics for both, the mean number of molecules with an absorption frequency within one homogeneous width of the excitation frequency and

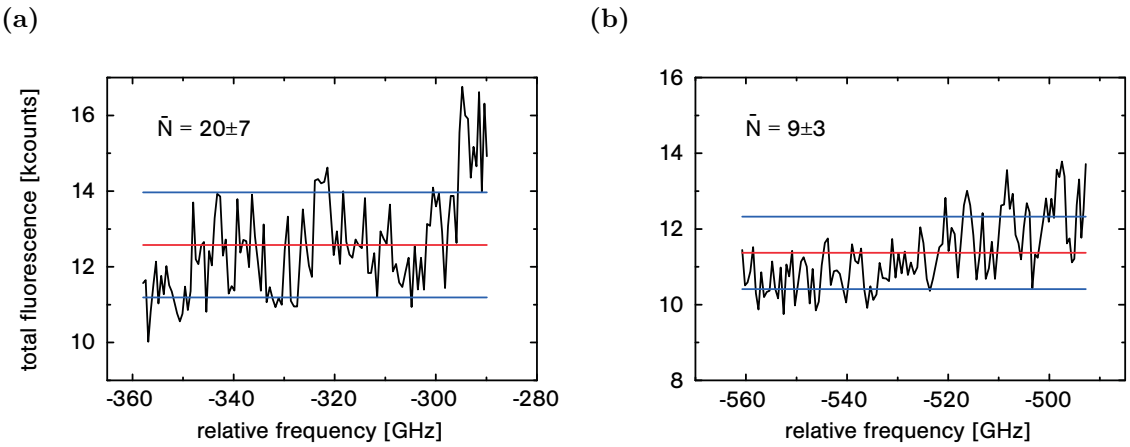

Figure 6.20.: A zoom into two sections of the low energy wing of the fluorescence excitation spectrum shown in Fig. 6.19. The red lines indicate the mean count rate in the respective frequency interval while the blue lines mark the FWHM of the signal variations. A rough estimate for the mean number $\bar{N}$ of molecules with an absorption frequency within one homogeneous linewidth of the excitation wavelength is given for each section.

the total fluorescene counts, the variance of the fluorescence counts is given by

$$\begin{aligned}(\Delta N^i_{fl})^2 &= \bar{N}^i \cdot N^2_{1mol} + \bar{N}^i \cdot N_{1mol} + \bar{N}^i_{bg} \\ &= (N_{1mol} + 1) \cdot \bar{N}^i_{fl} - \bar{N}^i_{bg} \cdot N_{1mol}. \end{aligned} \tag{6.3}$$

In order to determine the average emission rate N_{1mol} of one molecule and the average number of background counts, the low energy wing of the fluorescence excitation spectrum of sample D shown in Fig. 6.19 has been cut into six sections of about 60 GHz width. Two of these sections are exemplarily shown in Fig. 6.20. The mean number of fluorescence counts and the full width half maximum (FWHM) of the signal variations are indicated by the horizontal lines for each section. Figure 6.21 shows the variance of the number of fluorescence counts as a function of the mean number of fluorescence counts for all six sections. A linear fit to the data yields a slope of 313 ± 55 and an intercept of $(-2.2 \pm 0.7) \times 10^6$. Assuming that, for each of these sections, the mean number of molecules is constant and that, for all of these sections, the mean number of background counts is the same ($\bar{N}^i_{bg} =: \bar{N}_{bg} \forall i$), the average emission rate of one molecule and the average number of background counts can be determined from the fit results using Eq. (6.3) to be $N_{1mol} = 312 \pm 55$ and $\bar{N}_{bg} = 7051 \pm 2537$. The large errors of the resulting values indicate that, due to the rough assumptions that have been made here, the values determined from Fig. 6.21 can only be used to obtain a very rough estimate for the mean number $\bar{N}$ of molecules with an absorption frequency within one homogeneous linewidth of the excitation frequency.

The approach described above yields mean numbers $\bar{N}$ of molecules with an absorption frequency within one homogeneous linewidth of the excitation wavelength between 33 and 9 with an error of 35 % for sections of the fluorescence excitation spectrum which are red-shifted between 150 and 630 GHz with respect to the center of the line. For the two sections exemplarily shown in Fig. 6.20, the estimated mean molecule numbers are 20 ± 7 ((a)) and 9 ± 3 ((b)).

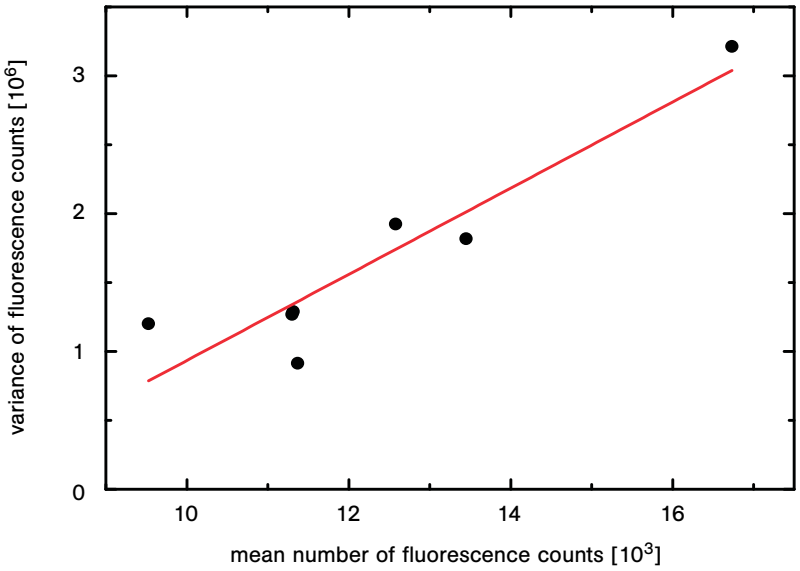

Figure 6.21.: Variance of the fluorescence counts as a function of the mean number of fluorescence counts for six sections of the fluorescence excitation spectrum shown in Fig. 6.19. A linear fit to the data (red line) yields a slope of 313±55 and a y-intercept of $(-2.2\pm0.7)\times10^6$.

Determination of the homogeneous linewidth

For the determination of the homogeneous linewidth γ of the terrylene molecules in sample D from the statistical fine structure, the SFS has to be measured with a sufficiently high resolution. The measurements shown here have been performed at a temperature of 4.5 K measured at the top of the sample chamber. Assuming the same temperature for the sample as for the top of the sample chamber and a temperature-independent linewidth of approximately 50 MHz [162], the expected homogeneous linewidth of the transition can be calculated to be about 260 MHz. Figure 6.22(a) shows the fluorescence excitation spectrum in the low energy wing of the X_2 transition with a spectral resolution of 25 MHz which is sufficient to resolve the expected homogeneous linewidth. Note that, even though the spectrum in Fig. 6.22(a) has been measured with the same integration time and normalized to the same average excitation power, the total number of fluorescence counts is much higher than for the spectra shown in Figs. 6.19 and 6.20. This might be due to a higher background signal for the measurement with higher resolution. The origin of such a possible higher background is, however, unknown.

The autocorrelation function for the spectrum shown in Fig. 6.22(a) can be calculated via [187]:

$$g^{(2)}(\tilde{\nu}) = \frac{\langle I(\nu)\cdot I(\nu+\tilde{\nu})\rangle}{\langle I(\nu)\rangle^2}, \tag{6.4}$$

where the intensities $I(\nu)$ and $I(\nu+\tilde{\nu})$ are given by the measured count rates and a constant intensity $\langle I(\nu)\rangle = \langle I(\nu+\tilde{\nu})\rangle$ has been assumed. The effect of finite sampling has been corrected for as discussed in [187].

Figure 6.22 shows the autocorrelation function $g^{(2)}(\tilde{\nu})$ near $\tilde{\nu} = 0$ which is expected to

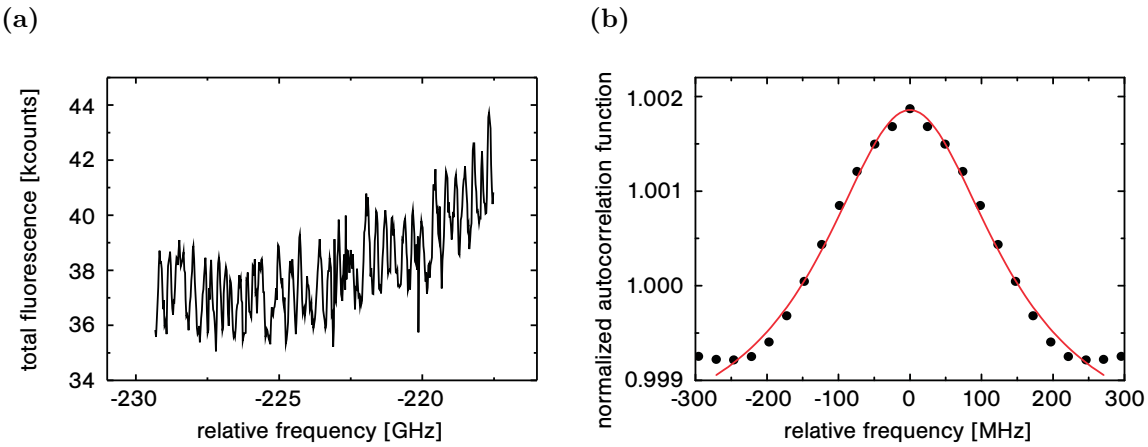

Figure 6.22.: (a) Fluorescence excitation spectrum in the low enery wing of the X_2 transition of sample D (zero detuning) with a spectral resolution of 25 MHz. The shown counts have been measured for an integration time of 5 s and have been normalized to an excitation power of 135 nW. (b) Normalized autocorrelation function of the fluorescence excitation signal shown in (a). The Lorentzian fit to the data (red line) yields a FWHM of (299 ± 16) MHz.

exhibit a Lorentzian line shape with a FWHM equal to 2γ [103]. A Lorentzian fit to the data yields a FWHM of (299 ± 16) MHz and, thus, an estimate for the homogeneous linewidth of $\gamma \approx (150 \pm 8)$ MHz. This result is on the same order of magnitude as the value expected from the temperature dependence of the homogeneous linewidth of 260 MHz determined above. However, the estimated value is lower than the theoretically expected one. This discrepancy might be due to the rough assumption of a constant signal intensity. Moreover, it could possibly indicate that the sample temperature is actually lower than the temperature measured at the top of the sample chamber. To distinguish between these two effects, measurements below 2.2 K could be performed where the linewidth has been found to be almost temperature independent [85].

7. Summary and outlook

Within the framework of this thesis, I have studied the use of tapered optical fibers (TOFs) with a nanofiber waist as a tool for spectroscopy of surface-adsorbed and crystal-embedded organic molecules. The pronounced evanescent field of the light guided by an optical nanofiber provides a highly efficient optical interface for the interaction of light with particles on or near the nanofiber surface. In combination with the efficient coupling of light into and out of the nanofiber via the taper transitions of the TOF, this yields a promising approach for quantum information processing and quantum optical experiments.

For tapered optical fibers, the efficiency of coupling light into and out of the nanofiber depends crucially on the shape of the taper transitions. In order to describe this dependence, I have developed a theoretical model for the light propagation in the taper transition of a TOF. This model considers all three layers of the TOF - the fiber core, the fiber cladding and the surrounding vacuum or air - and provides the local modes for each section of the taper transition. An undisturbed propagation of these local modes can only be assumed, if the radius of the TOF changes sufficiently slowly along the fiber axis. Otherwise, coupling between modes will lead to losses from the fundamental mode to higher order modes. The TOFs used here are fabricated from single mode optical fibers and their nanofiber waists are designed for single mode operation. Therefore, power loss from the fundamental mode to higher order modes results in a reduced overall transmission of the TOF, i. e., a reduced efficiency for coupling light into and out of the nanofiber waist. Using the local modes determined from the theoretical model, I have calculated the coupling between the modes in the taper transitions for different taper diameter profiles. A strong dependence of the theoretically predicted overall TOF transmission on the taper diameter profile could be observed.

In addition, I have studied experimentally how the transmission properties of a TOF depend on the taper diameter profile. The transmission has been shown to be tunable via the local taper angle of the TOF. In particular, I have designed a broadband TOF with a waist diameter of 320 nm and a transmission exceeding 70 % over a wavelength range from 470 nm to 690 nm. This transmission band has been optimized to match the absorption and emission bands of the organic molecules under study in this thesis. At the same time, the overall length of the TOF could be reduced to 81.2 mm in order to ensure the mechanical stability of the TOF. For this TOF, the spectral shape of the transmission theoretically predicted by the coupling of local modes agrees well with the shape of the measured transmission spectrum. However, the measured losses are about two orders of magnitude higher than the theoretically predicted ones. This suggests that the coupling strength is influenced by additional factors which have not been considered in the theoretical calculations. To determine these additional factors, detailed measurements of the fiber surface quality and the refractive index profile in the taper transitions by, e. g., electron microscopy or energy-dispersive X-ray spectroscopy could be made. These studies could identify a possible surface roughness or diffusion of the doping material from the fiber core to the cladding induced by the fiber pulling process. Testing the TOFs for these effects could enable us to even further improve the quality of the flame pulling process and, thereby, the transmission properties of the fabricated TOFs.

The broadband TOF designed in the framework of this thesis has been used for highly sensitive surface spectroscopy of 3,4,9,10-perylene-tetracarboxylic dianhydride (PTCDA). Using absorption spectroscopy at different fiber temperatures, I have studied the homogeneous broadening of the molecular transitions and verified the linear dependence of the homogeneous linewidth on temperature as expected for molecules interacting with a dielectric surface at high temperatures. Due to the high sensitivity of nanofiber-based surface absorption spectroscopy, the reorganization of PTCDA molecules to crystalline films on a second to minutes timescale can be resolved [27]. By studying this reorganization via its spectral signature in different environments and at different temperatures, I have deduced a catalyzing effect due to the presence of water on the nanofiber surface. Moreover, I have observed the formation of charge-transfer (CT) complexes on the nanofiber surface via their spectral signature in the absorption signal. A further study of these CT complexes could possibly give information about localized surface defects on the nanofiber surface and the binding energies of organic molecules to these defects [151].

From interlaced measurements of nanofiber-based absorption and fluorescence spectra of sub-monolayers of PTCDA molecules, the underlying surface coverages for these measurements have been determined to be on the order of 1 ‰. I have analyzed and quantified the observed self-absorption effects due to reabsorption of the emitted fluorescence light by circumjacent surface-adsorbed molecules distributed along the fiber waist. The measured collection efficiency for the emitted fluorescence light by the optical nanofiber mode of about 10 % in one direction of the nanofiber agrees very well with the value calculated for a single dipole emitter on the nanofiber surface [31]. By excitation of surface-adsorbed PTCDA molecules in the low energy tail of the absorption spectrum, I could observe the emission of anti-Stokes fluorescene with a higher energy than the excitation energy. However, for the experimental parameters chosen here, this deduction of energy from the system has been compensated by energy deposition via vibrational relaxation yielding an overall positive energy input into the system. By choosing even lower excitation energies and/or different emitters with fewer non-radiative decay channels, this effect could be used for optical cooling of the nanofiber as already shown for a variety of systems [155–158].

Furthermore, by comparing the spectral position of the fluorescence spectra for two different excitation wavelengths, I have determined the inhomogeneous broadening of the transitions due to the local environment seen by each molecule to be on the same order of magnitude as the homogeneous broadening. Moreover, using fluorescence measurements, I have observed the formation of excited dimers (excimers) on the nanofiber surface. These excimers exhibit a monomeric absorption spectrum and can, therefore, only be studied via fluorescence spectroscopy. Hence, the nanofiber-based approach offers an attractive set of optical spectroscopy tools for the investigation of self-organization of organic semiconductor layers on glass surfaces. A better knowledge of such a self-organization process might prove useful for simpler and cheaper fabrication of organic semiconductor devices which typically is performed under ultra-high vacuum conditions [28].

The observed movement of surface-adsorbed molecules on the nanofiber surface as well as the interaction of the molecules with the surface are disadvantageous for applications in quantum information processing. Therefore, I have performed first experiments with crystal-embedded organic molecules deposited on the nanofiber surface. Such a solid state system is typically very robust and easy to localize.

For this purpose, terrylene-doped para-terphenyl crystals have been grown from solution and subsequently attached to the nanofiber waist of a TOF. The preparation of highly

monocrystalline samples with a low defect concentration which are, at the same time, small enough to not significantly disturb the guided nanofiber mode has proven to be a challenging task. As a result, the nanofiber-crystal-samples studied here can be assumed to consist of organic crystals large enough to significantly disturb the guided nanofiber mode. This most likely leads to a scattering of the light out of the fiber mode and, therefore, the molecules embedded in the crystal couple to a random field generated by the presence of the crystal rather than to the evanescent field of the nanofiber.

However, also for large crystals attached to the fiber surface, the TOF could be used as an interface between light and the crystal-embedded terrylene molecules. Thus, I have performed fluorescence and fluorescence exitation spectroscopy studies of these samples at low temperatures where the homogeneous linewidth of the terrylene molecules is significantly reduced. The characteristic transitions of terrylene in p-terphenyl could be identified and the saturation power for a specific sample could be determined to be $(42 \pm 3)\,\mu W$. Moreover, I have measured the statistical fine structure (SFS) of a purely electronic transition. This structure arises from the statistical variations in the spectral density of absorbing molecules. From the SFS, I found an estimate for the minimum average number of 9 molecules that resonate, within one homogeneous linewidth, with the laser frequency in the low energy wing of the inhomogeneously broadened transition for this specific sample. In addition, an estimate for the homogeneous linewidth of about 150 MHz at 4.5 K could be given.

As a next step, smaller crystals which do not significantly disturb the nanofiber mode should be prepared and attached to the nanofiber in a highly controlled way. The SFS can then be used as a test signal to optimze the detection conditions for single molecules in the sample [102]. Furthermore, the techniques discussed above can be employed to identify single molecules in the inhomogeneously broadened spectrum obtained from a small crystal. After the spectral selection of a single molecule, it can be identified experimentally by autocorrelation measurements.

In essence, this work has shown that tapered optical nanofibers exhibit a high potential for the spectroscopy of organic molecules and for the realization of building blocks for quantum information processing. Using a well-placed dye-doped nanocrystal on the nanofiber surface of a TOF, it should be possible to functionalize the crystal embedded organic molecules as single photon sources or for the storage of information in their internal degrees of freedom.

A. Solution of the scalar wave equation

In the taper transitions of a tapered optical fiber (TOF) the modes extend over core, cladding, and the surrounding medium. Therefore, the local modes of the taper transition should be determined by considering the full three layer system consisting of fiber core and cladding as well as the surrounding vacuum or air. For the considerations presented in this thesis, the solution of the vector wave equation (Eq. (1.6)) in the approximation of weak guidance is used and discussed in detail in the following.

Following the same argument for the weak guidance approximation as in Sec. 1.1.2, the y-component of the electric field takes the form of

$$E_y(\vec{r},t) = R(r)\exp[i(\omega t - \beta z) \pm il\phi], \tag{A.1}$$

where $R(r)$ is a solution of the Bessel differential equation.

For the three layer system, the axial propagation constant β has to lie within the range of values given by

$$k_0 \leq \beta \leq n_{\text{core}} k_0. \tag{A.2}$$

Depending on the value of β, the solutions are either called core modes ($\beta > n_{\text{clad}}k_0$) or cladding modes ($\beta < n_{\text{clad}}k_0$). Due to the properties of the Bessel functions discussed in Sec. 1.1.1, the y-component of the electric field can thus be expressed as

$$\begin{aligned} E_y(r,\phi,z,t) &= AJ_l(hr)\exp[i(\omega t \pm l\phi - \beta z)], & \text{(A.3)}\\ \text{with } h &= \sqrt{n_{\text{core}}^2 k_0^2 - \beta^2} & \text{(A.4)} \end{aligned}$$

in the fiber core ($r \leq a$),

$$\begin{aligned} E_y(r,\phi,z,t) &= BK_l(qr)\exp[i(\omega t \pm l\phi - \beta z)], & \text{(A.5)}\\ \text{with } q &= \sqrt{\beta^2 - n_{\text{vac}}^2 k_0^2} & \text{(A.6)} \end{aligned}$$

in the surrounding vacuum ($r \geq b$),

$$\begin{aligned} E_y(r,\phi,z,t) &= (CI_l(sr) + DK_l(sr))\exp[i(\omega t \pm l\phi - \beta z)], & \text{(A.7)}\\ \text{with } s &= \sqrt{\beta^2 - n_{\text{clad}}^2 k_0^2} & \text{(A.8)} \end{aligned}$$

for core modes in the cladding ($a \leq r \leq b$), and

$$\begin{aligned} E_y(r,\phi,z,t) &= (CJ_l(pr) + DY_l(pr))\exp[i(\omega t \pm l\phi - \beta z)], & \text{(A.9)}\\ \text{with } p &= \sqrt{n_{\text{clad}}^2 k_0^2 - \beta^2} & \text{(A.10)} \end{aligned}$$

for cladding modes in the cladding ($a \leq r \leq b$). The components E_x, E_z, H_x, H_y, and H_z can be expressed in terms of E_y, as described for the LP modes. They are given by

$$
\begin{aligned}
E_x(r,\phi,z,t) &= 0,\\
E_y(r,\phi,z,t) &= AJ_l(hr)\exp[i(\omega t \pm l\phi - \beta z)],\\
E_z(r,\phi,z,t) &= \pm\frac{h\beta}{n_{\text{core}}^2 k_0^2}\frac{A}{2}\Big[J_{l+1}(hr)\exp[\pm i(l+1)\phi] + J_{l-1}(hr)\exp[\pm i(l-1)\phi]\Big]\\
&\quad\times\exp[i(\omega t-\beta z)],
\end{aligned}
\tag{A.11}
$$

$$
\begin{aligned}
H_x(r,\phi,z,t) &= -\frac{\beta}{\omega\mu_0}AJ_l(hr)\exp[i(\omega t \pm l\phi - \beta z)],\\
H_y(r,\phi,z,t) &= 0,\\
H_z(r,\phi,z,t) &= -\frac{ih}{\omega\mu_0}\frac{A}{2}\Big[J_{l+1}(hr)\exp[\pm i(l+1)\phi] - J_{l-1}(hr)\exp[\pm i(l-1)\phi]\Big]\\
&\quad\times\exp[i(\omega t-\beta z)],
\end{aligned}
\tag{A.12}
$$

for all modes inside the core ($r \le a$);

$$
\begin{aligned}
E_x(r,\phi,z,t) &= 0,\\
E_y(r,\phi,z,t) &= BK_l(qr)\exp[i(\omega t \pm l\phi - \beta z)],\\
E_z(r,\phi,z,t) &= \pm\frac{q\beta}{n_{\text{vac}}^2 k_0^2}\frac{B}{2}\Big[K_{l+1}(qr)\exp[\pm i(l+1)\phi] - K_{l-1}(qr)\exp[\pm i(l-1)\phi]\Big]\\
&\quad\times\exp[i(\omega t-\beta z)],
\end{aligned}
\tag{A.13}
$$

$$
\begin{aligned}
H_x(r,\phi,z,t) &= -\frac{\beta}{\omega\mu_0}BK_l(qr)\exp[i(\omega t \pm l\phi - \beta z)],\\
H_y(r,\phi,z,t) &= 0,\\
H_z(r,\phi,z,t) &= -\frac{iq}{\omega\mu_0}\frac{B}{2}\Big[K_{l+1}(qr)\exp[\pm i(l+1)\phi] + K_{l-1}(qr)\exp[\pm i(l-1)\phi]\Big]\\
&\quad\times\exp[i(\omega t-\beta z)],
\end{aligned}
\tag{A.14}
$$

for all modes in the surrounding vacuum ($r \ge b$);

$$
\begin{aligned}
E_x(r,\phi,z,t) &= 0,\\
E_y(r,\phi,z,t) &= (CI_l(sr) + DK_l(sr))\exp[i(\omega t \pm l\phi - \beta z)],\\
E_z(r,\phi,z,t) &= \Big[\mp\frac{s\beta}{n_{\text{clad}}^2 k_0^2}\frac{C}{2}\Big[I_{l+1}(sr)\exp[\pm i(l+1)\phi] - I_{l-1}(sr)\exp[\pm i(l-1)\phi]\Big]\\
&\quad\pm\frac{s\beta}{n_{\text{clad}}^2 k_0^2}\frac{D}{2}\Big[K_{l+1}(sr)\exp[\pm i(l+1)\phi] - K_{l-1}(sr)\exp[\pm i(l-1)\phi]\Big]\Big]\\
&\quad\times\exp[i(\omega t-\beta z)],
\end{aligned}
\tag{A.15}
$$

$$
\begin{aligned}
H_x(r,\phi,z,t) &= -\frac{\beta}{\omega\mu_0}(CI_l(sr)+DK_l(sr))\exp[i(\omega t \pm l\phi - \beta z)],\\
H_y(r,\phi,z,t) &= 0,\\
H_z(r,\phi,z,t) &= \Big[+\frac{is}{\omega\mu_0}\frac{C}{2}\Big[I_{l+1}(sr)\exp[\pm i(l+1)\phi]+I_{l-1}(sr)\exp[\pm i(l-1)\phi]\Big]\\
&\quad -\frac{is}{\omega\mu_0}\frac{D}{2}\Big[K_{l+1}(sr)\exp[\pm i(l+1)\phi]+K_{l-1}(sr)\exp[\pm i(l-1)\phi]\Big]\Big]\\
&\quad \times\exp[i(\omega t-\beta z)], \qquad \text{(A.16)}
\end{aligned}
$$

for core modes in the cladding ($a \le r \le b$), and

$$
\begin{aligned}
E_x(r,\phi,z,t) &= 0,\\
E_y(r,\phi,z,t) &= (CJ_l(pr)+DY_l(pr))\exp[i(\omega t \pm l\phi - \beta z)],\\
E_z(r,\phi,z,t) &= \Big[\pm\frac{p\beta}{n^2_{\text{clad}}k_0^2}\frac{C}{2}\Big[J_{l+1}(pr)\exp[\pm i(l+1)\phi]+J_{l-1}(pr)\exp[\pm i(l-1)\phi]\Big]\\
&\quad \pm\frac{p\beta}{n^2_{\text{clad}}k_0^2}\frac{D}{2}\Big[Y_{l+1}(pr)\exp[\pm i(l+1)\phi]+Y_{l-1}(pr)\exp[\pm i(l-1)\phi]\Big]\Big]\\
&\quad \times\exp[i(\omega t-\beta z)], \qquad \text{(A.17)}
\end{aligned}
$$

$$
\begin{aligned}
H_x(r,\phi,z,t) &= -\frac{\beta}{\omega\mu_0}(CJ_l(pr)+DY_l(pr))\exp[i(\omega t \pm l\phi - \beta z)],\\
H_y(r,\phi,z,t) &= 0,\\
H_z(r,\phi,z,t) &= \Big[-\frac{ip}{\omega\mu_0}\frac{C}{2}\Big[J_{l+1}(pr)\exp[\pm i(l+1)\phi]-J_{l-1}(pr)\exp[\pm i(l-1)\phi]\Big]\\
&\quad -\frac{ip}{\omega\mu_0}\frac{D}{2}\Big[Y_{l+1}(pr)\exp[\pm i(l+1)\phi]-Y_{l-1}(pr)\exp[\pm i(l-1)\phi]\Big]\Big]\\
&\quad \times\exp[i(\omega t-\beta z)], \qquad \text{(A.18)}
\end{aligned}
$$

for cladding modes in the cladding ($a \le r \le b$).

Since the three layer system comprises two interfaces, the continuity condition for the tangential components of the electromagnetic fields leads to eight equations. However, the azimutal components of the fields can be expressed in terms of the x- and y- components, which means that E_ϕ and H_ϕ are proportional and thus impose the same condition on the system. Moreover, the coefficients of $exp[\pm i(l+1)\phi]$ and $exp[\pm i(l-1)\phi]$ have to be equated separately, because the continuity condition must hold for all azimuthal angles. As a result, the continuity of E_z and H_z yield the same equations. Therefore, only four relations for the determination of the constants A B, C, D and the propagation constant β remain. For core

modes, they are given by

$$\begin{aligned} AJ_l(ha) - CI_l(sa) - DK_l(sa) &= 0, \\ A\Big[\frac{h}{n_{\text{core}}^2}J_{l+1}(ha)\Big] + C\Big[\frac{s}{n_{\text{clad}}^2}I_{l+1}(sa)\Big] - D\Big[\frac{s}{n_{\text{clad}}^2}K_{l+1}(sa)\Big] &= 0, \\ BK_l(qb) - CI_l(sb) - DK_l(sb) &= 0, \\ B\Big[\frac{q}{n_{\text{vac}}^2}K_{l+1}(qb)\Big] + C\Big[\frac{s}{n_{\text{clad}}^2}I_{l+1}(sb)\Big] - D\Big[\frac{s}{n_{\text{clad}}^2}K_{l+1}(sb)\Big] &= 0, \end{aligned} \tag{A.19}$$

and for cladding modes, they are given by

$$\begin{aligned} AJ_l(ha) - CJ_l(pa) - DY_l(pa) &= 0, \\ A\Big[\frac{h}{n_{\text{core}}^2}J_{l+1}(ha)\Big] - C\Big[\frac{p}{n_{\text{clad}}^2}J_{l+1}(pa)\Big] - D\Big[\frac{p}{n_{\text{clad}}^2}Y_{l+1}(pa)\Big] &= 0, \\ BK_l(qb) - CJ_l(pb) - DY_l(pb) &= 0, \\ B\Big[\frac{q}{n_{\text{vac}}^2}K_{l+1}(qb)\Big] - C\Big[\frac{p}{n_{\text{clad}}^2}J_{l+1}(pb)\Big] - D\Big[\frac{p}{n_{\text{clad}}^2}Y_{l+1}(pb)\Big] &= 0. \end{aligned} \tag{A.20}$$

Equations (A.19) and (A.20) lead to a nontrivial solution for the constants provided that the determinant of their coefficients equals zero [37]. This requirement determines the mode condition for core modes:

$$\begin{aligned} & I_l(sb)K_l(sa)\Big(\frac{sI_{l+1}(sb)}{n_{\text{clad}}^2 I_l(sb)} + \frac{qK_{l+1}(qb)}{n_{\text{vac}}^2 K_l(qb)}\Big)\Big(\frac{hJ_{l+1}(ha)}{n_{\text{core}}^2 J_l(ha)} - \frac{sK_{l+1}(sa)}{n_{\text{clad}}^2 K_l(sa)}\Big) \\ = \; & I_l(sa)K_l(sb)\Big(\frac{sI_{l+1}(sa)}{n_{\text{clad}}^2 I_l(sa)} + \frac{hJ_{l+1}(ha)}{n_{\text{core}}^2 J_l(ha)}\Big)\Big(\frac{sK_{l+1}(sb)}{n_{\text{clad}}^2 K_l(sb)} - \frac{qK_{l+1}(qb)}{n_{\text{vac}}^2 K_l(qb)}\Big). \end{aligned} \tag{A.21}$$

For cladding modes, the mode condition is given by

$$\begin{aligned} & J_l(pb)Y_l(pa)\Big(\frac{pJ_{l+1}(pb)}{n_{\text{clad}}^2 J_l(pb)} - \frac{qK_{l+1}(qb)}{n_{\text{vac}}^2 K_l(qb)}\Big)\Big(\frac{pY_{l+1}(pa)}{n_{\text{clad}}^2 Y_l(pa)} - \frac{hJ_{l+1}(ha)}{n_{\text{core}}^2 J_l(ha)}\Big) \\ = \; & J_l(pa)Y_l(pb)\Big(\frac{pJ_{l+1}(pa)}{n_{\text{clad}}^2 J_l(pa)} - \frac{hJ_{l+1}(ha)}{n_{\text{core}}^2 J_l(ha)}\Big)\Big(\frac{pY_{l+1}(pb)}{n_{\text{clad}}^2 Y_l(pb)} - \frac{qK_{l+1}(qb)}{n_{\text{vac}}^2 K_l(qb)}\Big). \end{aligned} \tag{A.22}$$

The relations between the constants A, B, C, and D are given by

$$\begin{aligned} \frac{B}{A} &= \frac{J_l(ha)}{K_l(qb)}\frac{(I_l(sb)/I_l(sa))\tilde{U}_{\text{core}} + (K_l(sb)/K_l(sa))U_{\text{core}}}{W_{\text{core}}}, \\ \frac{C}{A} &= \frac{J_l(ha)}{I_l(sa)}\frac{\tilde{U}_{\text{core}}}{W_{\text{core}}}, \\ \frac{D}{A} &= \frac{J_l(ha)}{K_l(sa)}\frac{U_{\text{core}}}{W_{\text{core}}} \end{aligned} \tag{A.23}$$

for core modes and by

$$\begin{aligned}
\frac{B}{A} &= \frac{J_l(ha)}{K_l(qb)} \frac{(J_l(pb)/J_l(pa))\tilde{U}_{\text{clad}} - (Y_l(pb)/Y_l(pa))U_{\text{clad}}}{W_{\text{clad}}}, \\
\frac{C}{A} &= \frac{J_l(ha)}{J_l(pa)} \frac{\tilde{U}_{\text{clad}}}{W_{\text{clad}}}, \\
\frac{D}{A} &= -\frac{J_l(ha)}{Y_l(pa)} \frac{U_{\text{clad}}}{W_{\text{clad}}}
\end{aligned} \tag{A.24}$$

for cladding modes, with

$$\begin{aligned}
U_{\text{core}} &= \Big(\frac{sI_{l+1}(sa)}{n_{\text{clad}}^2 I_l(sa)} + \frac{hJ_{l+1}(ha)}{n_{\text{core}}^2 J_l(ha)}\Big), \\
\tilde{U}_{\text{core}} &= \Big(\frac{sK_{l+1}(sa)}{n_{\text{clad}}^2 K_l(sa)} - \frac{hJ_{l+1}(ha)}{n_{\text{core}}^2 J_l(ha)}\Big), \\
W_{\text{core}} &= \tilde{U}_{\text{core}} + U_{\text{core}} \\
&= \Big(\frac{sK_{l+1}(sa)}{n_{\text{clad}}^2 K_l(sa)} + \frac{sI_{l+1}(sa)}{n_{\text{clad}}^2 I_l(sa)}\Big), \\
U_{\text{clad}} &= \Big(\frac{pJ_{l+1}(pa)}{n_{\text{clad}}^2 J_l(pa)} - \frac{hJ_{l+1}(ha)}{n_{\text{core}}^2 J_l(ha)}\Big), \\
\tilde{U}_{\text{clad}} &= \Big(\frac{pY_{l+1}(pa)}{n_{\text{clad}}^2 Y_l(pa)} - \frac{hJ_{l+1}(ha)}{n_{\text{core}}^2 J_l(ha)}\Big), \\
W_{\text{clad}} &= \tilde{U}_{\text{clad}} - U_{\text{clad}} \\
&= \Big(\frac{pY_{l+1}(pa)}{n_{\text{clad}}^2 Y_l(pa)} - \frac{pJ_{l+1}(pa)}{n_{\text{clad}}^2 J_l(pa)}\Big).
\end{aligned} \tag{A.25}$$

Finally, the constant A can be expressed in terms of the power P of the electromagnetic field which is given by the z-component $\langle S_z \rangle$ of the time-averaged Poynting vector [37]:

$$P = \int_S \langle S_z \rangle dS. \tag{A.26}$$

Note that for the analysis presented here, the only simplifications made are the assumption of a scalar wave equation and a longitudinal component of the electric field which is much smaller than the transverse component. In contrast to the solution of the scalar wave equation for the three layer system presented in the literature [46,57,58], the complete refractive index profile of the three layer system has been considered in all other steps of the analysis, yielding, e. g., a non-zero longitudinal electric field component. Although this approach is still an approximation to the full vector solution, it should yield much more accurate results for the fields extending significantly towards the cladding/vacuum interface.

B. The shape of homogeneously and inhomogeneously broadened absorption and emission spectra with an effective vibronic progression

At room temperature, many molecules exhibit broad absorption and emission spectra without sharp lines. This is due to the fact that the spectra often are the Gaussian convolution of a multitude of vibronic lines originating from the characteristic energy structure of the molecule.

B.1. Absorption

The characteristic absorption lines of a molecule can be expressed by the sum of Dirac delta functions centered at the characteristic transition energies μ_i of the molecule with amplitudes A_i:

$$S^0_{\mathrm{abs}}(E) = \sum_i A_i \delta(E - \mu_i). \tag{B.1}$$

The homogeneous broadening of the transition is taken into account by a Gaussian convolution with a width σ_{hom}. Further, the inhomogeneous broadening results in a shift by μ_j and a weighting factor for each class j of molecules. Assuming a Gaussian line shape for the inhomogeneous broadening as typical for molecules in solutions, amorphous materials or on surfaces (cf. Sec. 3.1.3), the absorption spectrum caused by a class j of molecules can be described by

$$\begin{aligned} S^j_{\mathrm{abs}}(E) &= \int S^0_{\mathrm{abs}}(E - \tilde{E}) \cdot \frac{1}{\sigma_{\mathrm{hom}}\sqrt{2\pi}} \cdot \exp\left(\frac{-(E-\mu_j)^2}{2\sigma^2_{\mathrm{hom}}}\right) \\ &\quad \times \frac{1}{\sigma_{\mathrm{inhom}}\sqrt{2\pi}} \cdot \exp\left(\frac{-\mu_j^2}{2\sigma^2_{\mathrm{inhom}}}\right) \mathrm{d}\tilde{E} \\ &= \frac{1}{2\pi\sigma_{\mathrm{hom}}\sigma_{\mathrm{inhom}}} \sum_i A_i \cdot \exp\left(\frac{-(E-\mu_i-\mu_j)^2}{2\sigma^2_{\mathrm{hom}}}\right) \cdot \exp\left(\frac{-\mu_j^2}{2\sigma^2_{\mathrm{inhom}}}\right). \end{aligned} \tag{B.2}$$

The total absorption spectrum can be determined by integration over all possible shifts μ_j due to inhomogeneous broadening effects:

$$\begin{aligned} S^{tot}_{\mathrm{abs}}(E) &= \int S^j_{\mathrm{abs}}(E) \mathrm{d}\mu_j \\ &= \frac{1}{\sqrt{2\pi}\sqrt{\sigma^2_{\mathrm{hom}} + \sigma^2_{\mathrm{inhom}}}} \sum_i A_i \cdot \exp\left(\frac{-(E-\mu_i)^2}{2(\sigma^2_{\mathrm{hom}} + \sigma^2_{\mathrm{inhom}})}\right). \end{aligned} \tag{B.3}$$

The expectation value for the transition energy in the spectrum $S_{abs}^{tot}(E)$ can be calculated as

$$\begin{aligned} \langle E \rangle &= \frac{1}{\sum_i A_i} \cdot \sum_i \int E \cdot S_{\mathrm{abs}}^{tot}(E) \mathrm{d}E \\ &= \frac{\sum_i A_i \mu_i}{\sum_i A_i} \end{aligned} \tag{B.4}$$

and the expectation value for the squared transition energy is as follows:

$$\begin{aligned} \left\langle E^2 \right\rangle &= \frac{1}{\sum_i A_i} \cdot \sum_i \int E^2 \cdot S_{\mathrm{abs}}^{tot}(E) \mathrm{d}E \\ &= \frac{\sum_i A_i (\sigma_{\mathrm{hom}}^2 + \sigma_{\mathrm{inhom}}^2 + \mu_i^2)}{\sum_i A_i}. \end{aligned} \tag{B.5}$$

Hence, the variance of the total absorption band is given by

$$\begin{aligned} \sigma_{\mathrm{tot}}^2 &= \left\langle E^2 \right\rangle - \langle E \rangle^2 \\ &= \sigma_{\mathrm{hom}}^2 + \sigma_{\mathrm{inhom}}^2 + \frac{\sum_i A_i \mu_i^2}{\sum_i A_i} - \left(\frac{\sum_i A_i \mu_i}{\sum_i A_i} \right)^2. \end{aligned} \tag{B.6}$$

As a result, the width of the absorption band can be expressed by:

$$\begin{aligned} w_{\mathrm{tot}} &= \sigma_{\mathrm{tot}} \cdot \sqrt{8 \ln 2} \\ &= \sqrt{8 \ln 2} \cdot \sqrt{\sigma_{\mathrm{hom}}^2 + \sigma_{\mathrm{inhom}}^2 + \frac{\sum_i A_i \mu_i^2}{\sum_i A_i} - \left(\frac{\sum_i A_i \mu_i}{\sum_i A_i} \right)^2}. \end{aligned} \tag{B.7}$$

It is, therefore, determined by the standard deviations σ_{hom} and σ_{inhom} of the spectral lines as well as by the spectral positions μ_i and relative amplitudes A_i of the constituting lines.

B.2. Emission

In analogy to absorption, the characteristic emission lines of a molecule can be expressed by the sum of Dirac delta functions centered at characteristic transition energies $\tilde{\mu}_i$ of the molecule with amplitudes B_i:

$$S_{\mathrm{em}}^0(E) = \sum_i B_i \delta(E - \tilde{\mu}_i). \tag{B.8}$$

For rigid molecules, these emission lines are expected to be the mirror image of the characteristic absorption lines.

Assuming an equally strong excitation of all molecule classes, the emission spectrum for a class j of molecules can be described following the same argumentation as for the absorption spectrum:

$$\begin{aligned} S_{\mathrm{em}}^j(E) &= \int S_{\mathrm{em}}^0(E - \tilde{E}) \cdot \frac{1}{\sigma_{\mathrm{hom}} \sqrt{2\pi}} \cdot \exp\left(\frac{-(E - \mu_j)^2}{2\sigma_{\mathrm{hom}}^2} \right) \\ &\quad \times \frac{1}{\sigma_{\mathrm{inhom}} \sqrt{2\pi}} \cdot \exp\left(\frac{-\mu_j^2}{2\sigma_{\mathrm{inhom}}^2} \right) \mathrm{d}\tilde{E} \\ &= \frac{1}{2\pi \sigma_{\mathrm{hom}} \sigma_{\mathrm{inhom}}} \sum_i B_i \cdot \exp\left(\frac{-(E - \tilde{\mu}_i - \mu_j)^2}{2\sigma_{\mathrm{hom}}^2} \right) \cdot \exp\left(\frac{-\mu_j^2}{2\sigma_{\mathrm{inhom}}^2} \right). \end{aligned} \tag{B.9}$$

Again, a Gaussian line shape has been assumed for the homogeneous and inhomogeneous broadening of the transitions.

Integration over all possible shifts μ_j due to inhomogeneous broadening effects renders the total emission spectrum:

$$\begin{aligned} S_{\mathrm{em}}^{\mathrm{tot}}(E) &= \int S_{\mathrm{em}}^{j}(E)\mathrm{d}\mu_j \\ &= \frac{1}{\sqrt{2\pi}\sqrt{\sigma_{\mathrm{hom}}^2+\sigma_{\mathrm{inhom}}^2}}\sum_i B_i \cdot \exp\left(\frac{-(E-\tilde{\mu}_i)^2}{2(\sigma_{\mathrm{hom}}^2+\sigma_{\mathrm{inhom}}^2)}\right). \end{aligned} \tag{B.10}$$

As for the absorption spectrum, the variance of the emission spectrum is proportional to the variances σ_{hom}^2 and $\sigma_{\mathrm{inhom}}^2$ caused by homogeneous and inhomogeneous broadening effects, respectively, and depends further on the spectral positions $\tilde{\mu}_i$ and relative amplitudes B_i of the constituting lines.

For excitation of the molecules with light of a narrow band laser source, it cannot be assumed that all molecule classes are excited equally strong. Here, the excitation strength for each molecule class has to be taken into account when calculating the total emission spectrum. The emission spectrum for a class j of molecules therefore has to be weighted not only by the Gaussian distribution of the inhomogeneous broadening but also by the excitation efficiency determined by the energy difference between the excitation energy and the position of the characteristic absorption lines $(\mu_l - \mu_j)$ for the molecule class j, where μ_l is the position of the characteristic absorption line and μ_j is the shift for the molecule class j:

$$\begin{aligned} S_{\mathrm{em}}^{j}(E,E_{\mathrm{exc}}) &= \int S_{\mathrm{em}}^{0}(E-\tilde{E})\cdot\frac{1}{\sigma_{\mathrm{hom}}\sqrt{2\pi}}\cdot\exp\left(\frac{-(E-\mu_j)^2}{2\sigma_{\mathrm{hom}}^2}\right) \\ &\quad\times\frac{1}{\sigma_{\mathrm{inhom}}\sqrt{2\pi}}\cdot\exp\left(\frac{-\mu_j^2}{2\sigma_{\mathrm{inhom}}^2}\right) \\ &\quad\times\frac{1}{\sigma_{\mathrm{hom}}\sqrt{2\pi}}\cdot\sum_l A_l\exp\left(\frac{-(E_{\mathrm{exc}}-\mu_l-\mu_j)^2}{2\sigma_{\mathrm{hom}}^2}\right)\mathrm{d}\tilde{E} \\ &= \frac{1}{2\pi\sigma_{\mathrm{hom}}^2\sigma_{\mathrm{inhom}}}\sum_{i,l} B_iA_l\cdot\exp\left(\frac{-(E-\tilde{\mu}_i-\mu_j)^2}{2\sigma_{\mathrm{hom}}^2}\right) \\ &\quad\times\exp\left(\frac{-\mu_j^2}{2\sigma_{\mathrm{inhom}}^2}\right)\cdot\exp\left(\frac{-(E_{\mathrm{exc}}-\mu_l-\mu_j)^2}{2\sigma_{\mathrm{hom}}^2}\right). \end{aligned} \tag{B.11}$$

The total emission spectrum is obtained by integration over all possible shifts μ_j due to inhomogeneous broadening effects:

$$\begin{aligned} S_{\mathrm{em}}^{\mathrm{tot}}(E, E_{\mathrm{exc}}) &= \int S_{\mathrm{em}}^{j}(E, E_{\mathrm{exc}}) \mathrm{d}\mu_j \\ &= \frac{1}{\sqrt{2\pi}\sqrt{\sigma_{\mathrm{hom}}^2 + \sigma_{\mathrm{inhom}}^2}} \cdot \frac{1}{\sqrt{2\pi}\sigma_{\mathrm{hom}}\sqrt{1 + \frac{\sigma_{\mathrm{inhom}}^2}{\sigma_{\mathrm{hom}}^2 + \sigma_{\mathrm{inhom}}^2}}} \\ &\quad \times \sum_{i,l} B_i A_l \cdot \exp\left(\frac{-(E_{\mathrm{exc}} - \mu_l)^2}{2(\sigma_{\mathrm{hom}}^2 + \sigma_{\mathrm{inhom}}^2)}\right) \\ &\quad \times \exp\left(\frac{-(E - \tilde{\mu}_i - \frac{\sigma_{\mathrm{inhom}}^2}{\sigma_{\mathrm{inhom}}^2 + \sigma_{\mathrm{hom}}^2} \cdot (E_{\mathrm{exc}} - \mu_l))^2}{2\sigma_{\mathrm{hom}}^2(1 + \frac{\sigma_{\mathrm{inhom}}^2}{\sigma_{\mathrm{hom}}^2 + \sigma_{\mathrm{inhom}}^2})}\right). \end{aligned} \tag{B.12}$$

The first exponential function in this expression accounts for the fact that the emission will be stronger the closer the excitation energy E_{exc} is to the center μ_l of a characteristic absorption line. This effect is significantly influenced by the width of the absorption lines given by $\sigma_{\mathrm{hom}}^2 + \sigma_{\mathrm{inhom}}^2$. The second exponential function describes the shift of the different contributions to the emission spectrum due to the inhomogeneous broadening of the spectral lines. This shift is determined by the difference between the excitation energy E_{exc} and the characteristic transition energies μ_l of the molecule. If the inhomogeneous broadening dominates the homogeneous broadening ($\sigma_{\mathrm{hom}} \ll \sigma_{\mathrm{inhom}}$), this shift is maximized. If, however, the homogeneous broadening dominates the inhomogeneous broadening ($\sigma_{\mathrm{inhom}} \ll \sigma_{\mathrm{hom}}$), the shift is negligible and the spectral form approaches the form given in Eq. (B.10) weighted by the excitation energy-dependent absorption.

C. Experimental details

C.1. Continuity of upward air flow from the crucible to the nanofiber at ambient conditions

The continuity of the upward air flow from the crucible in the setup shown in Fig. 4.5, which is crucial for a constant flow of molecules from the crucible to the nanofiber surface, can be determined by the time-resolved measurement of the temperature at the position of the TOF by replacing the TOF with a horizontally oriented thermocouple.

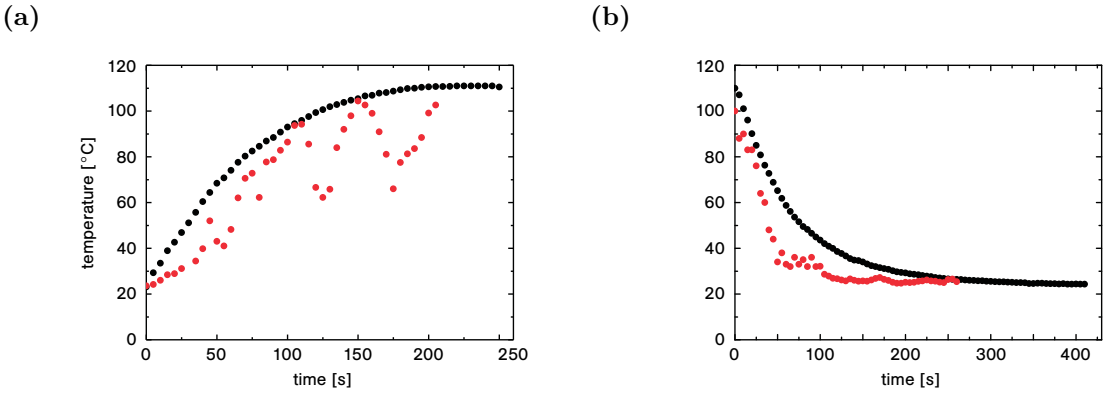

Figure C.1.: Temperature evolution at the position of the TOF for switching the heating current to 2.35 A (a) and back to 0 A (b). The evolution is much more stable for a closed box (black dots) than for an open box (red dots).

Figure C.1(a) shows the measured temperature at the position of the TOF as a function of time after switching the current of the crucible heater to 2.35 A. It is apparent from the figure that the temperature evolution and, thus, the characteristics of the air flow differ strongly depending on whether the box around the setup is open (red dots) or closed (black dots) at the top. For a closed box, the system thermalizes to about 110 °C at the position of the TOF after a time of three to four minutes. This behaviour corresponds to the thermalization of the crucible when the heating current is switched from 0.00 A to 2.35 A. In contrast, no thermal equilibrium can be achieved with an open box. This suggests that air which enters the box from the top disturbes the upward air flow from the crucible, therefore causing turbulences at the position of the TOF which rapidly change the temperature. Hence, the box has to be closed to ensure a continuous air flow and, thus, a constant flow of molecules from the crucible to the nanofiber surface. Figure C.1(b) shows the temperature evolution at the position of the TOF after the heating current has been switched off. For a closed box (black dots), the system thermalizes to room temperature within three to four minutes. However, cooling of the TOF is much faster for an open box due to the cold air flow from above.

Bibliography

[1] J. Hwang and E. A. Hinds, *Dye molecules as single-photon sources and large optical nonlinearities on a chip*, New J. Phys. **13**, 085009 (2011).

[2] R. Lettow, Y. L. A. Rezus, A. Renn, G. Zumofen, E. Ikonen, S. Götzinger, and V. Sandoghdar, *Quantum interference of tunably indistinguishable photons from remote organic molecules*, Phys. Rev. Lett. **104**, 123605 (2010).

[3] K. J. Vahala, *Optical microcavities*, Nature **424**, 839 (2003).

[4] http://www.nobelprize.org/nobel_prizes/physics/laureates/2012/advanced-physicsprize2012.pdf, (2012).

[5] H. J. Carmichael, *Quantum trajectory theory for cascaded open systems*, Phys. Rev. Lett. **70**, 2273 (1993).

[6] Y. L. A. Rezus, S. G. Walt, R. Lettow, A. Renn, G. Zumofen, S. Götzinger, and V. Sandoghdar, *Single-photon spectroscopy of a single molecule*, Phys. Rev. Lett. **108**, 093601 (2012).

[7] J. Bures and R. Ghosh, *Power density of the evanescent field in the vicinity of a tapered fiber*, J. Opt. Soc. Am. A **16**, 1992 (1999).

[8] G. Brambilla, *Optical fibre nanowires and microwires: a review*, J. Opt. **12**, 043001 (2010).

[9] J. Villatoro and D. Monzón-Hernández, *Fast detection of hydrogen with nano fiber tapers coated with ultra thin palladium layers*, Opt. Express **13**, 5087 (2005).

[10] P. Polynkin, A. Polynkin, N. Peyghambarian, and M. Mansuripur, *Evanescent field-based optical fiber sensing device for measuring the refractive index of liquids in microfluidic channels*, Opt. Lett. **30**, 1273 (2005).

[11] L. Zhang, F. Gu, J. Lou, X. Yin, and L. Tong, *Fast detection of humidity with a subwavelength-diameter fiber taper coated with gelatin film*, Opt. Express **16**, 13349 (2008).

[12] T. A. Birks, W. J. Wadsworth, and P. St. J. Russell, *Supercontinuum generation in tapered fibers*, Opt. Lett. **25**, 1415 (2000).

[13] W. J. Wadsworth, A. Ortigosa-Blanch, J. C. Knight, T. A. Birks, T.-P. Martin Man, and P. St. J. Russell, *Supercontinuum generation in photonic crystal fibers and optical fiber tapers: a novel light source*, J. Opt. Soc. Am. B **19**, 2148 (2002).

[14] J. Teipel, K. Franke, D. Türke, F. Warken, D. Meiser, M. Leuschner, and H. Giessen, *Characteristics of supercontinuum generation in tapered fibers using femtosecond laser pulses*, Appl. Phys. B **77**, 245 (2003).

[15] S. Leon-Saval, T. Birks, W. Wadsworth, P. St. J. Russell, and M. Mason, *Supercontinuum generation in submicron fibre waveguides*, Opt. Express **12**, 2864 (2004).

[16] V. Grubsky and A. Savchenko, *Glass micro-fibers for efficient third harmonic generation*, Opt. Express **13**, 6798 (2005).

[17] R. R. Gattass, G. T. Svacha, L. Tong, and E. Mazur, *Supercontinuum generation in submicrometer diameter silica fibers*, Opt. Express **14**, 9408 (2006).

[18] U. Wiedemann, K. Karapetyan, C. Dan, D. Pritzkau, W. Alt, S. Irsen, and D. Meschede, *Measurement of submicrometre diameters of tapered optical fibres using harmonic generation*, Opt. Express **18**, 7693 (2010).

[19] G. J. Pendock, H. S. MacKenzie, and F. P. Payne, *Dye lasers using tapered optical fibers*, Appl. Optics, **32**, 5236 (1993).

[20] X. S. Jiang, Q. H. Song, L. Xu, J. Fu, and L. M. Tong, *Microfiber knot dye laser based on the evanescent-wave-coupled gain*, Appl. Phys. Lett. **90**, 233501 (2007).

[21] G. Sagué, E. Vetsch, W. Alt, D. Meschede, and A. Rauschenbeutel, *Cold-atom physics using ultrathin optical fibres: light-induced dipole forces and surface interactions*, Phys. Rev. Lett. **99**, 163602 (2007).

[22] K. P. Nayak, P. N. Melentiev, M. Morinaga, F. Le Kien, V. I. Balykin, and K. Hakuta, *Optical nanofiber as an efficient tool for manipulating and probing atomic fluorescence*, Opt. Express **15**, 5431 (2007).

[23] K. P. Nayak and K. Hakuta, *Single atoms on an optical nanofibre*, New J. Phys. **10**, 053003 (2008).

[24] M. J. Morrissey, K. Deasy, Y. Q. Wu, S. Chakrabarti, and S. N. Chormaic, *Tapered optical fibers as tools for probing magneto-optical trap characteristics*, Rev. Sci. Instrum. **80**, 053102 (2009).

[25] E. Vetsch, D. Reitz, G. Sagué, R. Schmidt, S. T. Dawkins, and A. Rauschenbeutel, *Optical interface created by laser-cooled atoms trapped in the evanescent field surrounding an optical nanofiber*, Phys. Rev. Lett. **104**, 203603 (2010).

[26] A. Messica, A. Greenstein, and A. Katzir, *Theory of fiber-optic, evanescent-wave spectroscopy and sensors*, Appl. Optics **35**, 2274 (1996).

[27] F. Warken, E. Vetsch, D. Meschede, M. Sokolowski, and A. Rauschenbeutel, *Ultra-sensitive surface absorption spectroscopy using sub-wavelength diameter optical fibers*, Opt. Express **15**, 11952 (2007).

[28] H. Proehl, *Optische Eigenschaften ultradünner PTCDA & TiOPc Einzel- und Heteroschichten*, Dissertation, Technische Universität Dresden (2006).

[29] G. Wrigge, I. Gerhardt, J. Hwang, G. Zumhofen, and V. Sandoghdar, *Efficient coupling of photons to a single molecule and the observation of its resonance fluorescence*, Nature Phys. **4**, 60 (2008).

[30] M. Pototschnig, Y. Chassagneux, J. Hwang, G. Zumhofen, A. Renn, and V. Sandoghdar, *Controlling the phase of a light beam with a singler molecule*, Phys. Rev. Lett. **107**, 063001 (2011).

[31] F. Le Kien, S. D. Gupta, V. I. Balykin, and K. Hakuta, *Spontaneous emission of a cesium atom near a nanofiber: efficient coupling of light to guided modes*, Phys. Rev. A **72**, 032509 (2005).

[32] M. Fujiwara, K. Toubaru, T. Noda, H.-Q. Zhao, and S. Takeuchi, *Highly efficient coupling of photons from nanoemitters into single-mode optical fibers*, Nano Lett. **11**, 4362 (2011).

[33] R. Yalla, F. Le Kien, M. Morinaga, and K. Hakuta, *Efficient channeling of fluorescence photons from single quantum dots into guided modes of optical nanofiber*, Phys. Rev. Lett. **109**, 063602 (2012).

[34] L. Liebermeister, F. Petersen, A. v. Münchow, D. Burchardt, J. Hermelbracht, T. Tashima, A. W. Schell, O. Benson, T. Meinhardt, A. Krueger, A. Stiebeiner, A. Rauschenbeutel, H. Weinfurter, and M. Weber, *Tapered fiber coupling of single photons emitted by a deterministically positioned single nitrogen vacancy center*, Appl. Phys. Lett., in press, arXiv:1309.0421 (2013).

[35] T. Schröder, M. Fujiwara, T. Noda, H.-Q. Zhao, Oliver Benson, and S. Takeuchi, *A nanodiamond-tapered fiber system with high single-mode coupling efficiency*, Opt. Express **20**, 10490 (2012).

[36] F. P. Kapron, D. B. Keck, and R. D. Maurer, *Radiation losses in glass optical waveguides*, Appl. Phys. Lett. **17**, 423 (1970).

[37] A. Yariv, *Optical Electronics*, Saunders College Publishing (1991).

[38] B. E. A. Saleh and M. C. Teich, *Fundamentals of Photonics*, John Wiley & Sons (1991).

[39] L. Tong, R. R. Gattass, J.B. Ashcom, S. He, J. Lou, M. Shen, I. Maxwell, and E. Mazur, *Subwavelength-diameter silica wires for low-loss optical wave guiding*, Nature **426**, 816 (2003).

[40] G. Brambilla, V. Finazzi, and D. J. Richardson, *Ultra-low-loss optical fiber nanotapers*, Opt. Express **12**, 2258 (2004).

[41] A. M. Clohessy, N. Healy, D. F. Murphy, and C. D. Hussey, *Short low-loss nanowire tapers on singlemode fibres*, Electron. Lett. **41**, 954 (2005).

[42] M. Sumetsky, Y. Dulashko, P. Domachuk, and B. J. Eggleton, *Thinnest optical waveguide: experimental test*, Opt. Lett. **32**, 754 (2007).

[43] F. Warken, A. Rauschenbeutel, and T. Bartholomäus, *Fiber pulling profits from precise positioning*, Photon. Spectra **42**, 3, 73 (2008).

[44] S. Pricking and H. Giessen, *Tapering fibers with complex shape*, Opt. Express **18**, 3426 (2010).

[45] J. D. Love and W. M. Henry, *Quantifying loss minimization in single-mode fibre tapers*, Electron. Lett. **22**, 912 (1986).

[46] J. D. Love, W. M. Henry, W. J. Stewart, R. J. Black, S. Lacroix, and F. Gonthier, *Tapered single-mode fibres and devices, Part 1: Adiabaticity criteria*, IEE Proc-J, **138**, 343 (1991).

[47] A. W. Snyder and J. D. Love, *Optical Waveguide Theory*, Chapman & Hall (1983).

[48] E. Snitzer, *Cylindrical dielectric waveguide modes*, J. Opt. Soc. Am. **51**, 491 (1961).

[49] F. Le Kien, V. I. Balykin, and K. Hakuta, *Angular momentum of light in an optical nanofiber*, Phys. Rev. A **73**, 053823 (2006).

[50] G. Sagué Cassany, *Cold atom physics using ultra-thin optical fibers*, Dissertation, Rheinische Friedrich-Wilhelms Universität Bonn (2008).

[51] D. Gloge, *Weakly guiding fibers*, Appl. Opt. **10**, 2252 (1971).

[52] F. Le Kien, J. Q. Liang, K. Hakuta, and V. I. Balykin, *Field intensity distributions and polarization orientations in a vacuum-clad subwavelength-diameter optical fiber*, Opt. Commun. **242**, 445 (2004).

[53] C. Y. H. Tsao, D. N. Payne, and W. A. Gambling, *Modal characteristics of three-layered optical fiber waveguides: a modified approach*, J. Opt. Soc. Am. A **6**, 555 (1989).

[54] T. Erdogan, *Cladding-mode resonances in short- and long-period fiber grating filters*, J. Opt. Soc. Am. A **14**, 1760 (1997).

[55] T. Erdogan, *Cladding-mode resonances in short- and long-period fiber grating filters: errata*, J. Opt. Soc. Am. A **17**, 2113 (2000).

[56] Z. Zhang and W. Shi, *Eigenvalue and field equations of three-layered uniaxial fibers and their applications to the characteristics of long-period fiber gratings with applied axial strain*, J. Opt. Soc. Am. A **22**, 2516 (2005).

[57] A. S. Belanov, E. M. Dianov, G. I. Ezhov, and A. M. Prokhorov, *Propagation of normal modes in multilayer optical waveguides: I. Component fields and dispersion characteristics*, Sov. J. Quant. Electron. **6**, 43 (1976).

[58] M. Monerie, *Propagation in doubly clad single-mode fibers*, IEEE J. Quantum Elect. **18**, 535 (1982).

[59] S. G. Johnson and J. D. Joannopoulos, *Block-iterative frequency-domain methods for Maxwell's equations in a planewave basis*, Opt. Express **8**, 173 (2001).

[60] I. S. Gradshteyn and I. M. Ryzhik, *Table of integrals, series, and products*, Academic Press, Elsevier (2007).

[61] M. Abramowitz and I. Stegun, *Handbook of mathematical functions with formulas, graphs, and mathematical tables*, National Bureau of Standards, Applied Mathematics Series **55** (1972).

[62] A. W. Snyder, *Coupling of modes on a tapered dielectric cylinder*, IEEE T. Microw. Theory **MTT-18**, 383 (1970).

[63] A. Hartung, S. Brueckner, and H. Bartelt, *Limits of light guidance in optical nanofibers*, Opt. Express **18**, 3754 (2010).

[64] M. J. Adams, *An introduction to optical waveguides*, John Wiley & Sons (1981).

[65] A. Stiebeiner, R. Garcia-Fernandez, and A. Rauschenbeutel, *Design and optimization of broadband tapered optical fibers with a nanofiber waist*, Opt. Express **18**, 22677 (2010).

[66] R. Garcia-Fernandez, W. Alt, F. Bruse, C. Dan, K. Karpetyan, O. Rehband, A. Stiebeiner, U. Wiedemann, D. Meschede, and A. Rauschenbeutel, *Optical nanofibers and spectroscopy*, Appl. Phys. B **105**, 3 (2011).

[67] F. Warken, *Ultradünne Glasfasern als Werkzeug zur Kopplung von Licht und Materie*, Dissertation, Rheinische Friedrich-Wilhelms Universität Bonn (2007).

[68] J. Amlacher, *Versuche zur Herstellung von transmissions- und leitfähigen Glasfasern*, Bachelorarbeit, TU Wien (2013).

[69] T. A. Birks and Y. W. Li, *The shape of fiber tapers*, J. Lightwave Technol. **10**, 432 (1992).

[70] A.Jöckel, *Glasfaser-basierte Fabry-Pérot-Resonatoren mit integrierten ultradünnen Passagen*, Diplomarbeit, Johannes Gutenberg-Universität Mainz (2009).

[71] D. T. Cassidy, D. C. Johnson, and K. O. Hill, *Wavelength-dependent transmission of monomode optical fiber tapers*, Appl. Optics **24**, 945 (1985).

[72] Y. Jung, G. Brambilla, and D. J. Richardson, *Broadband single-mode operation of standard optical fibers by using a sub-wavelength optical wire filter*, Opt. Express **16**, 14661 (2008).

[73] M. Sumetsky, Y. Dulashko, and A. Hale, *Fabrication and study of bent and coiled free silica nanowires: Self-coupling microloop optical interferometer*, Opt. Express **12**, 3521 (2004).

[74] H. Haken and H. C. Wolf, *Molekülphysik und Quantenchemie*, Springer (2006).

[75] A. Szabo and N. S. Ostlund, *Modern quantum chemistry*, Dover (1996).

[76] J. Friedrich and D. Haarer, *Photochemical hole burning: a spectroscopic study of relaxation processes in polymers and glasses*, Angew. Chem. Int. Ed. Engl. **23** 113–140 (1984).

[77] C. Cohen-Tannoudji, J. Dupont-Roc, and G. Grynberg, *Atom-photon interactions*, John Wiley & Sons (1992).

[78] W. Demtröder, *Molecular physics*, Wiley-VCH (2005).

[79] B. H. Brandsden and C. J. Joachain, *Physics of atoms and molecules*, Prentice Hall (2003).

[80] D. Meschede, *Gerthsen Physik*, Springer (2002).

[81] M. Kasha, *Characterization of Electronic Transitions in Complex Molecules*, Discuss. Faraday Soc. **9**, 14 (1950).

[82] D. Meschede, *Optik, Licht und Laser*, Teubner (2005).

[83] W. Demtröder, *Laserspektroskopie*, Springer (2007).

[84] S. Kummer, S. Mais, and T. Basché, *Measurement of optical dephasing of a single terrylene molecule with nanosecond time resolution*, J. Phys. Chem. **99**, 17078 (1995).

[85] S. Kummer, F. Kulzer, R. Kettner, T. Basché, C. Tietz, C. Glowatz, and C. Kryschi, *Absorption, excitation, and emission spectroscopy of terrylene in p-terphenyl: Bulk measurements and single molecule studies*, J. Phys. Chem. **107**, 7673 (1995).

[86] D. Hsu and J. L. Skinner, *Nonperturbative theory of temperature-dependent optical dephasing in crystals. II. Pseudolocal phonons*, J. Chem. Phys. **83**, 2097 (1985).

[87] K. Huang, *Introduction to statistical physics*, Taylor and Francis (2001).

[88] S. Kummer, *Fluoreszenzspektroskopische Untersuchung einzelner Farbstoffmoleküle in kristallinen Festkörpern*, Dissertation, Ludwigs-Maximilians-Universität München (1996).

[89] W. Liptay, *Electrochromism and solvatochromism*, Angew. Chem. internat. Edit. **8** 177 (1969).

[90] A. S. Davydov, *Theory of molecular excitations*, McGraw-Hill (1962).

[91] A. M. Stoneham, *Shapes of inhomogeneously broadened resonance lines in solids*, Rev. Mod. Phys. **41**, 82 (1969).

[92] V. Bordo and H.-G. Rubahn, *Optics and spectroscopy at surfaces and interfaces* Wiley-VCH (2006).

[93] D. J. Norris, M. Kuwata-Gonokami, and W. E. Moerner, *Excitation of a single molecule on the surface of a spherical microcavity*, Appl. Phys. Lett. **71**, 297 (1997).

[94] W. E. Moerner and L. Kador, *Optical detection and spectroscopy of single molecules in a solid*, Phys. Rev. Lett. **26**, 2535 (1989).

[95] M. Orrit and J. Bernard, *Single pentacene molecules detected by fluorescence excitation in a p-terphenyl crystal*, Phys. Rev. Lett. **65**, 2716 (1990).

[96] W. P. Ambrose, T. Basché, and W. E. Moerner, *Detection and spectroscopy of single pentacene molecules in a p-terphenyl crystal by means of fluorescene excitation*, J. Chem. Phys. 95, 7150 (1991).

[97] V. Sandoghdar, J. Michaelis, C. Hettich, C. Schmitt, J. Zitzman, and S. Kühn, *Results and thoughts on optical microscopy using a single-molecule probe*, Single Mol. **2**, 277 (2001).

[98] E. Betzig and R. J. Chichester, *Single molecules observed by near-field scanning optical microscopy*, Science **262**, 1422 (1993).

[99] S. Nie, D. T. Chiu, and R. N. Zare, *Probing individual molecules with confocal fluorescence microscopy*, Science **266**, 1018 (1994).

[100] T. Funatsu, Y. Harada, M. Togunaga, K. Saito, T. Yanagida, *Imaging of single fluorescent molecules and individual ATP turnovers by single myosin molecules in aqueous solution*, Nature **374**, 555 (1995).

[101] F. Güttler, T. Irngartinger, T. Plakhotnik, A. Renn, U.P. Wild, *Fluorescence microscopy of single molecules*, Chem. Phys. Lett. **217**, 393 (1994).

[102] W. E. Moerner, T. Basché, *Optical spectroscopy of single impurity molecules in solids*, Angew. Chem. Int. Ed. Engl. **32**, 457 (1993).

[103] W. E. Moerner and T. P. Carter, *Statistical fine structure of inhomogeneously broadened absorption lines*, Phys. Rev. Lett. **59**, 2705 (1987).

[104] H. Talon, L. Fleury, J. Bernard, and M. Orrit, *Fluorescence excitation of single molecules*, J. Opt. Soc. Am B **9**, 825 (1992).

[105] R. Loudon, *The quantum theory of light*, London University Press (1983).

[106] H. J. Carmichael and D. F. Walls, *Proposal for the measurement of the resonant Stark effect by photon correlation techniques*, J. Phys. B **9** L43 (1976).

[107] H. J. Kimble, M. Dagenais, and L. Mandel, *Photon antibunching in resonance fluorescence*, Phys. Rev. Lett. **39**, 691 (1977).

[108] T. Basché, W. E. Moerner, M. Orrit, and H. Talon, *Photon antibunching in the fluorescence of a single dye molecule trapped in a solid*, Phys. Rev. Lett. **69**, 1516 (1992).

[109] L. Fleury, J.-M. Segura, G. Zumhofen, B. Hecht, and U. P. Wild, *Nonclassical photon statistics in single-molecule fluorescence at room temperature*, Phys. Rev. Lett. **84**, 1148 (2000).

[110] R. Brown, J. Wrachtrup, M. Orrit, J. Bernard, and C. v. Borczyskowski, *Kinetics of optically detected magnetic resonance of single molecules*, Chem. Phys. **100**, 7182 (1994).

[111] A. J. Lovinger, S. R. Forrest, M. L. Kaplan, P. H. Schmidt, and T. Venkatesan, *Structural and morphological investigation of the development of electrical conductivity in iron-irradiated thin films of an organic material*, J. Appl. Phys. **55**, 476 (1984).

[112] A. Stiebeiner, O. Rehband, R. Garcia-Fernandez, and A. Rauschenbeutel, *Ultra-sensitive fluorescence spectroscopy of isolated surface-adsorbed molecules using an optical nanofiber*, Opt. Express **17**, 21704 (2009).

[113] F. Güttler, M. Croci, A. Renn, and U. Wild, *Single molecule polarization spectroscopy: pentacene in p-terphenyl*, Chem. Phys. **211**, 421 (1996).

[114] P. Bordat and R. Brown, *Molecular mechanisms of photo-induced spectral diffusion of single terrylene molecules in p terphenyl*, J. Chem. Phys. **116**, 229 (2002).

[115] K. S. Sundararajan, *Optical studies on organic crystals Part I*, Zeitschrift für Kristallographie **93**, 238 (1936).

[116] S. Kummer, Th. Basché, and C. Bräuchle, *Terrylene in p-terphenyl: a novel single crystalline system for single molecule spectroscopy at low temperatures*, Chem. Phys. Lett. **229**, 309 (1994).

[117] *Datasheet Matisse DS*, Sirah Laser- und Plasmatechnik GmbH (2012).

[118] *Verdi Single FAP Lasers Operator's Manual*, Coherent Inc. (2007).

[119] D. W. Allan, *Statistics of atomic frequency standards*, Proc. IEEE **54**, 221 (1966).

[120] O. Rehband, *Aufbau einer Vakuumapparatur zur Spektroskopie dünner Schichten auf ultradünnen Glasfasern*, Diplomarbeit, Johannes Gutenberg-Universität Mainz (2009).

[121] http://www.ceramisis.com/advanced_ceramics_pbn.htm

[122] http://accuratus.com/boron.html

[123] J. Ekin, *Experimental Techniques for Low Temperature Measurements: Cryostat Design, Materials, and Critical-Current Testing*, Oxford University Press (2006).

[124] http://www.sigmaaldrich.com/catalog/product/aldrich/p11255

[125] E. R. I. Abraham and E. A. Cornell, *Teflon feedthrough for coupling optical fibers into ultrahigh vacuum systems*, Applied Optics **37**, 1762 (1998).

[126] S. Y. T. van de Meerakker, H. L. Bethlem, and G. Meijer, *Taming molecular beams*, Nature Physics **4**, 595 (2008).

[127] N. Konken, *Faserbasierte Spektroskopie von organischen Molekülen in Festkörpermatrizen bei kryogenen Temperaturen*, Diplomarbeit, Johannes Gutenberg-Universität Mainz (2010).

[128] M. Numrich, *Nanofaser-basierte Spektroskopie von Molekülen in organischen Kristallen bei kryogenen Temperaturen*, Diplomarbeit, Johannes Gutenberg-Universität Mainz (2012).

[129] G. K. White, *Thermal expansion of reference materials: copper, silica and silicon*, J. Phys. D **6**, 2070 (1973).

[130] H. G. Dorsey, *Coefficient of linear expansion at low temperatures*, Phys. Rev. **25**, 88 (1907).

[131] R. Menzel, *Photonics*, Springer (2007).

[132] P. Eiswirt, *Untersuchung der Speicherzeitlimitierung einer nanofaserbasierten Dipolfalle*, Diplomarbeit, Johannes Gutenberg-Universität Mainz (2011).

[133] I. Langmuir, *The constitution and fundamental properties of solids and liquids. Part I. Solids.*, J. Am. Chem. Soc. **38**, 2221 (1916).

[134] U. Gómez, M. Leonhardt, H. Port, and H. C. Wolf, *Optical properties of amorphous ultrathin films of perylene derivatives*, Chem. Phys. Lett. **268**, 1 (1997).

[135] H. Proehl, Th. Dienel, R. Nitsche, and T. Fritz, *Formation of solid-state excitons in ultrathin crystalline films of PTCDA: from single molecules to molecular stacks*, Phys. Rev. Lett. **93**, 097403 (2004).

[136] S. R. Forrest, *Ultrathin organic grown by organic molecular beam deposition and related techniques*, Chem. Rev. **97**, 1793 (1997).

[137] H. Zollinger, *Color Chemistry*, Wiley–VCH (2003).

[138] K. Glöckler, C. Seidel, A. Soukopp, M. Sokolowski, E. Umbach, M. Böhringer, R. Berndt, and W.-D. Schneider, *Highly ordered structures and submolecular scanning tunnelling microscopy contrast of PTCDA and DM-PBDCI monolayers on Ag(111) and Ag(110)*, Surf. Sci. **600**, 1 (1998).

[139] M. Klessinger, *Konstitution und Lichtabsorption organischer Farbstoffe*, Chem. unserer Zeit **12**, 1 (1978).

[140] K. Gustav, M. Leonhardt, and H. Port, *Theoretical investigations on absorption and fluorescence of perylene and its tetracarboxylic derivatives*, Monatsh. Chem. **128**, 105 (1997).

[141] M. Hoffmann, *Frenkel and charge-transfer excitons in quasi-one-dimensional molecular crystals with strong intermolecular orbital overlap*, Dissertation, Technische Universität Dresden (2000).

[142] R. Scholz, A. Y. Kobitzki, T. U. Kampen, M. Schreiber, D. R. T. Zahn, G. Jungnickel, M. Elstner, M. Sternberg, and T. Frauenheim, *Resonant Raman spectroscopy of 3,4,9,10-perylene-tetracarboxylic-dianhydride epitaxial films*, Phys. Rev. B **61**, 13659 (2000).

[143] M. Wewer and F. Stienkemeier, *Laser-induced fluorescence spectroscopy of 3,4,9,10-perylenetetracarboxylic-dianhydrid in helium nanodroplets*, J. Chem. Phys. **120**, 1239 (2004).

[144] C. Seidel, C. Awater, X. D. Liu, R. Ellerbrake, and H. Fuchs, *A combined STM, LEED and molecular modelling study of PTCDA grown on Ag(110)*, Surf. Sci. **371**, 123 (1997).

[145] E. Umbach, M. Sokolowski, and R. Fink, *Substrate-interaction, long-range order, and epitaxy of large organic adsorbates*, Appl. Phys. A. **63**, 565 (1996).

[146] H. Proehl, R. Nitsche, T. Dienel, K. Leo, and T. Fritz, *In situ differential reflectance spectroscopy of thin crystalline films of PTCDA on different substrates*, Phys. Rev. B **71**, 165207 (2005).

[147] T. Ogawa, K. Kuwamoto, S. Isoda, T. Kobayashi, and N. Karl, *3,4:9,10-Perylenetetracarboxylic dianhydride (PTCDA) by electron crystallography*, Acta Crystallogr. B **55**, 123 (1999).

[148] V. Bulović, P. E. Burrows, S. R. Forrest, J. A. Cronin, M. E. Thompson, *Study of localized and extended excitons in 3,4,9,10-perylenetetracarboxylic dianhydride (PTCDA): I. Spectroscopic properties of thin films and solutions*, Chem. Phys. **210**, 1 (1996).

[149] M. Meucci, E. Marotti, P. Bicchi, C. Marinelli, and L. Moi, *Light-induced atom desorption*, Europhys. Lett. **25**, 639 (1994).

[150] L. T. Zhuravlev, *Concentration of hydroxyl groups on the surface of amorphous silicas*, Langmuir **3**, 316 (1987).

[151] M. B. Haider, J. L. Pitters, G. A. DiLabio, L. Livadaru, J. Y. Mutus, and R. A. Wolkow, *Controlled coupling and occupation of silicon atomic quantum dots at room temperature*, Phys. Rev. Lett. **102**, 046805 (2009).

[152] P. G. Piva, G. A. DiLabio, J. L. Pitters, J. Zikovsy, M. Rezeq, S. Dogel, W. A. Hofer, and R. A. Wolkow, *Field regulation of single-molecule conductivity by a charged surface atom*, Nature **435**, 658 (2005).

[153] K. Puech, H. Fröb, M. Hoffmann, and K. Leo, *Luminescence of ultrathin organic films: transition from monomer to excimer emission*, Opt. Lett. **21**, 1606 (1996).

[154] J. L. Clark, P. F. Miller, and G. Rumbles, *Red edge photophysics of ethanolic Rhodamine 101 and the observation of laser cooling in the condensed phase*, J. Phys. Chem. A **102**, 4428 (1998).

[155] J. L. Clark and G. Rumbles, *Laser cooling in the condensed phase by frequency up-conversion* Phys. Rev. Lett. **76**, 2037 (1996).

[156] M. Sheik-Bahae and R. I. Epstein *Laser cooling of solids*, Laser Photonics Rev. **3**, 67 (2009).

[157] G. Nemova, and R. Kashyap, *High efficiency solid state laser cooling in Yb^{3+}:ZBLANP fiber with tilted fiber Bragg grating structures*, Phys. Status Solidi C **6**, 248 (2009).

[158] D. V. Seletskiy, S. D. Melgaard, A. di Lieto, M. Tonelli, and M. Sheik-Bahae, *Laser cooling of a semiconductor load to 165 K*, Opt. Express **18**, 18061 (2010).

[159] M. Leonhardt, *UHV-Aufdampfschichten von PTCDA: Korrelation von optischer Spektroskopie und Schichtaufbau*, Dissertation, Universität Stuttgart (2002).

[160] W. Bała, Z. Łukasiak, M. Rebarz, P. Dalasiński, A. Bratkowski, D. Bauman, and R. Hertmanowski, *Photoluminescence characterization of vacuum deposited PTCDA thin films*, Opto-Electron. Rev. **12**, 445 (2004).

[161] S. M. Karotke, *Stark-shift microscopy: interaction of a confined electric field with single emitters*, Dissertation, Universität Basel (2006).

[162] C. Hettich, *Coherent optical dipole coupling of two individual molecules at nanometre separation*, Dissertation, Universität Konstanz (2002).

[163] A. Bohnen, K.-H. Koch, W. Lüttke, and K. Müllen, *Oligorylene as a model for "Poly(perinaphthalene)"*, Angew. Chem. Int. Ed. **29**, 525 (1990).

[164] A. Drechsler, *Hochaufgelöste optische Spektroskopie einzelner Terrylen-Moleküle bei kryogenen Temperaturen mit einem Parabolspiegelmikroskop*, Dissertation, Universität Siegen (2002).

[165] J. Sepioł, J. Jasny, J. Keller, and Urs P. Wild, *Single molecules observed by immersion mirror objective. The orientation of terrylene molecules via the direction of its transition dipole moment*, Chem. Phys. Lett. **273**, 444 (1997).

[166] E. Clar, W. Kelly, and R. M. Laird, *Die Synthesen des Terrylens und Quaterrylens und über das vermeintliche Quaterrylen von A. Zinke*, Monatsh. Chem. **80**, 391 (1956).

[167] E. Clar, *Das Kondensationsprinzip, ein einfaches neues Prinzip im Aufbau der aromatischen Kohlenwasserstoffe*, Chem. Ber. **81**, 52 (1948).

[168] I. Deperasinska, B. Kozankiewiewicz, I. Biktchantaev, and J. Sepiol, *Anomalous fluorescence of terrylene in neon matrix*, J. Phys. Chem. A **105**, 810 (2001).

[169] G. Hoheisel and Achim Hese, *High resolution laser induced fluorescence excitation spectroscopy of jet-cooled terrylene*, J. Mol. Spectrosc. **235**, 211 (2006).

[170] H. M. Rietveld, E. N. Maslen, and C. J. B. Clews, *An x-ray and neutron diffraction refinement of the structure of p-terphenyl*, Acta Cryst. B **26**, 693 (1970).

[171] T. Kobayashi, *Conformational analysis of terphenyls by photoelectron spectroscopy*, Bull. Chem. Soc. Jpn. **56**, 3224 (1983).

[172] J. L. Baudour, *Structural phase transition in polyphenyls. X. Potential barrier heights in crystalline polyphenyls and in gaseous biphenyl determined uniquely from diffraction data*, Acta Cryst. B **47**, 935 (1991).

[173] J. L. Baudour, Y. Delugeard, and H. Cailleau, *Transition structurale dans les polyphényles. I. Structure cristalline de la phase basse température du p-terphényle à 113 K*, Acta Cryst. B **32**, 150 (1976).

[174] T. G. Pavlopoulos and P. R. Hammond, *Spectroscopic Studies of Some Laser Dyes*, J. Am. Chem. Soc. **96**, 6568 (1974).

[175] P. Bordat and R. Brown, *Elucidation of optical switching of single guest molecules in terrylene/p-terphenyl mixed crystals*, Chem. Phys. Lett. **331**, 439 (2000).

[176] J. N. Lalena, D. A. Cleary, E. Carpenter, and N. F. Dean, *Inorganic Materials Synthesis and Fabrication*, John Wiley & Sons (2008).

[177] R. A. Buckingham, *The Classical Equation of State of Gaseous Helium, Neon and Argon*, Proc. R. Soc. Lon. Ser. A **168**, 264 (1938).

[178] F. Kulzer, S. Kummer, R. Matzke, C. Bräuchle, and Th. Basché, *Single-molecule optical switching of terrylene in p-terphenyl*, Nature **387**, 688 (1997).

[179] A. W. Schell, G. Kewes, T. Schröder, J. Wolters, T. Aichele, and O. Benson, *A scanning probe-based pick-and-place procedure for assembly of integrated quantum optical hybrid devices*, Rev. Sci. Instrum. **82**, 073709 (2011).

[180] M. E. Noz and G. Q. Maguire, *Radiation Protection in the Health Sciences*, World Scientific Pub. Co. (2007).

[181] H.-H. Perkampus, *UV-VIS-Spektroskopie und ihre Anwendungen*, Springer (1986).

[182] K.-Th. Wilke, *Kristallzüchtung*, J. A. Barth (1993).

[183] J. Michaelis, *Mikroskopie mit einem einzelnen Molekül als Lichtquelle*, Dissertation, Universität Konstanz (2000).

[184] F. Kulzer, F. Koberling, Th. Christ, A. Mews, and Th. Basché, *Terrylene in p-terphenyl: single-molecule experiments at room temperature*, Chem. Phys. **247**, 23 (1999).

[185] http://www.andor.com/pdfs/specifications/Andor_Shamrock_303_Specifications.pdf

[186] A. B. Myers, P. Tchénio, M. Z. Zgierski, and W. E. Moerner, *Vibronic spectroscopy of individual molecules in solids*, J. Phys. Chem. **98**, 10377 (1994).

[187] D. Heine, *Single atom detection and non-classical photon correlations*, Dissertation, Ruperto-Carola Universität Heidelberg (2008).

Danksagung

An dieser Stelle möchte ich all denjenigen danken, die zum Gelingen dieser Arbeit beigetragen haben.

Mein besonderer Dank gilt meinem Doktorvater für die Gelegenheit, an diesem faszinierenden und innovativen Projekt arbeiten zu dürfen, sowie für die konstante Unterstützung, die vielen anregenden Diskussionen und die hervorragenden Arbeitsbedingungen, die er für die Arbeitsgruppe geschaffen hat.

Viele der gezeigten Ergebnisse wären ohne die großartige Arbeit des Molekül-Teams nicht möglich gewesen. Besonders glücklich schätze ich mich eine Betreuerin gehabt zu haben, auf die ich mich immer verlassen konnte und der ich für ihre Geduld und ihren Optimismus danken möchte. Meinem Mit-Doktoranden und unseren Diplomanden danke ich für die gute Zusammenarbeit, sei es bei langen Messungen, sei es bei technischen und organisatorischen Herausforderungen. Meiner Diplomandin danke ich für die Vakuum-Aperatur und weit darüber hinaus.

Ohne meine Arbeitsgruppe wären die letzten Jahre sicherlich um einiges trister und uninspirierender gewesen. Ich danke Euch allen für die tolle Zusammenarbeit und die herausragende Arbeitsatmosphäre. Mein Dank gebührt außerdem allen, die Teile dieser Arbeit Korrektur gelesen haben.

Zu der positiven Arbeitsatmosphäre haben sicherlich auch die benachbarten Arbeitsgruppen in der AG QUANTUM in Mainz und am Atominstiut in Wien beigetragen. In diesem Zusammenhang möchte ich besonders meinem Zweit-Gutachter für die Übernahme des Koreferats danken. Hier sollen auch auf keinen Fall die Mitarbeiter in der Verwaltung und den technischen Werkstätten unerwähnt bleiben, auf die man sich auch in dringenden Fällen immer verlassen kann.

Außerdem danke ich den Kollegen vom Institut für physikalische Chemie an der Uni Bonn, vom Max Planck Institut für Polymerforschung in Mainz und vom Institut für Physikalische Chemie an der Uni Mainz für die Unterstützung bei der Beschaffung und dem Umgang mit organischen Molekülen sowie den gelegentlichen Austausch.

Nicht zuletzt möchte ich mich bei meiner Familie und meinen Freunden für den Rückhalt, die Unterstützung und auch den ein oder anderen Anstoß bedanken. Danke für Eure Geduld und Euer Verständnis!